Hybrid resonators for light trapping and emission control

Ph.D. Thesis, University of Amsterdam, January 2019
Hybrid resonators for light trapping and emission control
Hugo Michiel Doeleman

ISBN: 978-94-92323-24-8

The work described in this thesis was performed at
AMOLF, Science Park 104, 1098 XG Amsterdam, The Netherlands.

This work is part of the Netherlands Organisation for Scientific Research (NWO).

A digital version of this thesis can be downloaded from
http://www.amolf.nl

Hybrid resonators for light trapping and emission control

ACADEMISCH PROEFSCHRIFT

ter verkrijging van de graad van doctor aan de Universiteit van
Amsterdam, op gezag van de Rector Magnificus
prof. dr. ir. K.I.J. Maex
ten overstaan van een door het College voor Promoties ingestelde commissie,
in het openbaar te verdedigen in de Agnietenkapel
op vrijdag 18 januari 2019, te 10:00 uur

door

Hugo Michiel Doeleman

geboren te Amsterdam.

Promotiecommissie

Promotor:	prof. dr. A. F. Koenderink	Universiteit van Amsterdam
Copromotores:	dr. R. J. C. Spreeuw	Universiteit van Amsterdam
	prof. dr. E. Verhagen	Technische Universiteit Eindhoven
Overige leden:	prof. dr. J. J. Baumberg	University of Cambridge
	prof. dr. L. Kuipers	Technische Universiteit Delft
	prof. dr. H. B. van Linden van den Heuvell	Universiteit van Amsterdam
	prof. dr. A. Polman	Universiteit van Amsterdam
	prof. dr. M. S. Golden	Universiteit van Amsterdam

Faculteit der Natuurwetenschappen, Wiskunde en Informatica.

Contents

Chapter 1

Introduction

Humans were shaped by light. Sight is our most versatile tool to perceive our surrounding, and thus to survive. Our very appearance is determined by light. The colour of our skin derives from its ability to protect us from sunlight, and our eyes combine beauty with a breathtaking capability to detect light intensities between a single photon [1] and bright sunlight (more than 10^{16} photons per second). While vision forms our natural connection to light, daily life in a modern society is impacted by light in many more ways. Light carries energy, which can be harvested in a solar panel or used to cut through steel. It also carries information, used in the optical fiber network that spans the globe and forms the backbone of the internet [2]. Its interaction with matter allows remarkably precise measurements, for example of individual viruses, antibodies or proteins [3, 4]. Imaging systems such as microscopes and telescopes are used to understand both the extremely distant — stars and galaxies — and the extremely close, such as cells, skin tumors or bacteria. Owing to the recent developments in computer processing power, imaging is expanding its impact on our lives by facilitating for example self-driving cars and automated face recognition. This increase in processing power, in turn, would not have been possible without light, as advances in optical lithography drive the exponential miniaturization of the elements on computer chips.

Despite everything we can do with light, there is still more we cannot do. The interaction between light and matter is extremely weak. Visible light has a wavelength around 500 nm, and the diffraction limit [5] prevents focusing it to a spot smaller than half this wavelength. Electrons, on the other hand, which form the part of matter that interacts mostly with light, are typically localized on the scale of an atom or molecule: $\sim$1 nm or less. This enormous size mismatch makes the probability of light absorption or emission very low, limiting for example the miniaturization of light sources and detectors. It also prevents optical non-linearities at low power, a requirement for all-optical

information processing which could make computers much faster and more energy-efficient [6]. Such practical applications aside, a whole realm of fascinating new physics is accessible only with stronger light-matter interaction.

Luckily, light-matter interaction can be enhanced. One can either make the light pass the atom (or whatever it needs to interact with) multiple times, or squeeze the light to sizes below the diffraction limit. The first is achieved by an optical cavity [7] — a resonator that traps light for many oscillation periods — while the second can be done through plasmonics [8–10], which couples the light to free electrons in a (noble) metal to create extremely confined fields.

Although both cavities and plasmonic structures have enjoyed great successes, each is troubled by fundamental limitations, as we will discuss further in this chapter. To unlock the full potential of strong light-matter interactions, alternative methods are required. This thesis concerns alternative strategies to store and confine light, based on hybrid resonators. These resonators combine two or more coupled optical resonances, and the resulting hybrid system can have unique properties that are unavailable with the individual constituents. In this chapter, we first discuss how light-matter interaction strength can be quantified and compare figures of merit for various applications. We then briefly discuss the current state of the art in controlling interaction strength using optical cavities or plasmonic antennas. The bulk of this thesis deals with combinations of such cavities and antennas. We therefore provide an overview of the work done on such hybrid antenna-cavity systems. We conclude with a motivation and outline of this thesis.

1.1 Quantifying light-matter interaction

One of the most common light-matter interactions is the absorption or emission of a photon by a small particle, for example an atom or a molecule. The energy of a photon is transferred via an optical transition to an excited state in the particle, or vice versa. To quantify light-matter interaction strength, let us consider such a system of an emitter — treated as an ideal two-level system — coupled to a light field, using the formalism of cavity quantum electrodynamics (CQED) [11]. This will deliver several fundamental figures of merit that govern the interaction strength. We will find that these figures of merit are applicable not just for typical situations studied in CQED, but for other physical processes and applications as well.

The interaction strength between light and a small emitter is determined by the electric dipole interaction Hamiltonian $\hat{\mathcal{H}} = -\hat{\boldsymbol{\mu}} \cdot \hat{\mathbf{E}}$, where $\hat{\boldsymbol{\mu}}$ is the dipole moment operator of the optical transition, and $\hat{\mathbf{E}}$ is the electric field operator [11, 12]. If the electric field is that of a single, empty optical mode, we can write $\langle i| \hat{\mathcal{H}} |f\rangle = \hbar g$, with $g = \mu\sqrt{\omega/(2\hbar V \epsilon_0 \epsilon)}$ the emitter-field coupling rate from the Jaynes-Cummings Hamiltonian and $\mu = |\boldsymbol{\mu}| = |\langle g| \hat{\boldsymbol{\mu}} |e\rangle|$ the dipole moment of the transition from electronic excited state $|e\rangle$ to ground

state $|g\rangle$ [12, 13]. Here, V represents the volume occupied by the optical mode, and $\epsilon = n^2$ is the relative permittivity of the material embedding the emitter. From this we recognize that the coupling rate g depends both on purely electronic properties of the emitter, captured in μ, and on the confinement of the optical mode, captured in V. Thus, it is possible to modify light-matter interactions by shaping the photonic environment. This has been the main endeavour in the field of CQED since 1946 [14, 15]. These efforts have greatly improved our understanding of both light and matter, and have been lauded with many awards including the 2012 Nobel prize for Haroche and Wineland.

The manner in which the coupling rate g affects an emitter depends on the losses in the system. If we assume that the emitter losses are negligible, losses are determined by the decay rate κ of the optical mode, or its quality factor $Q = \omega/\kappa$.* Two distinct regimes can be considered — the weak coupling regime, with $2g < \kappa$, and the strong coupling regime, with $2g > \kappa$. We discuss them here briefly.

1.1.1 Weak coupling — Spontaneous emission and the Purcell effect

If $2g < \kappa$, energy in the optical mode is lost more rapidly than it is exchanged between the mode and the emitter [13]. This is known as the weak coupling regime, and it renders the process of spontaneous emission irreversible. The rate of spontaneous emission is then determined by Fermi's Golden Rule, which prescribes that the transition rate from an initial (excited) state $|i\rangle$ to a set of final states $|f\rangle$ with energy difference $E_i - E_f = \hbar\omega$ is [12]

$$\Gamma = \sum_f \frac{2\pi}{\hbar} \left| \langle i | \hat{\mathcal{H}} | f \rangle \right|^2 \delta(E_i - E_f). \tag{1.1}$$

Importantly, $|i\rangle$ and $|f\rangle$ are states of the complete emitter-radiation system. Hence, even if there is only one electronic ground-state for the emitter to decay to, the summation in Eq. (1.1) should nevertheless be taken over all possible photonic states at frequency ω. Equation (1.1) applies in any photonic system, whether dominated by a single cavity mode, or characterized by a continuum. We can rewrite Eq. (1.1) as [12]

$$\Gamma = \frac{\pi\omega}{3\hbar\epsilon_0} |\boldsymbol{\mu}|^2 \rho_\mu(\omega, \boldsymbol{r}), \tag{1.2}$$

where we introduced $\rho_\mu(\omega, \boldsymbol{r})$, the optical local density of states (LDOS) [17]. This represents the density per unit volume and unit frequency range of optical states at frequency ω, available to an emitter at position $\boldsymbol{r}$ and with a dipole orientation $\boldsymbol{\mu}$. Although spontaneous emission is

*For a derivation including finite emitter losses and dephasing, see [16].

an inherently quantum-mechanical process, the LDOS can be calculated classically [12, 18] and depends only on the photonic environment. In a homogeneous medium, $\rho(\omega, \boldsymbol{r}) = \omega^2 n/(\pi^2 c^3)$ for any dipole orientation (see Fig. 1.1) [12]. LDOS is a convenient figure of merit in photonics, as it quantifies the *photonic* contribution to the spontaneous emission rate. In contrast, the electronic contribution is commonly quantified by the oscillator strength $f = 2\mu^2 m\omega/(\hbar e^2)$ of a transition, with e and m respectively the electron charge and mass [13].

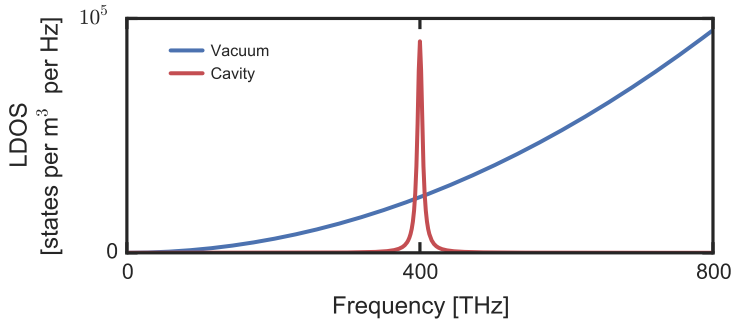

Figure 1.1: LDOS in a cavity and in vacuum. In a homogeneous medium such as vacuum (blue), LDOS scales as ω^2, whereas in a single-mode cavity (red), LDOS shows a single peak at cavity resonance, with a linewidth given by κ. Although in the cavity there is only one state, the density of states can be very high if κ and V are small. The Purcell factor is the ratio of cavity LDOS and the LDOS of the homogeneous medium, evaluated at cavity resonance.

The LDOS can in principle be found for any optical environment, including an optical cavity supporting a single mode. In this case, the LDOS at cavity resonance can be found by inserting $\langle i|\,\hat{\mathcal{H}}\,|f\rangle = \hbar g$ into Eq. (1.1) and using the *energy* density of states $2/(\pi\hbar\kappa)$ of a single cavity mode at cavity resonance to replace the sum by an integral over photon energy and remove the delta function [13]. This yields a cavity LDOS $\rho_\mathrm{c} = 6/(\pi\kappa V)$ (see Fig. 1.1) and decay rate $\Gamma_\mathrm{c} = 4g^2/\kappa$. Normalizing Γ_c to the emitter decay rate γ in a medium of index n yields the famous Purcell factor[†]

$$F_\mathrm{P} = \frac{\Gamma_\mathrm{c}}{\gamma} = \frac{4g^2}{\gamma\kappa} = \frac{3}{4\pi^2}\frac{Q}{V}\left(\frac{\lambda}{n}\right)^3. \tag{1.3}$$

This expression was first derived in 1946 by Purcell [14], who was the first to realize that the probability of a spontaneous transition mediated by a photon

[†]The terms LDOS, Purcell enhancement, emission enhancement and Purcell factor are often (confusingly) used interchangeably in literature. In this thesis, LDOS refers to ρ_μ as used in Eq. (1.2). By Purcell enhancement, emission enhancement or relative LDOS we mean ρ_μ relative to that in a homogeneous medium (usually vacuum). The Purcell factor exclusively refers to the *peak value* of the Purcell enhancement due to a particular resonance.

could be modified by the environment. In his case, this involved radiative transitions of nuclear magnetic moments at radio frequencies, which he found could be strongly accelerated by coupling to a resonant electric circuit. In the late 1960's, this fact was first observed experimentally at optical frequencies by Drexhage [19], not using a cavity but instead by modifying LDOS through the distance of emitters to a mirror. For completeness, we note that the photonic environment not only modifies the emitter decay rate, but also its resonance frequency, although this so-called 'Lamb shift' is typically very small [12, 20].

Spontaneous emission control has proven useful in several important applications. Enhancing the emission rate of light-emitting diodes (LEDs), which are currently limited to switching speeds of ∼100 MHz, would make these ideally suited as light sources in optical interconnects on a microprocessor, which could dramatically decrease the power consumption of microcomputing [21, 22]. Moreover, enhancing the spontaneous emission rate additionally provides control over where the light is going [23], which enables, for example, directional emission or efficient collection of the light from such on-chip LEDs. Reciprocity guarantees that a strongly directional emitter also has a directional absorption pattern, which has been proposed as a key parameter enabling nano-scale solar cells to surpass the Shockley-Queisser efficiency limit [24]. LDOS enhancements can also benefit the development of small, low-threshold lasers. Spontaneous emission and stimulated emission are intimately linked through the Einstein coefficients. It is therefore not surprising that the pump power required to reach the lasing threshold is proportional to V/Q, with Q and V the quality factor and mode volume of the laser cavity mode [25]. Hence, improving Q/V decreases the minimal operation power of a laser, which can lead to a reduction of energy usage in optical communication [22, 25]. A fact that is surprising, is that the Purcell factor can also influence processes that are not related to emission at all. Optical resonators can be used to sense small particles such as single viruses or molecules [3, 26]. The detection sensitivity is determined by $\Delta\omega/\kappa$, with $\Delta\omega$ the resonator lineshift induced by the particle. Cavity perturbation theory [27] states that, for a single small particle perturbing a resonator, $\Delta\omega \propto V^{-1}$. As a consequence, sensitivity is directly proportional to the Purcell factor. Going beyond currently available technologies, an hotly pursued outstanding challenge is the development of a quantum network, which would enable quantum-secure communications, quantum information processing and quantum simulations [28–31]. Photons are one of the preferred candidates to transport quantum information between the nodes in this network, due to their high speed and low-noise properties at optical frequencies. An essential component of such a network would be a fast, deterministic and efficient source of single photons [30]. Quantum emitters such as atoms, molecules or quantum dots could be at the heart of such a source [32]. However, their intrinsic decay rates are typically around 100 MHz, preventing high-frequency operation, and emission patterns are isotropic, which is detrimental to achieve a high collection efficiency [33].

Coupling these emitters to an optical resonator solves both issues — emission rates are enhanced and emission is redistributed into the resonator with efficiency $F_\mathrm{P}/(1+F_\mathrm{P})$ [23].

1.1.2 Strong coupling — Photon-photon interaction

If the Purcell factor is increased to the point where the emitter decay rate $\Gamma = F_\mathrm{P}\gamma$ approaches the cavity linewidth κ, such that $2g \approx \kappa$, one enters the regime of strong coupling. If $2g > \kappa$, energy is exchanged between emitter and optical mode more rapidly than it decays. Emitted light can thus be reabsorbed and re-emitted several times before it is lost, leading to the well-known vacuum Rabi oscillations — the probabilities of finding an excitation in the emitter or in the optical mode are periodically exchanged. The Purcell effect no longer holds in this regime — stronger coupling rates g increase the exchange rate between cavity and emitter, yet the total decay rate of the system is fixed at κ (or to $\kappa + \gamma + 2\gamma^*$, if emitter decay γ and dephasing γ^* are not neglected [13, 16]). Whereas in the time domain, strong coupling is marked by Rabi oscillations, in the frequency domain this corresponds to a splitting of the emission peak known as vacuum Rabi splitting.

Single-emitter strong coupling to an optical cavity mode has been one of the major goals in CQED [34], and was first observed at radio frequencies by Rempe *et al.* in 1987 [35], and at optical frequencies by Thompson *et al.* in 1992 [36]. This fascinating phenomenon shows that not just decay rates, but even the eigenstates of matter depend on the photonic environment. In the strong coupling regime, these eigenstates become so-called dressed states — hybridized states of light and matter excitation. This effect can be used to coherently manipulate the emitter through entanglement with single photons, and to establish an effective interaction between two photons. Another key component of the quantum photonic network mentioned in the previous section would be the node that processes the quantum information carried by single photons. However, information processing requires interaction between signals. Although photons normally do not interact, a cavity strongly coupled to an emitter responds very differently to a single photon than to two photons [6, 37]. As a consequence, whether a photon is transmitted or reflected by the cavity depends on the presence of another photon, which corresponds to an effective interaction between the photons and allows quantum logical operations with single photons [23].

1.2 Optical cavities

Historically, the first attempts to reach high Purcell factors or strong coupling have focused on obtaining very high Q by using optical cavities [7]. Typically, very high reflectivity mirrors or lossless dielectrics are used, which have

enabled quality factors up to $Q \approx 8 \cdot 10^9$ [38]. Mode volumes, however, are limited approximately to $(\lambda/(2n))^3$ because cavities rely on interference effects [39]. Here, we summarize the current state of the art for cavities in the context of emission enhancement and strong coupling. Because most applications require on-chip integration, we focus mainly on cavities in the solid state.

Optical cavities can be subdivided (see Fig. 1.2a-d) into (1) Fabry-Perot cavities, which trap light between two metallic or Bragg mirrors, (2) whispering-gallery-mode cavities, where waves circulate in a microsphere, -disk or -toroid, trapped by continuous total internal reflection at the walls, and (3) photonic crystal cavities, which use the band gap of a periodic dielectric to trap light in a defect [7, 40]. The first cavities at optical frequencies were Fabry-Perot cavities based on highly reflective metallic mirrors (Fig. 1.2a), which enabled the first observations of cavity Purcell enhancement [41] and strong coupling [36] at optical frequencies. Such cavities have reached Q up to $4.4 \cdot 10^7$ [42], but typically have large mode volumes [40]. Microposts (Fig. 1.2c) form a solid-state version of the Fabry-Perot cavity and have delivered, for example, single-photon sources with high brightness and indistinguishability [43, 44], record-high single-photon emission rates of 4 MHz [45] and the first single-emitter strong coupling in the solid state [46]. Whispering-gallery-mode cavities (Fig. 1.2b) can reach record Q [38, 47] for large diameter, and mode volumes of a few cubic wavelengths [48] for small-diameter microdisks. Single-emitter strong coupling was reached in a high-index microdisk [48, 49], and high-Q microtoroids were used, among others, for low-threshold lasers [50] and single-particle biosensing [3]. Photonic-crystal cavities (Fig. 1.2d) combine very high Q (up to $1.1 \cdot 10^7$ [51]) with near-diffraction limited mode volumes ($\sim 1(\lambda/n)^3$ [51, 52]). Single-emitter strong coupling [37, 53–56], very low-threshold lasers [57–59] and — to our knowledge — the highest experimental cavity Purcell enhancement of 75 [60] have been reported using photonic-crystal cavities.

Cavities, however, suffer from important drawbacks that prevent the realization of a large-scale quantum photonic network. Because V is fundamentally limited, Q must be very high to achieve large Purcell enhancement or strong coupling. This necessitates cryogenic temperatures of 10 K or lower, since only then are emitters available with such narrow linewidths. Furthermore, in a network, all elements must operate at the same wavelength, which implies that the cavities have to be kept in tune to within their ultra-small bandwidth — an unscalable challenge. Finally, response times of the nodes are limited to the inverse cavity bandwidth. High Q thus limits the speed of switching operations and addressing of the nodes for loading or retrieving quantum information.

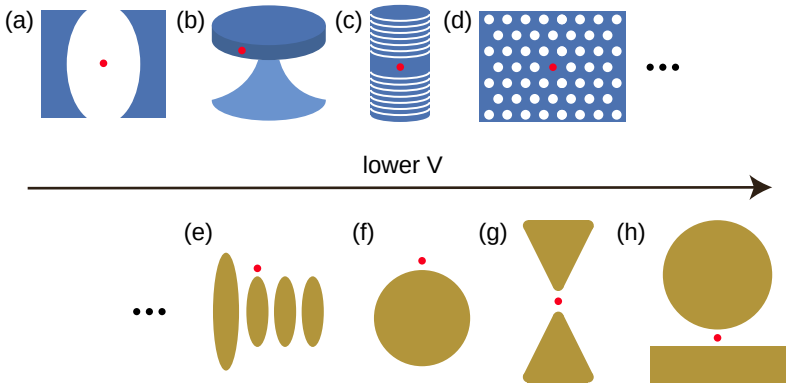

Figure 1.2: Cavity and antenna designs. (a) Fabry-Perot cavity. **(b)** Whispering-gallery-mode (microdisk) cavity. **(c)** Micropillar cavity, the solid-state analogue of the Fabry-Perot cavity. **(d)** Photonic crystal cavity. **(e)** Phased array (Yagi-Uda) antenna. **(f)** Dipole antenna. **(g)** Dimer (bow-tie) antenna. **(h)** Nano-patch antenna. The cavities and antennas are ordered according to their typical mode volumes. The red dots represent a usual location for the emitter.

1.3 Plasmonic antennas

At the interface between a metal and a dielectric, strong interaction of the free-electron gas in the metal with light can lead to hybridized light-matter waves named plasmon polaritons [12]. Their wavelengths can lie far below that in free-space. Therefore, plasmonic antennas — finite-size metallic structures that act as cavities for plasmon polaritons — can confine light to mode volumes far below the diffraction limit.[‡] Ohmic absorption in the metal, however, typically limits Q to $\sim 5-20$. Hence, compared to cavities, plasmonic antennas operate at the other extreme of Q and V, offering high LDOS over a very broad bandwidth. This makes them ideally suited for coupling to emitters at room temperature, which typically have severely broadened linewidths [65].

Because in antennas, radiative processes have to compete with non-radiative Ohmic decay, it is crucial to verify that high LDOS is accompanied by a high radiative efficiency. This requires the use of low-loss (noble) metals, but it also depends on antenna geometry. Plasmonic structures which support large LDOS while maintaining a reasonably high radiative efficiency can be categorized (see Fig. 1.2e-h) [66] into dipole antennas [67], patch or nano-patch antennas [68–70] and phased-array antennas [71, 72]. First works focused on dipole antennas (Fig. 1.2f) such as spheres or nano-rods.

[‡]Note that the conventional definition of the mode volume, discussed further in Chapter 2 and applicable to high-Q cavities, does not apply to low-Q plasmonic resonators [61]. Although an analytical expression for plasmonic mode volumes is beyond the scope of this thesis, we note that a possible solution is offered by the use of quasi-normal modes [62–64].

In such resonators, increasingly high LDOS is obtained when the emitter is placed closer to the metal interface [18]. Radiation efficiency, however, drops sharply at distances of a few nanometers due to quenching by non-radiative processes in the metal. It was long believed that this limited the attainable Purcell factors to a few hundred, if radiative efficiencies above 50% were to be maintained [13]. However, recently it was realized that quenching can be overcome by placing the emitter inside a nano-gap between two metals. Such structures support highly confined 'gap plasmons', which can couple efficiently to radiation. Importantly, both the emitter decay rate into the gap mode and the quenching rate depend on gap thickness d as d^{-3} [73]. Hence radiation efficiency is roughly independent of the gap size, while the Purcell enhancement grows sharply with decreasing gaps. This forms the working principle of (nano-)patch or 'particle-on-mirror' antennas (Fig. 1.2h), which have shown record LDOS enhancements of 1800 for a silver nanowire on a silver substrate [74] and $\sim$1000 for a silver nanocube on a gold mirror [68], with claimed radiative efficiencies above 50%. Not just patch antennas but also antenna dimers (Fig. 1.2g) enjoy this gap enhancement, and LDOS enhancements up to $\sim$750 in a gold sphere dimers [75] (at >50% efficiency) and $\sim$760 in a bow-tie antenna [76] (at $\sim$25% efficiency) have been demonstrated. Very recently, two works have observed first signatures of plasmonic strong-coupling with a gold nanosphere on a gold mirror [70] and a gold nano-slot waveguide antenna [77]. Additional field confinement can be created through the 'lightning-rod effect', which leads to strong fields at sharp metal tips. This partly underlies the good performance of the bow-tie antenna and that of the nano-cone antenna, for which experimental LDOS enhancements of $\sim$100 [78] were found at efficiencies above 60%, while theory predicts that enhancements around 5000 are possible at similarly high efficiency [79, 80]. Most of these antennas have dipolar, that is, almost isotropic, radiation patterns. Even a bow-tie or a small particle on a mirror, despite their complex near-field patterns, show a simple dipolar coupling to propagating waves, as long as they are small compared to the wavelength. Phased array antennas (Fig. 1.2e), on the other hand, such as Yagi-Uda [71, 81] or bulls-eye [72] antennas, can have more directional emission patterns, which can improve the collection efficiency. Purcell factors are typically lower in these antennas, due to decreased confinement.

These results show that plasmonics can bring the fascinating physics of cavity quantum electrodynamics into the domain of extremely high coupling rates g, possibly allowing the generation of single photons and coherent manipulation of emitters at >10 THz rates. However, the large bandwidth and Ohmic losses of plasmonics still pose major challenges. For one, bandwidths are so large as to make switching of the device — which requires a resonance shift of approximately the linewidth — practically impossible. Moreover, high photon generation, transport and collection efficiencies are key to scaling the current systems to a multi-node quantum network [23, 82]. For example,

generation of n-manifold single photons in a network scales as the total single-photon source efficiency to the power n [32]. It is not clear how significant efficiency improvements of current plasmonic antennas should be obtained.

1.4 Antenna-cavity hybrids

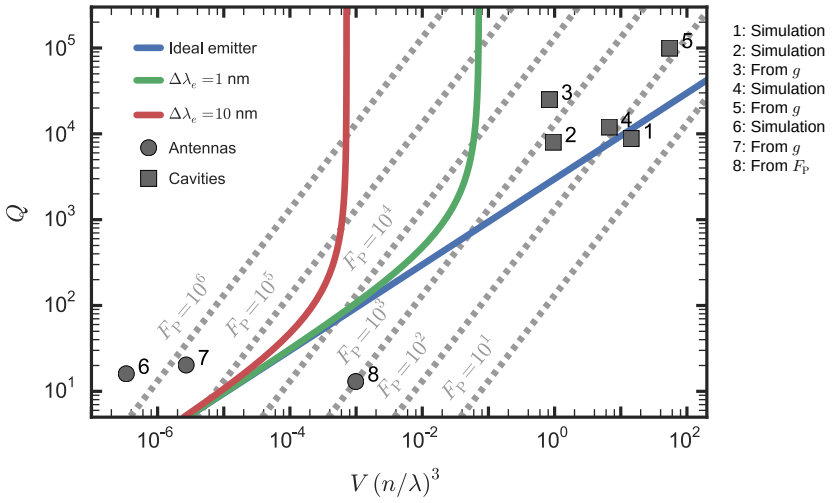

Figure 1.3: Phase diagram of cavity and antenna Q and V. Data are shown from several state-of-the art cavities (1: [46], 2: [53], 3: [37], 4: [49], 5: [48]) and antennas (6: [70], 7: [77], 8: [68]). We indicate whether V was obtained from simulations, from observed Rabi splitting $2g$ or from the Purcell factor F_P. Simulated V were always cross-checked with observed Rabi splitting. Dashed lines show constant Purcell factor F_P, and the coloured curves mark the separation between strong (left of the curves) and weak coupling, given by the condition $2g = \kappa + \gamma_e$ [16], with $\gamma_e = \gamma + 2\gamma^*$ the emitter linewidth. We assume an emitter at 800 nm emission wavelength with oscillator strength $f = 100$ (typical for epitaxially grown quantum dots [49]), and linewidths $\Delta\lambda_e$ of 0 (blue), 1 (green) and 10 (red) nm. At room temperature, most emitters have $\Delta\lambda_e \geq 10$ nm. Hybrid systems could occupy the intermediate region between cavities and antennas.

As we have seen, both cavities and antennas suffer from fundamental constraints, particularly limiting the scaling of single photon sources and quantum logic gates into a larger network. Hence, alternative methods to trap and confine light are required. In this thesis, we study how combinations of different resonators provide such alternatives. The first of such combinations, is a hybrid system composed of a high-Q cavity coupled to an antenna. Intuitively, one might expect that, by storing the light partially in a cavity and partially in an antenna, such a system could combine the small mode volumes of a plasmonic antenna with the high quality factors of a cavity. In Fig. 1.3, we summarize the best cavities and antennas from literature through

their quality factors and mode volumes. Cavities are located at one extreme in this diagram — at high Q and high V — whereas antennas are found at the opposite extreme. Hybrids could potentially reach high Q and low V, but more realistically could fill the gap between these two extremes, working at intermediate, practical Q and V. This could alleviate antenna losses, offer linewidths compatible with those of realistic emitters and allow switching operations. Moreover, this intermediate regime offers 'sweet spots' where strong coupling could be achieved with a realistic emitter, even if a high-Q cavity or low-Q antenna with the same Purcell factor would not reach it.

Hybrid systems were first studied in 1999 [83] and have since been proposed for a great variety of applications. In the context of (bio-)sensing, systems that were typically based on whispering-gallery-mode cavities functionalized with metallic particles have been experimentally studied [84–89], with notable successes including the detection of such small particles as single ions in solution [90]. Hybrid systems have furthermore been studied in the context of optical trapping [91–94], surface-enhanced Raman scattering [95, 96], nano-scale lasers [97, 98] and interfaces between on-chip propagating signals and far-field radiation [99–103]. Naturally, the promise of combining small mode volumes with high quality factors renders hybrid systems highly interesting for emission enhancement or strong coupling. This has prompted several theoretical works to predict very high LDOS [104–106], and even the possibility of strong coupling [107–109] for a number of different antenna-cavity geometries. Experimentally, only few works [110, 111] have studied spontaneous emission in a hybrid system. Thus far, no clear evidence was found for large LDOS effects, partially due to the difficulty of separating pump enhancement, changes in the collection efficiency and LDOS effects [66]. Finally, although this is not a route to large single-emitter emission enhancement, we should note that there is also an active field of research into hybrid plasmonic-photonic systems with one-dimensional confinement, such as antenna arrays in a Fabry-Perot etalon [112–116].

1.5 Motivation and outline

This thesis concerns two types of hybrid resonances, each of which offers exciting opportunities unavailable with the underlying individual components. The first are resonances in hybrid antenna-cavity systems, and the second are bound states in the continuum.

Antenna-cavity hybrids

Hybrid antenna-cavity systems could combine the best of cavities and of plasmonics, to benefit applications ranging from single-particle sensing to quantum information processing. Although a number of specific geometries have

been studied, many important questions remain unanswered. These could be summarized into three main questions: (1) Could we find fundamental limits that govern the LDOS or optical responses of any hybrid system, regardless of cavity or antenna geometry? (2) If so, under what conditions could those limits be approached? (3) Experimentally, how can we make these systems, and deterministically load them with emitters? This thesis addresses these questions both theoretically and experimentally.

Theory

Chapter 2 discusses a simple and intuitive theoretical model to describe the interaction between a cavity and an antenna, as well as LDOS in such systems. Unlike previous works, the model is generic to any geometry. This chapter serves as an introduction to the physics of antenna-cavity hybrids and provides the theoretical basis for several subsequent chapters.

In **Chapter 3**, we theoretically demonstrate that hybrids can support larger LDOS than their bare constituents. We elucidate how interference lets these systems break a fundamental limit governing the LDOS for a single antenna, and show how cavity-antenna frequency detuning can serve as a tuning mechanism to achieve Q and V anywhere in between those of the cavity and of the antenna. Importantly, we show that photon collection efficiency can be high, despite plasmonic losses.

In **Chapter 4** we regard hybrid systems from an electrical engineering perspective by deriving a circuit analogy for these systems. First, we review two different circuits from literature, which describe a nano-antenna, and show that the two are equivalent. The well-known maximum power transfer theorem from circuit theory is then used to find a second fundamental bound on antenna scattering and LDOS. We show how a hybrid system can be viewed as a conjugate-matching network between antenna and radiation load, allowing these systems to reach this fundamental bound.

Experiments

In **Chapter 5** we present the deterministic fabrication of hybrid antenna systems consisting of whispering-gallery-mode microdisk cavities and aluminium antennas. A novel method is demonstrated for high-precision placement of fluorescent quantum dots in these systems.

Chapter 6 builds upon the developed fabrication method to study the perturbation of our microdisk cavities by the antennas. Through a combination of tapered-fiber spectroscopy and free-space microscopy, we measure antenna-induced linewidth broadening and shifts for antennas and disks of various sizes. These measurements reveal that changing antenna length can lead to a linewidth tuning of more that two orders of magnitude, in good agreement with cavity perturbation theory. Such extreme flexibility in linewidth makes hybrid systems very attractive as single-photon sources.

Chapter 7 discusses fluorescence measurements of the hybrid systems loaded with quantum dots. This reveals striking asymmetric resonances in the fluorescence spectra, corresponding to the hybrid modes. Linewidth and shape show excellent agreement to theory, and give evidence of a strongly boosted LDOS at the hybrid mode, as compared to the bare antenna. Fluorescence decay rate measurements show a strong increase of decay rate, which we attribute mainly to the antenna.

In **Chapter 8** we go beyond systems with a single antenna, and experimentally study an antenna lattice instead, coupled to an ultra-high-Q microtoroid cavity. The cavity is shown to induce a strong suppression of the antenna polarizability, demonstrating that cavities and antennas need not always work symbiotically. The lattice, however, does lead to interesting new phenomena that are absent for a single antenna, such as an antenna-cavity coupling that depends on angle of incidence.

Bound states in the continuum

The last **Chapter 9** is concerned with an alternative strategy for trapping light, involving a very different hybrid resonance. Recently, it was discovered that an otherwise leaky mode inside a photonic crystal slab could become perfectly confined (*i.e.* with infinite Q) at one particular wavelength. We experimentally demonstrate that such a state, known as a bound state in the continuum (BIC), is associated with a polarization vortex in momentum-space. This implies that the state is topologically protected, making it robust against small variations in geometry. At first sight, it may appear that there is little connection between these resonant states and the hybrid antenna-cavity resonances studied in the earlier chapters. However, we show that similar physics is at work — both are in fact hybrids of two distinct resonances. While the coupling between an antenna and a cavity (usually) occurs in the near field, a BIC arises due to coupling of resonances via far-field interference. We show that such far-field coupling between an electric and a magnetic dipolar resonance inside the crystal unit cell can lead to a BIC if complete destructive interference is obtained.

Chapter 2

A coupled-oscillator model for cavity-antenna systems

In this chapter, we derive a simple, fully classical and intuitive model to describe a cavity-antenna hybrid sytem, based on coupled oscillators. The coupled equations of motion are derived, and we study local density of states in these systems by including a dipolar constant current source. This model is independent of cavity and antenna geometry, and provides a unified framework through which we can understand various physical effects in these systems, including cavity perturbation, enhancements or suppression of the local density of states and observables in taper-coupled measurements of the cavity. Moreover, the model serves as the basis for the theoretical results and interpretation of experimental data discussed in Chapters 3, 4, 6 and 7.

2.1 Introduction

The major part of this thesis is devoted to the study of hybrid cavity-antenna systems. Both optical cavities and plasmonic antennas have become ubiquitous instruments in the manipulation of light-matter interaction [7, 117]. This interaction strength, which can be quantified as an increased local density of states (LDOS), depends on the photon storage time and confinement volume. While optical cavities have developed increasingly sophisticated techniques to reach extremely long photon storage times (up to $8 \cdot 10^9$ oscillations [38]), plasmonic particles instead achieve strong interactions by concentrating the light to volumes far below the diffraction limit. Hybrid cavity-antenna systems (see Fig. 2.1) have been proposed recently as a platform in which to combine the favourable properties of cavities and antennas [104, 105, 110]. If indeed a symbiotic relationship between a cavity and an antenna could be established, this could have large implications for applications including single-photon sources for quantum information processing [29, 31], optical particle sensing [26] and nano-scale lasers [25]. Therefore, important questions when studying these systems are: Can hybrid systems support stronger light-matter interactions (higher LDOS) than their constituents? If so, what are the requirements for this symbiosis? Could we design a system with high LDOS at any desired bandwidth of operation (something which is not possible with plasmonics or cavities alone)? High LDOS means an increase of emission rate, so where does this emitted light go? Are there fundamental limits to LDOS in these systems?

Early theoretical works on hybrid systems have shown that LDOS as well as figures of merit for particle sensing or trapping can indeed be increased by combining antennas with cavities [87, 93, 104, 105, 118]. While this shows the promise of these structures, these studies have focused on particular cavity or antenna geometries and are thus unable to explain the general physical phenomena underlying this symbiosis. Another problem is that most studies have thus far used finite-element simulations, which are particularly challenging and time-consuming for hybrids due to the widely different element and domain sizes required for cavities and plasmonics.

In this chapter, we introduce a simple, intuitive coupled-oscillator model which is applicable to any cavity-antenna system. The only assumptions are that the antenna is dipolar and that there is no radiation overlap between cavity and antenna. Despite its simplicity, this model captures the essential physics of cavity-antenna interaction, which allows us to answer the questions above. In Section 2.2, we derive from first principles the coupled equations of motion for the hybrid. These equations can be solved to find the hybridized eigenmodes of the system, which is done in Section 2.3. To study LDOS, in Section 2.4 we let the system be driven by a fixed-current source dipole placed in close proximity to the antenna. This classical source models a fluorescent emitter in the weak-coupling limit, and the LDOS experienced by the emitter can be obtained from the power radiated by the source. Finally, in Section 2.5

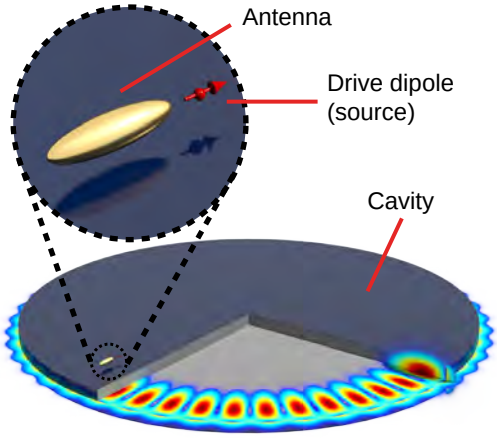

Figure 2.1: Example of a hybrid cavity-antenna system. The cavity is represented by a disk supporting a high quality factor whispering-gallery mode (WGM) shown in the cut-out, and the antenna by a gold ellipsoid. LDOS effects can be studied through the emission of a drive dipole (modelling a fluorescent emitter) placed in the system.

we derive expressions for the experimental observables in the specific case of antennas coupled to a degenerate pair of counter-propagating whispering-gallery modes, driven not by an emitter but through a waveguide coupled to the cavity modes.

This chapter provides a didactical introduction to the physics of coupled antenna-cavity systems, particularly suited for those who have never studied such systems before. It provides a single framework that connects many different facets of these systems, including mode hybridization, LDOS effects, radiative or collection efficiency, temporal coupled-mode theory for waveguide-coupled cavities, multiple-scattering theory and the famous Bethe-Schwinger cavity perturbation theory. The more experienced reader may find many things to be familiar, and may treat this chapter as a reference for the results presented in subsequent chapters, since this chapter lays the foundations for the results and interpretations presented in Chapters 3, 4, 6 and 7. The model for LDOS derived in Section 2.4 is used in Chapter 3, where we discuss the resulting LDOS spectra and provide answers to the questions above, for example under what conditions one can optimally harness the strengths of optical cavities and plasmonics. Also Chapter 4 builds upon this model to construct an equivalent electrical circuit that describes an emitter in a hybrid system, which can be used to derive a fundamental limit on the radiated power. We employ the results from Section 2.5 to compare to experimental resonance shifts and linewidths in Chapter 6, and in Chapter 7 we use the LDOS results from Section 2.4 to explain our experimental fluorescence spectra.

2.2 Equations of motion for a cavity-antenna system

Here we derive the equations of motion for a coupled cavity-antenna system. We model the antenna as a point dipole with the familiar Lorentzian polarizability, as found *e.g.* for the Fröhlich mode of a small metal sphere [119] in vacuum. Radiation damping is included to make the model self-consistent and adhering to the optical theorem [120]. Interaction with the cavity mode is explicitly separated out from this radiation damping due to other modes, and included in a second equation of motion. This equation of motion, describing a single cavity mode, is based on temporal coupled mode theory. Its derivation is analogous to deriving the classical equation of motion for an atom in a cavity, as given by Haroche [121], where in our work the 'atom' will be representing the antenna. This approach requires no assumptions on the type of cavity or antenna, other than that the antenna is dipolar and that there is no radiation overlap between cavity and antenna. Throughout this derivation, all quantities are in SI units.

2.2.1 A dipolar antenna

We consider a system of a small nano-antenna positioned in the field of a cavity at position $\boldsymbol{r}_0$. The antenna is described as a point dipole with dipole moment $\mathbf{p} = p\hat{\mathbf{p}}$, where $\hat{\mathbf{p}}$ is the unit vector pointing along $\mathbf{p}$, and we assume for simplicity that it is only polarizable along $\hat{\mathbf{p}}$ [122]. This analysis can be easily extended to a tensor polarizability.

The antenna response is modelled as a harmonic oscillator of charge q and mass m with resonance frequency ω_0 that suffers from intrinsic damping due to Ohmic heating described by an energy damping rate γ_i. The equation of motion (EOM) that governs the time dependence of the (complex) dipole amplitude $p(t)$ is that of a damped, driven harmonic oscillator:

$$\ddot{p} + \gamma_\mathrm{i}\dot{p} + \omega_0^2 p = \beta E, \tag{2.1}$$

where $\beta = q^2/m$ is the oscillator strength and $E = \mathbf{E}(\boldsymbol{r}_0) \cdot \hat{\mathbf{p}}$ is the total electric field $\mathbf{E}$ present at the antenna position, projected on $\hat{\mathbf{p}}$. While in a Drude model for a metal sphere of volume V_ant in vacuum, β simply reads $3V_\mathrm{ant}\epsilon_0\omega_0^2$, in general it may be found for any antenna by polarizability tensor retrieval from a full wave simulation [123, 124]. We now separate E in three contributions:

$$E = E_c + E_p + E_\mathrm{ext}. \tag{2.2}$$

Here, E_c is the field of the cavity mode of interest at $\boldsymbol{r}_0$, along the dipole direction. The second term is the field at the antenna, caused by the antenna

itself. It can be formally written as

$$E_p(t) = \int_{-\infty}^{\infty} \mathrm{d}t' \, \mathcal{G}_{\mathrm{bg}}(t-t')p(t') = \left(\mathcal{G}_{\mathrm{bg}} * p\right)(t), \tag{2.3}$$

where $\mathcal{G}_{\mathrm{bg}}(t-t')$ is a linear response function that describes the field at the position of the antenna at time t due to a delta function excitation at time t'. Choosing $\mathcal{G}_{\mathrm{bg}}(t-t')$ as the retarded Green's function ensures that the integrand is zero for $t' > t$, thus respecting causality [125]. Its Fourier transform is $G_{\mathrm{bg}}(\boldsymbol{r}_0, \boldsymbol{r}_0, \omega) \equiv \hat{\mathbf{p}} \cdot \overleftrightarrow{G}_{\mathrm{bg}}(\boldsymbol{r}_0, \boldsymbol{r}_0, \omega) \cdot \hat{\mathbf{p}}$ — the projection along the antenna direction of the Green's tensor $\overleftrightarrow{G}_{\mathrm{bg}}$ that describes the field $\mathbf{E}_p$ of the antenna in its environment via $\mathbf{E}_p(\boldsymbol{r}, \omega) = \overleftrightarrow{G}_{\mathrm{bg}}(\boldsymbol{r}, \boldsymbol{r}_0, \omega) \cdot \mathbf{p}\,(\omega)$. Importantly, we need to explicitly omit the contribution of the cavity field in this response, since that will be accounted for in the next section. Instead, it is composed of the antenna radiation expanded in all modes *except* the cavity mode. It is for that reason that we use the subscript 'bg' to mean that only the dielectric 'background' contributes to $\mathcal{G}_{\mathrm{bg}}$. This dielectric background can in principle be inhomogeneous, and as such the response can be altered from that in a homogeneous medium due to the excitation of for example modes in a substrate or other cavity modes. If those contributions are negligible, the well-known expression for the Abraham-Lorentz force in a homogeneous medium can be used such that*

$$E_p = \frac{\sqrt{\epsilon}\,\dddot{p}}{6\pi\epsilon_0 c^3}, \tag{2.4}$$

where $\epsilon = \epsilon(\boldsymbol{r}_0)$ is the relative permittivity of the medium, ϵ_0 the vacuum permittivity and c the speed of light [12].

The final term E_{ext} in Eq. (2.2) is the external driving field, *i.e.* the electric field at the position of the antenna which does *not* find its origin in the antenna itself, and is distributed over other modes than the cavity mode. This can for example be the field due to an oscillating source dipole or an incident plane wave.

2.2.2 A cavity

Next, we seek to find a similar equation of motion for the cavity field E_{c}. First, we must assume that the field can be expanded in orthogonal modes $\mathbf{E}_m$, of which the cavity mode $\mathbf{E}_{\mathrm{c}}$ is just one. This is a standard approach to describe the physics of high-Q cavities in quantum optics. We note that for very open systems, there is currently a strong debate about quasi-normal modes appropriate for non-hermitian systems [62–64, 126]. We note that generalization of our formalism to deal with quasi-normal modes is outside the scope of this

*Note that this describes the *imaginary* part of E_p, which governs *e.g.* radiated power. The real part of E_p, which diverges in a homogeneous medium, is typically ignored [122].

thesis. Such a generalization would also require to revisit the definitions of mode normalization, inner product, and energy density.

The assumed orthogonal eigenmodes satisfy the wave equation without sources, [125]

$$\nabla \times \nabla \times \mathbf{E}_m(\boldsymbol{r},t) + \frac{\epsilon\left(\boldsymbol{r}\right)}{c^2}\frac{\partial^2}{\partial t^2}\mathbf{E}_m(\boldsymbol{r},t) = 0, \tag{2.5}$$

and can be factorized as

$$\mathbf{E}_m(\boldsymbol{r},t) = a_m(t)\mathbf{e}_m(\boldsymbol{r}), \tag{2.6}$$

such that $\mathbf{e}_m$ satisfies both

$$\nabla \times \nabla \times \mathbf{e}_m(\boldsymbol{r}) - \epsilon(\boldsymbol{r})\frac{\omega_m^2}{c^2}\mathbf{e}_m(\boldsymbol{r}) = 0 \tag{2.7}$$

and

$$\int \mathrm{d}\boldsymbol{r}\,\frac{1}{2}\epsilon_0\epsilon(\boldsymbol{r})\mathbf{e}_m^*(\boldsymbol{r})\cdot\mathbf{e}_n(\boldsymbol{r}) = \delta_{mn}, \tag{2.8}$$

where we have assumed harmonic time dependence $e^{-i\omega t}$ of the modes with eigenfrequencies ω_m.

The time dependence of each mode is captured in the (complex) mode amplitude a_m, and the orthonormality condition defined in Eq. (2.8) ensures that

$$|a_m|^2 = \int \mathrm{d}\boldsymbol{r}\,\frac{1}{2}\epsilon_0\epsilon(\boldsymbol{r})\left|\mathbf{E}_m(\boldsymbol{r},t)\right|^2 = U_m \tag{2.9}$$

is the total energy in mode m.

The total field is

$$\mathbf{E}(\boldsymbol{r},t) = \sum_m a_m(t)\mathbf{e}_m(\boldsymbol{r}) \tag{2.10}$$

and hence

$$a_m = \int \mathrm{d}\boldsymbol{r}\,\frac{1}{2}\epsilon_0\epsilon(\boldsymbol{r})\mathbf{E}\left(\boldsymbol{r},t\right)\cdot\mathbf{e}_m^*(\boldsymbol{r}). \tag{2.11}$$

At this point we may introduce the antenna (or any other dipole) by including it as a dipolar 'source' in the wave equation. Note that the antenna is not actually a source but instead a polarizable dipolar particle which does not produce energy. In contrast, a real source like *e.g.* a fluorescent molecule is modelled as a dipole oscillating at a fixed amplitude, as we will discuss in Section 2.4.1. Nevertheless, in the wave equation both antenna and source are inserted in the same position. The total field then obeys the wave equation including this dipolar 'source' term

$$\nabla \times \nabla \times \mathbf{E}\left(\boldsymbol{r},t\right) + \frac{\epsilon(\boldsymbol{r})}{c^2}\frac{\partial^2}{\partial t^2}\mathbf{E}\left(\boldsymbol{r},t\right) = -\frac{1}{\epsilon_0 c^2}\frac{\partial^2}{\partial t^2}\mathbf{P}\left(\boldsymbol{r},t\right), \tag{2.12}$$

where we will write the polarization by the antenna:

$$\mathbf{P}(\boldsymbol{r},t) = p(t)\delta(\boldsymbol{r}-\boldsymbol{r}_0)\,\hat{\mathbf{p}}. \tag{2.13}$$

Starting with the wave equation (Eq. (2.12)), taking the product of both sides with $\frac{1}{2}\epsilon_0\mathbf{e}_\mathrm{c}^*(\boldsymbol{r})$ (where $\mathbf{e}_\mathrm{c}(\boldsymbol{r})$ is the field profile of the cavity mode), making use of Eq. (2.6) and Eq. (2.7), and finally integrating over all space yields

$$\sum_m \int \mathrm{d}\boldsymbol{r}\,\frac{1}{2c^2}\epsilon_0\epsilon(\boldsymbol{r})\mathbf{e}_m(\boldsymbol{r})\cdot\mathbf{e}_\mathrm{c}^*(\boldsymbol{r})\left(\omega_m^2 a_m + \ddot{a}_m\right) = -\int \mathrm{d}\boldsymbol{r}\,\frac{\delta(\boldsymbol{r}-\boldsymbol{r}_0)}{2c^2}\hat{\mathbf{p}}\cdot\mathbf{e}_\mathrm{c}^*(\boldsymbol{r})\ddot{p}, \tag{2.14}$$

which results in

$$\ddot{a} + \omega_\mathrm{c}^2 a = -\frac{1}{2}\hat{\mathbf{p}}\cdot\mathbf{e}_\mathrm{c}^*(\boldsymbol{r}_0)\ddot{p}, \tag{2.15}$$

where, for simplicity, we have replaced the mode amplitude a_c by the symbol a. Eq. (2.15) represent a lossless cavity. We can introduce a phenomenological damping rate κ that describes cavity losses (excluding those related to the dipole), as well as a driving term [127], to arrive at

$$\ddot{a} + \kappa\dot{a} + \omega_\mathrm{c}^2 a = -\frac{1}{2}\hat{\mathbf{p}}\cdot\mathbf{e}_\mathrm{c}^*(\boldsymbol{r}_0)\ddot{p} + 2\sqrt{\kappa_\mathrm{ex}}\dot{s}_\mathrm{in}. \tag{2.16}$$

Here, $\kappa = \kappa_\mathrm{i} + \kappa_\mathrm{ex}$ includes both an intrinsic loss rate κ_i and coupling losses κ_ex due to coupling to the feeding channel (a waveguide, for example). This assumes ideal coupling, *i.e.* the waveguide does not induce any other losses to the cavity than those due to coupling to the input-output waveguide mode [128, 129]. It is important to realize that we can only include damping in this manner if we explicitly assume that there is no radiation overlap between the bare cavity and antenna. If that would be the case, neither cavity nor antenna loss rate could be assumed to be constants, as interference would make both depend on each other and on a and p [130]. The last term on the right hand side describes driving through the waveguide coupled to the cavity mode with a coupling rate κ_ex. We normalize s_in such that $|s_\mathrm{in}|$ is the input power in this channel. In cavity literature, a different version of Eq. (2.16) is often used, namely [127, 131, 132]

$$\dot{\tilde{a}}(t) = \left(i\Delta - \frac{\kappa}{2}\right)\tilde{a}(t) + \sqrt{\kappa_\mathrm{ex}}\tilde{s}_\mathrm{in}(t), \tag{2.17}$$

with $\Delta = \omega - \omega_\mathrm{c}$. The difference, beside the absence of the antenna term, stems from the fact that we have not made the slowly varying envelope approximation. This assumes that cavity and driving oscillate at some carrier frequency ω, and amplitudes vary much more slowly than ω, which typically holds for narrowband driving. It can be easily verified that this approximation leads to the correct expression. For this, one transforms to a rotating frame by

writing $a(t) = e^{-i\omega t}\tilde{a}(t)$, $p(t) = e^{-i\omega t}\tilde{p}(t)$ and $s_{\rm in}(t) = e^{-i\omega t}\tilde{s}_{\rm in}(t)$, with ω the carrier frequency and $\tilde{a}(t), \tilde{p}(t)$ and $\tilde{s}_{\rm in}(t)$ the envelope functions, which are assumed to vary slowly such that $\dot{\tilde{a}}(t) \ll \omega\tilde{a}(t)$ (and similarly for $\tilde{p}(t)$ and $\tilde{s}_{\rm in}(t)$). Furthermore assuming that we have a good cavity ($\kappa \ll \omega_{\rm c}$) and evaluating near the cavity resonance frequency ($|\Delta| \ll \omega_{\rm c}$), we can rewrite Eq. (2.16) as

$$\dot{\tilde{a}}(t) = \left(i\Delta - \frac{\kappa}{2}\right)\tilde{a}(t) + \frac{i\omega}{4}\hat{\mathbf{p}}\cdot\mathbf{e}_{\rm c}^{*}(\boldsymbol{r}_0)\tilde{p}(t) + \sqrt{\kappa_{\rm ex}}\tilde{s}_{\rm in}(t) \tag{2.18}$$

Except for the antenna term, which is new, this matches Eq. (2.17) exactly.

2.2.3 Equations of motion in the Fourier domain

The obtained equations of motion Eqs. (2.1) and (2.16), are most easily solved in the Fourier domain, where they result in[†]

$$\left(\omega_0^2 - \omega^2 - i\omega\gamma_{\rm i} - \beta G_{\rm bg}(\boldsymbol{r}_0, \boldsymbol{r}_0, \omega)\right) p - \beta\,\hat{\mathbf{p}}\cdot\mathbf{e}_{\rm c}(\boldsymbol{r}_0)a = \beta E_{\rm ext}, \tag{2.19}$$

$$\left(\omega_{\rm c}^2 - \omega^2 - i\omega\kappa\right) a - \frac{\omega^2}{2}\hat{\mathbf{p}}\cdot\mathbf{e}_{\rm c}^{*}(\boldsymbol{r}_0)p = -2i\omega\sqrt{\kappa_{\rm ex}}s_{\rm in}. \tag{2.20}$$

Note that p, a, $s_{\rm in}$ and $E_{\rm ext}$ now represent the Fourier transforms of the corresponding time-dependent quantities in Eqs. (2.1) and (2.16). We may absorb the real part of $G_{\rm bg}(\boldsymbol{r}_0, \boldsymbol{r}_0, \omega)$ in ω_0 and the imaginary part in the total antenna damping rate γ, such that [120]

$$\gamma = \gamma_{\rm i} + \gamma_{\rm r} = \gamma_{\rm i} + \frac{\beta}{\omega}\,\mathrm{Im}\left\{G_{\rm bg}(\boldsymbol{r}_0, \boldsymbol{r}_0, \omega)\right\} \tag{2.21}$$

with $\gamma_{\rm r}$ denoting the radiative damping rate. Note that, using the relation between $\mathrm{Im}\left\{G_{\rm bg}(\boldsymbol{r}_0, \boldsymbol{r}_0, \omega)\right\}$ and the partial local density of states of the background $\rho_{\rm bg}$, the radiative damping rate $\gamma_{\rm r}$ may also be expressed as [12]

$$\gamma_{\rm r} = \frac{\beta\pi}{6\epsilon_0}\rho_{\rm bg}, \tag{2.22}$$

where, for example, $\rho_{\rm bg} = \omega^2\sqrt{\epsilon}/(\pi^2c^3)$ for a homogeneous medium of permittivity ϵ. To further simplify Eqs. (2.19) and (2.20), we multiply Eq. (2.20) with $\hat{\mathbf{p}}\cdot\mathbf{e}_{\rm c}(\boldsymbol{r}_0)$ and introduce the effective mode volume

$$V_{\rm eff} = \frac{\int \mathrm{d}\boldsymbol{r}\,\epsilon(\boldsymbol{r})\left|\mathbf{E}_{\rm c}(\boldsymbol{r})\right|^2}{\epsilon(\boldsymbol{r}_0)\left|\hat{\mathbf{p}}\cdot\mathbf{E}_{\rm c}(\boldsymbol{r}_0)\right|^2} = \frac{2}{\epsilon_0\epsilon(\boldsymbol{r}_0)\left|\hat{\mathbf{p}}\cdot\mathbf{e}_{\rm c}(\boldsymbol{r}_0)\right|^2} \tag{2.23}$$

which determines antenna-cavity coupling strength. Note that this is the effective mode volume as it is felt by the antenna at position $\boldsymbol{r}_0$, and it is therefore

[†]In this thesis, we always use the time convention in which $e^{-i\omega t}$ describes the time-dependence of a harmonically oscillating field. The Fourier transform of a function $f(t)$ is defined as $f(\omega) = \int f(t)e^{i\omega t}dt$.

tunable by moving the dipole in the cavity mode. In that respect it differs from the more usual definition of a cavity mode volume [14, 47] that uses the *maximum* field in the cavity mode instead. Also introducing the cavity field $E_\mathrm{c} = a\,\hat{\mathbf{p}}\cdot\mathbf{e}_\mathrm{c}(\boldsymbol{r}_0)$ projected on the antenna dipole axis, we finally obtain

$$\left(\omega_0^2 - \omega^2 - i\omega\gamma\right) p - \beta E_\mathrm{c} = \beta E_\mathrm{ext}, \tag{2.24}$$

$$\left(\omega_\mathrm{c}^2 - \omega^2 - i\omega\kappa\right) E_\mathrm{c} - \frac{\omega^2}{\epsilon_0\epsilon V_\mathrm{eff}} p = -2i\omega\sqrt{\kappa_\mathrm{ex}}\left(\hat{\mathbf{p}}\cdot\mathbf{e}_\mathrm{c}(\boldsymbol{r}_0)\right) s_\mathrm{in}, \tag{2.25}$$

where $\epsilon = \epsilon(\boldsymbol{r}_0)$.

Let us briefly interpret this result. In absence of the cavity, we recognize the bare antenna polarizability α_hom, defined through $p = \alpha_\mathrm{hom} E_\mathrm{ext}$, as

$$\alpha_\mathrm{hom} = \frac{\beta}{\omega_0^2 - \omega^2 - i\omega\gamma}, \tag{2.26}$$

which is corrected for radiation damping through γ_r. We see that the bare antenna shows a Lorentzian[‡] response, with a linewidth determined by γ. Inclusion of γ_r ensures that our model is valid for both strongly and weakly scattering particles. Expressed in scattering terms, with radiation damping Eq. (2.24) represents the t-matrix of a dipolar scatterer with a consistent optical theorem for scattering, absorption and extinction [120]. Similar to the antenna, the cavity in absence of the antenna has a Lorentzian response with linewidth κ, which is typically much smaller than the linewidth of the antenna. When the two components couple, we can expect that the system forms new, hybridized eigenmodes, and that response functions can be strongly affected. This will be discussed in the following section.

2.3 Hybridized eigenmodes

Eqs. (2.24) and (2.25) can be recognized as the equations of motion of two coupled, driven oscillators. In the absence of driving, they reduce to a quartic equation for ω that can in principle be solved analytically. It will have two complex roots with negative imaginary parts, which correspond to the two eigenfrequencies of the coupled system. While the full solution is too lengthy to include here, we can consider an approximate solution if we assume that $|\omega - \omega_\mathrm{c}| \ll \{\gamma, \omega_\mathrm{c}\}$. In other words, we are then looking for a solution close to the original cavity resonance frequency, with $\kappa \ll \gamma$. We find in this case

$$\omega = \omega_\mathrm{c} - i\frac{\kappa}{2} - \frac{\omega_\mathrm{c}\alpha(\omega_\mathrm{c})}{2\epsilon_0\epsilon V_\mathrm{eff}}.$$

[‡]Strictly speaking, the mathematical definition of a Lorentzian lineshape is $C\frac{(\gamma/2)^2}{(\omega-\omega_0)^2-(\gamma/2)^2}$, with C a pre-factor. Only in the 'good cavity limit' of small losses and evaluated near the resonance frequency ω_0, do Im $\{\alpha\}$ or $|\alpha|^2$ assume this lineshape. In this thesis, however, we use the term 'Lorentzian' both for resonant lineshapes of the form in Eq. (2.26), and for resonances following the exact Lorentzian shape.

We can write this as

$$\omega = (\omega_{\mathrm{c}} + \delta\omega_{\mathrm{c}}) - i\frac{\kappa + \delta\kappa}{2}, \tag{2.27}$$

where we defined the frequency shift $\delta\omega_{\mathrm{c}}$ and linewidth change $\delta\kappa$ as

$$\delta\omega_{\mathrm{c}} = -\frac{\omega_{\mathrm{c}}}{2\epsilon_0\epsilon V_{\mathrm{eff}}}\,\mathrm{Re}\left\{\alpha_{\mathrm{hom}}(\omega_{\mathrm{c}})\right\}, \tag{2.28}$$

$$\delta\kappa = \frac{\omega_{\mathrm{c}}}{\epsilon_0\epsilon V_{\mathrm{eff}}}\,\mathrm{Im}\left\{\alpha_{\mathrm{hom}}(\omega_{\mathrm{c}})\right\}, \tag{2.29}$$

respectively. Hence, the eigenfrequency of the coupled system is equal to the original complex cavity resonance frequency $(\omega_{\mathrm{c}} - i\kappa/2)$ plus a complex frequency shift $\delta\omega = \delta\omega_{\mathrm{c}} - i\delta\kappa/2$. These expressions match exactly those found by Bethe-Schwinger cavity perturbation theory [27, 133]. This is consistent with the fact that we have explicitly assumed in the derivation of the equations of motion that there is no far-field interference between the antenna and the cavity radiation. Under these assumptions Bethe-Schwinger perturbation theory holds [130]. Note that the assumptions we have made do not permit us to find the complex frequency of the other mode of the system in this case, which is however expected to be close to the complex frequency of the isolated antenna $(\omega_0 - i\gamma/2)$.

2.4 Local density of states in a hybrid system

In Chapter 3 we will discuss the local density of states (LDOS)[§] experienced by a fluorescent emitter coupled to a hybrid antenna-cavity system. In this section, we therefore extend the coupled-oscillator model to allow the study of LDOS. This requires the inclusion of a driving term associated to a fluorescent emitter, which will be derived in Section 2.4.1. We then continue to identify the response functions of the cavity and antenna, which hybridize when the two are coupled. The properties of these hybridized responses are discussed in Section 2.4.2. In Section 2.4.3 we obtain expressions for the total LDOS in a hybrid system. To study *e.g.* radiative efficiency or β-factor, knowledge is required of how the emitted light is distributed over different radiative and non-radiative decay channels. Expressions for the LDOS contribution of each decay channel are derived in Section 2.4.4. Finally, we test the consistency of our theory by verifying that the sum of these contributions equals the total LDOS.

2.4.1 Driving by a dipolar source

A fluorescent emitter in the limit of weak coupling to the photon field can be modelled as a 'constant current' driving dipole, *i.e.* a small, non-polarizable,

[§]In this chapter, LDOS will always refer to the relative local density of states, *i.e.* compared to that in the surrounding homogeneous medium.

dipole with harmonically oscillating dipole moment $p_{\mathrm{dr}}\hat{\mathbf{p}}_{\mathrm{dr}}$ at position $\boldsymbol{r}_{\mathrm{dr}}$ [18]. This source dipole drives the antenna with a field

$$E_{\mathrm{ext}} = G_{\mathrm{bg}}(\boldsymbol{r}_0, \boldsymbol{r}_{\mathrm{dr}}, \omega)\, p_{\mathrm{dr}} = G_{\mathrm{bg}} p_{\mathrm{dr}}, \tag{2.30}$$

where $G_{\mathrm{bg}}(\boldsymbol{r}_0, \boldsymbol{r}_{\mathrm{dr}}, \omega) = \hat{\mathbf{p}} \cdot \overleftrightarrow{G}_{\mathrm{bg}}(\boldsymbol{r}_0, \boldsymbol{r}_{\mathrm{dr}}, \omega) \cdot \hat{\mathbf{p}}_{\mathrm{dr}}$. The emitter being a point source, it will be able to drive all modes that have non-zero electric field at its position, including the cavity mode. If we redo the derivation of the cavity equation of motion Eq. (2.25), starting from Eq. (2.12) and including including a drive dipole term in the polarization such that

$$\mathbf{P}(\boldsymbol{r}, t) = p(t)\delta(\boldsymbol{r} - \boldsymbol{r}_0)\, \hat{\mathbf{p}} + p_{\mathrm{dr}}(t)\delta(\boldsymbol{r} - \boldsymbol{r}_{\mathrm{dr}})\, \hat{\mathbf{p}}_{\mathrm{dr}}, \tag{2.31}$$

we find

$$\left(\omega_{\mathrm{c}}^2 - \omega^2 - i\omega\kappa\right) E_{\mathrm{c}} - \frac{\omega^2}{\epsilon_0 \epsilon V_{\mathrm{eff}}} p = \frac{\omega^2}{\epsilon_0 \epsilon V_{\mathrm{eff}}} \phi\, p_{\mathrm{dr}}, \tag{2.32}$$

where we have set s_{in} to zero, since we study fluorescence and not waveguide driving. Here, $\phi = (\hat{\mathbf{p}}_{\mathrm{dr}} \cdot \mathbf{e}_{\mathrm{c}}^*(\boldsymbol{r}_{\mathrm{dr}})) \,/\, (\hat{\mathbf{p}} \cdot \mathbf{e}_{\mathrm{c}}^*(\boldsymbol{r}_0))$ is a complex factor accounting for a difference in orientation between $\hat{\mathbf{p}}$ and $\hat{\mathbf{p}}_{\mathrm{dr}}$ and different cavity mode field at $\boldsymbol{r}_0$ and $\boldsymbol{r}_{\mathrm{dr}}$. In a scenario where spontaneous emission effects are desired, the source is typically placed very close to the antenna, where the antenna may create strong field enhancement. If we take the source to be polarized along the antenna axis and we assume that source and antenna are very close compared to the wavelength, we obtain $\phi \approx 1$. The EOMs including the dipolar driving terms then become

$$\left(\omega_0^2 - \omega^2 - i\omega\gamma\right) p - \beta E_{\mathrm{c}} = \beta G_{\mathrm{bg}} p_{\mathrm{dr}}, \tag{2.33}$$

$$\left(\omega_{\mathrm{c}}^2 - \omega^2 - i\omega\kappa\right) E_{\mathrm{c}} - \frac{\omega^2}{\epsilon_0 \epsilon V_{\mathrm{eff}}} p = \frac{\omega^2}{\epsilon_0 \epsilon V_{\mathrm{eff}}} p_{\mathrm{dr}}. \tag{2.34}$$

2.4.2 The hybridized polarizability and cavity response

Before discussing the LDOS in our system, let us briefly consider the cavity and antenna response functions. As we will see in this chapter as well as Chapters 3 and 8, these quantities play a crucial role in LDOS as well as the response in a scattering measurement. If we consider first the uncoupled EOMs, we can recognize the bare antenna polarizability α_{hom}, given in Eq. (2.26), and bare cavity response χ_{hom}, defined through $E_{\mathrm{c}} = \chi_{\mathrm{hom}} p_{\mathrm{dr}}$ as

$$\chi_{\mathrm{hom}} = \frac{1}{\epsilon_0 \epsilon V_{\mathrm{eff}}} \frac{\omega^2}{\omega_{\mathrm{c}}^2 - \omega^2 - i\omega\kappa}. \tag{2.35}$$

When cavity and antenna are coupled, their own scattered fields act as additional driving terms, leading to the hybridized antenna polarizability α_{H} and cavity response function χ_{H}, defined similarly as the responses of the antenna

and cavity to *any* external field or dipole, respectively. Solving Eqs. (2.33) and (2.34) for p and E_{c}, respectively, we find

$$\alpha_{\mathrm{H}} = \alpha_{\mathrm{hom}} \left(1 - \alpha_{\mathrm{hom}} \chi_{\mathrm{hom}}\right)^{-1}, \tag{2.36}$$

$$\chi_{\mathrm{H}} = \chi_{\mathrm{hom}} \left(1 - \alpha_{\mathrm{hom}} \chi_{\mathrm{hom}}\right)^{-1}. \tag{2.37}$$

These expressions can be viewed as response functions dressed by an infinite series of cavity-antenna interactions, similar to a multiple-scattering series in a coupled point-scatterer model [122, 134]. As shown in Fig. 2.2, the hybridized cavity response χ_{H} shows a Lorentzian lineshape that is shifted and broadened with respect to the bare cavity resonance. Using the same approximations as in Section 2.3, i.e evaluating near a narrow cavity resonance, it is straightforward to show that the shift $\delta\omega_{\mathrm{c}}$ and broadening $\delta\kappa$ are equal to those in Eqs. (2.28) and (2.29) found for the hybrid eigenmode and predicted by Bethe-Schwinger cavity perturbation theory [27, 133]. The hybridized polarizability α_{H}, on the other hand, resembles the broad, Lorentzian lineshape of α_{hom}, yet with a sharp Fano-type resonance close to ω_{c} [135]. This is similar to the polarizability discussed by Frimmer *et al.* [118]. In fact, we can strictly show that α_{H} has a Fano lineshape by rewriting it as $\alpha_{\mathrm{H}} = \alpha_{\mathrm{hom}} \left(1 + \alpha_{\mathrm{hom}} \chi_{\mathrm{H}}\right)$. Observables like the antenna scattering cross-section σ_{s}, which is proportional to $|\alpha_{\mathrm{H}}|^2$, are thus described (again, in the vicinity of the cavity resonance) by the familiar equation for a Fano lineshape [12]

$$\sigma_{\mathrm{s}} \propto |e^{i\theta} + E_1 \frac{\kappa'/2}{-i\Delta + \kappa'/2}|^2, \tag{2.38}$$

with $\kappa' = \kappa + \delta\kappa$, $\theta = -\arg\{\alpha_{\mathrm{hom}}(\omega_{\mathrm{c}})\} - \pi/2$ and $E_1 = |\alpha_{\mathrm{hom}}(\omega_{\mathrm{c}})|\, \omega_{\mathrm{c}} / (\epsilon_0 \epsilon V_{\mathrm{eff}} \kappa')$. The imaginary part of α_{H} shows a very similar lineshape. The shape of the Fano resonance depends on Fano phase θ, which is determined by the phase of $\alpha_{\mathrm{hom}}(\omega_{\mathrm{c}})$. As such, the shape varies with antenna-cavity detuning, from a peak-dip structure at far red-detuning to the reverse at far blue detuning, with complete destructive interference (*i.e.* a dip) when antenna and cavity are on resonance ($\theta = \pi$). Increased radiation damping experienced by the antenna due to the cavity mode, as measured by Buchler *et al.* for a dipole near a mirror [136], is also captured in α_{H}. Recent experiments were even able to verify these Fano lineshapes in α_{H}, by measuring the absorption cross section of antennas coupled to microtoroid cavities [137, 138].

2.4.3 Total LDOS

The power emitted by the drive dipole is equal to the work done by its own field on itself, *i.e.* [12]

$$P_{\mathrm{dr}} = \frac{\omega}{2} \operatorname{Im}\left\{p_{\mathrm{dr}}^{*}\, E_{\mathrm{tot}}\right\}, \tag{2.39}$$

where E_{tot} the total field at its position. Dividing P_{dr} by the power that the drive dipole emits in a homogeneous medium yields the local density of

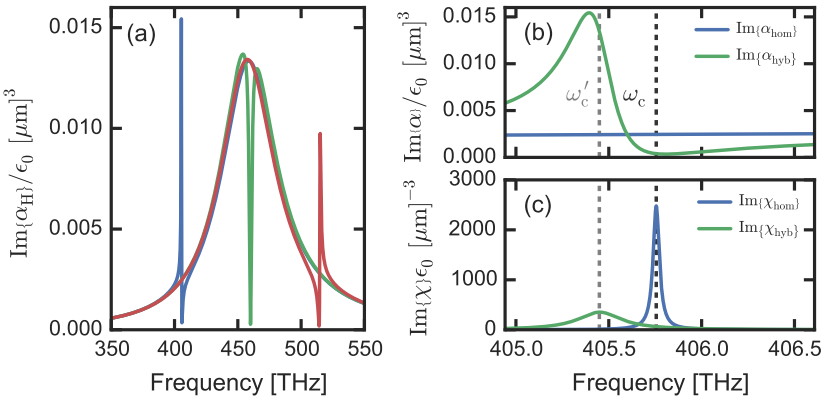

Figure 2.2: Example spectra of hybridized polarizability α_{H} and cavity response χ_{H}. **(a)** Broadband spectra of α_{H}. We show 3 cases with different cavity-antenna detuning of -1 (blue), 0 (green) and 1 (red) antenna linewidth γ. **(b)** Narrowband spectra of the bare antenna and hybridized polarizabilities α_{hom} (blue) and α_{H} (green), for cavity-antenna detuning of -1γ. While the bare polarizability is virtually constant, α_{H} shows a Fano lineshape. Dashed lines indicate the bare and hybridized cavity resonance frequencies ω_{c} and ω_{c}', respectively. **(c)** Bare and hybridized cavity responses χ_{hom}(blue) and χ_{H} (green), for the same system as used in (b). Contrary to the hybridized polarizability, χ_{H} does not have a Fano lineshape, but rather that of a Lorentzian resonance, shifted and broadened compared to the bare cavity resonance. In these calculations, we use β =0.12 C^2/kg, corresponding to a 50 nm radius sphere in vacuum with resonance frequency $\omega_0/(2\pi) = 460$ THz, and the ohmic damping rate $\gamma_{\mathrm{i}}/(2\pi) = 19.9$ THz of gold [139]. For the cavity we take $Q \equiv \omega_{\mathrm{c}}/\kappa = 10^4$ and V_{eff} to be 10 cubic wavelengths.

optical states (LDOS) experienced by the drive dipole, relative to that of the surrounding medium [18]. In the context of emitters coupled to cavities, this relative LDOS evaluated at the cavity resonance is the Purcell factor.

To find E_{tot}, let us first use Eqs. (2.33) and (2.34) to express the antenna dipole moment p in terms of the drive dipole amplitude p_{dr} by eliminating the cavity field E_{c} from the equations. We obtain

$$p = \alpha_{\mathrm{H}}\ (G_{\mathrm{bg}} + \chi_{\mathrm{hom}})\, p_{\mathrm{dr}}. \tag{2.40}$$

It can be seen that p is polarized in response to both the direct excitation by the source ($G_{\mathrm{bg}} p_{\mathrm{dr}}$) and the cavity field ($\chi_{\mathrm{hom}} p_{\mathrm{dr}}$). However, it responds with a hybridized polarizability, due to coupling with the cavity. With p known, we can then express the field scattered by the antenna at the position of the source dipole as:

$$E_{\mathrm{s}}(\boldsymbol{r}_{\mathrm{dr}}) = G_{\mathrm{bg}}(\boldsymbol{r}_0, \boldsymbol{r}_{\mathrm{dr}}, \omega)\, p = G_{\mathrm{bg}}\, p, \tag{2.41}$$

where we have used reciprocity, *i.e.* $G_{\mathrm{bg}}(\boldsymbol{r}_0, \boldsymbol{r}_{\mathrm{dr}}, \omega) = G_{\mathrm{bg}}(\boldsymbol{r}_{\mathrm{dr}}, \boldsymbol{r}_0, \omega)$.

Similarly, we can eliminate p from Eqs. (2.33) and (2.34) to express E_{c} as a function of p_{dr}:

$$E_{\mathrm{c}} = \chi_{\mathrm{H}} \left(1 + \alpha_{\mathrm{hom}} G_{\mathrm{bg}}\right) p_{\mathrm{dr}}. \tag{2.42}$$

Similar to the situation in Eq. (2.40), we recognize that the cavity is excited by both the source and the induced dipole moment of the antenna, and responds with the hybridized cavity response χ_{H}. The cavity field returning at the source position is equal to E_{c}. We can now express the total field at the location of the source as:

$$E_{\mathrm{tot}}(\boldsymbol{r}_{\mathrm{dr}}) = E_{\mathrm{hom}}(\boldsymbol{r}_{\mathrm{dr}}) + E_{\mathrm{s}}(\boldsymbol{r}_{\mathrm{dr}}) + E_{\mathrm{c}}, \tag{2.43}$$

where $E_{\mathrm{hom}}(\boldsymbol{r}_{\mathrm{dr}}) = G_{\mathrm{bg}}(\boldsymbol{r}_{\mathrm{dr}}, \boldsymbol{r}_{\mathrm{dr}}, \omega) p_{\mathrm{dr}}$ is the field that has interaction with the homogeneous background medium only (*i.e.* the field responsible for Larmors expression for dipole radiation in a homogeneous medium [12]).

Inserting Eq. (2.43) into Eq. (2.39), we get

$$\begin{aligned} P_{\mathrm{dr}} = \frac{\omega}{2} |p_{\mathrm{dr}}|^2 \,\mathrm{Im}\{\, & G_{\mathrm{bg}}(\boldsymbol{r}_{\mathrm{dr}}, \boldsymbol{r}_{\mathrm{dr}}, \omega) + \alpha_{\mathrm{H}} G_{\mathrm{bg}}^2 \\ & + 2 G_{\mathrm{bg}} \alpha_{\mathrm{H}} \chi_{\mathrm{hom}} + \chi_{\mathrm{H}} \}. \end{aligned} \tag{2.44}$$

Where we have used $\alpha_{\mathrm{H}} \chi_{\mathrm{hom}} = \alpha_{\mathrm{hom}} \chi_{\mathrm{H}}$. To arrive at LDOS, one should calculate the ratio of this power and that emitted by the same dipolar source in a homogeneous medium. The latter is given by Larmors formula [12] and is equal to the contribution of the first term in Eq. (2.44):

$$P_{\mathrm{hom}} = \frac{\omega^4 \sqrt{\epsilon}}{12 \pi \epsilon_0 c^3} |p_{\mathrm{dr}}|^2. \tag{2.45}$$

The total LDOS experienced by the source dipole, normalized to LDOS in the embedding homogeneous medium, is thus

$$\begin{aligned} \mathrm{LDOS}_{\mathrm{tot}} &= \frac{P_{\mathrm{dr}}}{P_{\mathrm{hom}}} \\ &= 1 + \frac{6\pi\epsilon_0 c^3}{\omega^3 n} \,\mathrm{Im}\left\{ \alpha_{\mathrm{H}} G_{\mathrm{bg}}^2 + 2 G_{\mathrm{bg}} \alpha_{\mathrm{H}} \chi_{\mathrm{hom}} + \chi_{\mathrm{H}} \right\}. \end{aligned} \tag{2.46}$$

Note that each of the terms in $\mathrm{LDOS}_{\mathrm{tot}}$ corresponds to a multiple scattering path that radiation can take, departing from and returning to the source. The contributions of each path will be discussed in Chapter 3. Fig. 2.3 shows an example of a hybrid LDOS spectrum calculated using Eq. (2.46).

Finally, the normalized LDOS for a dipolar source coupled to a *bare* antenna or cavity can, by taking respectively $V_{\mathrm{eff}} \to \infty$ or $\beta \to 0$, be straightforwardly found as

$$\mathrm{LDOS}_{p,\mathrm{tot}} = 1 + \frac{6\pi\epsilon_0 c^3}{\omega^3 n} \,\mathrm{Im}\left\{ \alpha_{\mathrm{hom}} G_{\mathrm{bg}}^2 \right\}. \tag{2.47}$$

$$\mathrm{LDOS}_{c,\mathrm{tot}} = 1 + \frac{6\pi\epsilon_0 c^3}{\omega^3 n} \,\mathrm{Im}\left\{ \chi_{\mathrm{hom}} \right\}. \tag{2.48}$$

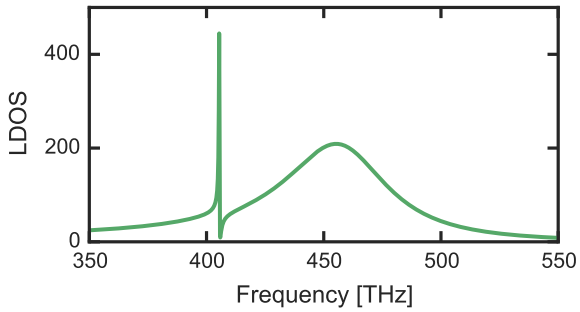

Figure 2.3: LDOS spectrum for a hybrid system. We have taken the same antenna and cavity as used for the blue line in Fig. 2.2, *i.e.* a cavity red-detuned from the antenna resonance by 1γ. The source dipole is place 10 nm from the antenna surface and is aligned normal to this surface. The spectrum contains a narrow peak and a broad peak, corresponding to the 'cavity-like' and the 'antenna-like' eigenmode of the hybrid system, respectively. We recognize the characteristic Fano lineshape that was also visible for α_{H} in Fig. 2.2. For all figures in this chapter, LDOS is normalized to vacuum.

In Chapter 3, we will discuss in detail the implications of these results for the LDOS in a hybrid system. Amongst other things, it will be demonstrated that the LDOS in a hybrid system can be significantly higher than in the bare cavity or antenna, as one might already suspect from observing Fig. 2.3.

2.4.4 LDOS per loss channel

Having found an expression for the total LDOS, we may now proceed to derive the LDOS per loss channel in the system. This allows the study of *e.g.* radiative efficiency or extraction efficiency (*i.e.* β-factor [23]), which are crucial figures of merit for any single photon source. Moreover, we use these expressions in Chapter 3 to extract antenna and cavity parameters from finite-element simulations. In Chapter 7 they are used to calculate radiative LDOS, which governs our experimental emission spectra. The loss channels in a antenna-cavity hybrid are Ohmic absorption by the antenna, dipole radiation by source and antenna, and the cavity losses. A cartoon of these channels is shown in Fig. 2.4d.

Antenna absorption

The work done by any force F on a particle moving a distance dx is Fdx. From the equation of motion Eq. (2.1), we can recognize the 'absorptive' force, *i.e.* the force describing material absorption, working on the antenna as

$$F_{\mathrm{abs}} = \mathrm{Re}\left\{m\gamma_{\mathrm{i}}\frac{\dot{p}}{q}\right\}. \tag{2.49}$$

Assuming harmonic time dependence, the power absorbed in the antenna is the oscillation frequency times the cycle-integrated work done by the absorptive force:

$$P_{\mathrm{abs}} = \frac{\omega}{2\pi}\int_0^{\tau} F_{\mathrm{abs}}\frac{dx}{dt}dt \tag{2.50}$$

with $\tau = \frac{2\pi}{\omega}$ the cycle time. With $\frac{dx}{dt} = \mathrm{Re}\left\{\frac{\dot{p}}{q}\right\}$ we find

$$P_{\mathrm{abs}} = \frac{\omega^2}{2\beta}\gamma_{\mathrm{i}}|p|^2. \tag{2.51}$$

Using Eq. (2.40) for the antenna dipole moment, we arrive at:

$$P_{\mathrm{abs}} = \frac{\omega^2}{2\beta}\gamma_{\mathrm{i}}|\alpha_{\mathrm{H}}|^2\left|G_{\mathrm{bg}} + \chi_{\mathrm{hom}}\right|^2|p_{\mathrm{dr}}|^2 \tag{2.52}$$

We then divide by the homogeneous radiated power (Eq. (2.45)) to obtain normalized absorptive LDOS as

$$\mathrm{LDOS}_{\mathrm{abs}} = \frac{6\pi\epsilon_0 c^3}{\omega^2 n}\frac{\gamma_{\mathrm{i}}}{\beta}|\alpha_{\mathrm{H}}|^2|G_{\mathrm{bg}} + \chi_{\mathrm{hom}}|^2 \tag{2.53}$$

Dipole radiation by antenna and source

To calculate exactly the power radiated by the source and the antenna, one should calculate the overlap in their radiation patterns by integrating the Poynting flux of their added scattered fields over an enclosing surface. However, to first order we can assume that if the distance $\delta\boldsymbol{r}$ between source and antenna is sufficiently small (*i.e.* $\delta\boldsymbol{r} \ll \lambda$), their radiation patterns overlap entirely. In that case, we may consider them as one effective dipole with total dipole moment $p_{\mathrm{tot}} = p_{\mathrm{dr}} + p$ [140]. We can write down the radiation reaction force on a dipole p in analogy to the absorptive force in Eq. (2.49) as

$$F_{\mathrm{rad}} = \mathrm{Re}\left\{-m\gamma_{\mathrm{r}}\frac{\dot{p}}{q}\right\}. \tag{2.54}$$

We may recognize that this equals the real part of the Abraham-Lorentz force (for harmonic time dependence) if we insert γ_{r} for a homogeneous medium [12]. A similar analysis as done for the antenna dissipation then leads to a radiated power by the antenna and source

$$\begin{aligned} P_{\mathrm{p,rad}} &= \frac{\omega^2}{2\beta}\gamma_{\mathrm{r}}|p_{\mathrm{tot}}|^2 \\ &= \frac{\omega^2}{2\beta}\gamma_{\mathrm{r}}\left|1 + \alpha_{\mathrm{H}}\left(G_{\mathrm{bg}} + \chi_{\mathrm{hom}}\right)\right|^2|p_{\mathrm{dr}}|^2. \end{aligned} \tag{2.55}$$

If we assume that γ_{r} is given by the radiative decay in a homogeneous medium (Eq. (2.22)), the corresponding normalized radiative LDOS then becomes:

$$\mathrm{LDOS}_{p,\mathrm{rad}} = \left|1 + \alpha_{\mathrm{H}} \left(G_{\mathrm{bg}} + \chi_{\mathrm{hom}}\right)\right|^2 . \tag{2.56}$$

This answer is intuitive: the power radiated by a dipole is proportional to the square of the dipole moment, so we recognize that the radiative LDOS can be interpreted as an enhancement of the total dipole moment p_{tot} with respect to that of the source, p_{dr}. In general, if γ_{r} is not given by the radiative decay in a homogeneous medium, for example because the antenna and source are near an interface or inside a photonic bandgap medium [141], an additional factor $\rho_{\mathrm{bg}}(\omega)/\rho_{\mathrm{hom}}(\omega)$ appears in front of Eq. (2.56) which accounts for the difference in (radiative) local density of states between the background (ρ_{bg}) and a homogeneous medium (ρ_{hom}).

Losses by the cavity

The power P_{i} emitted into the cavity intrinsic loss channel is simply the intrinsic cavity loss rate κ_{i} times the energy in a cavity mode, *i.e.*

$$\begin{aligned} P_{\mathrm{i}} &= \kappa_{\mathrm{i}} U_{\mathrm{m}} = \kappa_{\mathrm{i}} |a|^2 \\ &= \frac{\kappa_{\mathrm{i}}}{2} \epsilon_0 \epsilon V_{\mathrm{eff}} \left|E_{\mathrm{c}}\right|^2, \end{aligned} \tag{2.57}$$

where we have used Eqs. (2.9) and (2.23) to rewrite the mode energy U_m. We can use Eq. (2.42) for E_{c}, which leads to:

$$P_{\mathrm{i}} = \frac{\kappa_{\mathrm{i}}}{2} \epsilon_0 \epsilon V_{\mathrm{eff}} \left|\chi_{\mathrm{H}} \left(1 + \alpha_{\mathrm{hom}} G_{\mathrm{bg}}\right)\right|^2 \left|p_{\mathrm{dr}}\right|^2. \tag{2.58}$$

Division by the homogeneous radiated power gives the normalized LDOS in the cavity loss channel as

$$\mathrm{LDOS}_{\mathrm{i}} = \frac{6\pi\epsilon_0 c^3}{\omega^4 n} \kappa_{\mathrm{i}} \epsilon_0 \epsilon V_{\mathrm{eff}} \left|\chi_{\mathrm{H}} \left(1 + \alpha_{\mathrm{hom}} G_{\mathrm{bg}}\right)\right|^2 . \tag{2.59}$$

In Section 3.6, we will discuss how the collection efficiency or β-factor of an on-chip single-photon source based on a hybrid system can be described as the ratio of light emitted into the cavity decay channel to the total emission, that is, as $\mathrm{LDOS}_{\mathrm{i}}/\mathrm{LDOS}_{\mathrm{tot}}$.

An example

Fig. 2.4a-c show example spectra of the LDOS contributions by each loss channel. We notice that radiation and absorption both have a Fano lineshape, with shape (*i.e.* Fano phase) depending on cavity-antenna detuning. In fact, it can easily be shown that both $\mathrm{LDOS}_{p,\mathrm{rad}}$ and $\mathrm{LDOS}_{\mathrm{abs}}$ can be rewritten into the

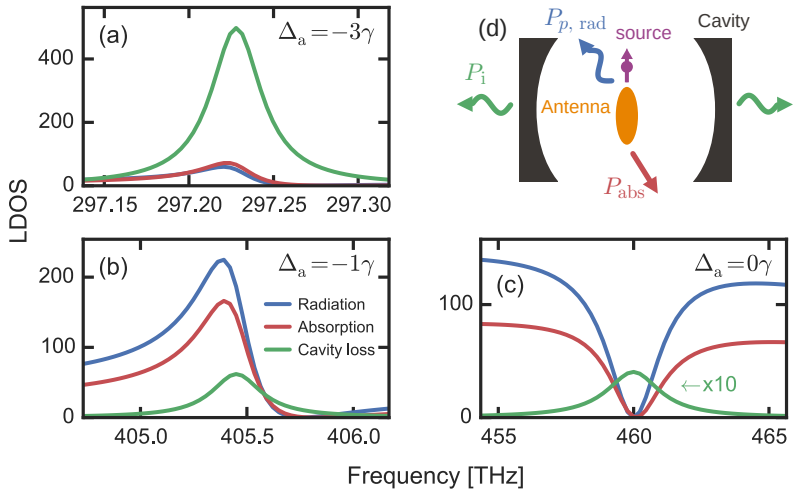

Figure 2.4: LDOS contributions of the loss channels in a hybrid system. (a-c) Spectra showing the LDOS contributions of dipole radiation ($\mathrm{LDOS}_{p,\mathrm{rad}}$, blue), absorption in the antenna ($\mathrm{LDOS}_{\mathrm{abs}}$, red) and the cavity loss channel ($\mathrm{LDOS}_{\mathrm{i}}$, green). We show spectra for cavities red-detuned by 3 **(a)** and 1 **(b)** antenna linewidth, and for a cavity at resonance with the antenna **(c)**. Apart from this detuning, the same parameters were used as for Fig. 2.3. We notice that radiation and absorption show a Fano lineshape, while cavity losses always show a Lorentzian lineshape. Moreover, antenna losses become increasingly dominant as the cavity is tuned closer to resonance. Note that $\mathrm{LDOS}_{\mathrm{i}}$ was multiplied by 10 in **(c)** for visibility. **(d)** Cartoon of a hybrid system and the emitted power flowing in the various loss channels. Note that the cavity losses are drawn here as radiation leaking through the mirrors, but they could also be *e.g.* absorption.

expression for a Fano resonance (Eq. (2.38)), as they depend on the square modulus of both resonant and non-resonant terms. The cavity losses, on the other hand, always show a Lorentzian lineshape, governed by the hybridized cavity response χ_{H}. We also notice that antenna losses (radiation and absorpion) are dominant when the cavity is near antenna resonance (*e.g.* in Fig. 2.4c), whereas far from resonance the cavity losses can become dominant. The ratio of radiation and absorption, which is mostly governed by the bare antenna albedo, also changes with cavity-antenna detuning. This is because the radiative rate γ_{r} depends on frequency as ω^3, causing lower albedo at lower frequencies.

2.4.5 Consistency check

The sum of the LDOS in separate loss channels should match our expressions (Eqs. (2.46) to (2.48)) for total LDOS. Indeed, in Fig. 2.5 we see that this is the case, both for the bare components and for the hybrid system. For a

bare cavity, there is perfect agreement. For a bare antenna, a small deviation remains, which can be assigned to the approximation made by assuming a 100% overlap between source and antenna radiation profiles. The deviation in LDOS is less than 0.5% of the total LDOS for this antenna-source geometry.

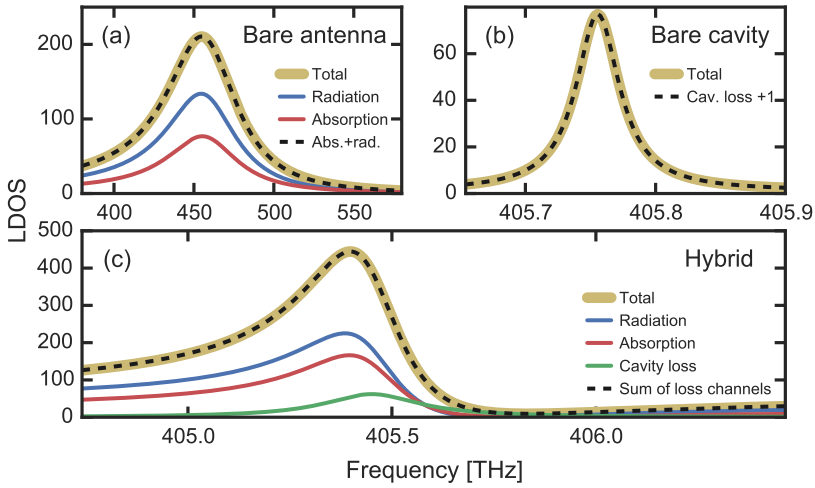

Figure 2.5: Comparing total LDOS to LDOS per loss channel. (a) A bare antenna. We compare total ($\mathrm{LDOS}_{p,\mathrm{tot}}$) to radiative ($\mathrm{LDOS}_{p,\mathrm{rad}}$) and absorptive ($\mathrm{LDOS}_{\mathrm{abs}}$) LDOS. The sum of the latter two equals the total LDOS to within 0.5%. **(b)** A bare cavity. We see that total LDOS ($\mathrm{LDOS}_{c,\mathrm{tot}}$) equals 1 (for the radiation into the background medium) plus the LDOS in the cavity loss channel ($\mathrm{LDOS}_{\mathrm{i}}$). **(c)** A hybrid system, comparing $\mathrm{LDOS}_{\mathrm{tot}}$ to LDOS in the 3 possible loss channels: dipole radiation, absorption and the cavity loss channel. Again, the sum of these 3 channels equals the total LDOS to within 0.5%. In this figure, the same parameters were used as for Fig. 2.3.

2.5 Whispering-gallery modes and taper-coupled measurements

In the experimental studies of hybrids presented in this thesis, we make use of whispering-gallery-mode cavities. Here, each whispering-gallery mode occurs in (ideally) degenerate pairs: a clockwise and an anticlockwise mode. Moreover, these cavities are often studied using waveguide or tapered-fiber coupling. It is therefore useful to generalize the derived coupled equations of motion for a single cavity mode and a single antenna to the case of two counter-propagating cavity modes and N antennas. Furthermore, we will derive expressions the observables in such a taper-coupled scattering experiment. Finally, we will discuss in more detail the case of a single antenna

on a taper-coupled whispering-gallery-mode cavity, which is relevant to the experiments in Chapter 6.

2.5.1 Equations of motion

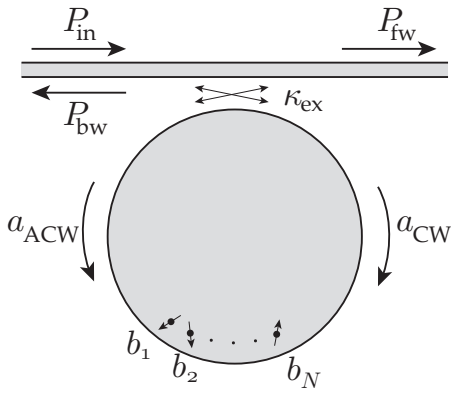

Figure 2.6: A system of 2 whispering-gallery modes with N antennas coupled to them. The modes are coupled to a waveguide at rate κ_{ex}, which has input power P_{in} flowing from left to right. P_{fw} and P_{bw} are powers flowing in the forward (*i.e.* transmission) and backward (*i.e.* reflection) direction in the waveguide.

We consider 2 counterpropagating, degenerate whispering-gallery modes, coupled to N dipolar antennas, as sketched in Fig. 2.6. We assume for simplicity that there is no coupling between the antennas, other than through the two cavity modes. This is a reasonable assumption if the antennas are placed sufficiently far apart to avoid near-field coupling and if the cavity has a sufficiently high Purcell factor, such that antenna-cavity coupling is stronger than coupling of the antennas to other modes in the background environment.

Before discussing the equations of motion for this system, let us recast those for a single cavity and antenna (Eqs. (2.19) and (2.20)) in a simpler, more symmetric form. We can define a universal antenna-cavity coupling rate Ω as

$$\Omega = \sqrt{\frac{\beta}{2}}\hat{\mathbf{p}} \cdot \mathbf{e}_{\text{c}}(\boldsymbol{r}_0), \tag{2.60}$$

which is generally a complex number. Furthermore, we replace the dipole moment p by the new variable

$$b \equiv \frac{\omega}{\sqrt{2\beta}}p. \tag{2.61}$$

Its square magnitude $|b|^2$ is an energy. We will see in Section 2.5.2 that we can think of this as the energy stored in the antenna. Together, this simplifies the

equations of motion for a single antenna and cavity mode to

$$\left(\omega_0^2 - \omega^2 - i\omega\gamma\right) b - \omega\Omega a = \omega\sqrt{\frac{\beta}{2}} E_{\mathrm{ext}}, \tag{2.62}$$

$$\left(\omega_{\mathrm{c}}^2 - \omega^2 - i\omega\kappa\right) a - \omega\Omega b = -2i\omega\sqrt{\kappa_{\mathrm{ex}}} s_{\mathrm{in}}. \tag{2.63}$$

Now let us consider the case of 2 WGMs coupled to N antennas. For each antenna, an equation of motion similar to Eq. (2.62) can be straightforwardly set up, now including two terms describing coupling to each of the cavity modes. The cavity equations of motion, analogous to Eq. (2.63), can be derived starting from Eq. (2.12) and including N different dipoles in the polarization such that

$$\mathbf{P}(\boldsymbol{r}, t) = \sum_{m=1}^{N} p_m(t)\delta(\boldsymbol{r} - \boldsymbol{r}_m)\,\hat{\mathbf{p}}_m. \tag{2.64}$$

We then find the equations of motion for the cavity modes and for the m-th antenna as

$$(\omega_{\mathrm{c}}^2 - \omega^2 - i\omega\kappa)\, a_{\mathrm{CW}} - \omega \sum_{m=1}^{N} \Omega_{\mathrm{CW},m}^{*} b_m = -2i\omega\sqrt{\kappa_{\mathrm{ex}}} s_{\mathrm{in}}, \tag{2.65}$$

$$(\omega_{\mathrm{c}}^2 - \omega^2 - i\omega\kappa)\, a_{\mathrm{ACW}} - \omega \sum_{m=1}^{N} \Omega_{\mathrm{ACW},m}^{*} b_m = 0, \tag{2.66}$$

$$(\omega_m^2 - \omega^2 - i\omega\gamma_m)\, b_m - \omega\Omega_{\mathrm{CW},m} a_{\mathrm{CW}} - \omega\Omega_{\mathrm{ACW},m} a_{\mathrm{ACW}} = \omega\sqrt{\frac{\beta_m}{2}} E_{m,\mathrm{ext}}. \tag{2.67}$$

This sets up a total of $N + 2$ coupled equations of motion. The clockwise and anticlockwise cavity modes are described by their mode amplitudes a_{CW} and a_{ACW}, respectively, and each antenna by its mode amplitude $b_m = \omega p_m/\sqrt{2\beta_m}$. We assumed that the waveguide only has power flowing in one direction, such that it only drives the clockwise mode. Note, however, that both cavity modes experience the same coupling losses, *i.e.* both have loss rate $\kappa = \kappa_{\mathrm{i}} + \kappa_{\mathrm{ex}}$. Each antenna may have different resonance frequency, linewidth and oscillator strength and may feel a different driving field $E_{m,\mathrm{ext}}$. The coupling rates of each antenna to the clockwise and anticlockwise modes are given as

$$\Omega_{\mathrm{CW},m} = \sqrt{\frac{\beta_m}{2}} (\mathbf{e}_{\mathrm{CW}}(\boldsymbol{r}_m) \cdot \hat{\mathbf{p}}_m), \tag{2.68}$$

$$\Omega_{\mathrm{ACW},m} = \sqrt{\frac{\beta_m}{2}} (\mathbf{e}_{\mathrm{ACW}}(\boldsymbol{r}_m) \cdot \hat{\mathbf{p}}_m), \tag{2.69}$$

respectively. At this point we can use a property of whispering-gallery modes in rotationally symmetric cavities, which is that the mode profiles of the CW and CCW modes must obey [142]

$$\mathbf{e}_{\mathrm{CW}}(\boldsymbol{r}) = \mathbf{e}^*_{\mathrm{ACW}}(\boldsymbol{r}), \tag{2.70}$$

i.e. they are equal except for opposite rotation directions. This implies that $\Omega_{\mathrm{ACW},m} = \Omega^*_{\mathrm{CW},m}$. Defining the coupling rate $\Omega_m \equiv \Omega_{\mathrm{CW},m}$, we can simplify the equations of motion to

$$\left(\omega_{\mathrm{c}}^2 - \omega^2 - i\omega\kappa\right) a_{\mathrm{CW}} - \omega \sum_{m=1}^{N} \Omega_m^* b_m = -2i\omega\sqrt{\kappa_{\mathrm{ex}}} s_{\mathrm{in}}, \tag{2.71}$$

$$\left(\omega_{\mathrm{c}}^2 - \omega^2 - i\omega\kappa\right) a_{\mathrm{ACW}} - \omega \sum_{m=1}^{N} \Omega_m b_m = 0, \tag{2.72}$$

$$\left(\omega_m^2 - \omega^2 - i\omega\gamma_m\right) b_m - \omega\Omega_m a_{\mathrm{CW}} - \omega\Omega_m^* a_{\mathrm{ACW}} = \omega\sqrt{\frac{\beta_m}{2}} E_{m,\mathrm{ext}}. \tag{2.73}$$

2.5.2 Transmission, reflection and output powers

We can now write down expressions for the powers flowing into the different output channels of the system, as well as waveguide transmission and reflection, which are typically observables in a taper-coupled measurement.

The intrinsic cavity losses are given by Eq. (2.57), *i.e.* (for the clockwise mode)

$$P_{i,\mathrm{CW}} = \kappa_{\mathrm{i}} U_{\mathrm{CW}} = \kappa_{\mathrm{i}} |a_{\mathrm{CW}}|^2 \tag{2.74}$$

and similarly for the anticlockwise mode. The forward power flow in the waveguide P_{fw} (*i.e.* transmitted power) is the result of interference between the input field s_{in} and the field coupled out by the CW mode into the waveguide, *i.e.* [143]

$$P_{\mathrm{fw}} = \left| -s_{\mathrm{in}} + \sqrt{\kappa_{\mathrm{ex}}} a_{\mathrm{CW}} \right|^2. \tag{2.75}$$

As there is no input power in the backward direction, we can simply write

$$P_{\mathrm{bw}} = \left| \sqrt{\kappa_{\mathrm{ex}}} a_{\mathrm{CCW}} \right|^2 \tag{2.76}$$

for the power in this direction (*i.e.* the reflected power). Division by the input power $P_{\mathrm{in}} = |s_{\mathrm{in}}|^2$ gives the transmittance and reflectance,

$$T = \frac{P_{\mathrm{fw}}}{P_{\mathrm{in}}} = \left| -1 + \sqrt{\kappa_{\mathrm{ex}}} \frac{a_{\mathrm{CW}}}{s_{\mathrm{in}}} \right|^2, \tag{2.77}$$

$$R = \frac{P_{\mathrm{bw}}}{P_{\mathrm{in}}} = \left| \sqrt{\kappa_{\mathrm{ex}}} \frac{a_{\mathrm{CCW}}}{s_{\mathrm{in}}} \right|^2. \tag{2.78}$$

Antenna absorption and radiation are derived analogously to Eqs. (2.51) and (2.55). The only difference is that, since there is no source dipole here, radiation is simply proportional to the dipole moment of each antenna alone. This assumes that there is no radiation overlap between the antennas (which is consistent with our assumption of uncoupled antennas, as radiation overlap would lead to complex coupling rates [130]). The absorbed and radiated powers by the m-th antenna are then simply given by

$$P_{\mathrm{abs},m} = \gamma_{m,\mathrm{i}} |b_m|^2, \tag{2.79}$$

$$P_{\mathrm{r},m} = \gamma_{m,\mathrm{r}} |b_m|^2, \tag{2.80}$$

respectively, with $\gamma_{m,\mathrm{i}}$ ($\gamma_{m,\mathrm{r}}$) the ohmic loss rate (radiative loss rate) of this antenna. Here, we used Eq. (2.61) to express the powers in terms of b_m. The similarity between these elegantly simple expressions for $P_{\mathrm{abs},m}$ and $P_{\mathrm{r},m}$ on the one hand and for $P_{i,\mathrm{CW}}$ and $P_{i,\mathrm{ACW}}$ on the other, show that we can interpret $|b_m|^2$ as the energy stored in the m-th antenna. This energy, multiplied by the energy decay rate into a particular channel, must be equal to the power flowing into that channel. Inserting $\gamma_{m,\mathrm{r}}$ from Eq. (2.22) with the density of states for a homogeneous medium into Eq. (2.80) and expressing in terms of the dipole moment p_m, we find

$$P_{\mathrm{r},m} = \frac{\omega^4 \sqrt{\epsilon}}{12\pi\epsilon_0 c^3} |p_m|^2, \tag{2.81}$$

which is exactly Larmors familiar expression for the radiation of a dipole in a homogeneous medium [12].

2.5.3 Special case of a single antenna, evaluated close to cavity resonance

Let us consider the special case of a waveguide-coupled WGM cavity containing only a single antenna. This simple example will help to gain intuition about these coupled systems. Moreover, in Chapter 6 we perform taper-coupled measurements of exactly such systems, so the results from this section can be directly applied to interpret those results.

We assume the system is excited only through the taper, such that the antenna is not directly driven ($E_{\mathrm{ext}} = 0$). This corresponds to the experimental situation in Chapter 6. If we are interested only in its properties close to the (high-Q) cavity resonance, we can use $\kappa, \Delta \ll \omega_{\mathrm{c}}$, where $\Delta = \omega - \omega_{\mathrm{c}}$ is

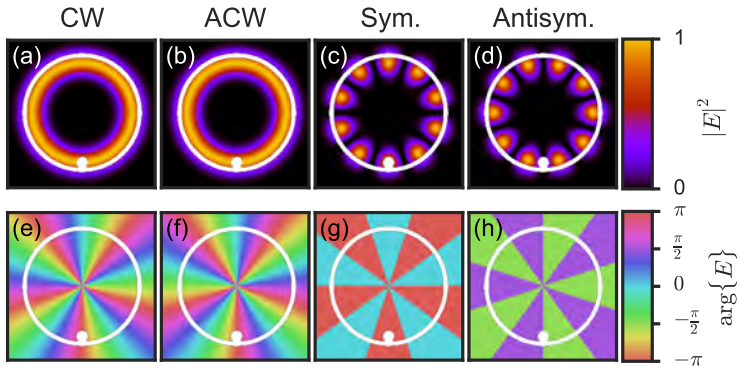

Figure 2.7: WGM field profiles. Sketch of intensity $|E|^2$ **(a-d)** and phase **(e-h)** for an example set of WGMs in a cylindrically symmetric cavity. All modes have intensity peaked at the edge of the disk. The basis of a CW (a,e) and ACW (b,f) eigenmode corresponds to running waves, whereas the basis of a symmetric (c,g) and an antisymmetric eigenmode (d,h) corresponds to standing waves, shifted from each other by a quarter period. The symmetric mode couples to the antenna, because it has a maximum at the antenna location. The antisymmetric mode has a node there, and therefore does not couple. The white lines indicate the edge of the cavity, and the antenna position is indicated by a white dot at the lower edge of the disk.

detuning, to simplify the three equations of motion to[¶]

$$(-i\Delta + \kappa/2)\, a_{\mathrm{CW}} - i\Omega b/2 = \sqrt{\kappa_{\mathrm{ex}}} s_{\mathrm{in}}, \tag{2.82}$$

$$(-i\Delta + \kappa/2)\, a_{\mathrm{ACW}} - i\Omega b/2 = 0, \tag{2.83}$$

$$(\omega_1^2 - \omega_{\mathrm{c}}^2 - i\omega_{\mathrm{c}}\gamma)\, b - \omega_{\mathrm{c}}\Omega a_{\mathrm{CW}} - \omega_{\mathrm{c}}\Omega a_{\mathrm{ACW}} = 0. \tag{2.84}$$

Here we have dropped the subscript in b_m, γ_m and Ω_m, since there is only one antenna. Also, we have the freedom to define the phase of the mode $\mathbf{e}_{\mathrm{c}}$ at will, and we have fixed it such that $\hat{\mathbf{p}} \cdot \mathbf{e}_{\mathrm{c}}(\boldsymbol{r}_0) \in \mathbb{R}$ and thus $\Omega \in \mathbb{R}$. Note that we can then relate Ω to the effective mode volume through

$$\Omega = \sqrt{\frac{\beta}{\epsilon_0 \epsilon(\boldsymbol{r}_0) V_{\mathrm{eff}}}}. \tag{2.85}$$

We now transform to the new basis

$$a_{\mathrm{s}} = \frac{1}{\sqrt{2}}(a_{\mathrm{CW}} + a_{\mathrm{ACW}}), \tag{2.86}$$

$$a_{\mathrm{as}} = \frac{1}{\sqrt{2}}(a_{\mathrm{CW}} - a_{\mathrm{ACW}}) \tag{2.87}$$

[¶]Note that by making this approximation, Eq. (2.82) now contains the again the familiar waveguide coupling term, as also found by making the slowly varying envelope approximation (Eq. (2.18)) [132, 144].

of respectively the symmetric and antisymmetric modes (around the location of the antenna). These modes, together with the CW and ACW modes, are sketched in Fig. 2.7. By respectively adding and subtracting Eqs. (2.82) and (2.83), the EOMs for the symmetric and antisymmetric modes, as well as for the antenna, can be found as

$$(-i\Delta + \kappa/2)\, a_\mathrm{s} - i\Omega b/\sqrt{2} = \sqrt{\kappa_\mathrm{ex}/2}\, s_\mathrm{in}, \tag{2.88}$$

$$(-i\Delta + \kappa/2)\, a_\mathrm{as} = \sqrt{\kappa_\mathrm{ex}/2}\, s_\mathrm{in},, \tag{2.89}$$

$$(\omega_1^2 - \omega_\mathrm{c}^2 - i\omega_\mathrm{c}\gamma_1)\, b - \sqrt{2}\omega_\mathrm{c}\Omega a_\mathrm{s} = 0. \tag{2.90}$$

By making this basis transformation, we can see that we have gone from a system of 3 coupled EOMs to just 2 coupled and 1 independent EOM. This implies that the antenna is only coupled to the symmetric cavity mode, which has a maximum at the antenna position (see Fig. 2.7), and not to the antisymmetric mode, which has a node there [26]. Using Eq. (2.90) to eliminate b from Eq. (2.88) and defining the backscattering rate γ_bs and antenna-induced loss rate γ_l as

$$\gamma_\mathrm{bs} = 2\Omega^2 \,\mathrm{Re}\left\{\frac{\omega_\mathrm{c}}{\omega_1^2 - \omega_\mathrm{c}^2 - i\omega_\mathrm{c}\gamma_1}\right\} \tag{2.91}$$

$$\gamma_\mathrm{l} = 2\Omega^2 \,\mathrm{Im}\left\{\frac{\omega_\mathrm{c}}{\omega_1^2 - \omega_\mathrm{c}^2 - i\omega_\mathrm{c}\gamma_1}\right\}, \tag{2.92}$$

we arrive at

$$(-i\Delta_\mathrm{s} + \kappa_\mathrm{s}/2)\, a_\mathrm{s} = \sqrt{\kappa_\mathrm{ex}/2}\, s_\mathrm{in}, \tag{2.93}$$

$$(-i\Delta + \kappa/2)\, a_\mathrm{as} = \sqrt{\kappa_\mathrm{ex}/2}\, s_\mathrm{in},, \tag{2.94}$$

where

$$\Delta_\mathrm{s} = \Delta + \gamma_\mathrm{bs}/2, \tag{2.95}$$

$$\kappa_\mathrm{s} = \kappa + \gamma_\mathrm{l} \tag{2.96}$$

are the detuning from resonance and total loss rate of the symmetric mode. These two uncoupled equations tell us that the antenna causes a shift and broadening of the symmetric mode with respect to the unperturbed, antisymmetric mode. These perturbations are related to the antenna properties and the antenna-cavity coupling rate. In fact, we can recognize that the shift $\gamma_\mathrm{bs}/2$ and broadening γ_l are the same as those of the hybridized eigenmode in Eqs. (2.28) and (2.29), except for a factor 2. In other words, the perturbed symmetric mode a_s *is* the eigenmode of the coupled antenna-cavity system, and we can think of bare cavity mode as the symmetric cavity mode in the absence of an antenna. The factor 2 difference comes from the fact that in Eqs. (2.91) and (2.92), $\Omega = \Omega_\mathrm{CW}$ which contains the effective mode volume of

the *clockwise* mode, whereas Eqs. (2.28) and (2.29) contain the effective mode volume $V_{\mathrm{eff,s}}$ of the *symmetric* mode. Since $\mathbf{e}_{\mathrm{s}} = (\mathbf{e}_{\mathrm{CW}} + \mathbf{e}_{\mathrm{ACW}})/\sqrt{2}$, one finds $V_{\mathrm{eff,CW}} = 2V_{\mathrm{eff,s}}$, such that Eqs. (2.91) and (2.92) match exactly the shift and broadening in Eqs. (2.28) and (2.29).

We may now derive explicit expressions for the power in the different output channels of the system. The power in the forward and backward direction can be derived from Eqs. (2.75) and (2.76) as

$$\begin{aligned} P_{\mathrm{fw}} &= \left| -s_{\mathrm{in}} + \sqrt{\frac{\kappa_{\mathrm{ex}}}{2}}(a_{\mathrm{s}} + a_{\mathrm{as}}) \right|^2 \\ &= P_{\mathrm{in}} \left| -1 + \frac{\kappa_{\mathrm{ex}}}{2}\left(\frac{1}{-i\Delta_{\mathrm{s}} + \kappa_{\mathrm{s}}/2} + \frac{1}{-i\Delta + \kappa/2}\right) \right|^2, \end{aligned} \tag{2.97}$$

$$\begin{aligned} P_{\mathrm{bw}} &= \left| \sqrt{\frac{\kappa_{\mathrm{ex}}}{2}}(a_{\mathrm{s}} - a_{\mathrm{as}}) \right|^2 \\ &= P_{\mathrm{in}} \frac{\kappa_{\mathrm{ex}}^2}{4} \left| \frac{1}{-i\Delta_{\mathrm{s}} + \kappa_{\mathrm{s}}/2} - \frac{1}{-i\Delta + \kappa/2} \right|^2. \end{aligned} \tag{2.98}$$

In the limit of two strongly split modes, we can write for the transmission coefficient at resonance with one of the two modes (for example the unperturbed mode):

$$\begin{aligned} T &\approx \left| 1 - \frac{\kappa_{\mathrm{ex}}}{2}\frac{1}{\kappa/2} \right|^2 \\ &= \left| 1 - \frac{\kappa_{\mathrm{ex}}}{\kappa_{\mathrm{i}} + \kappa_{\mathrm{ex}}} \right|^2. \end{aligned} \tag{2.99}$$

This shows that in this case, we can only reach critical coupling (*i.e.* T=0) if $\kappa_{\mathrm{ex}} \to \infty$ (see Fig. 2.8). This is because the coupling to the symmetric mode is twice lower than to the clockwise mode, where one can reach critical coupling for $\kappa_{\mathrm{ex}} = \kappa_{\mathrm{i}}$ [143]. In reality, however, critical coupling can usually be reached either because of small splitting or because of slightly unequal coupling rates for the symmetric and the antisymmetric modes [144].

The intrinsic cavity losses are given through Eqs. (2.74) and (2.93) as the sum of the losses in the CW and ACW modes, or equivalently in the symmetric and antisymmetric modes

$$P_{\mathrm{i}} = \kappa_{\mathrm{i}}\left(|a_{\mathrm{s}}|^2 + |a_{\mathrm{as}}|^2\right) = \frac{\kappa_{\mathrm{i}}\kappa_{\mathrm{ex}}}{2}\left(\left|\frac{1}{-i\Delta_{\mathrm{s}} + \kappa_{\mathrm{s}}/2}\right|^2 + \left|\frac{1}{-i\Delta + \kappa/2}\right|^2\right). \tag{2.100}$$

Using Eqs. (2.79), (2.80), (2.90) and (2.93) we can also express the scattered and

absorbed power in the antenna as

$$P_{\mathrm{abs}} = \gamma_{\mathrm{i}}|b|^2 = P_{\mathrm{in}}\gamma_{\mathrm{i}}\frac{\gamma_{\mathrm{bs}}^2+\gamma_{\mathrm{l}}^2}{2\Omega^2}\,\frac{\kappa_{\mathrm{ex}}}{2}\left|\frac{1}{-i\Delta_{\mathrm{s}}+\kappa_{\mathrm{s}}/2}\right|^2, \tag{2.101}$$

$$P_{\mathrm{r}} = P_{\mathrm{in}}\gamma_{\mathrm{r}}\frac{\gamma_{\mathrm{bs}}^2+\gamma_{\mathrm{l}}^2}{2\Omega^2}\,\frac{\kappa_{\mathrm{ex}}}{2}\left|\frac{1}{-i\Delta_{\mathrm{s}}+\kappa_{\mathrm{s}}/2}\right|^2. \tag{2.102}$$

Example spectra of the power in each of these different output channels are shown in Fig. 2.8.

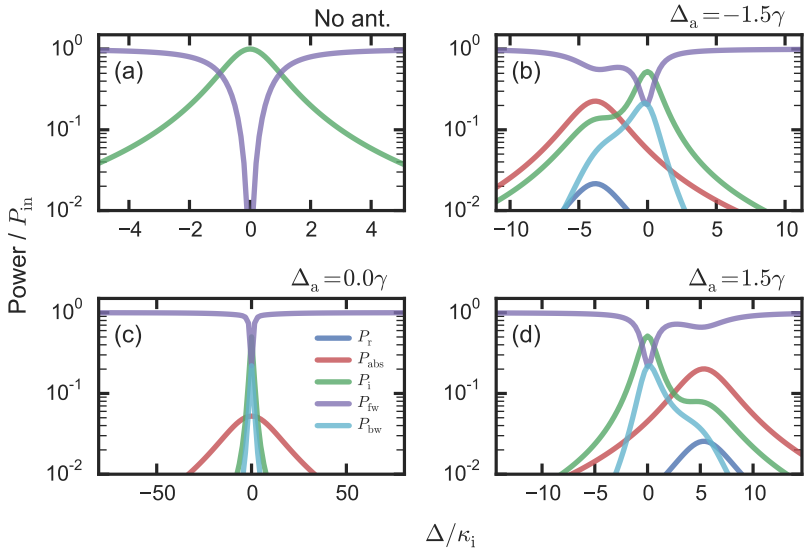

Figure 2.8: Powers in the different output channels. Four example spectra, showing power (normalized to input power) in the various output channels during a taper-coupled experiment. We use a cavity with $Q = 10^5$, $V_{\mathrm{eff}} = 50\lambda^3$ and an spherical gold antenna of 20 nm radius, resonant at 460 THz. Taper-cavity coupling rate κ_{ex} is chosen as $\kappa_{\mathrm{ex}} = \kappa_{\mathrm{i}}$. **(a)** Without an antenna, we are critically coupled to the CW mode, causing transmission (P_{fw}) to go to zero. At resonance, all power flows into the cavity loss channel (Π). **(b-d)** Spectra for cavity modes detuned from the antenna by -1.5 **(b)**, 0 **(c)** and 1.5 **(d)** antenna linewidths. Spectra show a narrow and a broad resonance, corresponding to the antisymmetric and the symmetric modes, respectively. At red-detuning (b), we notice a redshift of the symmetric mode ($\gamma_{\mathrm{bs}} > 0$), whereas at blue-detuning (d), there is a blueshift ($\gamma_{\mathrm{bs}} < 0$). At zero detuning (c), the modes are not split but the linewidth difference (*i.e.* γ_{l}) is maximal. The antisymmetric mode is no longer at critical coupling. Antenna scattering and absorption peak only at the symmetric mode.

Let us consider briefly the case of an antenna close to resonance, causing a strongly broadened mode. We assume weak coupling, such that $\kappa_{\mathrm{s}} \approx \gamma_{\mathrm{l}}$, and

driving at the perturbed resonance ($\Delta_\mathrm{s} = 0$). It is then easy to show that

$$P_\mathrm{r} \approx P_\mathrm{in}\kappa_\mathrm{ex}\frac{\gamma_\mathrm{r}}{\Omega^2}\frac{\gamma_\mathrm{bs}^2+\gamma_\mathrm{l}^2}{\gamma_\mathrm{l}^2} = 2P_\mathrm{in}\kappa_\mathrm{ex}\epsilon_0\epsilon(\boldsymbol{r}_1)V_\mathrm{eff}\frac{\gamma_\mathrm{r}}{\beta}\frac{|\alpha|^2}{\left(\mathrm{Im}\left\{\alpha\right\}\right)^2} \tag{2.103}$$

where V_eff is the effective mode volume of the *symmetric* mode and α the bare antenna polarizability. If the particle is close to resonance, $|\alpha| \approx \mathrm{Im}\left\{\alpha\right\}$. Since γ_r scales linearly with oscillator strength β, we can see that P_r is independent of β. This implies that, contrary to intuition, bigger (*i.e.* larger β) particles do not scatter more strongly when excited through the taper! In other words, the increase in scattering rate that comes with an increase in size is countered by a decrease in energy circulating in the cavity due to the increased losses. Only if the antenna is far off-resonance do we see an increase of scattering with increasing particle size. We will see in Chapter 6 that this can pose some difficulties when measuring the induced cavity shift and broadening by a resonant antenna. It is convenient to use the scattered light for detecting the perturbed modes, but this scaling implies that on-resonant antennas are difficult to see.

2.6 Conclusion and discussion

We have developed a simple coupled-oscillator model to describe hybrid antenna-cavity systems. The model can predict both mode hybridization and familiar expressions for cavity perturbation. By including a source dipole, we show that we can calculate local density of states (LDOS) in these systems, as well as the fractions of light emitted into each of the system decay channels. Finally, explicit expressions are derived for the observables in a system of one or multiple antennas coupled to two counter-propagating whispering-gallery modes. Beside providing a general framework for understanding the physics of coupled antenna-cavity systems, this chapter provides the foundation for several of the following chapters. Chapters 3 and 4 use this model for theoretical studies of LDOS in hybrid systems, and in Chapters 6 and 7 expressions from this chapter are used to fit or compare to experimental data.

Our coupled-oscillator model is completely self-consistent, within the limits of the assumptions that were made. The first of these is that the antenna is dipolar. This holds only for antennas much smaller than the wavelength, and we shall see in Chapter 6 that a breakdown of the model can be observed for aluminium nano-rod antennas longer than 140 nm (at $\sim$780 nm wavelength). The second important assumption is that there is no radiation overlap between the cavity and antenna, in which case also first-order cavity perturbation theory is valid [27]. While this holds for most geometries, recent experimental work has shown that a dramatic deviation from this perturbation theory is observed for arrays of antennas coupled to a microtoroid cavity [130]. Through the use of quasi-normal modes [62, 63, 106], which correctly

describe the radiation properties of leaky resonators, this far-field interference between cavity and antenna can be included. For the LDOS studies, we make a third assumption, namely that the emitter-antenna coupling is described by the background Green's function. This is not strictly valid for antennas with complex near-field patterns such as bow-tie [76] or nanoparticle-on-mirror geometries [68]. The model can be used in this case, however the Green's function should then be interpreted as an effective parameter capturing this coupling.

Chapter 3

Antenna-cavity hybrids: matching polar opposites for Purcell enhancements at any linewidth

In this chapter, we demonstrate that a hybrid antenna-cavity system can achieve stronger Purcell enhancements than the cavity or antenna alone. We show that these systems can in fact break the fundamental limit governing a single antenna. Additionally, hybrid systems can be used as a versatile platform to tune the bandwidth of operation to any desired value between that of the cavity and the antenna, while simultaneously boosting Purcell enhancement. The self-consistent analytical model, which we derived in Chapter 2, allows to identify the underlying mechanisms of boosted Purcell enhancement in hybrid systems, including radiation damping and constructive interference between multiple-scattering paths. Finally, we demonstrate that hybrid systems can simultaneously boost Purcell enhancement and maintain a near-unity out-coupling efficiency into a single cavity decay channel, such as a waveguide.

3.1 Introduction

For many nanophotonic applications, such as single photon sources operated at high frequency [23, 31, 145], nano-scale lasers [25], quantum logical gates for photons [29, 30] and highly sensitive, low detection volume sensing devices [26, 146, 147], strong interactions between a single quantum emitter and light are vital. This interaction can be enhanced by coupling emitters to nanophotonic structures that enhance their emission rates by increasing the local density of states (LDOS) available to the emitter [12], also known as the Purcell effect [14]. Tradionally, this is done by placing emitters in dielectric microcavities. The relative LDOS enhancement of an emitter at resonance with a cavity mode, *i.e.* the Purcell factor (F_{P}), then relates to the quality factor (Q) and the mode volume (V) as

$$F_{\mathrm{P}} = \left(3/(4\pi^2)\right)(\lambda/n)^3 (Q/V), \tag{3.1}$$

with n the index of the medium around the emitter. Microcavity modes typically reach large Purcell factors because of their long photon lifetimes and consequently high quality factors [7]. Additionally, most light is then emitted into a single cavity mode, facilitating efficient collection through *e.g.* a waveguide, which is a major advantage for applications such as single photon sources [23, 148]. Plasmonic nano-antennas are a popular alternative solution [117, 149]. Rather than storing photons for a very long time, antennas are able to concentrate their energy in volumes far below the diffraction limit [10, 150], thus achieving unparalleled LDOS enhancement over large bandwidths [68].

Both microcavities and antennas also suffer from important drawbacks. Microcavities are limited in their mode volume by the diffraction limit, hence requiring high quality factors to compensate. Unfortunately, high-Q cavities are often extremely sensitive to minor fabrication errors and changes in temperature or environment, making it difficult to scale to multiple connected devices in *e.g.* a quantum photonic network [29, 30]. Moreover, such narrow resonances typically do not match with the broad emission spectra of room temperature single-photon emitters. Antennas, on the other hand, suffer from strong radiative and dissipative losses, which limit Q to $\sim$10-50. This limits their application in quantum information processing, which requires single emitter-antenna strong coupling, *i.e.* coupling rates higher than the antenna loss rate [34, 151]. Although strong coupling has been demonstrated very recently for optical antennas supporting highly confined gap modes [70, 77], quantum logical operations remain difficult due to the extremely short coherence times. Also, their non-directional emission patterns tend to make efficient collection of the emission difficult. Ideally, one would be free to choose any desired Q, independent of the Purcell factor. An attractive candidate for such tunability is a hybrid antenna-cavity system. Recently such systems were proposed for a selection of applications including emission enhancement [104, 110], molecule or nano-particle detection [85–87, 91–93] and nano-scale

lasers [97, 98]. Recent theoretical work has suggested that an emitter coupled to a high-Q cavity could gain in LDOS through the inclusion of a small nanoparticle [105]. A similar effect was found in a very recent work for larger nanocone antennas [109]. Another study, however, found a strong *suppression* of the Purcell effect for a larger, strongly scattering antenna coupled to a cavity [118].

Here we propose hybrid systems as a versatile platform for LDOS enhancements that are not only significantly larger than those of cavities and antennas, but can also be tuned to work over any desired intermediate bandwidth. Using the simple but self-consistent coupled harmonic oscillator model discussed in Chapter 2, we show that enhancements in these systems result from a trade-off between additional losses and confinement, and we elucidate under what conditions one can profit maximally from these effects. We demonstrate that hybrid systems allow to tune the bandwidth of emission — often up to several orders of magnitude increase — while maintaining Purcell factors comparable to or even higher than the bare cavity. Since our model is applicable to any cavity or antenna geometry, this provides a general guideline for designing devices that can match any desired emitter spectrum. Moreover, we propose a realistic design for a hybrid system that can be fabricated lithographically, and find excellent agreement between LDOS spectra from our model and from finite-element simulations on this design. Finally, we demonstrate that hybrid systems can boost LDOS while retaining a high power out-coupling efficiency into a single cavity decay channel (such as a waveguide), making them excellent candidates for single photon sources.

3.2 LDOS in hybrids and bare components

We begin by comparing hybrid LDOS enhancements with those in the bare cavity and antenna. For concreteness we focus on a particular example cavity and antenna, for which Fig. 3.1a shows LDOS spectra. In Chapter 2, the relative LDOS in a hybrid system was found as (Eq. (2.46))

$$\mathrm{LDOS}_{\mathrm{tot}} = 1 + \frac{6\pi\epsilon_0 c^3}{\omega^3 n}\,\mathrm{Im}\left\{\alpha_{\mathrm{H}} G_{\mathrm{bg}}^2 + 2G_{\mathrm{bg}}\alpha_{\mathrm{H}}\chi_{\mathrm{hom}} + \chi_{\mathrm{H}}\right\}, \tag{3.2}$$

with α_{H} and χ_{H} the hybridized antenna polarizability and cavity response function, respectively, χ_{hom} the bare cavity response and G_{bg} the (projected) Greens function of the surrounding environment describing the direct antenna-emitter coupling. The expressions for the bare antenna and cavity LDOS are given in Eqs. (2.47) and (2.48). We assume an antenna in vacuum with a resonance frequency of $\omega_0/(2\pi) = 460$ THz, an oscillator strength $\beta = 3V_{\mathrm{ant}}\epsilon_0\omega_0^2$ with V_{ant} the volume of a sphere of 50 nm radius, and the ohmic damping rate $\gamma_{\mathrm{i}}/(2\pi) = 19.9$ THz of gold [139]. We place the source at 60 nm distance from the antenna center, chosen such that we can safely neglect quenching by dark multipoles [152]. Its dipole moment points away

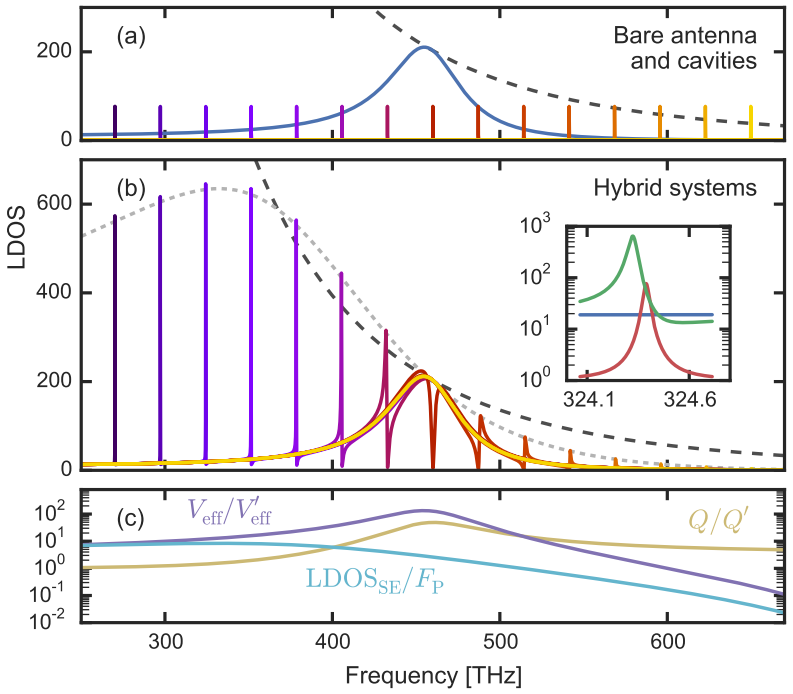

Figure 3.1: LDOS in hybrids and their bare components. **(a)** LDOS for a dipole coupled to a bare antenna (blue line) or to a set of bare cavity modes (other colors). Cavity resonances are spaced half an antenna linewidth (*i.e.* 27.1 THz) from each other. Each cavity peak represents a different calculation, indicated by a different color. The antenna limit $\eta_{\rm ant}^{\rm lim}$ discussed in Section 3.3 is shown by the dashed dark grey line. Note that throughout this chapter, LDOS is always taken relative to that of the surrounding medium (vacuum). **(b)** LDOS for the hybrid system (colored lines) composed of the same elements as shown in (a), compared to $\eta_{\rm ant}^{\rm lim}$ (dashed dark grey line). The peak LDOS derived from a super-emitter approximation ($\rm LDOS_{SE}$, light grey dashed line) shows good agreement with the narrow peaks away from the antenna resonance. The inset contains a zoom-in on the peak with highest LDOS, showing antenna (blue), cavity (red) and hybrid (green) LDOS. **(c)** Broadening (yellow) and confinement (purple) of the hybrid system, approximated as a super-emitter, relative to the bare cavity. The cyan line shows the ratio of the confinement and the broadening, which equals $\rm LDOS_{SE}$ relative to the bare cavity Purcell factor $F_{\rm P}$.

from the antenna. This yields an LDOS of ∼200 at resonance. For the cavity we assume $Q \equiv \omega_{\rm c}/\kappa = 10^4$ and $V_{\rm eff}$ to be 10 cubic wavelengths (λ), leading to a cavity Purcell factor of 76, and typical of modest-confinement cavities, like microdisks. We present results for several different cavity resonance frequencies $\omega_{\rm c}$.

Fig. 3.1b shows LDOS spectra for hybrid systems at various detunings. Each spectrum has 2 features, corresponding to the two eigenmodes of the system: a broad and a narrow resonance due to modes similar to the bare an-

tenna and the bare cavity resonance, respectively. A single spectrum example was shown in Fig. 2.3. In the remainder of this chapter, we will focus only on the narrow resonance. Because the source excites both hybrid eigenmodes, the narrow resonance presents a distinct Fano-type lineshape. Importantly, these Fano-resonances show a peak LDOS that can far exceed the LDOS in the bare components. The hybrid system outperforms the antenna *at resonance* by more than a factor 3, and the cavity by more than a factor 8. At the same detuned frequency, the antenna can be outperformed by up to a factor 25 for the lowest frequency peaks shown. Similar behaviour was also predicted in earlier work for much smaller, quasistatic antennas [105], and very recently for larger nano-cone antennas coupled to a Fabry-Perot microcavity [109]. Contrary to intuition, however, the strongest LDOS is not found for a cavity and an antenna tuned to resonance, but rather for cavities significantly red-detuned from the antenna. On resonance the cavity and antenna modes destructively interfere to yield a strongly suppressed LDOS, consistent with the findings of Frimmer *et al.* for hybrid system with a strongly radiatively damped antenna [118].

To understand the strong LDOS increase, we can employ a 'super-emitter' point of view. This concept was originally proposed by Farahani *et al.*, who claimed that an emitter coupled to an antenna could be considered as one large effective dipole when interacting with its environment [153]. In this view, for a super-emitter coupled to a cavity the emitted power should be given by

$$P_{\mathrm{dr,SE}} = \frac{\omega}{2}|p_{\mathrm{SE}}|^2 \,\mathrm{Im}\left\{\chi\right\}, \tag{3.3}$$

where $p_{\mathrm{SE}} = p_{\mathrm{dr}} + p = p_{\mathrm{dr}}\left(1 + G_{\mathrm{bg}}\alpha\right)$ is the effective dipole moment of the super-emitter, χ is the cavity response and α is the antenna polarizability. First intuition suggests to use both the bare antenna polarizability α_{hom} and the bare cavity response χ_{hom} (Eqs. (2.26) and (2.35)). However, Frimmer *et al.* demonstrated that this procedure fails to describe the dispersive Fano lineshapes and the strongly suppressed LDOS at the antenna resonance [118], which indicates that either antenna, or cavity, or both, are spoiled when tuned on resonance. Better results are obtained if the hybridized polarizability α_{H} (Eq. (2.36)) paired with χ_{hom} is used instead. A third, alternative approach would be to use α_{hom} and the hybridized cavity response χ_{H} (Eq. (2.37)). Note that, compared to the full, self-consistent expression Eq. (3.2) for LDOS, all three super-emitter descriptions are oversimplified. The merit of using α_{hom} and χ_{H} is that it accurately predicts the *envelope* function (grey dashed curve in Fig. 3.1b) encompassing the Fano features. In this approach, at a hybrid resonance the LDOS experienced by a drive dipole in a super-emitter reads $\mathrm{LDOS_{SE}} = 3/(4\pi^2)Q'/V'_{\mathrm{eff}}$, with $V'_{\mathrm{eff}} = V_{\mathrm{eff}}/|1 + G_{\mathrm{bg}}\alpha_{\mathrm{hom}}|^2$ a perturbed cavity mode volume (in cubic wavelengths) and $Q' \approx \omega_{\mathrm{c}}/\kappa'$, where $\kappa' = \kappa + (\omega_{\mathrm{c}}/\epsilon_0\epsilon V_{\mathrm{eff}})\,\mathrm{Im}\left\{\alpha_{\mathrm{hom}}(\omega_{\mathrm{c}})\right\}$. In the second term of κ', one recognizes the familiar result from perturbation theory, which states that a cavity resonance

is broadened by the scatterer [133]. This super-emitter description thus allows us to describe the LDOS increase as a balance between enhanced broadening and improved confinement.

Fig. 3.1c shows the extra confinement $V_{\text{eff}}/V'_{\text{eff}}$ and broadening Q/Q' of the super-emitter relative to the bare cavity. We see broadening is dominant on the blue side of the resonance, because of increased radiation damping of the antenna for higher frequencies [12]. Confinement, instead, favours detunings to the red of the antenna resonance. This is due firstly to the lower radiation damping, and secondly to the positive sign of $\mathrm{Re}\{\alpha_{\text{hom}}\}$, which leads to constructive interference between source and antenna when radiating into the cavity. On the blue side the effect is opposite.* Combined, these effects cause the LDOS relative to the bare cavity (cyan line in Fig. 3.1c) to be largest on the red side of the antenna resonance. Based on the expressions for Q' and V'_{eff}, we speculate that confinement can be further boosted without increasing broadening using an antenna with stronger coupling to emitters. For instance, bow-tie antennas [76] and nano-cone antennas [80, 109] have similar dipole moments yet larger field enhancements (captured in G_{bg}). In fact, simulations on a hybrid system composed of a nano-beam cavity and a bow-tie antenna showed a reduction of the cavity mode volume, due to inclusion of the antenna, of more than a factor 1000, with only a minor effect on Q [93]. These results show that hybrid systems can achieve the best of two worlds: a high Q-factor typical for dielectric cavities, combined with a strongly decreased mode volume due to the high field confinement by the antenna. As an example, the inset in Fig. 3.1b shows a hybrid mode with Q=$6.9 \cdot 10^3$ very similar to the bare cavity (10^4), but mode volume decreased by an order of magnitude (from $10\lambda^3$ to $0.82\lambda^3$).

3.3 Breaking the antenna limit with hybrid systems

Hybrid systems can improve not only the bare cavity LDOS, but also that of the antenna. In fact, we find that these systems can break the fundamental limit governing antenna LDOS. This limit follows from the well-known upper bound of $3\lambda^2/(2\pi n^2)$ set by energy conservation on the extinction cross section of a single dipolar scatterer, also known as the unitary limit [118, 154, 155]. Consequently its polarizablity is limited to $|\alpha^{\text{lim}}| = \mathrm{Im}\left\{\alpha^{\text{lim}}\right\} = (3\epsilon_0/(4\pi^2 n))\lambda^3$. An antenna with an albedo $A = \gamma_{\text{r}}/(\gamma_{\text{i}} + \gamma_{\text{r}})$ of 1 reaches this limit at its resonance frequency. For an antenna with a finite albedo at resonance, $\mathrm{Im}\{\alpha\} = \mathrm{Im}\left\{\alpha^{\text{lim}}\right\} A$. Following Eq. (2.47), this limit on α leads to

*Note that at this small antenna-source distance, G_{bg} is almost entirely real over the spectrum shown in Fig. 3.1.

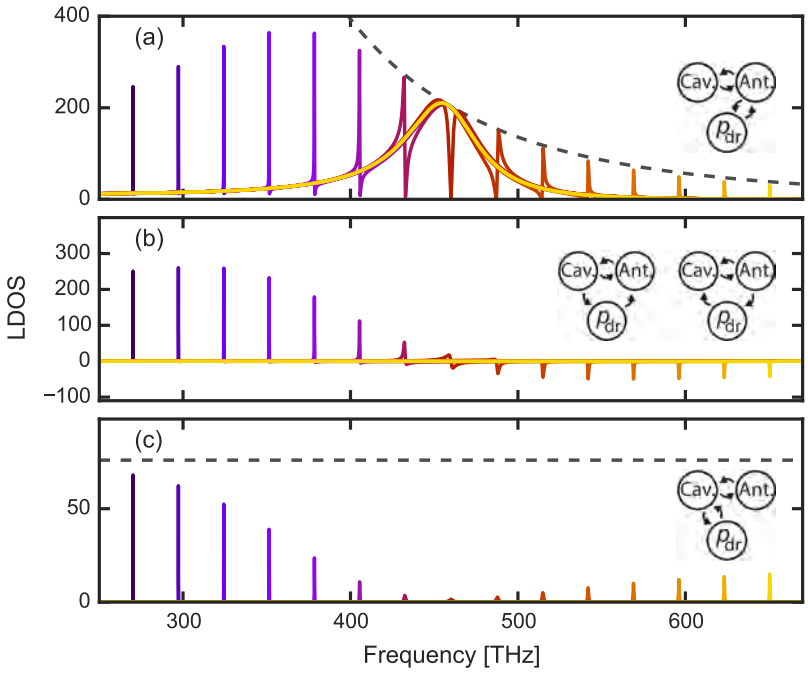

Figure 3.2: LDOS for the hybrid system, split by multiple-scattering path. The LDOS is decomposed into 3 contributions corresponding to the terms in brackets in Eq. (3.2) — the 'antenna' term **(a)**, the 'cross-terms' **(b)** and the 'cavity' term **(c)**. Each contribution corresponds to a multiple-scattering path, shown in the insets. The grey dotted lines in (a) and (c) show $\mathrm{LDOS}_{\mathrm{ant}}^{\mathrm{lim}}$ and the bare cavity Purcell factor F_{P}, respectively.

a limit on antenna LDOS given by

$$\mathrm{LDOS}_{\mathrm{ant}}^{\mathrm{lim}} = 1 + 6\pi\epsilon_0 c^3 / \left(\omega^3 n\right) \mathrm{Im}\left\{\alpha^{\mathrm{lim}} G_{\mathrm{bg}}^2\right\} A(\omega) \tag{3.4}$$

for an antenna with albedo $A(\omega)$. How a hybrid system can break this limit is best understood by analyzing Eq. (3.2), which indicates that three different multiple-scattering pathways contribute to the LDOS. We will refer to the first, second and last term in brackets in Eq. (3.2) as the 'antenna' term, 'cross-term' and 'cavity' term, respectively. Fig. 3.2 shows the hybrid LDOS from Fig. 3.1b decomposed into these three terms. Fig. 3.2a evidences that the antenna term, corresponding to scattering paths that start and end with an antenna-source interaction, is dominant over most of the spectrum. However, we also recognize that this term alone cannot break the bare antenna limit, shown as the grey dotted line. In other words, not only a bare antenna but also the antenna term in Fig. 3.2a obeys the antenna limit.

In principle there is no reason for a hybrid system, which involves a cavity mode that is not assumed to be dipolar, to be bound by the limit governing a

single dipolar antenna. Yet it is tempting to think that, since the antenna has a far greater dipole moment than the source and consequently couples more strongly to the cavity, energy transfer between the source and the cavity is completely dominated by the path that passes through the antenna first. In that case, only the antenna term in Fig. 3.2a would contribute, and the limit would be obeyed. This is because the antenna is still a dipolar scatterer bound by energy conservation, and so long as all energy passes through the antenna, LDOS is therefore also bound to the same limit. However, we see in Fig. 3.2b and c that the cavity term and particularly the cross-terms, all of which require direct interaction between cavity and source, contribute significantly to the LDOS. The cavity term in Fig. 3.2c, which represents all scattering paths starting and ending with a direct source-cavity interaction, remains below the cavity Purcell factor F_{P}, since the perturbed cavity response χ_{H} is always weaker than that of the unperturbed cavity (χ_{hom}). This stands to reason, given that the antenna spoils the cavity Q. The cross-terms in Fig. 3.2b, on the other hand, contribute strongly to the hybrid LDOS. These terms describe scattering paths starting at the antenna and ending at the cavity, and vice versa. Their contribution is largest on the red side of the antenna resonance ω_0 (up to nearly half the total LDOS for the lowest frequency peaks), and switches in sign at ω_0. The sign of the cross-term indicates constructive or destructive (negative contribution) interference. In this hybrid system, the interference is between source and antenna radiation into the cavity. From Fig. 3.1b we conclude that the sum of all three LDOS terms breaks the antenna limit, indicated by the dark dashed grey curve, for frequencies where this constructive interference takes place. Thus, through a subtle interference phenomenon, hybrids can attain larger LDOS than the antenna alone could ever achieve.

3.4 The range of effective hybrid Q and V

Hybrid systems do not only offer increased LDOS, they also open up an entirely new range of quality factors and mode volumes. Fig. 3.3 shows a 'phase diagram' of Q and V. Plasmonic antennas are found in the bottom left of this diagram, at low Q and V. Conversely, cavities are in the top right, with high Q and V. However, for most applications, neither of these extrema is optimal. For example, if one desires a high Purcell factor, yet wants to avoid strong coupling — demands that are critical to a good, low-jitter single photon source [23] — the high quality factors of cavities are unpractical. A device with an intermediate Q would be ideal, provided that the Purcell factor remains high. Such an intermediate Q would also better match the emission spectrum of an emitter, which is often broader than that of a high-Q cavity yet narrower than that of an antenna [156]. Moreover, to obtain a an optimal trade-off between stability and tunability, one should be able to reach this regime of intermediate Q: high Q renders cavities easily detuned by undesired perturbations,

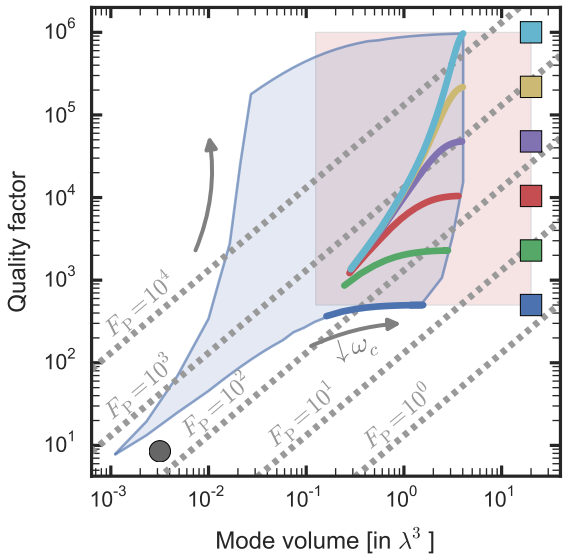

Figure 3.3: Phase diagram of quality factors Q and dimensionless mode volumes V/λ^3. Shown are the values for the bare antenna (dark circle) and a set of bare cavities (■), as well as the values of the corresponding hybrid modes. The colored lines show corresponding hybrid results for these components, for all cavity-antenna detunings used (see text). For decreasing ω_c (that is, further red-detuning of the cavity) hybrid Q and V lie closer to those of the bare cavity. The light blue area indicates the location of the hybrid values attained for cavities with $500 < Q < 10^6$ and $0.5^3 < V_{\rm eff}/\lambda^3 < 20$ (bare cavity parameters indicated by the light red area). Dashed grey lines are lines of constant Purcell factor $F_{\rm P}$ — that is, constant relative LDOS.

whereas the very low Q of antennas makes them difficult to tune. Here we will show that hybrid systems allow precisely this — choosing the Q-factor to a desired, intermediate value, while retaining or even improving on the bare cavity Purcell factor.

In Fig. 3.3, we compare Q and $V_{\rm eff}$ of modes in hybrid systems with those in the bare cavities and antenna. We assume the same antenna as in Figs. 3.1 and 3.2. Cavities were used with $500 < Q < 10^6$ and $0.5^3 < V_{\rm eff}/\lambda^3 < 20$, and for each combination of Q and $V_{\rm eff}/\lambda^3$ we take several cavity resonance frequencies $100\ \text{THz} < \omega_c/2\pi < 433\ \text{THz}$, corresponding to cavity-antenna detunings ranging from 0.5 to 6.6 antenna linewidths. Cavities were always red-detuned from the antenna. To position hybrid structures in this diagram, we calculate LDOS for frequencies around the cavity resonance. We retrieve Q from the linewidth of the Fano-resonance, which is the linewidth of the perturbed cavity mode $\kappa' = \kappa + \delta\kappa$, with $\delta\kappa$ given by Eq. (2.29). While mode volume is only well defined for a single (non-leaky) mode [61–64], here we employ an operational definition through Purcell's formula

(Eq. (3.1)) and the peak value of the LDOS ($\mathrm{LDOS}_{\mathrm{tot}}^{\mathrm{peak}}$). This leads to $V_{\mathrm{eff}}^{\mathrm{hyb}} = \left(3/(4\pi^2)\right) Q/\mathrm{LDOS}_{\mathrm{tot}}^{\mathrm{peak}}$, with $V_{\mathrm{eff}}^{\mathrm{hyb}}$ in units of the cubic resonance wavelength. We use the same definition for the antenna mode volume. Note that, because we keep cavity Q and $V_{\mathrm{eff}}/\lambda^3$ constant when varying ω_{c}, cavities with different ω_{c} appear at the same point in Fig. 3.3. Hybrid Q and V, however, depend strongly on cavity-antenna detuning, as we have seen in Fig. 3.1. Therefore the hybrid systems composed of cavities with different ω_{c} appear as lines in Fig. 3.3.

From Fig. 3.3 we see that hybrid systems provide exactly the tunability discussed earlier: through variation of the cavity-antenna detuning, any practical Q between that of the cavity and the antenna can be chosen. The subset displayed by the colored lines shows that this extreme tunability typically does not come at the price of LDOS enhancement. If the bare cavity provides an LDOS far below that of the antenna (blue and green), hybrid systems can gain strongly in LDOS compared to the cavity, yet the Q-factor remains close to that of the bare cavity. For cavities with LDOS similar to the bare antenna (red, purple and yellow), one can gain with respect to both bare components, and Q can be tuned over a large range while maintaining very high LDOS. As can be expected, the LDOS of the cavities with highest Q (light blue) is reduced by inclusion of the antenna, as cavities with such narrow resonances are easily spoiled by the losses introduced by an antenna. Yet it is remarkable that an LDOS of order 10^3 can be maintained over a large range of strongly reduced Q-factors in such systems. To illustrate the full attainable range of hybrid Q and V, the light grey area shows where all the hybrid systems are located, for the full range of cavities examined here. From this we see that any Q between that of the cavity and the antenna can be obtained, at high Purcell factor. In summary, hybrid systems can bridge the gap in Q and V_{eff} between cavities and plasmonic antennas, reaching any desired, practical Q with similar or better LDOS.

3.5 Finite-element simulations on a realistic hybrid system

Let us now discuss a possible physical implementation of the proposed hybrid systems. We perform finite-element simulations on a realistic antenna-cavity design using COMSOL Multiphysics 5.1, which also serve to verify the validity of our analytical oscillator model. As a cavity, we take a silicon nitride (n=1.997) disk in vacuum with a radius of 2032 nm and a thickness of 200 nm. To tune the cavity Q and to help trace how much power flows into the cavity mode we include a small amount of absorption as imaginary component ($4\cdot 10^{-6}$) in the permittivity of the silicon nitride. The disk supports a radially polarized m=22 whispering-gallery mode (WGM) at 382.584 THz ($\sim$784 nm)

with Q=7.28· 10^4 (see Fig. 3.4a and c). The antenna we use is a gold prolate ellipsoid with a long (short) axis radius of 70 (20) nm. Optical constants are described by a modified Drude model [139]. Fig. 3.4b shows the antenna field profile. The hybrid systems is obtained by placing the antenna 50 nm above the disk, just next to the source. In an experiment, one could use an antenna that is fabricated (*e.g.* by e-beam lithography) directly on top of the disk, as demonstrated earlier for qualitatively similar geometries [97, 157]. In Chapter 5, we will further discuss the experimental implementation of such a system.

To verify the predictions of the oscillator model, we first retrieve LDOS spectra for the bare components from the simulations, and through a fit retrieve all the input parameters for our oscillator model. We then compare the oscillator model prediction for the LDOS spectrum of the hybrid to that obtained from finite-element simulation of the hybrid system.

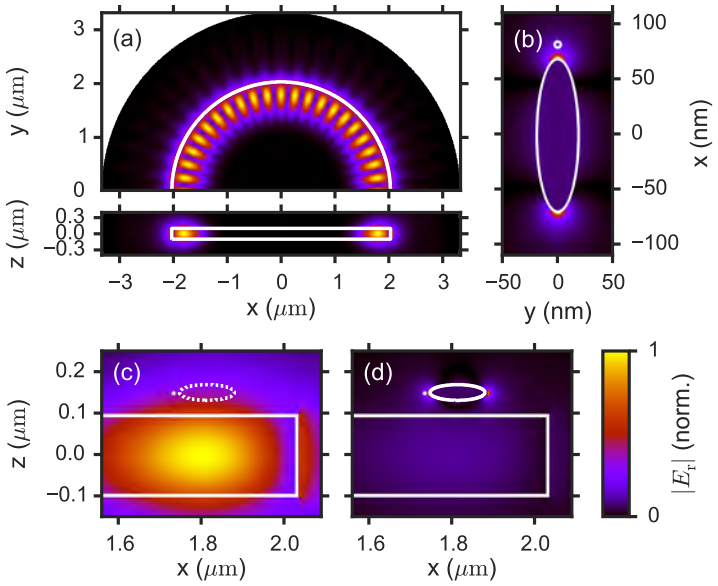

Figure 3.4: Cross-cuts of the cavity, antenna and hybrid mode profiles. All fields are normalized to their maximum values. Cross-cuts are taken at symmetry planes of the structures. White lines indicate the edges of the structures. **(a)** Top view and side view of the bare cavity eigenmode. Only the dominant (radial) field component is shown. **(b)** Field profile of the bare antenna in vacuum, illuminated by an x-polarized plane wave at its resonance frequency. The x-component of the scattered field is shown. The small white circle above the antenna tip indicates where we will place the source dipole. **(c)** Zoom-in of the bare cavity eigenmode profile. The position of the antenna in the hybrid system is indicated with the dashed line. Note that no antenna was used in this simulation. The position of the drive dipole is indicated beside the antenna tip. **(d)** Zoom-in of the hybrid eigenmode profile. Hot-spots are visible near the antenna tips.

From the fit to the bare cavity emission and absorption spectra (see Section 3.A), we find the cavity parameters ω_c, $\kappa_r/2\pi = 5$ GHz, $\kappa_{abs}/2\pi = 0.3$ GHz and $V_{eff} = 22.8\lambda^3$. This leads to a peak LDOS (Purcell factor) of 242. The bare antenna spectra yield the antenna parameters $\omega_0/2\pi = 436$ THz, $\gamma_i/2\pi = 18.1$ THz, β =0.073 C^2/kg and an effective source-antenna distance of 55.2 nm (smaller than the physical source-to-center distance of 70+12 nm owing to the lightning rod effect). These values lead to a bare radiative (absorptive) antenna LDOS of 186 (174) at maximum. Fig. 3.5 shows the comparison between the oscillator model prediction based on these values and the full simulations on the hybrid system where the antenna was placed beside the source, just above the disk, as shown in Fig. 3.4d. We find a peak LDOS of ∼914 in the hybrid system, which is a large increase with respect to the bare cavity (242) and antenna (360 at resonance and ∼65 near cavity resonance). The bandwidth over which this LDOS occurs is increased by a factor 9.4 (to 49 GHz) with respect to the cavity. There is excellent agreement between the model and the simulation for all components of the LDOS. Remaining differences can be largely attributed to errors in the antenna fit (see Section 3.A). These results demonstrate that the oscillator model correctly predicts LDOS in a coupled antenna-cavity system, based on the response of the bare components. Moreover, it shows that a realistic antenna-cavity system can combine the best features of both cavity and antenna, achieving much stronger LDOS than the bare components.

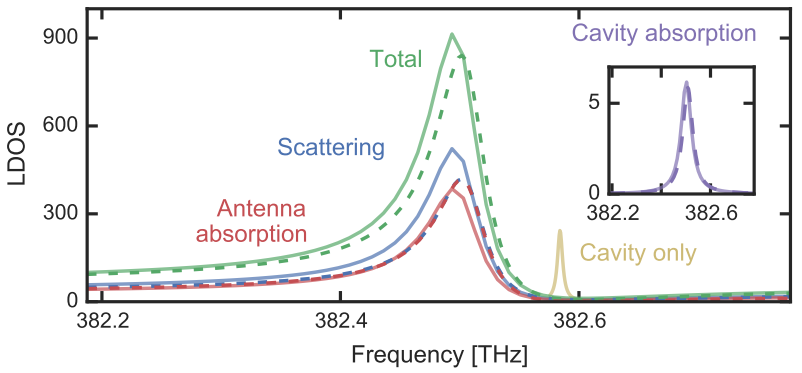

Figure 3.5: LDOS in a hybrid system from the oscillator model (dashed) and from simulations (solid). We LDOS contributions from scattering into free space (blue) and antenna absorption (red), as well as total LDOS (green). LDOS from to cavity absorption (purple) in the hybrid system is visible in the inset. LDOS from the bare cavity (yellow) is shown for comparison.

3.6 Efficiency of radiation into the cavity

In the previous sections, we demonstrated that hybrid systems allow strongly boosted LDOS at any desired quality factor Q. Here we will show that one can also control by hybridization into what channels energy is emitted. Depending on the application, one may *e.g.* wish to design a system that emits all power into free-space, or rather into a single-mode waveguide. The latter is often the case for an on-chip single-photon source, for example. In Section 2.4, we derived expressions for the power dissipated in the antenna, radiated by antenna and source into free space, and the power flowing into the cavity decay channel. Here we use this to study the fraction of power going into the cavity decay channel, as this is usually most efficiently extracted in *e.g.* a waveguide. This fraction, *i.e.* the efficiency of extraction into single mode output channel, is also known as the β-factor in the context of single-photon sources [23]. Note that, as we generally have not specified the origin of the cavity loss κ, one could assume it to be dominated by coupling to a waveguide. In experiments this is commonly achieved by evanescent coupling of a cavity to a nearby integrated waveguide or fibre taper [128, 129]. Overcoupling then ensures that the waveguide or taper is the dominant loss channel.

Fig. 3.6a and b show the relative cavity outflux and the peak value of the total hybrid LDOS ($\mathrm{LDOS}_{\mathrm{tot}}^{\mathrm{peak}}$) as function of cavity resonance ω_{c} and

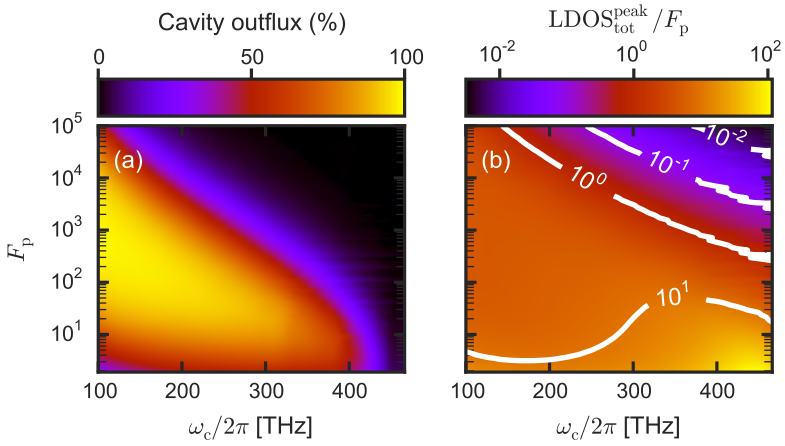

Figure 3.6: Radiation efficiency and LDOS in hybrids. **(a)** Fraction of power into the cavity decay channel κ, as function of cavity resonance ω_{c} and bare cavity Purcell factor F_{P}. This fraction was evaluated at the peak of the total hybrid LDOS ($\mathrm{LDOS}_{\mathrm{tot}}$, Eq. (3.2)). We use the same antenna as in Figs. 3.1 and 3.3. **(b)** Peak value of total LDOS in the hybrid system ($\mathrm{LDOS}_{\mathrm{tot}}^{\mathrm{peak}}$), relative to F_{P}. The same cavities and antenna were used as in (a).

bare cavity Purcell factor F_{P}. The same cavities and antenna were used as in Fig. 3.3, and detuning now ranged between 0 and 6.6 antenna linewidths. Note that relative cavity outflux and $\mathrm{LDOS}_{\mathrm{tot}}^{\mathrm{peak}}$ are fully determined by antenna properties, detuning and F_{P} (*i.e.* Q/V_{eff}), not by Q and V_{eff} separately. There is a large region in which hybrid LDOS can be increased with respect to the cavity, while maintaining a very high fraction of power flux into the cavity channel. This implies that the plasmonic antenna helps to boost LDOS though its field confinement while adding almost no additional losses, consistent with the results in Fig. 3.1c. Fig. 3.6 shows that this works particularly well for cavities with F_{P} between 10 and $\sim 10^3$. Close to the antenna resonance (460 THz), cavity outflux drops, as power outflux is dominated by the antenna. For very good cavities with F_{P} around 10^4, power outflux is also dominated by the antenna, even for far red-detunings. This reflects the fact that either intrinsic cavity losses are very low (high Q), or coupling to the antenna is very strong (low V). Both cases lead to the antenna decay channels being dominant. Importantly, dominant outcoupling through the antenna does not mean that all the power is dissipated: it is distributed between dipolar radiation and dissipation according to the bare antenna albedo. For applications where radiative efficiency rather than coupling to a waveguide is important, these antenna-dominated regimes can be highly interesting.

In conclusion, one can generally engineer the system in such a way that the power flows in any of the desired channels. Specifically, we have shown that it can be designed for a high extraction efficiency into a single cavity loss channel, such as a waveguide. This is of particular interest for applications such as an on-chip single-photon source with a high β-factor.

3.7 Conclusions and outlook

We have shown that hybrid antenna-cavity systems can support larger local density of states (LDOS) than either the antenna or the cavity alone. These systems can benefit simultaneously from the high cavity quality factor and the low mode volume of the antenna. This benefit occurs only when the cavity is red-detuned from the antenna. We have demonstrated that this is partly due to the reduced radiation damping of the antenna, and partly due to constructive interference between source and antenna radiation. The latter also allows the LDOS in hybrid systems to break the fundamental limit governing antenna LDOS. Moreover, we have shown that hybrid structures allow to design any desired quality factor while maintaining similar or higher LDOS than the bare cavity and antenna. A study of the cavity power outflux as a fraction of total emitted power demonstrated that one can furthermore engineer the system to emit efficiently into a desired output channel, such as a waveguide. Finally, a physical implementation using a WGM cavity and a gold antenna was proposed and tested using finite-element simulations,

showing strongly increased LDOS and excellent agreement with the oscillator model.

These results highlight hybrid systems as a highly versatile and promising platform for enhancement of light-matter interactions. Such systems can leverage the existing expertise on high-Q cavities and plasmonic antennas for devices that combine the best of both worlds, while avoiding the disadvantages such as losses in the metal. While one has to pay the price of a multi-step fabrication process to integrate cavity, antenna and emitter, the advantage is that it could open up arbitrary bandwidth cavity QED to fit a wide variety of emitters, including single molecules, quantum dot nano-crystals and nano-diamond color centers. This paves the way to further studies, *e.g.* an experimental demonstration of Purcell enhancements in the proposed design or studies of hybrid systems as efficient interfaces between free-space radiation and on-chip waveguides.

Appendices

3.A Finite-element simulations

In this section we describe the finite-element simulations of the bare cavity and antenna, and of the hybrid system, which were discussed in this chapter. We describe how we retrieved radiative and dissipative LDOS from the simulations, and how we fitted bare component LDOS spectra to obtain the cavity and antenna parameters.

The antenna and cavity geometries are described above in Section 3.2, and shown in Fig. 3.4 there. Cavity spectra are obtained by sweeping the oscillation frequency of a point source placed 50 nm above the disk surface, 300 nm inward from the disk edge (see Fig. 3.4c) and oriented in the radial direction (in a cylindrical coordinate system with the center of the disk as origin). We integrate the Poynting flux over a surface enclosing the cavity and source, and calculate the absorption in the disk, which are then both normalized to Larmors formula (Eq. (2.45)) to obtain respectively the radiative and absorptive LDOS.

A similar procedure was used for the antenna LDOS spectra, with the source now placed 12 nm from the tip of the antenna (see Fig. 3.4b) and oriented along the antenna long axis. Radiative and absorptive LDOS was calculated as described above. In the simulation of the hybrid system, the antenna is placed 50 nm above the surface of the disk. The presence of high-index silicon nitride in the antenna near-field red-shifts the antenna resonance frequency slightly (by $\sim$5 THz), which is not captured by the coupled-oscillator model. We account for it by simulating the bare antenna 50 nm above an infinite substrate of silicon nitride.

In Fig. 3.7 we show the LDOS spectra obtained from COMSOL simulations for the bare antenna and bare cavity. Also shown are the fits to these spectra. We use Eq. (2.53) and Eq. (2.56) to fit antenna radiation and dissipation, respectively, with ω_0, γ_i, β and the antenna-source center-to-center distance Δr as fitting parameters. Fitting the cavity radiation and absorption is done using Eq. (2.59). To account for the two separate cavity decay mechanisms, *i.e.* radiation and absorption, we replace the prefactor κ_i in Eq. (2.59) by radiative loss rate κ_r and absorptive loss rate κ_abs, respectively, while setting the total cavity loss rate $\kappa = \kappa_\mathrm{abs} + \kappa_\mathrm{r}$. Fit parameters are ω_c, κ_r, κ_abs and V_eff. Importantly, for both the cavity and the antenna, the fit routine fits absorption and radiation simultaneously. That is, it calculates the sum of the squared errors between the radiation data and fit, and between the absorption data and fit, and minimizes the sum of the two, using a nonlinear minimization routine. This allows an unambiguous retrieval of the cavity and antenna parameters.

During the simulation of the hybrid system, the antenna was centered 50 nm above the disk and 218 nm from the edge of the disk. This ensured that

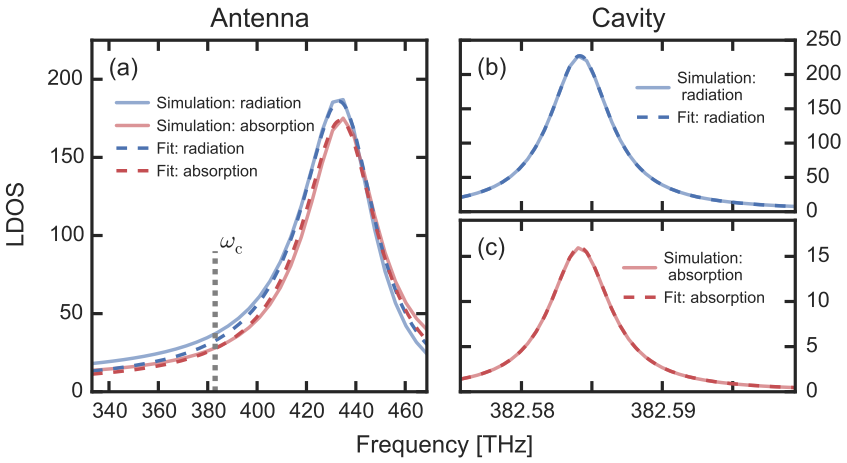

Figure 3.7: Fitting the bare cavity and antenna. **(a)** Fits to the bare antenna LDOS spectra. The grey dashed line indicates the cavity resonance frequency ω_c. The bare antenna was placed 50 nm above an infinite silicon nitride substrate. It can be seen that the fit to the antenna radiation slightly underestimates the radiative LDOS at ω_c, which explains why the prediction of the oscillator model also underestimates radiative LDOS for the hybrid system, as shown in Fig. 3.5. Deviations of the antenna spectra from the lorentzian fits are likely because only a spherical or elipsoidal antenna in vacuum, with metal parameters described by the *unmodified* Drude model, has a strictly lorentzian lineshape. Here we use a modified Drude model [139]. **(b)** and **(c)**: Fits to the bare antenna radiative **(b)** and absorptive **(c)** LDOS spectra.

the source position with respect to neither disk nor antenna was changed with respect to the simulations of the bare components. The antenna and source positions above the disk were chosen such that cavity mode intensity was approximately equal (within 12%) at the source and the antenna positions, as was assumed in the oscillator model (see Chapter 2).

All finite-element simulations were performed with the frequency domain module (radio frequency) of COMSOL Multiphysics, version 5.1. The simulation domain for the cavity and the hybrid structure was a sphere of 2932 nm radius (*i.e.* extending 900 nm beyond the disk edge), surrounded by a perfectly matched layer (PML) of 390 nm thickness. For the simulations of the antenna above an infinite substrate, a spherical domain of 819 nm radius with a 390 nm thick PML was used. Because of the mirror symmetry of the geometries, all the simulations used only half of the simulation domain, with a perfect magnetic mirror placed on the symmetry plane. For the antenna and a small ($\sim$50 nm) region around the source dipole, a tetrahedral mesh with an element size of 9.8 nm and 12 nm, respectively, was used. The disk cavity was meshed by creating a triangular mesh on the top surface with element sizes of 40 nm and 78 nm at the disk edge and center, respectively,

and subsequently sweeping this mesh down to the bottom of the disk in 8 partitions. A tetrahedral mesh with maximal element size of 195 nm was used in the vacuum surrounding the structures. The PML used a swept mesh with 6 partitions. For the simulations with a dipolar source on the cavity and hybrid, the iterative solver GMRES was used. Those on the antenna used the direct solver MUMPS. The eigenfrequency calculations done to make Fig. 3.4a,c and d used MUMPS as well. Quadratic element discretization of the electric field was used in all simulations.

Chapter 4

Cavities as conjugate-matching networks for antennas at optical frequencies

This chapter discusses an electrical circuit analogue of a hybrid antenna-cavity system. First, two different electrical circuits that were proposed in literature to describe an optical antenna are discussed, and they are shown to be equivalent. We then apply the maximum power transfer theorem to find a fundamental bound for the radiation by a lossy nano-antenna, which is independent of its environment. This bound is reached when antenna and radiation load are conjugate-matched. Based on the derivation of the antenna circuit, we propose an equivalent circuit for a hybrid antenna-cavity system driven by an external field or a fluorescent emitter. We show how a cavity can be used to reach the conjugate-matching limit with an optically small nano-antenna, and elucidate the conditions for which this can be achieved. These results provide a useful analogy between nanophotonics and circuit theory, showing how cavities can be viewed as a matching network between an antenna and the radiation load and directly providing design rules for optimized scattering.

4.1 Introduction

Electromagnetic waves, whether at radio frequencies or optical frequencies, are all governed by the Maxwell equations. This fact has prompted many researches to make analogies between the older and more established field of radio-frequency engineering and the relatively new field of nanophotonics. Such analogies have aided research into several exciting phenomena in the optical domain, including strongly scattering [158], efficient [159] or directional [71, 160, 161] antennas, emission enhancement [162], plasmonic waveguides [163], optical cloaking [164, 165], epsilon-near-zero materials [166, 167], far-field super-resolution microscopy [168, 169] and optical metamaterials [170–172]. The connection with radio-frequencies has been useful also in a broader optics context — one of the works on compression of optical pulses that was awarded with the 2018 Nobel prize for physics was inspired by radar technology [173]. Among the efforts to connect radio-frequencies to plasmonics are several works that have described plasmonic nano-antennas by an equivalent electrical circuit containing lumped elements [160, 174–179]. This has led to novel design strategies for these antennas, including for example phased array nano-antennas [160], directive leaky-wave nano-antennas [161] or 'antenna loading' by dielectric spacers for tuning the scattering response [175, 176].

Inspired by the circuit analogy for a nano-antenna, in this chapter we present an equivalent circuit for a hybrid antenna-cavity system, and use it to show how cavities can be interpreted as a matching network between an antenna and the radiation load. Before we discuss this hybrid circuit, it is important to understand the equivalent circuit that describes a single nano-particle, as this will form the basis for our hybrid circuit. Therefore, in Section 4.2 we first discuss two nano-antenna circuits from the literature. While these circuits may appear completely different at first glance, we show that they can be made equivalent by a simple transformation. Section 4.3 then discusses the 'conjugate-matching limit' — a fundamental bound on antenna scattering imposed by the well-known maximum power transfer theorem applicable to circuits. The equivalent circuit for a hybrid system is introduced in Section 4.4, which can be used to study both scattering and local density of states. Using this circuit, in Section 4.5 we show how the cavity can strongly increase radiated power, even reaching the conjugate-matching limit if the antenna is sufficiently small. We discuss the two fundamental limits that govern scattering, and show how cavities act as a matching network between antennas and radiation. Such matching networks, which are an essential part of radio-frequency circuit design, are currently lacking at THz or optical frequencies due to a lack of high-quality lumped elements. Our results offer a perspective on matching networks at optical frequencies.

4.2 Equivalent circuits for an emitter coupled to a nano-antenna

Different circuit models have been proposed to describe a small nano-particle driven by an external field or by a fluorescent emitter. Here, we discuss two circuits proposed respectively by Krasnok *et al.* [179] and by Engheta *et al.* [174]. The first was proposed to study local density of states (LDOS) near an antenna, while the second has been used for example to study antenna resonance tuning [175, 176]. Although these circuits seem entirely different, we show that the two descriptions are equivalent.

4.2.1 The circuit proposed by Krasnok *et al.*

Krasnok *et al.* [179] proposed a circuit model to describe the Purcell effect experienced by an emitter near a nano-antenna, based largely on a circuit proposed earlier by Greffet *et al.* [177]. For clarity, and because this forms the basis of the hybrid circuit discussed in Section 4.4, we briefly discuss the derivation of this circuit. Let us start with a sub-wavelength antenna driven by an unspecified external field E_{ext}. This induces a dipole moment $p = \alpha E_{\mathrm{ext}}$ in the antenna, where α is the self-consistent antenna electric polarizability*

$$\alpha^{-1} = \alpha_0^{-1} - i\frac{k^3}{6\pi\epsilon_0 n^2}. \tag{4.1}$$

Here, α_0 is the static electric polarizability and the second term on the right hand side in Eq. (4.1) represents radiation damping, with $k = \omega n/c$ the wavenumber and n the index of the host material. For simplicity we restrict ourselves to particles in vacuum. To determine an equivalent circuit, we can define a driving voltage as $V_{\mathrm{a}} = l_{\mathrm{a}} E_{\mathrm{ext}}$ and an induced current $I_{\mathrm{a}} = \frac{1}{l_{\mathrm{a}}}\frac{\mathrm{d}p}{\mathrm{d}t} = -\frac{i\omega p}{l_{\mathrm{a}}}$, with l_{a} some effective length of the antenna. The antenna impedance can then be recognized as

$$Z_{\mathrm{a}} = \frac{V_{\mathrm{a}}}{I_{\mathrm{a}}} = -\frac{l_{\mathrm{a}}^2}{i\omega\alpha}. \tag{4.2}$$

If α_0 is assumed to be given by the classical Lorentz model (as also done in Section 2.2), we find

$$Z_{\mathrm{a}} = -\frac{l_{\mathrm{a}}^2}{i\omega}\left(\frac{\omega_0^2}{\beta} - \frac{\omega^2}{\beta} - \frac{i\omega\gamma_{\mathrm{i}}}{\beta} - i\frac{k^3}{6\pi\epsilon_0}\right) \tag{4.3}$$

*Following [179], we use scalar fields and dipole moments, which is valid for spherical particles or ellipsoidal particles driven along one of the main axes. To be consistent with the other chapters, however, we use a time convention $e^{-i\omega t}$, whereas the opposite convention is used in [179].

which maps onto the impedance of an inductor $L_\mathrm{s} = l_\mathrm{a}^2/\beta$, a capacitor $C_\mathrm{s} = \beta/(l_\mathrm{a}^2\omega_0^2)$ and two resistors $R_\mathrm{s} = l_\mathrm{a}^2\gamma_\mathrm{i}/\beta$ and $R_\mathrm{r} = \eta_0 k^2 l_\mathrm{a}^2/(6\pi)$, with $\eta_0 = (\epsilon_0 c)^{-1}$ the vacuum wave-impedance, in series connection. Here, β, ω_0 and γ_i are the antenna oscillator strength, resonance frequency and ohmic damping rate, respectively. We can also write this as the sum of the quasi-static antenna impedance $Z_\mathrm{s} = R_\mathrm{s} - i\omega L_\mathrm{s} - (i\omega C_\mathrm{s})^{-1}$ and the radiation resistance R_r. The corresponding equivalent circuit is thus composed of a voltage source driving a series connection of Z_s and R_r, and is shown as the rightmost circuit in Fig. 4.1a.

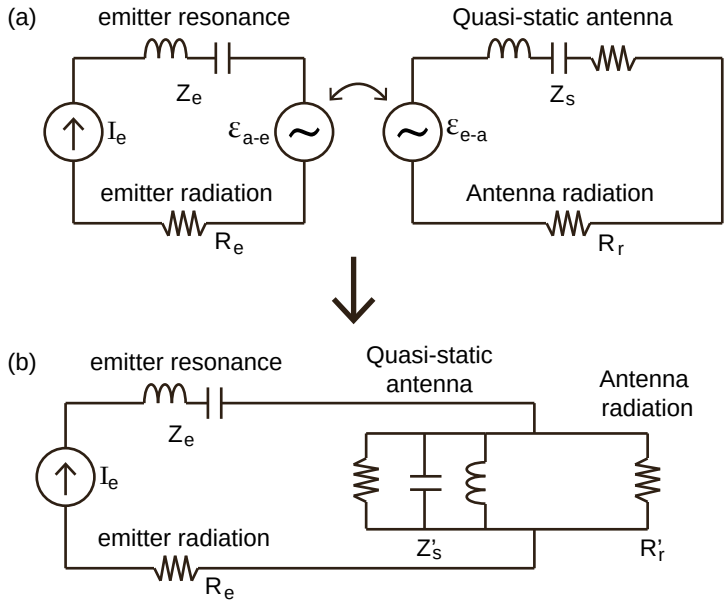

Figure 4.1: The equivalent circuit proposed by Krasnok for an emitter coupled to a nano-antenna. **(a)** Emitter and antenna can each be described by their own circuits, coupled through IEMFs $\varepsilon_{\text{e-a}}$ and $\varepsilon_{\text{a-e}}$. **(b)** The coupled circuits in (a) can be replaced by a single circuit, in which the antenna is described by a mutual impedance. This mutual impedance has the structure of a parallel circuit of an inductor, capacitor and two resistors.

To study Purcell enhancement, the external field is now assumed to come from a nearby emitter, which is modelled as a constant-current source [18, 179] with internal impedance $Z_\mathrm{e} + R_\mathrm{e}$, where Z_e is entirely reactive and determines the emitter resonance frequency, while $R_\mathrm{e} = \eta_0 k^2 l_\mathrm{e}^2/(6\pi)$ describes direct radiation to the background medium (vacuum).[†] Here, l_e is some effective length

[†]Note that, since the emitter is taken as a constant current source, the emitter reactance Z_e has no effect on the Purcell effect and could also be omitted here. However, it can be used for example to find the eigenfrequencies of the coupled emitter-antenna system [177], for which the current source is removed.

of the emitter and the current of this source is $I_\mathrm{e} = -i\omega p_\mathrm{e}/l_\mathrm{e}$, with p_e the emitter dipole moment. The corresponding emitter circuit is shown as the left circuit in Fig. 4.1. Note that this method of retrieving the Purcell effect is completely analogous to that used in Section 2.4. The emitter at location $\boldsymbol{r}_\mathrm{e}$ creates a field at the antenna location $\boldsymbol{r}_\mathrm{a}$ given by the Green's function of the background medium $G_\mathrm{bg} = G_\mathrm{bg}(\boldsymbol{r}_\mathrm{e}, \boldsymbol{r}_\mathrm{a})$. In circuit terms, this is included as an induced electromotive force (IEMF) $\varepsilon_\text{e-a} = G_\mathrm{bg} p_\mathrm{e}$ in the antenna circuit, which acts as its voltage source. The antenna, in turn, produces a field at the emitter location which is described by the same Green's function G_bg due to reciprocity. This is similarly included as an IEMF $\varepsilon_\text{a-e} = G_\mathrm{bg} p$ in the emitter circuit, which is opposite to the driving current I_e. The effect of this IEMF on the emitter can be captured by a mutual impedance $Z_\mathrm{m} = -\varepsilon_\text{a-e}/I_\mathrm{e}$ placed in the emitter circuit, which accounts for the contribution of the antenna to the power emitted by the source. Inserting the expressions for the IEMFs and for the antenna dipole moment, one finds

$$Z_\mathrm{m} = \frac{l_\mathrm{e}^2 l_\mathrm{a}^2 G_\mathrm{bg}^2}{\omega^2 Z_\mathrm{a}} = \frac{1}{(-i\omega L_\mathrm{s}')^{-1} - i\omega C_\mathrm{s}' + (R_\mathrm{s}')^{-1} + (R_\mathrm{r}')^{-1}}. \tag{4.4}$$

This describes the impedance of a parallel circuit of an inductor $L_\mathrm{s}' = N^2 C_\mathrm{s} \eta_0^2$, capacitor $C_\mathrm{s}' = L_\mathrm{s}/(\eta_0^2 N^2)$, and resistors $R_\mathrm{s}' = N^2\eta_0^2/Rs$ and $R_\mathrm{r}' = N^2\eta_0^2/R_\mathrm{r}$, where $N = l_\mathrm{e} l_\mathrm{a} G_\mathrm{bg}/(\omega\eta_0)$ is a dimensionless transformer parameter. Therefore, one may draw a single equivalent circuit for the total system as shown in Fig. 4.1b, where the antenna is included in the emitter circuit as this parallel circuit. We may again separate the quasi-static antenna impedance Z_s' and the radiation resistance R_r'. The total impedance in the circuit is $Z_\mathrm{tot} = Z_\mathrm{e} + Z_\mathrm{m} + R_\mathrm{e}$. The Purcell enhancement or LDOS relative to vacuum can be obtained by the ratio of the total power $P = \frac{1}{2}|I_\mathrm{e}|^2 \operatorname{Re}\{Z_\mathrm{tot}\}$ delivered by the emitter coupled to the antenna, to that of the emitter in vacuum. This leads to exactly the same expression as found from our coupled-oscillator model, in absence of the cavity (Eq. (2.47)).

4.2.2 The circuit proposed by Engheta *et al.*

In their seminal work — one of the first to discuss the analogy between plasmonic antennas and circuit theory — Engheta *et al.* propose a different circuit to describe a nano-antenna driven by an external field E_ext [174]. This circuit has later proven instrumental in explaining, for example, the effect of dielectric perturbation on an antenna in terms of the well-known concept of antenna loading [175, 176]. The existence of a second circuit for the same physical problem may seem confusing, as one would expect such a circuit to be uniquely defined. Here we therefore briefly discuss this circuit, and show that it is, in fact, equivalent to the circuit proposed by Krasnok.

For the case of an illuminated, optically small nano-sphere of relative permittivity ϵ and radius a in vacuum, Engheta *et al.* examine the solution for

the various field components inside and outside the particle [174]. Employing the boundary condition on the surface of the particle and neglecting radiation, this approach leads to the following equation for the displacement currents in the particle

$$-i\omega\epsilon_0(\epsilon-1)\pi a^2 E_{\mathrm{ext}} = -i\omega\epsilon_0\epsilon\pi a^2\frac{\epsilon-1}{\epsilon+2}E_{\mathrm{ext}} - i\omega\epsilon_0 2\pi a^2\frac{\epsilon-1}{\epsilon+2}E_{\mathrm{ext}}. \qquad (4.5)$$

Each of the three terms represents a current, which they respectively name (from left to right in Eq. (4.5)) the 'impressed displacement current source' I_{imp}, the 'displacement current circulating in the nano-sphere' I_{sph}, and the 'displacement current of the fringe field' I_{fringe}, respectively. Since currents are added, this effectively maps onto a parallel circuit as shown in Fig. 4.2a. They define the voltage across the elements as the average potential difference between the two hemispheres $V = a(\epsilon-1)E_{\mathrm{ext}}/(\epsilon+2)$, such that impedances can be found as

$$Z_{\mathrm{sph}} = \frac{-1}{i\omega\epsilon_0\epsilon\pi a}, \qquad Z_{\mathrm{fringe}} = \frac{-1}{i\omega\epsilon_0 2\pi a}. \qquad (4.6)$$

The fringe impedance Z_{fringe} is entirely reactive and describes a capacitor, while the sphere impedance Z_{sph} can be partly resistive if ϵ contains an imaginary part. If $\mathrm{Re}\{\epsilon\} < 0$, as is the case for example in noble metals at visible frequencies [180], the sphere impedance can be interpreted as a parallel resistor (representing ohmic losses) and an inductor which, combined with the fringe capacitance, determines the resonance frequency $\omega_0 = (LC)^{-1/2}$.

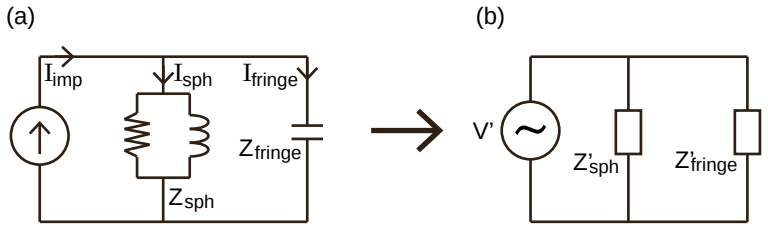

Figure 4.2: The equivalent circuit proposed by Engheta for a driven nano-antenna. (a) The parallel circuit of two impedances Z_{sph} and Z_{fringe}, described by Eq. (4.6), driven by the impressed displacement current source I_{imp} in the nanoparticle. **(b)** By redefining the current and voltage in the circuit in (a) and applying the Thévenin equivalent generator theorem, one finds a new circuit driven by a voltage source V' and with total impedances Z' equal to the impedance Z_{a} of the circuit on the right in Fig. 4.1a, which shows that the two circuits are equivalent.

The circuit in Fig. 4.2a can be compared to that proposed by Krasnok and shown on the right in Fig. 4.1a, without the radiation resistance R_{r}. The two are very different — not just the impedances of the individual lumped elements but even the manner in which they are connected, series or parallel,

differs. We thus have two completely different circuits describing the same problem. If both are correct, then how could we reconcile these two points of view? The difference between the circuits originates in different definitions of current and voltage. One has freedom in choosing these, provided that the dimensions remain correct. For example, the currents in Eq. (4.5) could have been multiplied by any dimensionless number, and the equation would still hold. However, a different choice of current and voltage can lead to different impedances and powers consumed by the circuit.

To reconcile the two pictures, we can redefine the current and voltage in the circuit proposed by Engheta, by multiplying each with a dimensionless quantity. We choose $V' = V(\epsilon+2)/(\epsilon-1) = aE_{\mathrm{ext}}$ and $I'_{\mathrm{imp}} = 4I_{\mathrm{imp}}/(\epsilon+2) = -i\omega\alpha_0 E_{\mathrm{ext}}/a$, such that V' and I' now match the total voltage and current in the circuit proposed by Krasnok (with a taking the role of effective length l_{a}). The impedances of the elements should then be multiplied by $(\epsilon+2)^2/(4(\epsilon-1))$ to ensure $Z' = V'/I'$. One then finds a total impedance of $Z' = -a^2/(i\omega\alpha_0)$, matching the impedance of the circuit by Krasnok in absence of radiation (Eq. (4.2)). Finally, we can use the Thévenin equivalent generator theorem to replace the current source and parallel impedances by a voltage source, which supplies a voltage V', connected in series with a single impedance Z'. This transformed circuit is shown in Fig. 4.2b, and is equal to the antenna circuit in Fig. 4.1a. This shows that the two circuits are in fact equivalent.

The redefinition of the currents and voltages affects not only impedances but also the power consumption, since $P = VI$. It is easy to verify that expressions from the two original circuits for power absorption P_{abs} through Ohmic damping are not equal. After the redefinition of current and voltage in the circuit by Engheta, we find that, if radiation is neglected, both circuits produce the same absorbed power $P_{\mathrm{abs}} = |E_{\mathrm{ext}}|^2\omega|\alpha_0|^2\,\mathrm{Im}\left\{-\alpha_0^{-1}\right\}/2$. Similarly, radiated power can be found if we include the series-connected radiation resistance R_{r}, which yields $\mathrm{Pr} = \frac{1}{2}|I_{\mathrm{a}}|^2 R_{\mathrm{r}} = \frac{|E_{\mathrm{ext}}|^2}{2\eta_0}\frac{k^4}{6\pi\epsilon_0^2}|\alpha|^2$. By division over the irradiance of the external field $|E_{\mathrm{ext}}|^2/(2\eta_0)$ one obtains the familiar expression for the scattering cross-section of a dipolar particle [119].

4.3 The conjugate-matching limit

Having established an equivalent circuit for an emitter coupled to a dipolar nano-antenna, we now move on to use the circuit to derive a fundamental limit on the power scattered by the antenna. This limit is set by the particle geometry and material, and is independent of its environment. In that sense it forms a counterpart to the well-known unitary limit [118, 181], which is independent of particle geometry yet dependent on the environment. We note that this derivation is completely analogous to that given in chapter 3 of [158] for the maximum power scattered or absorbed by a nanoparticle. We merely repeat it here because it is important to understand the case of a

single antenna, before we include the cavity in Section 4.5. For simplicity, and because the phenomena we will discuss can be understood from the antenna circuit alone, we will restrict our discussion to the circuit describing a nano-antenna driven by an external field (rightmost circuit in Fig. 4.1a).

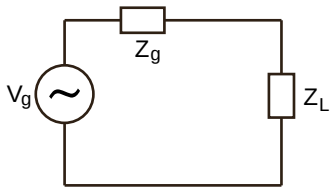

Figure 4.3: A generator driving a load. The generator is a fixed voltage source of voltage V_g with an internal impedance Z_g, while the load is represented by its complex impedance Z_L. The Thévenin equivalent generator theorem ensures that any generator circuit can be represented in this manner.

In circuit theory it is well known from the maximum power transfer theorem that the maximum power delivered by a generator to a load (see Fig. 4.3) is given by the 'conjugate-matching limit' — the power delivered to the load when load and generator impedances Z_g and Z_L are conjugate-matched, that is $Z_\mathrm{L} = Z_\mathrm{g}^*$ [182, 183]. This power is given as

$$P_\mathrm{cm} = \frac{|V_\mathrm{g}|^2}{8R_\mathrm{g}}, \tag{4.7}$$

where $R_\mathrm{g} = \mathrm{Re}\{Z_\mathrm{g}\}$. For load resistance R_L higher than R_g, the transfer efficiency $R_\mathrm{L}/R_\mathrm{g}$ may go up, however, the power P_L delivered to the load decreases. Note the difference between conjugate matching and the well known impedance matching condition ($Z_\mathrm{L} = Z_\mathrm{g}$), which minimizes reflections instead.

Conjugate matching sets a limit on the scattered power by a lossy nano-antenna, as is evident from the antenna circuit in Fig. 4.1a. Scattering is given by the power P_L consumed in the radiation load $Z_\mathrm{L} = R_\mathrm{r}$, and the rest of the circuit (that is, the driving voltage and the quasi-static antenna) can be interpreted as the generator. Figure 4.4a-c shows scattered power as well as load and generator impedances for the specific example of a spherical antenna of 5 nm radius in vacuum, with permittivity given by the Drude model for gold [184]. We see that scattering peaks at the resonance frequency ω_0, which is given as the point where $Z_\mathrm{L} = Z_\mathrm{g}^*$, i.e. the imaginary parts of load and generator impedances are matched. Their real parts, however, are not matched for this particle, so scattering remains below the conjugate-matching limit. We can find the requirements for reaching this limit by setting $Z_\mathrm{L} = Z_\mathrm{g}^*$. For a particle described by a Lorentzian polarizability (Eq. (4.3)) — as is the case for a Drude

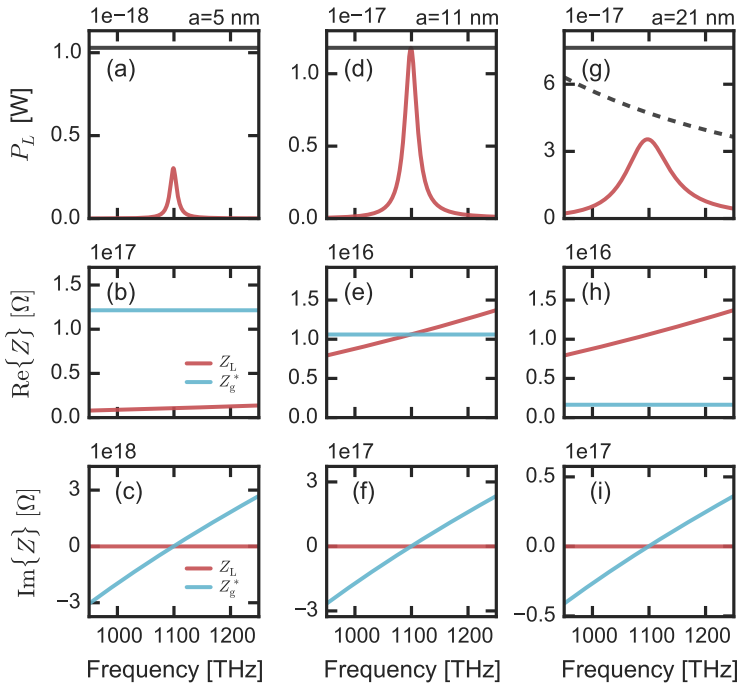

Figure 4.4: Conjugate matching with a nano-antenna. We show scattered power **(a,d,g)**, real **(b,e,h)** and imaginary **(c,f,i)** parts of the generator and load impedances $Z_\mathrm{g} = Z_\mathrm{s}$ and $Z_\mathrm{L} = R_\mathrm{r}$, respectively, for spherical gold antennas of 5 nm **(a-c)**, 11 nm **(d-f)** and 21 nm **(g-i)** radius. The imaginary parts of the impedances are always conjugate-matched at the resonance frequency, yet only for an antenna of 11 nm radius the real parts also match, allowing this antenna to reach the conjugate-matching limit (solid grey line in (a,d,g)). For the largest antenna, scattering is limited by the unitary limit (dashed grey line (g)) more than by the conjugate-matching limit. Note that y-axes are different for each antenna, and that for the smaller antennas, the unitary limit lies far above the conjugate-matching limit. For calculating impedances, we set $l_\mathrm{a} = 1$.

metal sphere in vacuum —we then find

$$\omega = \omega_0 \qquad \text{and} \qquad a^3 = \frac{3\gamma_\mathrm{i} c^3}{2\omega_0^4}, \tag{4.8}$$

which is reached for a 'critical radius' a_c of ∼11 nm for Drude gold. Note that gold is no longer well described by a Drude model at the frequencies shown in Fig. 4.4. A critical radius can, however, still be found for realistic (tabulated) permittivities. Figure 4.4d-f show that indeed, this antenna reaches the conjugate-matching limit. This coincides with the radius for which antenna albedo A is exactly 50%, that is, half the total consumed power is radiated and the other half is absorbed in the antenna. Scattered power is then given by Eq. (4.7) as $P_\mathrm{L} = P_\mathrm{cm} = |E_\mathrm{ext}|^2\beta/8\gamma_\mathrm{i}$. For antennas larger

than this critical radius, P_{L} falls below the conjugate-matching limit, as shown in Fig. 4.4g-i. Note, however, that in an absolute sense these particles do scatter more, as the conjugate-matching limit grows in proportion to volume ($\beta \propto a^3$). The conjugate-matching limit could therefore also be interpreted as a fundamental limit on the scattering *per unit volume* by a dipolar particle of a given lossy material. For particle size much beyond the critical radius (or a very low loss rate gi), the conjugate-matching limit forms only a very loose constraint. Instead, these particles approach another fundamental limit — the unitary limit. As discussed in Section 3.3, this limit follows from energy conservation and bounds the extinction and scattering cross-sections to $\sigma_{\mathrm{ul}} = 3\lambda^2/(2\pi n^2)$ [118, 154, 155, 181]. Consequently, the scattered power is bound by σ_{ul} times the driving beam irradiance. The fulfillment of this upper bound is guaranteed in the circuit model by the radiation resistance R_{r}, which is independent of the particle yet dependent on the surrounding medium as $R_{\mathrm{r}} \propto n$ (see Eq. (4.1)).

This analysis shows that there are two fundamental limits that govern the scattered power by a dipolar nano-antenna. The conjugate-matching limit depends only on the antenna and poses the strongest constraint for antennas small or lossy enough for dissipation to be the dominant loss source. Particles that are sufficiently big to be dominated by radiation, on the other hand, are constrained by the unitary limit, which depends not on the particle but on the environment. In general, this limit is inversely proportional to the local density of states of the antenna surrounding [118]. This implies that if one aims at designing an antenna for optimal scattering in a fixed environment, the unitary limit provides the ultimate bound. If, however, one aims at designing the environment instead (for example, in a Drexhage-type experiment [185]), the ultimate bound is set by the conjugate-matching limit. In Section 4.5, we will see how a cavity coupled to the antenna can be used to reach this limit.

4.4 An equivalent circuit for a hybrid system

Following a similar approach as used in Section 4.2.1 for an antenna, we can find an equivalent circuit for a hybrid antenna-cavity system. Based on the equations of motion for the coupled system (Eqs. (2.33) and (2.34)), this circuit would involve three separate circuits for emitter, antenna and cavity, which are all coupled to each other through induced electromotive forces or induced currents (for the emitter driving the cavity). For simplicity, however, we neglect direct cavity-emitter coupling, focusing only on the effect of the cavity on the antenna. Effectively, this corresponds to neglecting the cross-terms and cavity term responsible for the LDOS contributions shown in Fig. 3.2b and c, respectively. This approach is accurate if the antenna is simply driven by a plane wave, or for driving by an emitter if antenna-emitter coupling is much stronger than the cavity-emitter coupling. In this case, we can combine the

equations of motion into one equation and lump the effect of the cavity into the hybridized antenna polarizability α_{H}, given by Eq. (2.36) as

$$\alpha_{\mathrm{H}}^{-1} = \alpha_0^{-1} - i\frac{k^3}{6\pi\epsilon_0 n^2} - \chi_{\mathrm{hom}}, \tag{4.9}$$

with

$$\chi_{\mathrm{hom}} = \frac{1}{\epsilon_0 \epsilon V_{\mathrm{eff}}} \frac{\omega^2}{\omega_{\mathrm{c}}^2 - \omega^2 - i\omega\kappa} \tag{4.10}$$

the bare cavity response function. The hybridized antenna impedance $Z_{\mathrm{a,hyb}}$ is given by Eq. (4.2). If we assume again a Lorentz model for α_0, its equivalent circuit contains the familiar antenna elements from Fig. 4.1a, connected in series with the cavity impedance $Z_{\mathrm{c}} = -l_{\mathrm{a}}^2 \chi_{\mathrm{hom}}/(i\omega)$ representing a parallel RLC connection. This circuit is shown in Fig. 4.5a. Similar to the case of an antenna only, to study LDOS effects one can construct an equivalent circuit describing the interaction with the emitter by finding the emitter-hybridized-antenna mutual impedance $Z_{\mathrm{m,hyb}}$. This yields

$$Z_{\mathrm{m,hyb}}^{-1} = Z_{\mathrm{m}}^{-1} + (Z_{\mathrm{c}}')^{-1}, \qquad Z_{\mathrm{c}}' = i\frac{N^2 \eta_0^2 \omega}{l_{\mathrm{a}}^2 \chi_{\mathrm{hom}}}. \tag{4.11}$$

Figure 4.5 shows this circuit. In the following section, we will proceed to analyse how the presence of the cavity affects the antenna radiation and LDOS in this system.

4.5 Conjugate matching in a hybrid system

Apart from the emitter radiation into the background medium, the power consumed by the circuit — and thus the LDOS — is entirely determined by the impedance $Z_{\mathrm{a,hyb}}$ of the hybridized antenna, up to a pre-factor containing the emitter-antenna coupling. We can therefore simply analyse the hybridized antenna circuit on the right in Fig. 4.5a to learn how the cavity affects the LDOS and the radiation by the antenna.

The effect of the cavity is very different for small and large antennas. Figure 4.6 shows power consumption P_{L} by the load, as well as impedances of the load and generator in the hybrid circuit from Fig. 4.5a. We define the load as the antenna radiation resistance R_{r} and the cavity impedance Z_{c} combined, while the generator impedance is set by the quasi-static antenna impedance Z_{s}, just as for a bare antenna. This ensures that the conjugate-matching limit is the same as for the bare antenna. Moreover, as cavities are typically made of lossless dielectrics, we can assume their losses to be radiative as well. For a small antenna (radius below the critical radius of 11 nm), Fig. 4.6a-d shows that a cavity can help the system reach the conjugate-matching limit. However, this is only reached for a specific cavity quality

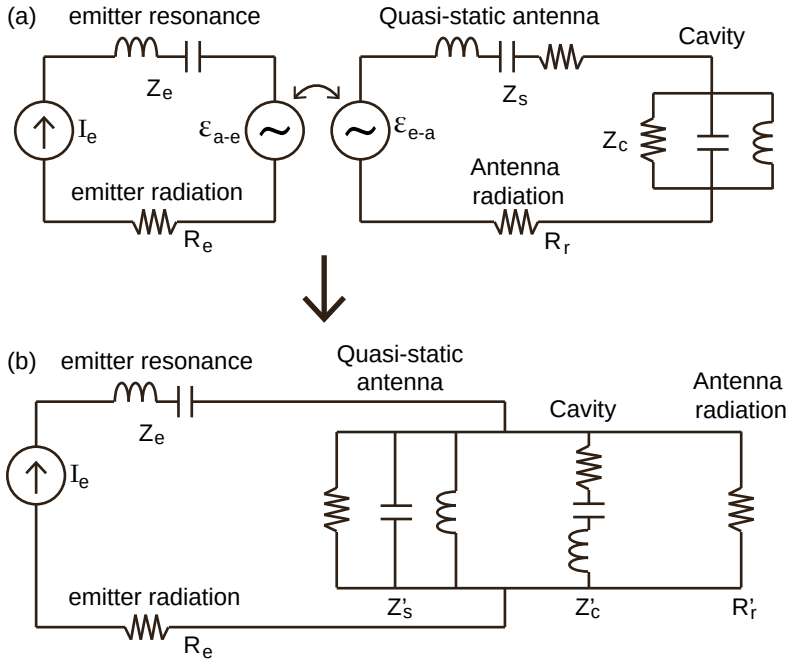

Figure 4.5: Equivalent circuits for a hybrid antenna-cavity system. (a) Two circuits describing emitter and hybridized antenna, coupled through IEMFs. The cavity is modelled by a parallel RLC connection in the antenna circuit. **(b)** Just as in Fig. 4.1, the coupled circuits in (a) can be replaced by a single circuit.

factor Q or, equivalently, cavity Purcell factor F_{P}. Indeed, we see that only this cavity reaches perfect conjugate matching, while cavities with different Q may match both real and imaginary parts of Z_{L} and Z_{g}, yet not at the same frequency. This surprising result shows that there is an 'optimal' cavity for which power transfer to the load is maximized — a highly counter-intuitive result, considering that conventional cavity wisdom states that higher Q is always better. It can be shown that such an optimal Q can always be found for antennas with $R_{\mathrm{r}} < R_{\mathrm{s}}$ (that is, albedo $< 50\%$). This behaviour is in stark contrast with that of a hybrid containing a large antenna (radius above the critical radius) shown Fig. 4.6e-h. This system cannot reach conjugate matching and is bound instead by the unitary limit. This can be seen from the impedance, as the cavity can only increase load resistance $\mathrm{Re}\{Z_{\mathrm{L}}\}$. Since this antenna has $\mathrm{Re}\{Z_{\mathrm{g}}\} < R_{\mathrm{r}}$, the cavity thus cannot bring the system to perfect conjugate matching. Reactances can be matched, however, leading to a resonance peak. Here, there is no optimum and instead, peak scattering grows with Q, saturating for very high Q. We note that in reality, the unitary limit *can* be exceeded in a hybrid system, as discussed in Section 3.3. This is

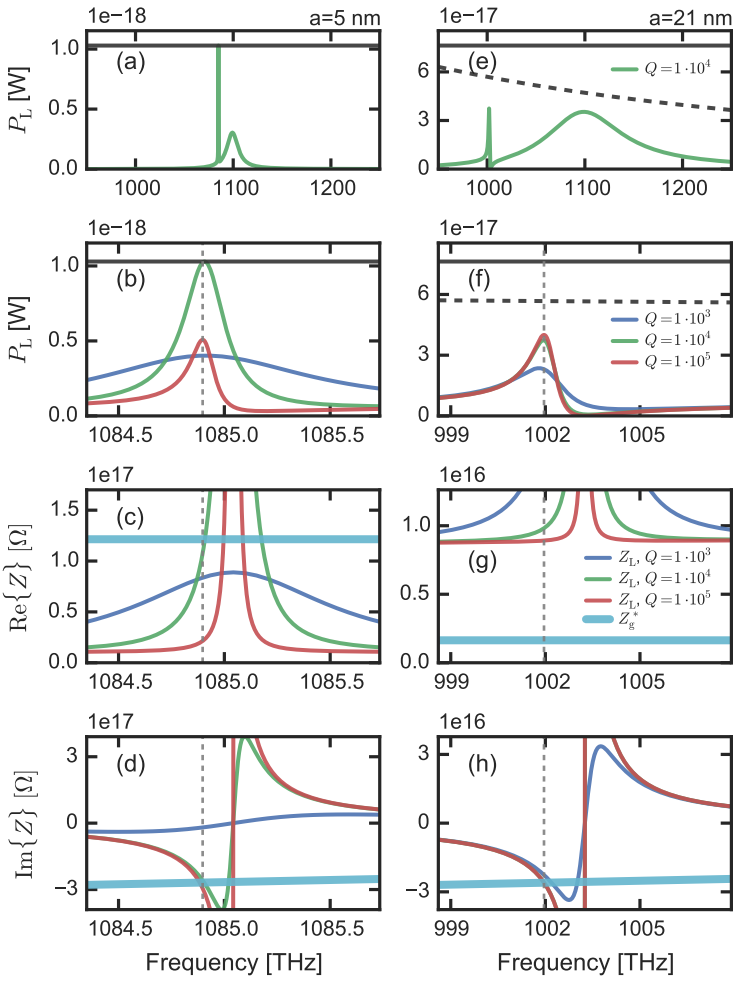

Figure 4.6: Conjugate matching in a hybrid system. We show broadband spectra of load power P_L **(a,e)** and narrowband spectra of load power **(b,f)**, real **(c,g)** and imaginary **(d,h)** parts of the generator and load impedances Z_g and $Z_\mathrm{L} = R_\mathrm{r} + Z_\mathrm{c}$, respectively, for hybrid antenna-cavity systems with spherical gold antennas of 5 nm **(a-d)** and 21 nm **(e-h)** radius. Narrowband spectra are shown for three different cavity Q-factors. For the small antenna, the conjugate-matching limit (solid horizontal grey line in (a,b,e,f)) can be reached near the cavity resonance, yet only for a specific cavity Q. This can also be seen from $\mathrm{Re}\{Z\}$ and $\mathrm{Im}\{Z\}$, which are simultaneously matched only for this cavity Q. Conversely, for a large antenna conjugate matching cannot be reached, as $\mathrm{Re}\{Z_\mathrm{g}\} < R_\mathrm{r}$ and the cavity can only increase $\mathrm{Re}\{Z_\mathrm{L}\}$. Dashed vertical lines show peak frequencies and the dashed grey curves in (e,f) shows the unitary limit. Again, y-axes are different for each antenna. We take cavities with $V_\mathrm{eff} = 10\lambda^3$, red-detuned from the antenna by one antenna linewidth. We set $l_\mathrm{a} = 1$.

due to interference effects arising from the direct emitter-cavity coupling that was neglected in this analysis.

In analogy with circuit design, we may also interpret the cavity as a matching network between the generator (quasi-static antenna) and the load (radiation). Such matching networks are typically designed to maximize power transfer by bringing the generator and load impedance to conjugate matching. Matching networks can be easily designed at radio frequencies, where high-quality lumped circuit elements are available. However, at THz frequencies and above, such elements are lacking, making matching circuits very difficult to attain. Our results show that optical cavities may provide this functionality, offering perfect conjugate matching networks for small optical antennas.

4.6 Conclusion and outlook

We have compared two distinct circuit models from literature for a nano-antenna, and shown that the two models are equivalent. Using this circuit, we have discussed how the well-known maximum power transfer theorem sets a fundamental upper bound on the radiation by a lossy dipolar nano-antenna. This 'conjugate-matching limit' — which is reached if the generator (antenna) and load (radiation) impedances are conjugate-matched — is independent of the antenna environment and complements the unitary limit, which depends on the photonic environment yet is independent of antenna geometry.

In analogy with the antenna circuit, we then proposed an equivalent circuit for a hybrid antenna-cavity system, driven by an external field or by a fluorescent emitter. It was shown that the cavity can help the antenna reach the conjugate-matching limit, if the antenna is sufficiently small to have albedo below 50%. Surprisingly, we find an 'optimal' cavity Q for which this limit is reached. For antennas with albedo larger than 50%, we find that perfect conjugate matching cannot be reached by introducing a cavity, and scattering is bound instead by the unitary limit.

By making a connection between nanophotonics and the well-established field of electrical circuit theory, we have thus gained insight into the fundamental limits governing nano-antenna scattering. This directly provides a tool for the design of strongly scattering antennas or high Purcell factor systems, showing that cavities can be viewed as matching networks for optimizing the power transfer from optically small nano-antennas to radiation. We expect that the circuit analogy presented here can lead to further developments in uniting the fields of nanophotonics and electrical engineering, possibly leading to improved nanophotonic designs.

Chapter 5

Design and fabrication of hybrid antenna-cavity systems

We present the design and fabrication of hybrids consisting of microdisk cavities and aluminium nano-rod antennas. Using a two-step lithography process, we place the antennas on the disk edge to ensure coupling to the whispering-gallery modes in the disks, with high accuracy and excellent reproducibility. Taper-coupled spectroscopy is enabled by placing the hybrids on a diamond-sawed mesa. For fluorescence measurements, we develop a novel method to position colloidal quantum dots with nanometer accuracy at the antenna hotspot. We optimize the conditions to obtain near-100% success rate and virtually no quantum dots outside the intended areas. These results pave the way to experiments on hybrid systems. The quantum dot positioning method can also be applied for fabrication of *e.g.* single-photon sources based on other nanophotonic structures.

5.1 Introduction

When making a hybrid antenna-cavity system, the crucial question to ask is: how does one place an antenna near the cavity mode maximum? Various approaches have been used, with different degrees of control over antenna position. The most straightforward method, with no position control, is to use random distributed antennas in solution, either dropcasted onto the cavity or deposited in a flow-cell geometry [86, 90, 137, 138, 186, 187]. In some cases, this leads to an antenna with the right location and orientation. More control can be obtained by using a self-assembly technique where the cavities (polymer beads) are trapped within a template of gold nano-particles on posts [104, 188]. A truly deterministic methods that can place the antenna with approximately diffraction-limited resolution is direct laser printing [189]. Accuracies in the order of a few nm can be achieved if the antenna is grown directly on the cavity using ion-beam-assisted chemical vapour deposition [85], deposited in a multi-step lithography process [94, 97] or placed using an AFM tip [110]. An approach that offers both high positioning accuracy and in-situ tuning, is to use a near-field tip as the antenna, which can be moved through the cavity mode profile [142, 190]. Such tips may even be structured for *e.g.* magnetic response [191] or strong field enhancement [98, 192]. Recently, a similar and very promising approach used the reverse mechanism: a gold colloid is positioned on a flat mirror, and a Fabry-Perot-type cavity is formed between this flat mirror and a moveable cantilever containing a concave mirror [193].

Each approach has its advantages in terms of flexibility, scalability, fabrication time and precision. We have chosen to employ a two-step electron-beam lithography process. This technique allows great flexibility in the cavity and antenna geometries, and the relative alignment can, in principle, be done with extremely high precision (down to the e-beam resolution of a few nm). Its main disadvantages are a relatively laborious fabrication process and, since we use evaporation to deposit the antennas, lower antenna material quality than can be obtained with solution-processed techniques [4, 68]. It also somewhat restricts the choice of cavities. For example we cannot use a microtoroid cavity as it is not clear how to accurately place an antenna on it after the glass has been re-flown [47].

Once the hybrid systems are made, a second challenge arises: to benefit from the enhancement of local density of states (LDOS) that was predicted in Chapter 3, emitters need to be placed at LDOS 'hotspots' created by the antenna. These hotspots are typically just $\sim$1-10 nm in size for plasmonic antennas [4, 76], putting extreme demands on the positioning accuracy. Although several methods have been proposed, emitter positioning remains one of the major bottlenecks in harnessing the potential of plasmonics for LDOS enhancement and field confinement [66]. For most emitters used in cavity quantum electrodynamics, such as epitaxially grown quantum dots [23], defect centers in diamond [194, 195] or organic molecules [196], little to no

position control is available and emitters are typically randomly distributed over a sample. A common strategy is then to first locate the emitter, and fabricate the cavity around it. An exception is the recent development of controlled color center generation in diamond using a focused ion beam [56, 197]. Several experiments in plasmonic systems have demonstrated some degree of control over emitter position. Linker molecules, with one functional group binding to the emitter and another to the metal, have been used to bind emitters specifically to plasmonic structures [4, 71, 198–200]. Additional positioning accuracy can be obtained by using the local curvature of nanoparticles to decrease screening by other molecules [4], or by screening parts of the sample by a lithographically patterned resist mask [71, 199, 200]. The latter method, however, has proven difficult to reproduce because the emitters may also diffuse through the mask [201]. An alternative approach has been to cover a sample with a homogeneous layer of emitters and to remove or extinguish the undesired emitters using reactive ion etching [185, 201, 202]. This, however, would not be suitable for our samples, since they contain overhanging structures and any emitters underneath them would be screened from the etch. Another interesting new method uses electro-hydrodynamic printing to deposit quantum dots with $\sim$50 nm resolution [203, 204]. Yet, alignment to a photonic structure requires a transparent substrate. A clever alternative approach has been to use the high intensity plasmonic hotspots to do highly localized photo-chemistry. For example, multi-photon absorption in the hotspots can bind proteins [205] or polymerize photoresists locally [206, 207], and if emitters are functionalized for binding to the protein or dissolved into the resist [208], these become self-aligned to the antenna hotspot. Similarly, hot electron emisssion from plasmonic structures can also cause resist exposure [209] or drive a local chemical reaction [210] that enables covalent binding of an emitter.

We have chosen to use a combination of material-specific linker molecules and a nanopatterned resist mask for the positioning of our emitters, which are CdSeTe/ZnS colloidal quantum dots. This method provides excellent spatial resolution limited only by the e-beam resist. Under the right circumstances it can offer high success rate and very high selectivity, *i.e.* virtually no quantum dots present outside the intended areas. Moreover, it is a natural extension of the two-step lithography process used to create the hybrids: we can use the same alignment markers and mostly the same methods as used for positioning the antenna. A disadvantage is that the linker chemistry is specific to a certain combination of metal and emitter, and therefore not necessarily extendible to all other combinations.

In this chapter, we explain the design and fabrication of antenna-cavity hybrids. In Section 5.2, we focus on the cavities, after which we discuss the antennas in Section 5.3. Section 5.4 discusses how the hybrids can be accessed by a tapered fiber, through placement on an elevated mesa. We then move on to discuss the positioning of fluorescent emitters. Section 5.5 explains our

choice of fluorescent quantum dots as LDOS probes, and Section 5.6 describes how they are positioned with high accuracy in the antenna hotspots of our hybrid systems.

5.2 Microdisk cavities

As cavities, we use silicon nitride microdisks supporting whispering-gallery modes (WGM). While these do not possess the highest quality factors or lowest mode volumes known, they are in fact very suitable for hybrid systems. Most importantly, an antenna can be placed very near the mode maximum, which lies inside the disk at the disk edge [144]. This ensures we can attain high antenna-cavity coupling strengths or, in other words, low effective mode volumes. Moreover, both mode volume V and quality factor Q can be tuned through disk size [211], providing a convenient tuning mechanism. One can even study modes of different coupling strength within the same physical structure, because microdisks support several modes of different radial order m_r.

5.2.1 Design

To design microdisk cavities, we perform numerical simulations using the finite-element method (FEM) in COMSOL multiphysics v5.1. We use the axial symmetry of the system to perform two-dimensional simulations. The disks consist of Si_3N_4 ($n = 2$), surrounded by air, with a thickness of 200 nm and a varying diameter. We use the eigenmode solver to find the modes. Mode volumes are obtained by evaluating Eq. (2.23) for the mode profiles, *i.e.* dividing the total integrated mode energy by the squared field at the mode maximum. To obtain *effective* mode volumes V_{eff}, which govern the antenna-cavity coupling strength, we divide this energy by the squared field in the radial direction (dominant direction for these modes) at the center of the antenna, which we choose as 300 nm from the edge. Fig. 5.1a and b show examples of eigenmode profiles of the fundamental ($m_r = 0$) and first order ($m_r = 1$) radial mode in a microdisk. The first order mode couples less strongly to the antenna, due to a lower mode amplitude at the antenna location compared to the $m_r = 0$ mode. Fig. 5.1c shows that, in theory, quality factor scales exponentially with diameter. This theoretical quality factor is only limited by bending losses, *i.e.* light escaping due to the finite curvature of the disk. For all but the smallest disks, quality factors will in practice be limited by other losses such as absorption and scattering from edge roughness, which scale linearly with diameter [211]. Fig. 5.1d demonstrates the approximate linear scaling of mode volume with diameter. Also *effective* mode volume V_{eff} scales linearly and lies between $123\lambda^3$ to $21\lambda^3$ for $m_r = 0$ modes in 15 to 4 μm diameter disks. The $m_r = 1$ modes always have $\sim$2.5 times higher V_{eff} than the $m_r = 0$ modes

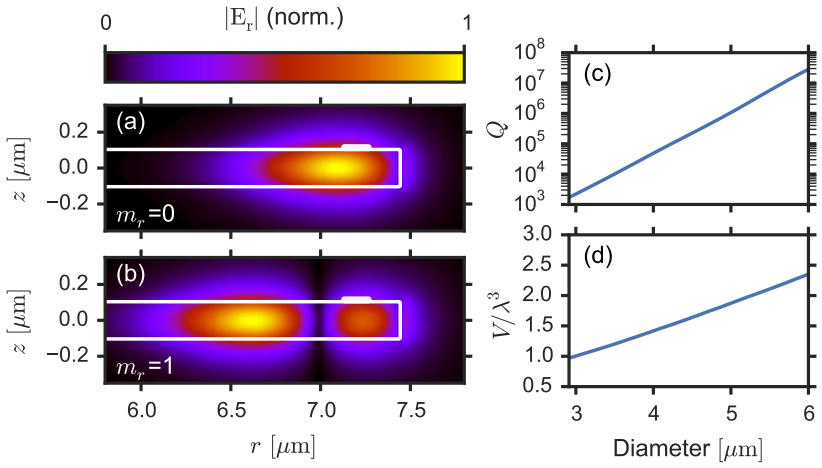

Figure 5.1: Whispering-gallery modes in silicon nitride microdisks. (a) Cross-cut of the radial field component E_r for the fundamental ($m_r = 0$) radially polarized whispering-gallery mode in a disk with a 14.9 µm diameter and 200 nm thickness. We zoom in near the outer edge of the disk (edges indicated by white lines). The white patch on top of the disk indicates the location of the antenna (absent in this simulation). **(b)** Same as **(a)**, for the $m_r = 1$ mode. **(c)** Exponential dependence of the fundamental mode quality factor Q on disk diameter. **(d)** Approximately linear dependence of the dimensionless mode volume V/λ^3 of the fundamental mode. Results are obtained from FEM simulations. At diameters above 6 µm, Q is limited by numerical errors.

at similar frequency. See Table 5.1 for V_{eff} for modes in disks between 8 and 15 µm diameter. These results show that we can tune cavity losses and antenna-cavity coupling strength by changing the diameter. We can use this to choose a desired hybridized linewidth, as we will demonstrate in Chapter 6.

5.2.2 Fabrication

The microdisk fabrication process is sketched in Fig. 5.2a-c. We start with a 12x12 mm sample of 200 nm low-loss stoichiometric silicon nitride (Si_3N_4) on silicon. The Si_3N_4 was grown by Lionix international on silicon wafers by low-pressure chemical vapour deposition(LPCVD), which usually creates layers with lower optical losses and defect densities than plasma-enhanced chemical vapour deposition (PECVD) [212–214]. We spin coat a 450 nm layer of positive electron-beam (e-beam) resist (CSAR 6200, Allresist GmbH, nominal resolution ∼10 nm) on the sample*. We then use an e-beam lithography system (Raith Voyager, 50 kV) to write the disks as well as alignment markers that can be used for relative alignment of subsequent lithography steps.

*Although negative resist would decrease our writing time, the only known resist with similar resolution (hydrogen silsesquioxane) can, once exposed, only be removed by HF etching, which also etches the Si_3N_4.

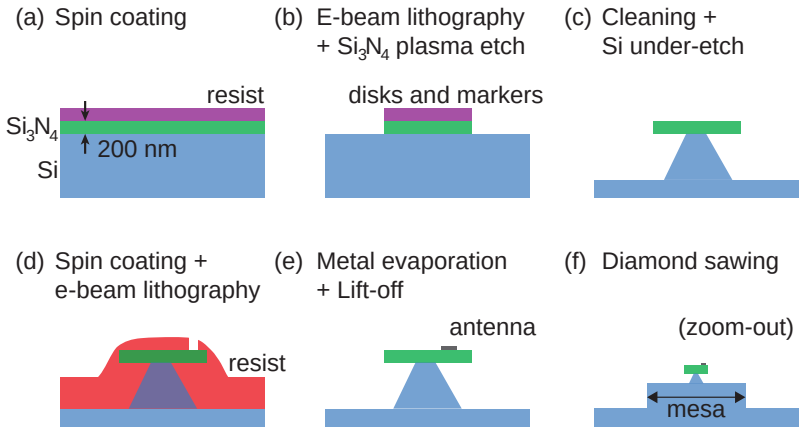

Figure 5.2: Fabrication of the hybrid system, step-by-step. (a) A positive e-beam resist is spin coated on a 200 nm layer of silicon nitride on silicon. **(b)** In the first electron lithography step, we define the disks and alignment markers. After development, this pattern is transferred into the silicon nitride by reactive ion etching. **(c)** Remaining resist is cleaned from the sample and the sample is immediately transferred to a KOH bath for silicon wet etching, which creates an undercut below the disk. **(d)** For the antenna deposition, the sample is spin coated again, now with a MMA/PMMA resist bilayer. In a second lithography step, antennas are defined at the edges of the disks. **(e)** After development, metal (Al) is thermally evaporated onto the sample, creating the antennas. The sample is then transferred to an acetone bath to remove the resist and lift off the excess metal. **(f)** Finally, the sample is covered by a thick layer of resist and a mesa was created using a diamond wafer saw. Afterwards, the remaining resist was dissolved in acetone.

Details on the markers and how to perform the relative alignment are given in Section 5.A. The disks are written in 500 μm write fields, all positioned in a straight line which will eventually form the mesa. Disks are written with diameters between 20 and 4 μm. We use an electron dose of 160 $\mu C/cm^2$ at 50 kV acceleration potential, and a (curved) area step size of 10 (5) nm. Note that it is crucial that the disks are recognized in the pattern generator software as curved objects (*i.e.* not as polygons), such that they can be written with the beam moving in a circular path outward. If they are written line-by-line, this typically creates defects along the edges, which lower the quality factor. After exposure, the sample is developed by consecutive immersion in pentyl acetate (120 seconds), o-xylene (7 s), a 1:9 mixture of methyl isobutyl ketone (MIBK) and isopropanol (15 s) and pure isopropanol (15 s). This removes the exposed resist.

The pattern is transferred into the silicon nitride by inductively coupled plasma (ICP) reactive ion etching (RIE) in a commercial etching system (Oxford PlasmaPro100 Cobra). We use a mix of SF_6 and CHF_3 gasses at flow rates of 16 and 80 standard cubic centimetres per minute (sccm) , respectively, with

50 W RIE forward power and 500 W ICP power at a gas pressure of 9 mTorr and a temperature of 0 °C . The sample is etched for 100 seconds. This recipe creates smooth and relatively straight side walls, as shown in the scanning electron microscopy (SEM) image in Fig. 5.3a. We use perfluoropolyether oil between the sample and carrier wafer for thermal conduction.

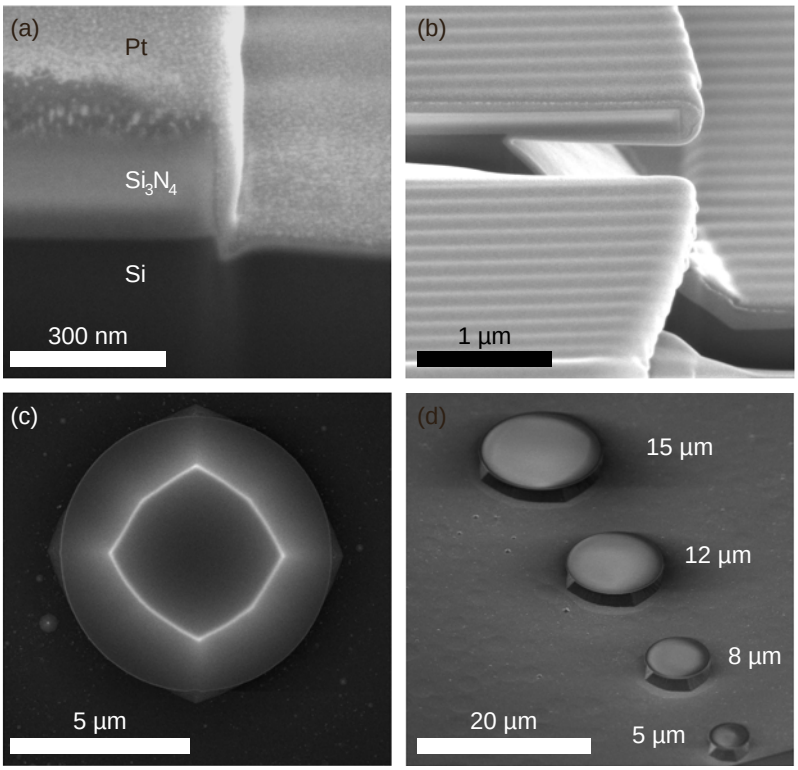

Figure 5.3: Microdisk fabrication results. (a) Cross-cut of a disk, just after the Si_3N_4 etch. We see that the Si_3N_4 has been etched through, and it has straight side walls. The Pt is for imaging only. **(b)** Cross-cut of a disk, taken after Si under etching. We see a free-standing edge and an angled Si pillar, typical of KOH etching. The horizontal stripes are from the Pt used for imaging. **(c)** Top view of an under-cut disk with 8 µm diameter. When using a high acceleration voltage (20 kV), the electrons penetrate the disk and we image the pillar edges below it. **(d)** Four disks with different diameters in a row, after the Si under etching.

After the plasma etch, we clean the remaining resist and oil from the samples by a 10-minute bath in warm acetone (45 °C), followed by a ∼15-minute base piranha etch. We then proceed to under-etch the silicon, creating free-standing disk edges. It is crucial that this etch is done within a few hours after the plasma etching, to avoid a native oxide layer forming on the bare silicon. Such a layer would make the under-etching process highly unpredictable, as

etch times depend strongly on the oxide layer thickness and the oxide screens some parts of the disk edges more than other parts, creating highly irregular etch patterns. The under etching is done by placing the samples in a 40 $\mathrm{wt}\%$ potassium hydroxide (KOH) solution at 70 $^\circ\mathrm{C}$ [†]. KOH etches preferentially along the Si $\langle 100 \rangle$ crystal direction, which leads to angled pillars with irregular shapes, as shown in Fig. 5.3b-c. The etch rate, however, depends on disk size, as the larger curvature of smaller disks relaxes the directionality of the etch. For example, we found the etch rates in the in-plane direction (*i.e.* the rate at which the pillar radius decreases) to be 400, 500 and 950 nm/min for a 20, 15 and 8 $\mu\mathrm{m}$ diameter microdisk, respectively. We typically used etch times around 4 minutes, leading to a $\sim$2 $\mu\mathrm{m}$ undercut at a 15 $\mu\mathrm{m}$ diameter disk. Our simulations show that a $\sim$1.6 $\mu\mathrm{m}$ undercut is sufficient to avoid perturbation by the pillar of the fundamental $m_r = 0$ mode in a 15 $\mu\mathrm{m}$ disk. An example of a sample after all the microdisk fabrication steps is shown in Fig. 5.3d.

From the taper-coupled measurements presented in Chapter 6, we find quality factors of more than 10^5 for the cavity modes in 8, 12 and 15 $\mu\mathrm{m}$ disks. These are shown in Table 5.1. The highest observed Q was $8.5 \cdot 10^5$, measured in a 15 $\mu\mathrm{m}$ disk. Furthermore, Table 5.1 shows that resonance frequencies in 8, 12 and 15 $\mu\mathrm{m}$ disks are equal (for nominally equal diameters) to within 0.037%, 0.015% and 0.015%, respectively, which amounts to a variability $< 2\%$ of the cavity free spectral range (frequency difference between modes of equal m_r) and can be translated to a reproducibility in disk diameter of 2-3 nm. These figures demonstrate the fidelity of the disk fabrication process. Results were measured on the antisymmetric WGMs in disks containing antennas (see Fig. 6.4), which were not significantly perturbed by the antenna.

Disk diameter [μm]	m_r	$V_{\mathrm{eff}}/\lambda^3$	Q	$\omega_c/2\pi$ [THz]
8	0	52	$1.2(2) \cdot 10^5$	384.29(14)
8	1	135	$0.9(2) \cdot 10^5$ [‡]	384.66(14)
12	0	89	$2.1(5) \cdot 10^5$	387.09(6)
12	1	238	$3.3(9) \cdot 10^5$	390.72(6)
15	0	123	$2.6(9) \cdot 10^5$	387.34(6)
15	1	301	$4(1) \cdot 10^5$	388.59(4)

Table 5.1: Cavity parameters. Dimensionless effective mode volume $V_{\mathrm{eff}}/\lambda^3$ from simulations, quality factor Q and bare cavity resonance frequency ω_c from the experiments discussed in Chapter 6, as function of microdisk diameter and radial order m_r. Errors correspond to standard deviations.

[†] Etch rate is extremely sensitive to temperature, so it is advised to place the beaker with the KOH solution in a large water bath to stabilize temperature.

[‡] The $m_r = 1$ modes in 8 $\mu\mathrm{m}$ disks were broadened due to overcoupling by the tapered fiber. Real quality factor is higher.

5.3 Aluminium nano-antennas

We use aluminium nano-rods as antennas. The main reason is that we want to study a wide range of cavity-antenna detunings, including in particular the range where the cavity is red-detuned from the antenna. Our results from Chapter 3 suggest that in this regime, hybrid systems should achieve optimal performance. The cavity modes we study will always be in the 765-781 nm range, set by the tuning range of our laser. Therefore we require antennas that are blue-detuned from these wavelengths. Due to the high plasma frequency of aluminium compared to *e.g.* gold, aluminium nano-rods can be tuned in resonance from the UV to the infra-red by changing particle aspect ratio [215]. Silver could also be used, however this is known to oxidise within days in ambient conditions, making experiments challenging. Aluminium rapidly forms an alumina (Al_2O_3) shell when exposed to oxygen in a self-terminating process that creates a stable shell of $\sim$3 nm thickness [216, 217]. A disadvantage of aluminium is that it shows inter-band absorption at 780 nm [184].

5.3.1 Design

We perform FEM simulations of aluminium nano-rod antennas on an infinite Si_3N_4 substrate (COMSOL v5.1). Antenna width and thickness are taken as 58 nm and 40 nm, respectively, and we assume a tapered shape in the vertical direction with a taper angle of 60°, based on cross-cut images of other evaporated structures. The aluminium refractive index is taken from tabulated data [184], and we include a 3 nm alumina shell. We drive the antenna with a plane wave at normal incidence from the air side, polarized along the antenna long axes (x-axis), and calculate scattered and absorbed power as well as induced dipole moments (along all 3 axes) as a function of frequency. Division of the dipole moments by the incident field at the antenna location yields antenna polarizability tensor elements α_{xx}, α_{xy} and α_{xz}. Fig. 5.4 shows the resulting antenna scattering and absorption spectra, as well as polarizability α_{xx} along the antenna long axis, which dominates total polarizability $\overleftrightarrow{\alpha}$ throughout most of the spectrum. These results show that we can indeed tune antenna resonance frequency by changing antenna length, *i.e.* increasing antenna length causes a red-shift of the antenna resonance. For most of these lengths, the cavity modes in our laser tuning range will be red-detuned from antenna resonance, where hybrid systems should achieve optimal performance. Despite the interband absorptions that cause non-Lorentzian behaviour near 780 nm wavelength, the largest antennas can also access the blue-detuned regime, as evident from the sign change in $\mathrm{Re}\{\alpha_{xx}\}$ for these antennas.

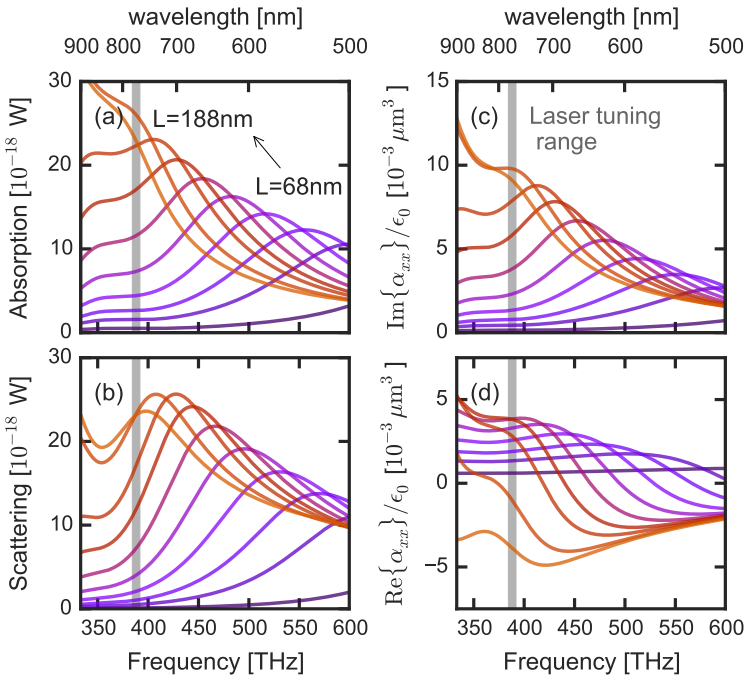

Figure 5.4: Finite-element simulations of aluminium antennas. (a-b) Absorption and scattering spectra of antennas on a Si_3N_4 substrate, driven by a plane wave of amplitude $E_0 = 1\,\mathrm{V/m}$ incident from the top medium. Different colors indicate antenna length, going from 68 to 188 nm. We observe Lorentzian peaks, red-shifting with increasing antenna length. In our frequency range of interest, given by the laser tuning range (grey vertical band), inter-band absorptions cause a deviation from a pure Lorentzian lineshape. **(c-d)** Real and imaginary parts of dominant polarizability component α_{xx}.

5.3.2 Fabrication

The antenna fabrication steps are schematized in Fig. 5.2d,e. First, we need to deposit an new layer of electron resist. At the location where we place the antennas, 300 nm from the disk edges, this resist needs to have an appropriate thickness for high-resolution lithography and easy lift-off. Using spin coating, we cover the under-etched samples with a layer of methyl methacrylate (MMA, Microchem MMA 8.5, dissolved in ethyl lactate), followed by a layer of polymethyl methacrylate (PMMA, Microchem 950 PMMA, dissolved in anisole). PMMA/MMA bilayers are frequently used for deposition processes, as the lift-off process is eased by the undercut that occurs naturally in such a bilayer [218]. The layer thickness, as measured on a scratch in the resist far away from the structures, is 780 nm (MMA) and 220 nm (PMMA). We use disk cross-cuts made by focused-ion-beam (FIB) milling on a test sample to determine the resist layer thickness on the disk. At 300nm from the edge of a

5 µm disk, MMA and PMMA thickness are found as ∼150 nm and ∼60 nm, respectively. Given an antenna thickness of 40 nm, the bilayer is sufficiently thick for an easy lift-off, while the thin PMMA layer allows good resolution.

Next, we expose our sample in a second e-beam lithography step. The markers written in the first step are used for relative alignment of the antennas to the disks (see Section 5.A for further details). We write rectangular antennas of 50 nm thickness and different lengths between 60 and 180 nm. Antennas are positioned 300 nm from the disk edge, with antenna long axis always aligned in the radial direction, matching the electric field of the radially polarized whispering-gallery modes. Each disk contains one antenna. An electron dose of 500 $\mu C/cm^2$, a 50 kV acceleration potential and an area step size of 5 nm are used. Following exposure, the sample is developed in a 1:3 mixture of MIBK and isopropanol (80 s), followed by immersion in two beakers of isopropanol (15 s each).

We deposit a layer of aluminium, typically 30-40 nm thick using thermal evaporation at a rate of 0.05 nm/s and a chamber pressure at evaporation start of $5 \cdot 10^{-7}$ mbar. As aluminium is easily contaminated by traces of oxygen [217], we ensure that no oxides (*e.g.* SiO_x) were evaporated in the chamber shortly before. Also, before depositing on the sample, we evaporate a ∼5 nm layer of aluminium into the chamber, which acts as a getter to bind gaseous oxygen. After evaporation, the sample is transferred to a warm acetone bath (50 °C) for ∼30 minutes for the metal lift-off. This removes the MMA and PMMA resist, as well as the excess metal on top of it, leaving only the antennas. After a dip in isopropanol, the sample is dried in a nitrogen flow. Fig. 5.5b,c show SEM images of the resulting antennas on a microdisk cavity. We find that antennas are present on ∼95% of the disks, and that length and width are on average ∼8 nm larger than designed for, due to slight overexposure.

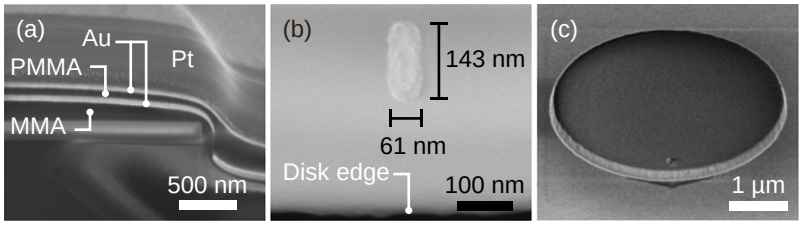

Figure 5.5: Antenna fabrication results. (a) FIB cross-cut of a 5 µm diameter disk, covered with a MMA/PMMA bilayer. Gold was added on top of the MMA and PMMA for imaging contrast. Platinum was deposited for FIB milling. At 300 nm from the disk edge, the MMA and PMMA thickness is 150 nm and 60 nm, respectively. **(b)** Aluminium antenna on 15 µm diameter disk, after lift-off. Dimensions are slightly larger than designed for, due to overexposure. **(c)** Image of a 4 µm diameter disk, viewed under a 52° tilt, with an antenna positioned at the lower edge.

5.4 Diamond-sawn mesas

To do cavity spectroscopy, we need to access the cavities using a tapered optical fiber [132]. As our samples are 12 mm wide and the cavities are only elevated above the substrate by a few micrometers, approaching the cavities to within less than a micrometer distance with a tapered fiber would be practically impossible, as the fiber would always touch the edge of the sample before reaching the cavity. One solution would be to use dimpled fibers [219]. However these are as difficult to make as they are easy to break. Instead, we chose to place our cavities on a thin mesa, elevated above the rest of the sample [144].

First, we spin-coat a several µm-thick layer of positive UV resist (MICROPOSIT S1800) on the sample, to protect against dust and the cooling water used during the wafer sawing. A wafer saw (DISCO DAC-2SP/86 Automated Dicing Saw) is then aligned to the row of cavities using large Si_3N_4 triangles fabricated in the first lithography step at the top and bottom of the row (see Fig. 5.6a). First, we use a fine 40 µm saw to make cuts of 150 µm depth on either side of the mesa. The mesa width is chosen as 150 µm. Repeating this five times while moving the saw in steps of 30 µm outward, we clear a ∼150 µm area on either side of the mesa. We then use a saw of 300 µm thickness to remove a 150 µm thick layer from the rest of the sample. After sawing, the resist is removed in a 45 °C acetone bath. Fig. 5.6 shows the resulting sample, with the 150 µm-wide mesa elevated above the rest of the sample.

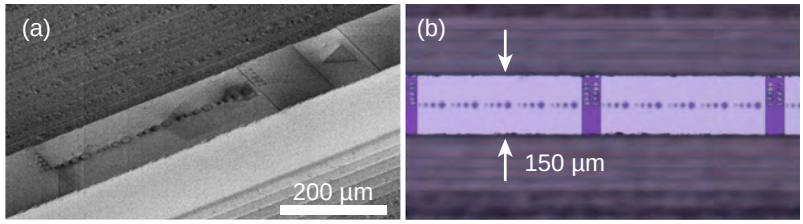

Figure 5.6: The diamond-sawed mesa. (a) SEM image (sample tilted) of a field of disks on top of the diamond-sawed mesa. The triangular marker next to the field is used to align the wafer saw, together with an identical marker at other end of the mesa. **(b)** Optical microscopy image of the disks on the mesa.

5.5 Fluorescent quantum dots as LDOS probes

To study LDOS effects, we need fluorescent emitters on our sample. Many excellent works have compared properties of various emitters [65, 185, 195, 220, 221]. Single photon emitters used in quantum information processing can be subdivided into five categories: single atoms (usually suspended in vacuum)

[222], organic molecules [223–225], rare-earth ions [226, 227], semiconductor quantum dots [23, 220, 228, 229] and optically active defect centers [230, 231]. For our purpose, the emitter should fulfil the following criteria: (1) There should be emission in the 765-780 nm wavelength range of our laser, such that fluorescence studies can be compared to taper-coupled characterization experiments of the hybrid modes. (2) Emitters should be placeable at the antenna hotspot. (3) For practical purposes, emitters should be stable for several days in ambient conditions and photo-bleaching should be minimal. (4) Quenching by metals in close proximity to the emitter should be minimal. (5) Eventually, we would like to place a *single* emitter per antenna. The second criterion disqualifies single atoms, which need to be in vacuum, typically at distances much larger than a few nm from any interface. Most organic molecules suffer from rapid photo-bleaching or oxidation, whereas the few exceptions such as dibenzoterrylene (DBT) [232] require embedding inside a specific host crystal for good stability and optical properties, which makes positioning on a hybrid difficult. Defect centers in bulk diamond can have excellent properties, but our application would require a nanometer-sized probe. While nitrogen vacancy (NV) centers in diamond nanocrystals have shown high variability in quality [233], other defects such as germanium vacancy centers have shown great promise as bright and reproducible emitters [231, 234]. Rare-earth ions embedded in nanocrystals recently emerged as promising LDOS probes [235, 236]. How to obtain a single emitter per crystal, however, which is required for application as a single-photon source, is currently not clear. Semiconductor quantum dots (QDs) are either epitaxially grown, typically in a III-V semiconductor [46, 237, 238], or solution-processed to form colloidal nanocrystals [77, 141, 200, 239, 240]. The first option is not available in our structure. Colloidal quantum dots, however, can be very bright, efficient and extremely stable emitters, although they tend to suffer from blinking [65, 241, 242]. They are available at almost any emission wavelength, as this can be tuned by size.

We have chosen to use CdSeTe/ZnS core/shell quantum dots (Invitrogen Qdot 800 ITK Organic, Q21771MP), stabilized in decane using long alkyl ligands (trioctylphosphine oxide, TOPO), emitting near 800 nm wavelength with a typical room-temperature single QD linewidth of 50 nm (see Fig. 5.7a). Owing to the relatively large ZnS shell, these are known to be extremely stable. Individual quantum dots were shown to blink, with a high fluorescent quantum efficiency of 94% associated with the bright state [243]. Their small diameter of $\sim$10 nm (see *e.g.* Fig. 5.12) enables positioning at the antenna hotspot, yet the large shell thickness [§] may help keep the exciton in the core at sufficient distance from the metal (also helped by the 3 nm alumina shell on the antenna) to mitigate fluorescence quenching [152]. Importantly, as will

[§]Exact core and shell thickness is not provided by the supplier, but typical cores sizes in CdSe quantum dots are 2-4 nm [244] and transmission electron microscopy images of Qdot 800 QDs suggest core sizes of 4-6 nm [245]

be explained in Section 5.6, functional chemical groups are available that bind specifically to the shell material, enabling covalent binding of the quantum dots to the antennas. Fig. 5.7b shows a typical fluorescence decay trace of one of the QDs, positioned on a glass substrate. We observe a bi-exponential decay trace with a fast and a slow lifetime, a common phenomenon in quantum dots which was suggested to originate from the bright and dark states [242, 246]. The slow decay is often associated to the bright state.

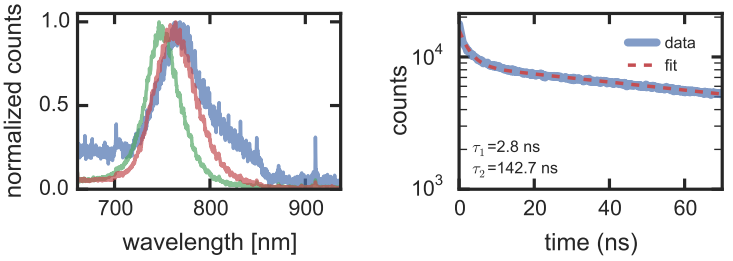

Figure 5.7: Single Qdot 800 spectra and decay trace. (a) Emission spectra measured on three individual quantum dots. Size polydispersity causes small differences in emission frequency. **(b)** Fluorescence decay trace of a single quantum dot, fitted with a bi-exponential decay. Extracted lifetimes τ_1 and τ_2 are indicated. Average lifetimes from measurements on multiple QDs were τ_1 =2.3 (0.7) ns and τ_2 =153 (11) ns. The measurement setup is explained in Chapter 7.

5.6 Positioning of quantum dots

Fig. 5.8 shows a step-by-step description of our quantum dot positioning method. This method is similar to that developed by Curto *et al.* [71, 199] for binding the same quantum dots to gold nano-antennas. The main difference is the linker chemistry: we use a functional group that can bind specifically to aluminium rather than to gold. Moreover, we use a thiol to bind directly to the QD, rather than binding to the QD ligands.

5.6.1 Binding quantum dots using MDPA

First, we separately test the quantum dot binding, which is done using 12-mercaptododecylphosphonic acid (MDPA, purchased from Sigma-Aldrich) as a linker molecule. Alkyl phosphonic acids were demonstrated to form self-assembled monolayers on metal oxide surfaces, including aluminium and titanium oxide [247–249]. High selectivity was found for binding to the metal oxides over binding to siliceous materials such as SiO_2, owing to the instability of Si-O-P bond compared to *e.g.* Al-O-P bonds [249–252]. The thiol group on the other end of the MDPA molecule can form a covalent bond with the sul-

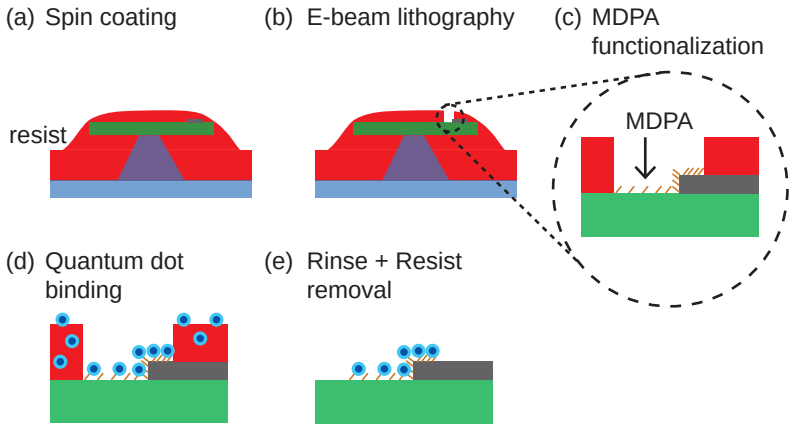

Figure 5.8: Quantum dot positioning, step-by-step. (a) A positive e-beam resist is spin coated on the sample with hybrids. **(b)** We define holes at the antenna tips using a third lithography step, and develop the resist. **(c)** After a brief oxygen etch the sample is immersed in a MDPA solution for 24 hrs. The MDPA molecules form a monolayer on the substrate, binding preferentially to metal oxides. We then rinse and bake the sample. **(d)** The sample is transferred to a quantum dot solution. Quantum dots bind covalently to the thiol groups on the MDPA, but also disperse in the resist. **(e)** After quantum dot immersion, we rinse the sample and dissolve the resist.

phur atoms in the quantum dot shell, a property often used to cover quantum dots with thiolated ligands [253, 254].

Using UV lithography, reactive ion etching and thermal evaporation, we prepare samples containing large (>10 μm) patches of aluminium, silicon nitride and silicon. Note that the Si surface contains a few-nm layer of native oxide. Following a recipe by Attavar *et al.* [251], we prepare a monolayer of MDPA on our samples. After cleaning the samples in an oxygen plasma etch for 10 minutes, they are immersed in a 1mM solution of MDPA in methanol for 24 hours to form the monolayers. We use methanol because de-mineralized water slowly degrades aluminium [247]. Samples are then rinsed in pure methanol and annealed for 1 hour on a hotplate at 90°C , after which physisorbed phosphonic acid is removed by a triple methanol and water wash. At this point, the presence of the monolayer can already be observed, as the Al surfaces become strongly hydrophobic. We then proceed with the quantum dot binding. For this test, we used large (∼12 nm) PbS quantum dots stabilized in octane with oleic acid ligands. The samples are immersed for 24 hrs in the QD solution at a concentration of 4.8 mg/ml. Unbound quantum dots are then removed by a double octane rinse followed by an acetone and isopropanol dip. Fig. 5.9 and Table 5.2 compare results with and without the MDPA monolayer. A clear preference for quantum dot binding to Al over Si is observed on both samples. We find that QD density

on Al increases by approximately a factor 3 when MDPA is used, indicating that it helps the binding. We would expect no quantum dots to be present on the sample without MDPA, as ligands should protect them from adsorption to the surface. These results suggest that this protection is imperfect, however for our purpose this is not a problem. We also find that QD density on the Si are not affected by the MDPA, which indicates that indeed the monolayer is only formed on the Al, and another mechanism is responsible for the QD attachment to Si. Densities on Si_3N_4 were roughly the same as for Si. When MDPA is used, selectivity of binding to Al over Si or Si_3N_4 is around 20-25.

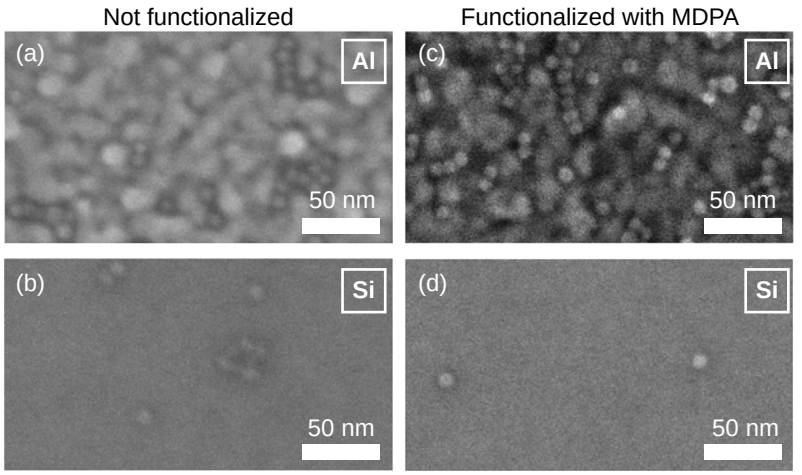

Figure 5.9: Selective QD binding using MDPA as a linker. SEM images of test samples after immersion for 24 hrs in a PbS quantum dot solution, without **(a-b)** and with **(c-d)** a preceding MDPA functionalization step. Quantum dots (size $\sim$10 nm) are visible as small dots on both samples. We see a strong selectivity of quantum dot binding to aluminium (a,c) over silicon (b,d) in both cases. Quantum dot density on silicon is not affected by the MDPA, but density on aluminium increases with MDPA.

5.6.2 PMMA masks for quantum dot screening

To make hybrids with quantum dots only present at antennas, higher selectivity is required than obtainable from just the chemical selectivity of the MDPA molecules. We therefore use a PMMA mask to screen parts of the sample from QDs. First tests are done on samples containing large patches of Si, Si_3N_4 and Al. We spincoat a 200-nm layer of PMMA (Microchem 950 PMMA, dissolved in anisole) on the samples and use e-beam lithography to define large crosses and circles of 0.5-4 μm diameter. Samples are developed and briefly exposed to an oxygen plasma etch for 20 seconds, which cleans the exposed sample yet does not etch through the PMMA. MDPA functionalization is performed

MDPA used	Substrate	QD density [μm^{-2}]
no	Si	80
yes	Si	60
no	Si_3N_4	30
yes	Si_3N_4	40
no	Al	480
yes	Al	1370

Table 5.2: Effect of MDPA on QD binding. Average quantum dot densities observed on Si and Al substrates, with and without MDPA functionalization. All samples were immersed in a quantum dot solution for 24 hours. Note that densities should be interpreted as a rough estimate, due to the limited sample size used. Densities were obtained by counting quantum dots in SEM images, where for each reported density approximately an area of 0.08-0.16 μm^2 was used for counting.

as described above.[¶] We decreased the annealing time from 1 hour to 15 minutes. After MDPA functionalization, samples are immersed in a 10 nM solution of Qdot 800 quantum dots in decane for 24 hours. They are then first rinsed in pure decane and subsequently kept in toluene for 5 hours, which both dissolves the PMMA and disperses the quantum dots that were dissolved in the PMMA. Fig. 5.10 shows SEM images of a sample. A clear difference between the parts covered and not covered by PMMA is visible, with high QD density inside the patterned areas and virtually none outside, both for the large cross and the small circles. This shows that PMMA masks are an excellent pathway to selective quantum dot positioning. We also find that the selectivity of Al vs. Si and Si_3N_4 has decreased, from 20-25 to $\sim$2.5 times more QDs visible on Al than on the Si or Si_3N_4. It is possible that the Qdot 800 quantum dots are more likely to adsorb onto the substrate than the PbS quantum dots, which have different ligands. Fig. 5.11 shows fluorescence images of the same sample shown in Fig. 5.10, optically pumped with a 532-nm pulsed laser, which confirm the successful localization by the PMMA mask. However, we also see some fluorescence from the parts that were covered by PMMA. This suggests that QDs do diffuse through the PMMA mask, as was also suggested for Qdot 800 QDs with amino-functionalized ligands in aqueous solution [201].

5.6.3 Effect of immersion time

Having confirmed that we can accurately position quantum dots on aluminium structures, we now position them on our hybrids. To avoid

[¶]Note that, while PMMA is not affected by immersion in the acidic MDPA solution (pH$\sim$5), we found that many other resists including Ma-N 2400 and CSAR 62, as well as the co-polymer MMA, became impossible to completely remove from the sample after MDPA immersion. It is likely that the acid causes cross-polymerization in the resist, making them insoluble in common solvents like acetone, anisole or n-methyl-2-pyrrolidone (NMP).

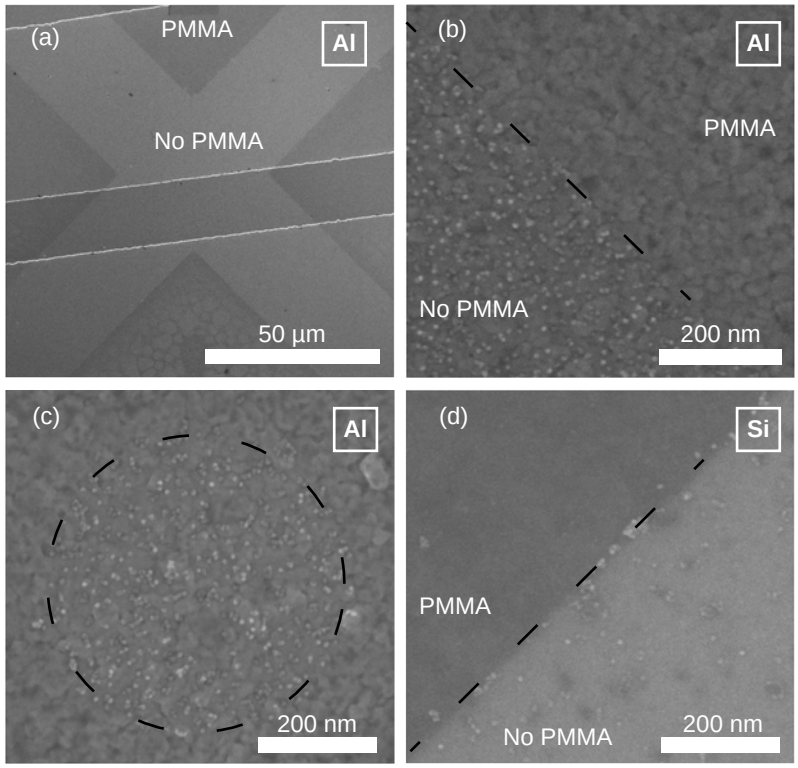

Figure 5.10: Controlling QD location using a PMMA mask. SEM images of a test sample with patches of aluminium, silicon (not shown) and silicon nitride, which was covered with a patterned PMMA mask during MDPA and quantum dot deposition. Qdot 800 quantum dots were used. PMMA was removed before imaging. **(a)** A cross defined in the PMMA, showing clear contrast due to quantum dot binding inside the cross. This part of the sample is fully covered with aluminium. Nearly horizontal lines are edges between Si and Si_3N_4 underneath the Al. **(b)** Zoom-in at the cross edge, showing high quantum dot density inside the cross and none outside, where the sample was screened by PMMA. **(c)** A 500-nm circle defined in the PMMA, on an aluminium patch, showing quantum dot localization with high precision. **(d)** A cross edge like in (b), now on a silicon patch. Quantum dot density is lower than on aluminium. Dashed lines in panels (b-d) indicate PMMA edges.

quantum dot diffusion through the PMMA, we use a thicker PMMA layer and shorter immersion time in the QD solution. The fabrication steps are shown in Fig. 5.8. The hybrids, consisting of 4-µm disk with 80-160-nm-long antennas, are covered with a 1100-nm layer of PMMA, which we measured to be 500 nm thick at the antenna location on the disks. At the disk edge, where the resist is most thin, thickness is still $\geq$270 nm. Following the procedure for alignment, exposure and development also used for the antennas, we define holes of 60 or 120 nm diameter, centered at the antenna apex pointing to the

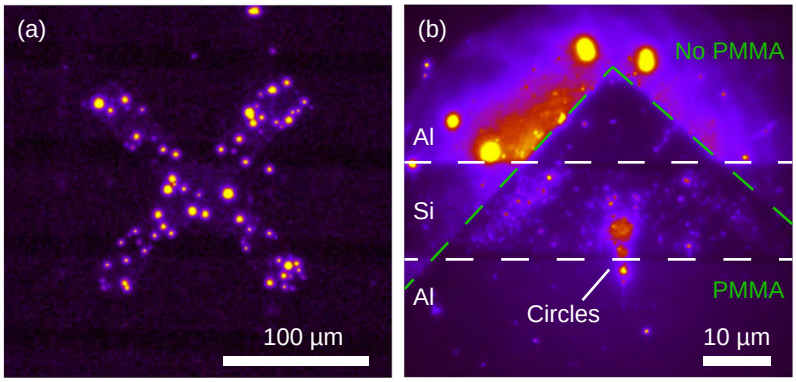

Figure 5.11: Fluorescence imaging of quantum-dot patterned substrates. (a) Strong fluorescence contrast between inside and outside the cross. Bright spots correspond to quantum dot clusters. Image taken with a 10x, NA 0.25 objective. **(b)** Zoom-in of the same cross, just below the center, taken with 100x, NA=1.4 oil immersion objective. We still see strong contrast between inside and outside the cross (edges indicated by green dashed lines), as well as for the small circles below. We observe more fluorescence coming from the aluminium than from the silicon parts (edges indicated by white dashed lines). Images were taken on the same sample as in Fig. 5.10.

disk center. We use an electron dose of 500 $\mu C/cm^2$ and step size of 5 nm. After a 20-second oxygen plasma etch, MDPA functionalization and quantum dot deposition is done as for the test samples in Fig. 5.10. Fig. 5.12 shows SEM and fluorescence images of two samples, after 24 hours and after 5 minutes immersion time in the quantum dot solution. For long immersion time, we see quantum dots everywhere on the disk, both in SEM and in fluorescence. On the other hand, for short immersion time, quantum dots are only visible at the antenna tip and fluorescence is confined to the antenna. Fluorescence spectra, which are discussed in Chapter 7, confirm that the emission comes from the quantum dots. Note that most often, no quantum dots are visible at all in SEM images, although in fluorescence we observe a near-100% success rate of quantum dot positioning for the 120-nm holes (success rate is lower for the 60-nm holes). This suggests that quantum dots are in most cases not attached to the disk but only to the antenna, where they are difficult to discern from the antenna itself due to our low SEM imaging quality, caused by sample charging. These results shows that we can accurately and with high success rate position quantum dots on our hybrids, with no quantum dots present outside the intended area.

5.7 Conclusions and outlook

We have, for the first time, successfully and reproducibly fabricated hybrid systems consisting of silicon nitride microdisks coupled to aluminium anten-

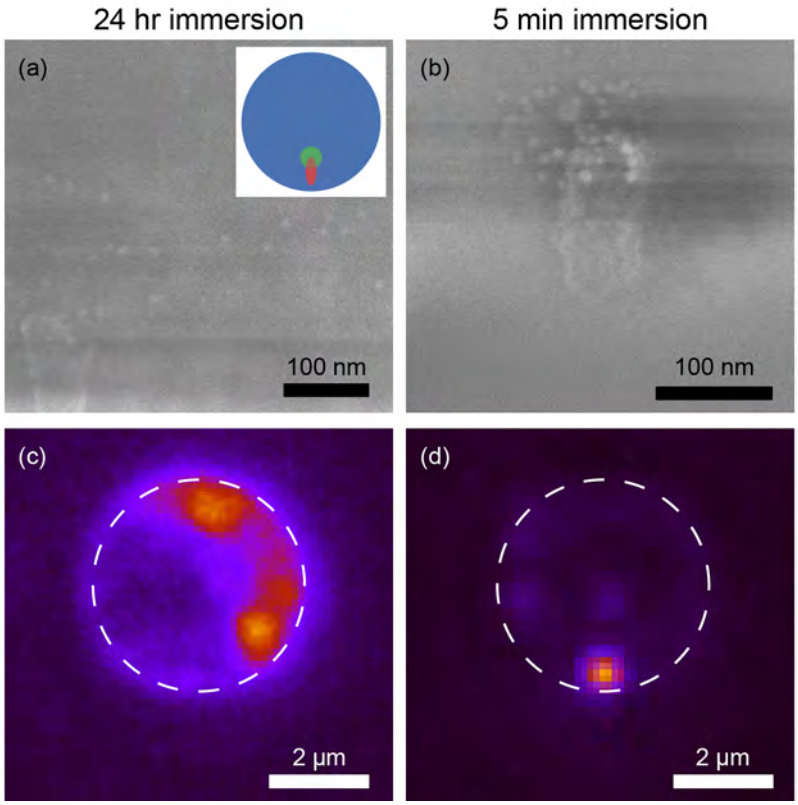

Figure 5.12: Quantum dots on hybrids, effect of immersion time. (a-b) SEM images of hybrids, showing an area on the disk near the antenna. The samples were functionalized with quantum dots using immersion times of 24 hours **(a)** or 5 minutes **(b)** in the quantum dot solution. The inset in (a) shows a cartoon of the disk (blue) with antenna (red) and the hole in the PMMA (green, 120 nm diameter) where QDs are expected to be. **(c-d)** Fluorescence images of hybrids made with 24 hours **(c)** or 5 minutes **(d)** immersion times. For both samples, an area much larger than the disk size was illuminated by the pump laser. Dashed lines roughly indicate the disk edge.

nas, with various cavity sizes and antenna lengths. Diamond-sawed mesas allow accessing the systems with tapered fibers for measurements. A novel technique was developed to position fluorescent quantum dots at the antenna hotspots on the hybrid systems. High precision and success rate, as well as near-perfect screening of areas that should remain free of quantum dots, is achieved using a combination of selective linker chemistry and a patterned resist mask. Material selectivity as well as effects of the linker molecules and quantum dot immersion time were studied, and we found that careful tuning of the immersion time is required for good results.

These methods pave the way for experiments on hybrid systems, which

will be the topic of Chapters 6 and 7. The quantum dot positioning method presented here is applicable to placing various types of quantum dots in any nanophotonic system. Although our linker molecules are specifically chosen for binding to metal oxides such as alumina, these could easily be exchanged to facilitate binding to other materials such as gold, silver or silicon. In future work, the accuracy and specificity of our method could easily be further improved by more suitable choices of quantum dot ligands, for example. By changing the hole size in PMMA, immersion time or quantum dot concentration, we are confident that this method can also be employed to position a *single* quantum dot in a nanophotonic device, which would enable high-fidelity fabrication of single photon sources.

Appendices

5.A Marker alignment procedure

A crucial step in hybrid fabrication is the relative alignment of cavity and antenna. This requires the use of markers in the e-beam lithography, with which we align the coordinates system in which the antennas are written to that of the disks. The procedure is largely based on the work of Zhang [255].

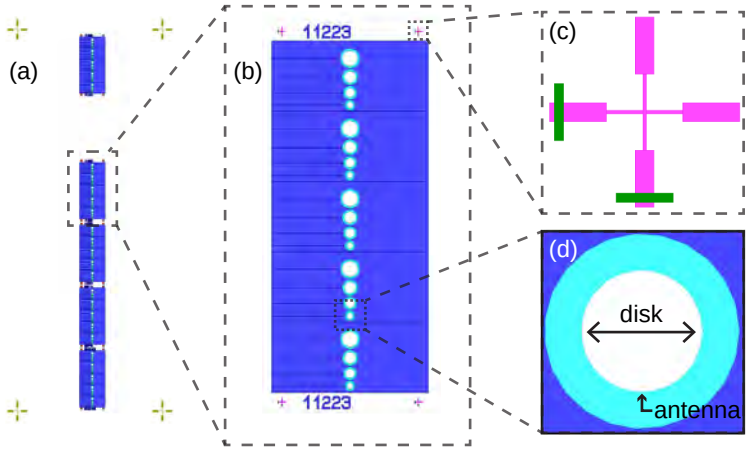

Figure 5.13: Marker alignment. Images of the sample design. **(a)** Full design, showing the 500-µm write fields containing the hybrids in a vertical row, as well as four 200-µm alignment crosses (yellow) at each corner, used for the coarse alignment. The top write field is a test field, on which we test alignment procedures. **(b)** Zoom-in of a write field, which contains 20 disks of 4 different diameters (8-20 µm). On the corners of the field, there are small alignment crosses for precise alignment. **(c)** Zoom-in of a small alignment cross, showing in green the area that is scanned in an automatic line scan during the precise alignment procedure. **(d)** Zoom-in of an 8 µm disk with an antenna at the bottom. The light blue rings, which define the disks, are separated from the big pads in dark blue, because the software recognizes them as circular elements. Therefore they are written in a concentric manner, which improves edge smoothness.

Fig. 5.13 shows the sample design. In the first lithography step, we write the disks as well as the alignment markers. We write a large (200 µm) cross at each corner of exposed area with disks, and small (12 µm) crosses at the corners of each write field (500×500 µm). Additionally, we write an extra test field on which we test the alignment procedure in the second exposure step. During the second exposure step, we first find three of the large markers manually and use the 3-point sample-to-stage correction to adjust the coordinate system to that used in the first exposure step. We then do a test run on the test field, where we use automatic line scans to scan over the arms of the small crosses and find their center coordinates. This line scan measures

an intensity profile across the arm, and a threshold algorithm is used to find the edges of the arms and from that the center coordinate. This threshold algorithm, as well as the scan parameters, needs to be adjusted carefully to give accurate position measurements. This is what we do on the test field. This information is then automatically processed by the software (Raith Voyager), and any shifts from the intended cross positions (*e.g.* due to imperfect stage positioning) are corrected for in the sample-to-stage alignment. After this, the write fields with the hybrids are written. It is important that new line scans and sample-to-stage alignments are done at each write field, because the sample moves between write fields and piezo drift or imprecision can cause alignment errors.

Chapter 6

Orders-of-magnitude linewidth tuning in hybrid antenna-cavity systems

One of the most important properties of hybrid systems for practical application as single photon sources or quantum logic devices, is the ability to tune their operation bandwidth over orders of magnitude without compromising their light-matter interaction strength. Here, we experimentally demonstrate linewidth tuning over two orders of magnitude. We combine these results with simulations to show that local density of states is mostly constant, and can even be boosted in some cases. Hybrids consisting of microdisk cavities and aluminium nano-rod antennas of various lengths are fabricated using a two-step lithography process. Linewidth and mode shifts are studied using a combination of tapered-fiber coupling and free-space microscopy. Our results show good agreement with perturbation theory, up to the point where the dipole approximation for the antenna breaks down. Finally, we use our experimental results to make a prediction of the local density of states in our systems.

6.1 Introduction

Outstanding challenges to the development of scalable quantum optical networks include the development of a fast and efficient single photon source, as well as robust all-optical single-photon logical gates, preferably at room temperature [30, 31]. Both devices require an enhancement of light-matter interaction strength. Currently, state-of-the-art solid-state single photon sources or logic gates rely on dielectric cavities or waveguides and have reached impressive figures of merit, such as high brightness and indistinguishability [43], single-photon collection efficiencies of >98% [148], purity of <99% [256] or single-photon emission rates of 4 MHz [45] for single photon sources, or the observation of a single-photon nonlinearities in a strongly-coupled cavity-emitter system [37, 55, 56]. Despite these impressive results, connecting many such elements into a network remains challenging due to the extremely narrow bandwidths of operation (high quality factors) and required operation at temperatures $\lesssim 10$ K. Emitters spectrally broaden at higher temperatures, causing a mismatch with these narrowband cavities. Plasmonics could alleviate this problem by offering extremely high light-matter coupling strengths over large bandwidths, however often at the expense of dissipative losses. This approach has already demonstrated single photon sources with GHz emission rates [239], and recently first indications of single-emitter strong coupling were observed [70, 77]. However, dissipation in the metal prevents high photon extraction efficiencies and current bandwidths are so large that strong coupling can only just be reached. Hence, a crucial factor in the further development of scalable quantum optical elements is control over resonator bandwidth. In Chapter 3, we have predicted that hybrid antenna-cavity systems allow precisely this bandwidth tuneability, while keeping Purcell enhancement high. Thus far, no experiments have demonstrated such orders-of-magnitude tuneability in these systems.

The potential for applications aside, there is a fundamental interest in studying the linewidth of a hybrid system. We have seen that this linewidth, as well as the cavity resonance shift induced by the antenna, are given by the well-known first-order cavity perturbation theory (Eqs. (2.28) and (2.29)) [27, 133]. This theory is at the heart many applications that use the influence of a perturbing atom, molecule, or dielectric object to establish an interaction that can be exploited for optical sensing or control [3, 34, 257–260]. However, it is strictly only valid under the assumptions that (1) the perturbation can be treated as a point dipole, and (2) far-field radiation by the cavity is negligible. This calls for an experiment that tests the limits of the cavity perturbation theory. In optics, the state of the art in cavity perturbation tests is that cavities have been perturbed by near-field probes [190, 191, 261–263]. The strength of this method is that the position of the perturbation can be scanned over the cavity to create a spatial map of perturbation strength, which effectively maps the cavity field profile or effective mode volume. A very different

approach has recently allowed a quantitative comparison between theory and experiment for a cavity perturbed by a *lattice* of scatterers, revealing a dramatic failure of perturbation theory for open systems with radiation overlap between cavity and perturbation [130].

It has turned out to be very difficult to perform measurements in which the polarizability and mode volume are systematically varied. The polarizability of a near-field probe cannot easily be modified *in situ*, and experiments where different particles are used to vary polarizability require a high degree of control and reproducibility in placing these particles to allow a good comparison. To our knowledge, no experiment exists which has quantitatively tested the validity of perturbation theory by varying both particle polarizability and cavity mode volume.

In this chapter, we present measurements of the linewidth and resonance frequency shifts of an optical cavity perturbed by a single aluminium nano-antenna. Hybrid antenna-cavity systems are fabricated lithographically, and we perform narrowband spectroscopy using a combination of tapered-fiber coupling and a free-space microscope, as discussed in Section 6.2. We obtain linewidths and frequencies from 60 physically different structures of various cavity and antenna sizes, supporting 120 different cavity modes. Section 6.3 discusses results found for the unperturbed (anti-symmetric) cavity modes in our system, from which we can gauge the quality and reproducibility of our sample fabrication process. Results for the perturbed (symmetric) cavity modes are shown in Section 6.4, and compared to first-order cavity perturbation theory, without any adjustable parameters. These results allow us to identify a range of antenna sizes for which the dipolar approximation works well, resulting in a good agreement between perturbation theory and experiment. For larger antennas, this approximation appears to break down, causing perturbation theory to overestimate the linewidth. This constitutes the first quantitative experimental test of cavity perturbation theory for optical cavities perturbed by a single scatterer. Moreover, we find that just by changing antenna length from $\sim$70 to 140 nm, we can tune the hybrid linewidth by more than two orders of magnitude, demonstrating the extreme tuneability available with hybrid systems. Finally, in Section 6.5 we use our experimental results to predict the local density of states (LDOS) in our hybrid systems, based on the coupled-oscillator model from Chapter 2.

6.2 Taper-coupled spectroscopy

6.2.1 Experimental setup

To measure the antenna-induced mode shifts and broadenings, we use a combination of fiber taper-coupling and free-space microscopy. Tapered optical fibers, or tapers, are widely used to probe whispering-gallery-mode cavities

[132, 142, 257, 264]. As the coupling strength between taper and cavity mode can be tuned in real-time through the cavity-taper distance, one can usually choose this strength to be in any desired coupling regime, *i.e.* under-coupled, critically coupled or over-coupled. For most of the hybrids studied here, however, coupling strengths are far too weak to observe the perturbed cavity modes in a cavity transmission spectrum. This is mainly because the antenna causes strong broadening of the mode, hence necessitating much higher coupling strengths to observe it. To be able to measure the perturbed cavity modes, we therefore need additional information. The light scattered by the antenna forms an excellent probe for these modes, as it is emitted mostly out of plane and thus easily collected by an objective. Since there is no scattering off resonance this is essentially a dark-field technique, enabling large sensitivity. We therefore construct a setup that combines taper-coupled spectroscopy with a free-space microscope.

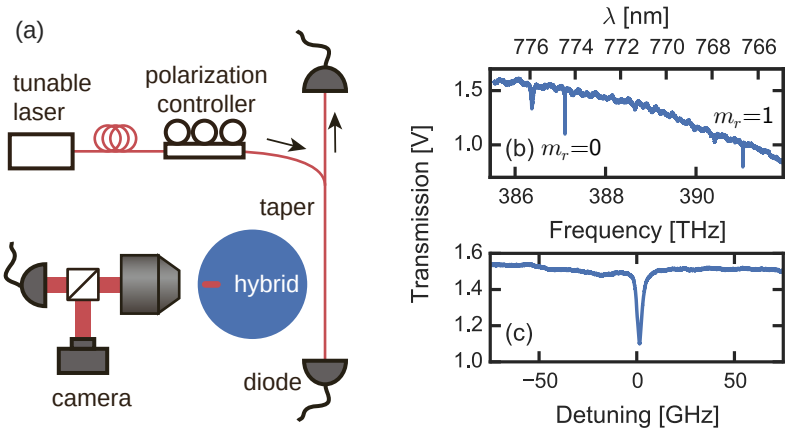

Figure 6.1: Experimental setup and transmission spectra. **(a)** Experimental setup. The light from the fiber-coupled laser is passed through the taper, which is coupled to the hybrid cavity. We use a fiber polarization controller to match the cavity mode polarization. Taper reflection and transmission are monitored on diodes, and using a free-space microscope we collect the scattered light on a diode and a camera. **(b)** Broadband transmission spectrum of a 12 μm diameter disk containing an antenna of 100 nm length. We see narrow dips corresponding to a fundamental ($m_r = 0$) and first order ($m_r = 1$) radial mode. A higher-order radial mode is also visible. **(c)** Zoom-in on the $m_r = 0$ mode. The narrow dip corresponds to the unperturbed, antisymmetric disk mode. The perturbed mode is strongly under-coupled and not visible in transmission.

Fig. 6.1a shows the experimental setup. We use a narrowband, tunable diode laser (Newport TLB-6712-P, <200 kHz linewidth, 765-781 nm) to excite the cavity through a tapered fiber. Single-mode tapered fibers are made by stretching a bare optical fiber (Thorlabs 780HP), positioned in a custom-made holder, over a hydrogen flame [143, 265]. The taper is transferred to the measurements setup in the same holder. Taper position is controlled via a 3-axis

piezoelectric actuator (Piezosystem Jena Tritor 38, open loop), and monitored through a free-space microscope with a high-NA objective (Olympus MPlan IR, 100x, NA 0.95). Reflection and transmission are monitored on amplified photo diodes (Thorlabs PDA36A), and scattered light is collected by the objective and passed through a beam splitter to the camera (The Imaging Source DMK 21 AU04) and an avalanche photo detector (Thorlabs APD410A/M). We use a fiber polarization controller to match the laser polarization to that of the radially polarized cavity modes. A homebuilt software program is used to control the piezoelectric actuator and the laser, and to read out diode signals and camera images.

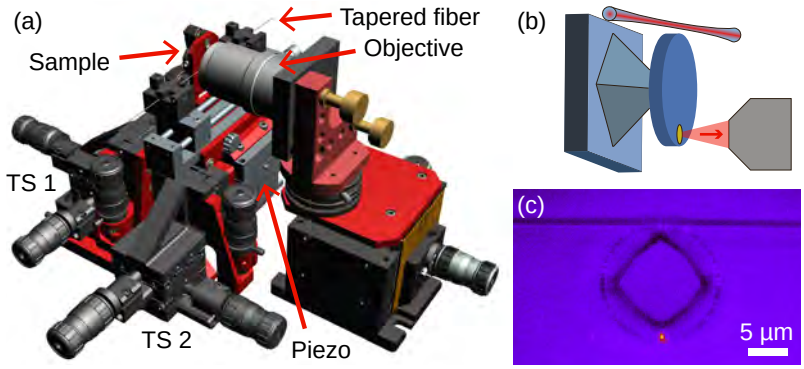

Figure 6.2: Positioning cavity and tapered fiber. (a) Mechanical design of the setup. The sample is mounted vertically in front of the objective. A tapered fiber runs horizontally across the sample. Three-axis translation stages (TS) and a piezoelectric actuator are used to move both sample and taper (TS 1) or only taper (TS 2 and piezo). **(b)** Sketch of sample, with tapered fiber positioned above and the antenna at the bottom of the disk, radiating into the objective. **(c)** Camera image of a 15 µm diameter hybrid, excited near its hybrid resonance frequency. The taper is visible extending from left to right in close proximity to the upper disk edge. The bright spot located at the lower disk edge is the antenna. The sample is homogeneously illuminated by an LED to see cavity and taper.

Fig. 6.2a shows the mechanical design used to position sample and taper. A three-axis translation stage moves both sample and taper with respect to the objective. Another such stage and the piezoelectric actuator are mounted on the first stage, and move only the taper. Taper angle with respect to the sample plane can be manually adjusted using a flexure hinge built into the taper mount, which is crucial for bringing the taper into micrometer proximity of the sample. Fig. 6.2b and c show respectively a sketch and a camera image of a hybrid system in our setup. It is excited through the taper, while antenna radiation is collected by the objective from the side. Taper position is always at the cavity edge opposite from where the antenna is located.

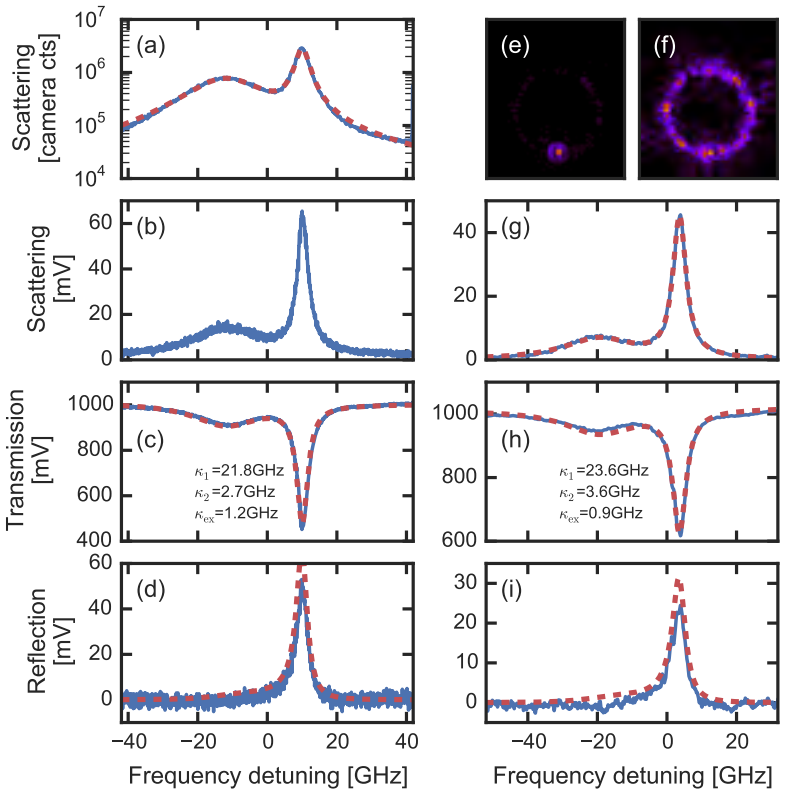

Figure 6.3: Narrowband spectroscopy and fits. (a-d) Scattering **(b)**, transmission **(c)** and reflection **(d)** spectra measured on the photo diodes during a step-by-step piezo scan of the laser wavelength. The corresponding scattering spectrum obtained from integrated camera images is shown in **(a)**. We show data (blue line) and a global fit (red dashed line). Obtained loss rates for the perturbed (κ_1) and unperturbed (κ_2) modes and the cavity-taper coupling rate κ_{ex} are displayed. **(e,f)** Normalized camera images of the cavity, taken at the resonance frequency of the perturbed **(e)** and the unperturbed **(f)** modes shown in (a-d). The antenna is located at the lower disk edge. **(g-i)** Same spectra as for (b-d), for the same cavity, in this case measured during a broadband (several THz) wavelength sweep, and zoomed in on the cavity mode. During such a sweep, the laser frequency changes more rapidly, and we cannot collect camera images. This data is fitted independently. The data in all figures was measured on a $m_r = 0$ mode of a 8 µm diameter cavity with an antenna of 80 nm length.

6.2.2 Processing cavity spectra

For each cavity, we measure a broadband (several nm range) spectrum by sweeping the laser wavelength and recording a time trace of the diode signals. Time traces are converted to spectra using the wavelength output signal from the laser, which is recorded simultaneously and corresponds directly to the

laser wavelength. An example of such a spectrum is shown in Fig. 6.1b,c. We find the modes which do not show scattering off the edge of the silicon pedestal, which correspond to the higher-order radial modes ($m \leq 2$ in our case). Comparison of the frequency spacings between modes to those obtained from simulations then allow identification of the $m_r = 0$ and $m_r = 1$ modes. We subsequently record a narrowband spectrum of each mode by fine-tuning the laser wavelength in a small range (approx. $\pm$40 GHz) using a built-in piezoelectric actuator. For these scans, the frequency axis is calibrated by simultaneously recording a transmission spectrum of a reference cavity (Thorlabs SA201-5B Fabry-Perot cavity) with a known free-spectral range of 10 GHz. As this scan is done step-by-step, we can also record a camera image at each frequency point. From the camera data, we integrate the pixel counts from a small region around the antenna to obtain an additional low-noise scattering spectrum. An example of spectra obtained from such a piezo scan and from a broadband scan are shown in Fig. 6.3, together with example camera images.

We fit the obtained spectra using a global least-squares fit to the transmission, reflection and scattering data, for which expressions are given in Eqs. (2.97), (2.98) and (2.102). To account for the fact that we also collect scattered light from the unperturbed antisymmetric mode, we use a modified version of Eq. (2.102)

$$P_{\mathrm{r}} = \left| \frac{A_{\mathrm{s}}}{-i\Delta_{\mathrm{s}} + \kappa_{\mathrm{s}}/2} \right|^2 + \left| \frac{A_{\mathrm{as}}}{-i\Delta_{\mathrm{as}} + \kappa_{\mathrm{as}}/2} \right|^2, \tag{6.1}$$

with A_{s} and A_{as} scattering amplitudes of the symmetric and antisymmetric modes, respectively. Fitting parameters are the input power in the taper P_{in}, the unperturbed cavity resonance frequency ω_{c} and linewidth κ_{i}, the resonance shift $\delta\omega_{\mathrm{c}}$ and broadening $\delta\kappa$ of the perturbed (hybridized) cavity mode with respect to the unperturbed mode, cavity-taper coupling rate κ_{ex} and the scattering amplitudes A_{s} and A_{as}. We separately fit both the narrowband piezo scan data (as shown in Fig. 6.3a-d) and a narrowband region of the broadband scan data (as shown in Fig. 6.3g-i). For the piezo scans, we use the integrated camera counts as scattering data, while for the broadband scans we use the photo diode trace. Although usually there is good agreement between the two scan methods, occasionally there are linewidth differences of up to $\sim$30%, which we attribute to a slightly non-linear camera response in the low-intensity regime. To avoid thermal bi-stability effects, we always do scans with increasing and decreasing wavelength, and verify that the obtained linewidths are similar (typically within 10%).

We measure cavities of 15, 12 and 8 $\mu\mathrm{m}$ diameter. For each diameter, there are cavities with 10 different antenna lengths between 68 and 188 nm and a thickness of 40 nm. These samples were fabricated as described in Chapter 5 (not adding the quantum dots). For each combination of diameter and antenna length, there are 2 cavities, bringing the total number of

measured cavities to 60. On each cavity, both the $m_r = 0$ and the $m_r = 1$ modes are measured. We average the results from cavities with identical diameter and antenna length, from narrowband and broadband scans and from scans with increasing and decreasing wavelength. Cavities with visible dirt and spectra with a failed fit routine or insufficient signal-to-noise ratio are excluded from the analysis. For hybrids with linewidths similar to or larger than the maximum piezo scan range of ∼80 GHz, we only use the results from the broadband scans.

6.3 Unperturbed modes

Fig. 6.4 shows the loss rates κ_{as} and resonance frequencies ω_{as} of the unperturbed (antisymmetric) cavity modes for the hybrids measured in this work. Linewidths typically lie in the 1-2 GHz range for the 12 and 15 $\mu\mathrm{m}$ diameter disks, and are around 3 GHz for the 8 $\mu\mathrm{m}$ diameter disks. Average quality factors and resonance frequencies are summarized in Table 5.1. Importantly, we observe only minor variations in the linewidth between different cavities of the same size, and no clear dependency of the linewidth on antenna size, indicating that this mode is insensitive to the antenna. While this is indeed predicted by the coupled-mode theory discussed in Section 2.5.3, it is surprising that it holds so well. The theory assumes the antenna to be a point dipole, yet in reality it has a finite width of ∼60 nm, causing finite overlap with the antisymmetric mode. Nevertheless, we find that perturbation is negligible. The unperturbed cavity mode data indicates the quality of the fabrication process. As discussed in Section 5.2, the observed low variance in ω_{as} shows that disks are fabricated with diameters equal to within 2-3 nm. The high quality factors are reproducible to within 20-30%, indicating low surface scattering and contamination. Finally, the $m_r = 1$ modes in the 8 $\mu\mathrm{m}$ disks seem more lossy than all other modes. However, these modes were measured with a higher taper-cavity coupling rate, and the non-ideality of the taper caused additional broadening. This does not affect the measured shifts and broadenings, as this broadening occurs roughly equally for the symmetric and the antisymmetric mode.

6.4 Linewidth and frequency tuning

Fig. 6.5 shows the hybridized mode resonance broadening $\delta\kappa$ and shift $\delta\omega_{\mathrm{c}}$ as function of antenna length, for both the $m_r = 0$ and the $m_r = 1$ mode. We can see that both modes show increasing broadening with increasing antenna length, up to a length around 150 nm, after which linewidth drops again. The shift, on the other hand, shows a dispersive behaviour: modes are red-shifted for small antennas and blue-shifted for larger antennas. Remarkably,

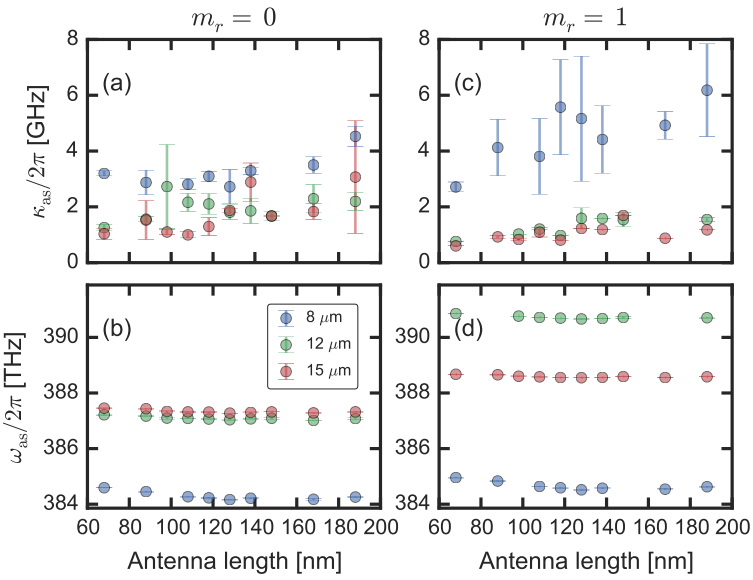

Figure 6.4: Resonance frequencies and unperturbed loss rates. Loss rates of the unperturbed (antisymmetric) $m_r = 0$ **(a)** and $m_r = 1$ **(c)** cavity modes. **(b)** and **(d)** show their respective resonance frequencies. Different colors correspond to different disk diameters (indicated). For cavities of the same diameter, resonance frequencies and quality factor are very similar.

the linewidth can be increased by two orders of magnitude by changing antenna length, *e.g.* from ∼1 to ∼100 GHz for the fundamental mode in 12 µm disks. For comparison to perturbation theory, we use the Bethe-Schwinger perturbation formulas Eqs. (2.28) and (2.29). These require as input the effective cavity mode volumes V_{eff} and bare antenna polarizabilities α, which we retrieve from finite-element simulations of disks and antennas separately, as discussed in Section 5.2 and Section 5.3, respectively. Based on SEM images of the disks, we assume the 15 and 12 µm (8 µm) disks to have 50 nm (100 nm) smaller radii than designed for. Antennas, which were designed to be centered 300 nm from the disk edge, are therefore assumed to be 250 nm (200 nm) from the edge. The resulting effective mode volumes vary from $301\lambda^3$ for the $m_r = 1$ mode in a 15 µm diameter disk, to $52\lambda^3$ for the fundamental mode in an 8 µm diameter disk. For polarizabilities, we only consider its dominant xx-component α_{xx}, evaluated at the cavity resonance frequency (taken to be fixed at 387 THz).

The resulting predictions from perturbation theory are shown by the solid lines in Fig. 6.5. We stress that these are not fitted: the curves are fully determined by the results of our simulations. For all disk sizes, and for both radial orders, we observe a good agreement between theory and data for the broad-

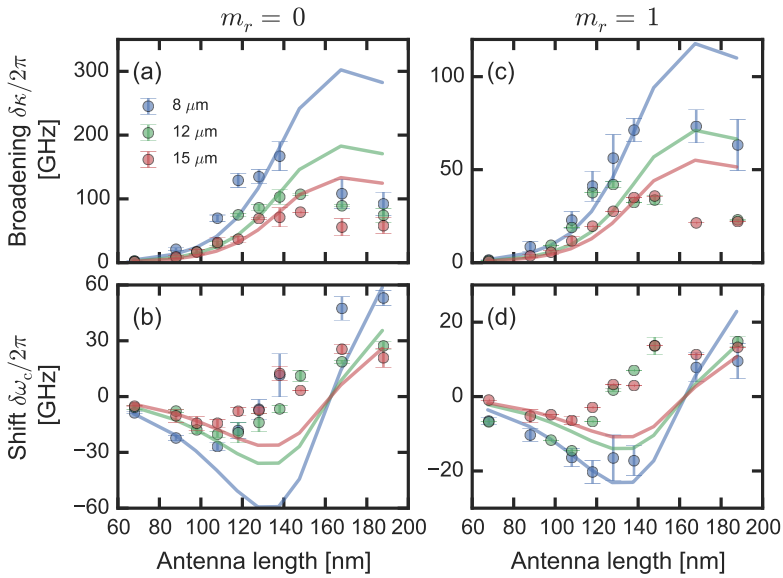

Figure 6.5: Hybrid broadening and shift. **(a-b)** show the broadening **(a)** and shift **(b)** of the hybridized fundamental radial mode ($m_r = 0$), with respect to the unperturbed mode, as function of antenna length. **(c-d)** show these quantities for the hybridized $m_r = 1$ mode. The markers correspond to data for the 8 µm (blue), 12 µm (green) and 15 µm (red) diameter cavities. The lines represent predictions by perturbation theory. For both radial orders, we observe good agreement between theory and data in the broadening, up to antenna lengths of 140 nm. For larger length, perturbation theory overestimates the effect of the antenna, which we attribute to a breakdown of the dipole approximation. For the mode shift, data and theory agree qualitatively.

ening, up to antennas of 140 nm length. For longer antennas, broadenings are overestimated by the perturbation theory. This theory relies on two important assumptions: that there is negligible radiation overlap between cavity and antenna, and that the antenna can be treated as a dipole. If the first assumption would break down, this would lead to a complex cavity-antenna coupling rate [130], causing a deviation from theory for all antenna sizes, which is not observed. Moreover, the antenna and the cavity have strongly different radiation patterns, with the former showing a dipolar radiation pattern and the latter radiating almost entirely in the disk plane. Hence, the observed deviation from theory at large antenna length is likely caused by a breakdown of the dipolar approximation. This is a striking result: despite the fact that measurements were performed on 60 different cavities, fabrication is sufficiently reproducible to observe a clear trend in linewidth which can be compared to theory. Earlier experimental studies that used a near-field tip scanned over a cavity have been able to observe the proportionality of perturbation strength to the cavity mode profile [190, 191]. Yet, a quantitative comparison, which requires

knowledge of both the cavity mode volume and antenna polarizability, has remained elusive. As such, this constitutes the first quantitative comparison between cavity perturbation theory and an experiment in optical systems. For the shifts shown in Fig. 6.5b,d, we find qualitative agreement with the theory, *i.e.* we observe a red-shift transitioning to a blue-shift. However, quantitative agreement is likely hampered by experimental uncertainties. For one, disk roughness or small dielectric particles cause negligible broadening compared to the antenna, but may cause shifts of a similar order of magnitude [144]. Also, near resonance the linewidths are about an order of magnitude larger than the shifts, making it difficult to determine the latter very accurately in a fit.

Summarizing, we have experimentally demonstrated antenna-induced cavity linewidth tuning by two orders of magnitude. Results agree very well with perturbation theory, up to 140 nm antenna length, at which point the dipole approximation of the antenna breaks down. We also observe either blue- or redshifted cavity modes depending on the sign of the cavity-antenna detuning, which agrees qualitatively with perturbation theory.

6.5 Implications for local density of states

We can use the results from our measurements to predict the local density of states (LDOS) in these systems. In Section 3.2, we learned that the peak values of relative LDOS (*i.e.* the Purcell factor) in hybrid systems can be derived from the 'superemitter' approximation as

$$\mathrm{LDOS}_{\mathrm{SE}} = 3/(4\pi^2) Q_{\mathrm{H}}/V_{\mathrm{eff,H}}, \tag{6.2}$$

with Q_{H} the quality factor of the hybridized mode and

$$V_{\mathrm{eff,H}} = V_{\mathrm{eff}}/|1 + G_{\mathrm{bg}}\alpha_{\mathrm{hom}}|^2 \tag{6.3}$$

its mode volume (in cubic wavelengths). We directly measured Q_{H} and comparison to perturbation theory confirmed the bare antenna polarizability α_{hom} and cavity mode volume V_{eff} (also in cubic wavelengths) extracted from simulations. Hence, the only missing ingredient is the antenna-emitter coupling strength, captured in the Greens function G_{bg} that describes the antenna scattered field at the location of the emitter.

Let us assume we study a fluorescent molecule, adsorbed on the antenna at the antenna apex. From the same simulations that were used to retrieve antenna polarizability, we may extract G_{bg} by probing the scattered field at the emitter location (we take it at 2 nm from the antenna apex, 2nm above the surface). Division by the antenna dipole moment yields G_{bg}. We may use Eq. (6.3) to calculate the relative reduction in mode volume $V_{\mathrm{eff}}/V_{\mathrm{eff,H}}$ caused by the antenna, which is shown in Fig. 6.6b. Note that it is independent of the

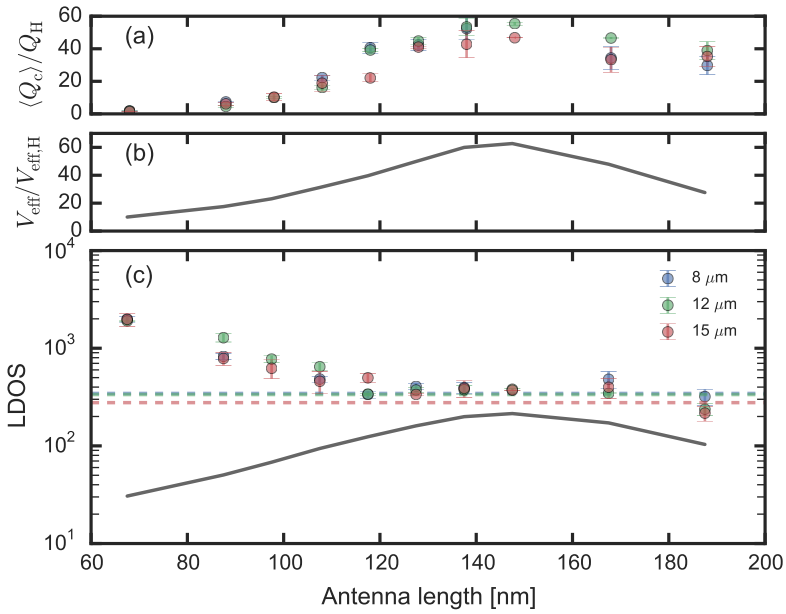

Figure 6.6: Hybrid LDOS. (a) Quality factor reduction $\langle Q_c \rangle / Q_H$ of the hybrid modes w.r.t. the average cavity quality factor Q_c of the unperturbed mode. **(b)** Mode volume reduction $V_{eff}/V_{eff,H}$ of the hybrid mode w.r.t. the bare cavity mode. **(c)** LDOS in the hybrids (at resonance). Dashed lines show corresponding cavity Purcell factors, and the dark solid line shows antenna LDOS at cavity resonance frequency. We see that the hybrids can outperform the cavity and antenna for strong antenna-cavity red-detuning, *i.e.* small antennas. For larger antennas, reduction in mode volume and in quality factor balance each other out. We show only results for the $m_r = 0$ modes. Results are similar for the $m_r = 1$ mode. LDOS is relative to vacuum.

cavity. Combined with the relative quality factor reduction obtained from our experimental data and shown in Fig. 6.6a, this gives the boost in peak LDOS in our hybrid system. Fig. 6.6c shows the bare cavity, bare antenna and hybrid LDOS obtained in this manner. Bare cavity Purcell factors are obtained from average experimental Q of the unperturbed modes combined with V_{eff} from simulations, and bare antenna LDOS from Eq. (2.47).

Somewhat surprisingly, we see that we can outperform the bare cavities only for antennas smaller than ∼120 nm. For larger antennas, mode volume and quality factor reduction are approximately equal, leading to hybrid Purcell factors similar to those of the bare cavity. For small antennas, however, mode volume reduction remains appreciable since an antenna in the reactive regime still creates a hotspot, yet the quality factor remains much higher. This matches the theoretical results in Section 3.2. Even though they do not show improved LDOS, hybrids with large antennas and broad lines can be very beneficial from a practical point of view. It is far easier to spectrally match

an emitter to a 100 GHz linewidth than to a 1 GHz linewidth, and the fact that most energy is radiated out-of plane can be an additional advantage for some applications. We further note that our hybrids *do* outperform the bare antennas of any length. This is because the antenna by itself is not very good, showing lower LDOS than the bare cavity. We expect that the use of bow-tie or nanocube antennas, which show intense field concentrations, should lead to even higher hybrid LDOS [68, 76].

Another surprising result is that relative quality factor reductions do not depend strongly on disk size, as seen in Fig. 6.6a. This is surprising, as from theory one would expect the disk quality factor to increase exponentially with diameter, whereas the mode volume, and therefore the hybrid quality factor, increases approximately linearly. However, in realistic disk cavities with edge roughness and absorption, the quality factor in fact scales linearly with disk radius [211]. This is supported by our data, which shows average unperturbed quality factors of $1.2 \cdot 10^5$, $2.1 \cdot 10^5$ and $2.6 \cdot 10^5$ for the $m_r = 0$ mode in 8, 12 and 15 μm disks, respectively (see Table 5.1). This explains why neither cavity nor hybrid Purcell factor shown in Fig. 6.6c depend strongly on disk diameter.

6.6 Conclusions and outlook

In conclusion, we have reproducibly fabricated antenna-cavity hybrids with various cavity sizes and antenna lengths. Using a combination of tapered fiber coupling and free-space microscopy, we measured antenna-induced mode shifts and broadening on these cavities. This revealed that one can tune hybrid linewidths over two orders of magnitude by changing antenna size, and thereby antenna-cavity detuning. Results agree well with perturbation theory, up to antenna lengths of 140 nm, at which point the antennas cannot accurately be described as dipoles. Combining the observed linewidth changes with mode volume reductions obtained from simulations, we conclude that LDOS in these hybrids will be similar to that in bare cavities, except for the smallest antennas, where one can outperform the cavities significantly. While perturbation theory has been tested by mapping the spatial dependence of detuning on perturbation position using NSOMs, to our knowledge this is the first quantitative test in which a systematic comparison of perturbation to the ratio of polarizability amplitude and phase, and of mode volume, was performed. This verifies the great potential of hybrid antenna-cavity systems for applications such as single-photon sources, which require large light-matter interaction strength over practical bandwidths. Not only can these systems support larger light-matter coupling strength than a bare cavity, it allows bandwidth tuning over orders of magnitude while keeping this strength constant. Moreover, we believe that these results will facilitate the rational design of devices for a wide variety of applications that rely on perturbation to achieve functionalities like sensing

or control. For example, this could be used for the design of structures operating at an exceptional point. It was shown that WGM cavities can be brought to an exceptional point, *i.e.* a coalescence of the two eigenmodes of the system, by introducing just two perturbing particles [142]. At such points, interesting behaviour may arise, such as intrinsically chiral modes and directional lasing [142, 266], loss-induced lasing [267] and enhanced sensing capability [268, 269]. Understanding the exact effect of a perturbing particle on cavity linewidth and frequency is crucial for designing such systems.

Chapter 7

Observation of strong and tunable fluorescence enhancement in hybrid systems

The promise of hybrid antenna-cavity systems relies to a large extent on the prediction that one can benefit simultaneously from the high cavity quality factor and the low cavity mode volume, leading to highly enhanced local density of states (LDOS). In this chapter, we experimentally verify this symbiotic behaviour. We study hybrid antenna-cavity systems with fluorescent quantum dots positioned at the antenna apex. Fluorescence spectra show asymmetric Fano lineshapes at the hybridized cavity mode frequencies that go from a strong peak to a dip, depending on antenna size. We discuss the role of LDOS and collection efficiency on the emission spectra and show that these measurements can be used to obtain a lower bound on the LDOS in these systems, which can be as much as 14 times higher at the hybrid mode than for the bare antenna. Finally, a study of quantum dot decay rates reveals a strong increase that correlates with the antenna resonance.

7.1 Introduction

Hybrid antenna-cavity systems are attractive candidates for single-photon sources, quantum logic gates or particle sensors, owing to their potential for large enhancement of the local density of states (LDOS) and their large bandwidth tuneability. Several theoretical studies have predicted very high LDOS in a variety of antenna-cavity geometries [93, 104–106, 109]. In Chapters 2 and 3, we discussed under which conditions these systems can work symbiotically and achieve such high LDOS, and when, in contrast, destructive interference causes LDOS to be reduced. Despite their great potential for light-matter interaction, to date very few experimental works exist that study LDOS in these systems, possibly due to the difficulty of deterministically integrating an emitter, an antenna and a cavity. Experiments have been done on hybrid structures where intrinsic fluorescence of the cavity material was used to study emission [110], or a gain material was embedded inside the cavity [97, 98]. To benefit from the plasmonic field enhancement, however, the emitters need to be placed at an antenna 'hot-spot', which was not the case for these studies. Without this field enhancement, the antenna merely acts as a source of loss, invariably decreasing LDOS.

In this chapter, we present the first experimental study of fluorescent emitters placed at the antenna hotspot inside a hybrid antenna-cavity system. We study fluorescence spectra and emitter decay rates from colloidal quantum dots, observing strongly enhanced emission at the hybridized cavity modes. Spectra assume asymmetric Fano-type lineshapes, matching LDOS spectra predicted by coupled-oscillator theory and full-wave simulations. We explain our results by showing that, for broadband emitters coupled to narrow photonic resonances, emission spectra trace the product of collection efficiency and LDOS, which indeed shows excellent agreement with the data. Our results give a lower bound on the LDOS increase at the hybrid resonance — relative to the bare antenna — which can assume values up to 14 for the smallest antennas used. Furthermore, we find fluorescent decay rates to be strongly increased in the hybrid system, with average decay rates peaked near the antenna resonance condition. These results constitute the first observation of strong LDOS enhancements in a hybrid antenna-cavity system.

Section 7.2 describes our experimental methods. The obtained fluorescence spectra and their analysis are then discussed in Section 7.3, after which we discuss the results from the quantum dot decay rate measurements in Section 7.4.

7.2 Experimental methods

Samples consisted of silicon nitride (Si_3N_4) disks with 5 different diameters between 3960 and 4120 nm. Each disk contained an antenna placed 300 nm

from the disk edge. We used 5 antenna lengths between 88 and 168 nm. Colloidal quantum dots (Invitrogen Qdot 800 ITK Organic) were positioned in an area approximately 120 nm in diameter around the antenna apex. Images of a typical hybrid and of the quantum dots (QD) near the antenna are shown in Fig. 5.5c and Fig. 5.12b, respectively. Further details of the sample fabrication are given in Chapter 5. Note that this procedure leads to multiple QDs present per antenna. We measure one structure for each of the 25 different combinations of disk size and antenna size. Out of these 25 measurements, three were discarded because the fluorescence signal was too low.

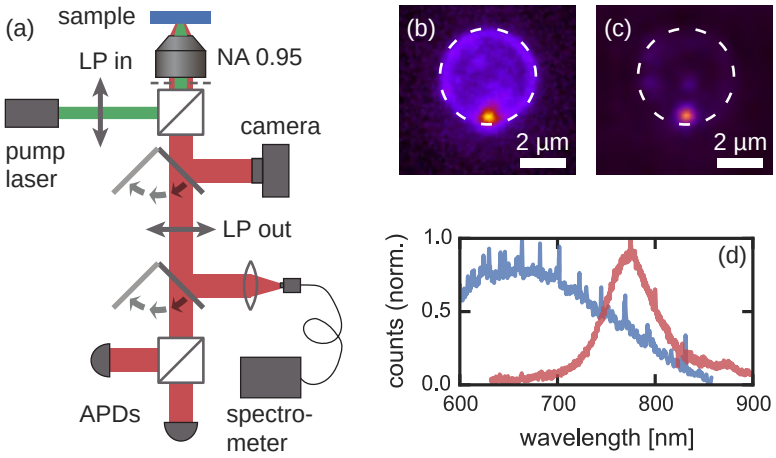

Figure 7.1: Experimental setup. (a) Sketch of the fluorescence microscope used in this study. Samples are illuminated by a pump laser, and fluorescence is collected either on a camera, a fiber-coupled spectrometer or two avalanche photodiodes (APDs) for lifetime measurements. The pump and fluorescence are linearly polarized by polarizers (LP). **(b-c)** Camera images of a hybrid, pumped by the 532 nm laser **(b)** or by the 640 nm laser **(c)**. The antenna is located at the bottom of the disk, and is clearly visible in fluorescence. In both cases, the pump is defocused, illuminating an area much larger than the disk. For 532 nm illumination, strong background fluorescence from the disk is visible, which is absent for 640 nm illumination. **(d)** Fluorescence spectra pumped by the 532 nm (blue) and 640 nm (red) laser. The 532 nm spectrum is taken from a part of the disk edge without quantum dots, and shows a broad peak from the intrinsic silicon nitride fluorescence. Sharp peaks correspond to enhanced fluorescence at the cavity modes. The 640 nm spectrum is taken from a single quantum dot on the disk, not near the antenna. No silicon nitride fluorescence is visible. The 532 nm (640 nm) spectrum is normalized to its maximum of $1.4 \cdot 10^3$ ($1.8 \cdot 10^3$) counts, acquired with 10 (20) MHz pulsed excitation at $\approx$ 0.1 mW (1.8 mW) average power and 60 s (120 s) integration time.

To investigate the modification of spontaneous emission by the quantum dots, we perform fluorescence spectroscopy and lifetime measurements. Fig. 7.1a shows the experimental setup, which is an adapted version of the

setup reported in [270]. The sample is illuminated through an objective (Olympus MPlan IR, 100x, NA 0.95) by a pulsed pump laser. In the detection path, this pump is removed by a dichroic beamsplitter and a long-pass filter. Pump and detection polarization are controlled by linear polarizers. Fluorescence is sent either to a camera, to a fiber-coupled spectrometer (Andor Shamrock 303i, equipped with an iVac DR316B-LDC-DD detector) or two avalanche photodiodes (APD) in a Hanbury-Brown-Twiss configuration [271]. The spectrometer uses a multimode fiber of 10 μm core size, which translates to a detection area of $\sim$1 μm on the sample. We performed broadband ($\Delta\lambda$ =314 nm, resolution $\sim$ 0.4 nm = 0.2 THz)* or high-resolution ($\Delta\lambda$ =62 nm, resolution $\sim$ 0.1 nm = 0.05 THz) measurements using a 300 lines/mm or a 1200 lines/mm spectrometer grating, respectively. By correlating the arrival times of photons on the APDs (Excelitas SPCM-AQRH-14-FC single photon counting modules, 350 ps timing resolution) to the timing of the pump pulses, we can measure emitter lifetime [272]. Fig. 5.7b shows a typical decay curve of a single quantum dot on a glass substrate. Correlating the events on the two APDs to each other corresponds to a measurement of the second order correlation function $g^{(2)}$, which shows antibunching if a single emitter is probed [233]. APD counts and pump pulse events are recorded on a Becker & Hickl DPC 230 timing card.

To avoid background signal from intrinsic silicon nitride fluorescence [273], we use a pump laser of 640 nm wavelength (PicoQuant LDH-P-C-640B pulsed diode laser, <500 ps pulse width) with repetition rate variable between 2.5 and 40 MHz. Unless stated otherwise, measurements were done with the pump beam focused on the sample. Fig. 7.1b and c show fluorescence images of a hybrid pumped by a 532 nm pulsed laser (Time-Bandwidth Products, 10 MHz, <10 ps pulse width) and by the 640 nm laser, respectively. With the 532 nm illumination, we observe fluorescence from the entire disk. With the 640 nm laser, in contrast, only fluorescence from the location of the antenna (and quantum dots) is visible. Fig. 7.1d compares spectra obtained under 532 nm and 640 nm illumination. In the first case, we see a broad spectrum peaking around 650 nm, typical of silicon nitride fluorescence [273]. In the second case, this background is absent and only a quantum dot fluorescence peak at $\sim$780 nm is visible.

All spectra are acquired using a 60 or 120 second camera integration time, with the laser set to a 20 MHz repetition time. Background spectra, taken without pumping, are subtracted. Pixels with anomalously high counts (usually attributed to cosmic rays) are removed in post-processing. The high-resolution spectra may show intensity fringes due to an etalon effect in the camera chip itself, with amplitudes up to 50% of the signal. As they occur at a specific frequency, we remove them by suppressing the corresponding frequency components in a Fourier transform of the signal. Fluorescent decay

*Bandwidth $\Delta\lambda$ and resolution specified at 780nm wavelength.

curves were measured with the laser set to 10 MHz repetition rate, acquisition times between 30 and 120 seconds and individual APD count rates around 10-50 kHz.

7.3 Observation of LDOS boosts from hybrid emission spectra

7.3.1 Experimental results

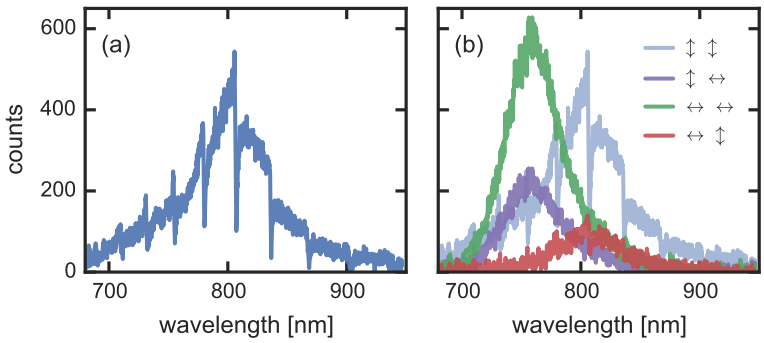

Figure 7.2: Polarization of QD emission. (a) Example of a typical emission spectrum, for QDs at the antenna apex. The broad QD emission peak is modulated with sharp Fano-type resonances. **(b)** Emission spectra recorded for in- and output polarization set to vertical-vertical (blue, same spectrum as shown in (a)), vertical-horizontal (purple), horizontal-horizontal (green) and horizontal-vertical (red). Fano resonances are only clearly visible for in- and outputs vertically polarized, *i.e.* along the antenna main axis. All spectra measured on the same hybrid, with antenna length 168 nm.

Fig. 7.2a shows a typical fluorescence spectrum from quantum dots at the antenna apex in a hybrid system. We recognize a broad fluorescence peak from the intrinsic QD emission spectrum. Remarkably, this emission spectrum is modulated at regular intervals by an asymmetric, Fano-type resonance. Emission can be reduced by as much as ∼70% at the dips of these resonances. These lineshapes are strongly reminiscent of the asymmetric LDOS resonances predicted by coupled-oscillator theory in Chapter 3 and shown for example in Fig. 3.1b. The notion that hybrid LDOS could be the cause behind these lineshapes matches the fact that the resonances appear only when both pump and detection polarization are chosen along the antenna main axis, as shown in Fig. 7.2b. In fact, when detection polarization is chosen horizontally, *i.e.* along the antenna short axis, entirely different spectra are observed. These peak at a shorter wavelength, and no Fano resonances are observed. This corresponds to the fact that near the antenna apex, no significant LDOS enhancement is

expected for emitters polarized transversely to the antenna main axis.

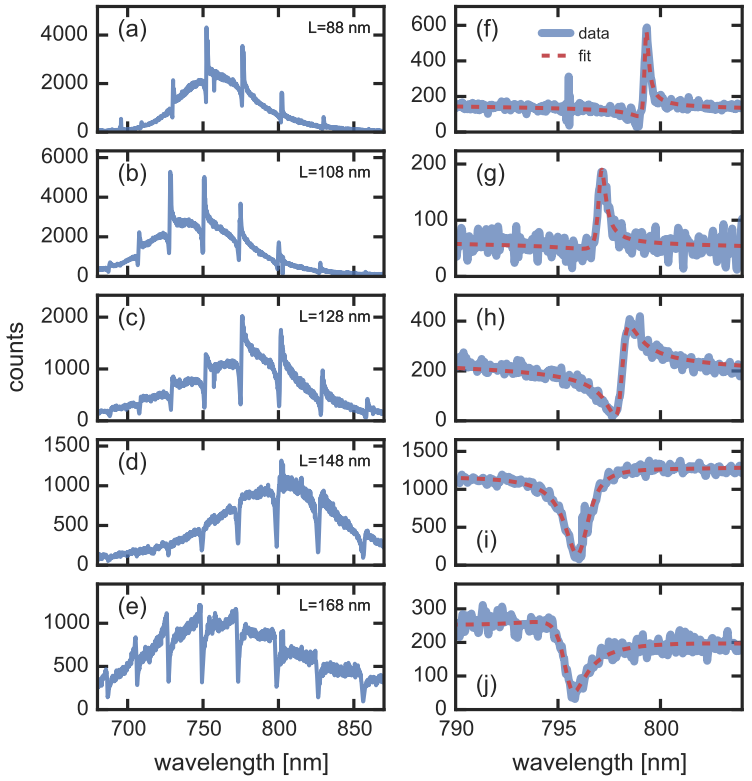

Figure 7.3: Emission spectra for different antenna lengths. (a-e) Broadband emission spectra from hybrids with equal disk size and 5 different antenna lengths L (indicated). The dispersive Fano resonances change gradually from a peak to a dip as L increases. **(f-j)** High-resolution emission spectra, zoomed in on the mode near 800 nm wavelength, for the same hybrids as in (a-e). The shape of the Fano resonances is more clearly visible. We show data (blue) and a fit (red).

If the resonances in the quantum dot spectra do indeed originate from the LDOS resonances in the hybrid system, we would expect from our calculations in Chapter 3 that the lineshape depends strongly on cavity-antenna detuning. Fig. 7.3a-e show broadband spectra for hybrids with 5 different antenna lengths, and consequently different cavity-antenna detunings. We indeed observe a gradual change from a resonance that is mostly peaked for short antennas (*i.e.* cavity modes far red-detuned) to complete destructive interference for an antenna length of 148 nm. At even larger length, the Fano lineshapes take on opposite asymmetry to that of the short antennas, *i.e.* first a peak, then a dip. This change of phase can be observed even more clearly in

the high-resolution spectra shown in Fig. 7.3f-j. This behaviour corresponds remarkably well to that of the Fano resonances in Fig. 3.1b.

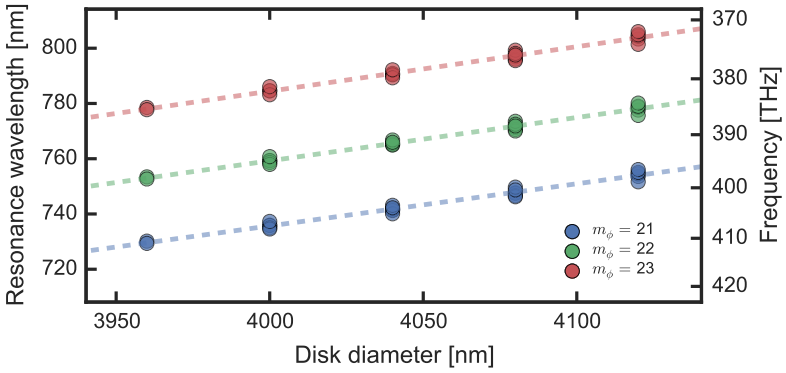

Figure 7.4: Resonance wavelength dependence on disk size. Resonance wavelengths for three of the Fano resonances in the emission spectra, for the 5 different disk sizes. Comparison to simulations suggests that these correspond to hybridized whispering-gallery modes of azimuthal order m_ϕ 21, 22 and 23. Dashed lines show linear fits.

To quantify these results, we fit the resonances in high-resolution spectra with the expression for a Fano lineshape [12]

$$I(\omega) = |E_2 e^{i\theta} + E_1 \frac{\kappa/2}{-i\Delta + \kappa/2}|^2. \tag{7.1}$$

Here, Δ and κ are frequency detuning and linewidth, respectively, and θ is the Fano phase. Fig. 7.3f-j show examples of resonances near 800 nm wavelength, fitted with Eq. (7.1). For each hybrid, we apply the fit routine to three different modes between 720 and 800 nm wavelength. The resulting resonance wavelengths are visible in Fig. 7.4. We find that resonances shift linearly with disk diameter, further confirming that these correspond to the hybridized whispering-gallery modes (WGM). To first approximation, WGMs are waves that fit an integer times within an effective disk circumference. As such, their resonance wavelengths depend approximately linearly on disk diameter [274]. By comparing these resonance wavelengths to those obtained from simulations, we can estimate them to be the WGMs of azimuthal order m_ϕ 21, 22 and 23. Note that these disks are too small to support high-Q modes of higher radial order than $m_r = 0$ in this wavelength range.

As we have seen in Chapter 6, hybrid linewidth depends strongly on antenna length. A similar dependence is visible for the Fano resonance linewidths, as can be seen in Fig. 7.5a. As for the linewidths measured in taper-coupled spectroscopy on larger disks, shown in Fig. 6.5, we observe a strong linewidth increase up to antenna lengths of 148 nm. At this length,

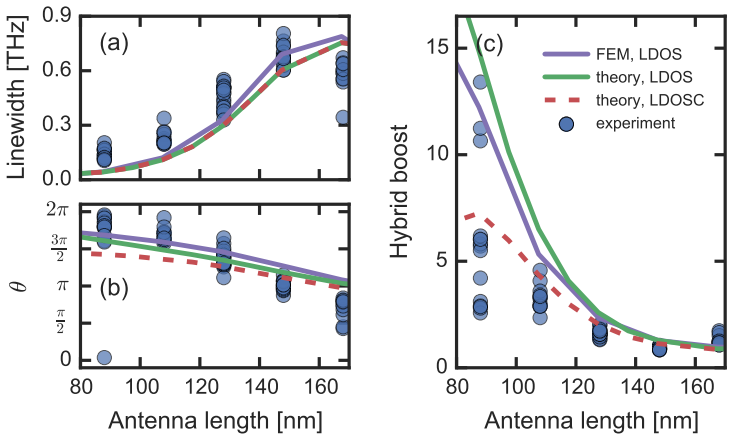

Figure 7.5: Dependence of hybrid resonance properties on antenna length. (a) Fano resonance linewidth, showing a strong increase as the antenna is tuned to resonance (around 150 nm length). **(b)** Fano phase θ transitions from a peak ($\theta \approx 0$) for short antennas to a dip ($\theta \approx \pi$) for antennas at resonance. For the largest antennas, the resonance takes on a Fano shape with opposite asymmetry, *i.e.* $\theta < \pi$. **(c)** Hybrid boost factor is strongest for small antennas, where cavity modes are far from antenna resonance. All experimental data (blue markers) are obtained from fits as shown in Fig. 7.3. Results are compared to values from the LDOS (green line) profiles or collected LDOS (LDOSC, red dashed line) profiles predicted by coupled-oscillator theory, as well as LDOS obtained from finite element simulations on the full hybrid system (purple line). Theory and simulations are discussed in Section 7.3.2.

antennas are on resonance with the cavity modes and induce maximum broadening. When increasing length further, linewidth drops slightly as the antenna is brought away from resonance. A plot of Fano phase θ in Fig. 7.5b confirms that the behaviour seen in Fig. 7.3 is generic to all cavity modes. The resonances change from nearly Lorentzian peaks ($\theta \approx 0$) for short antennas, to dips ($\theta \approx \pi$) at antenna resonance, and to opposite asymmetry $\theta < \pi$ at 168 nm antenna length.

All our observations suggest that the resonances lineshapes in the emission spectra follow the LDOS spectra of the hybrid systems. It is therefore interesting to compare the peak heights of the resonances to the background at the same frequency. This ratio, which we call hybrid boost, would then measure the peak LDOS, or Purcell factor, of the hybrid mode relative to the LDOS provided by the bare antenna at that frequency. From Chapter 6, we know that the broadband LDOS resonance corresponds to the bare antenna mode. Fig. 7.5c shows this hybrid boost for different antenna lengths. We see that for antennas near resonance (lengths near 140 nm), hybrid peak heights are not far above the background. This is not surprising, as for these resonances $\theta \approx \pi$, *i.e.* they are dips rather than peaks. In contrast, for short antennas, peak

heights can be as much as 14 times higher than the background. Again, this trend qualitatively matches that of the LDOS peaks in Fig. 3.1b, which extend far above the broad antenna background only if the antenna is significantly detuned. It is tempting to ascribe the observed boosts directly to a boost in LDOS at the hybrid modes. However, it is not straightforward to see why emission spectra should follow LDOS. Therefore, a more subtle analysis is required to correctly interpret this data, which is the topic of the next section.

7.3.2 Relation between emission spectra and LDOS

The manner in which emitters report on LDOS depends strongly on the emitter bandwidth. We can distinguish two different regimes. The first is the case of emitters that are narrowband compared to the LDOS spectrum. At unit efficiency, each emitter produces one photon per excitation, with a fluorescent decay rate proportional to LDOS as dictated by Fermi's golden rule [11]. Hence, intensity is independent of LDOS. This is the regime discussed in most literature concerning LDOS measurements, particularly in plasmonics [68, 270, 275]. If the emitters are very inefficient, intensity may report on LDOS through an effective increase in radiative efficiency [76]. The second regime, often referred to as the 'bad emitter' regime, is that of emitters with bandwidths much larger than the LDOS features. Particularly, to be in this regime the emitters are required to be individually broadband on time scales shorter than the fluorescence decay time. Hence, an emitter showing slow spectral diffusion [276, 277] or a polydisperse ensemble of individually narrowband emitters can be classified under the first regime. In this limit of broadband emitters, the decay rate averages over all decay channels (*i.e.* energies), while the emission spectrum shows differences that are proportional to LDOS. For efficient emitters, the total, spectrally integrated intensity remains independent of LDOS, as is the case for narrowband emitters. An obvious example are emitters that can decay into a multitude of electronic levels. In this case, Fermi's golden rule states that each transition probability is proportional to the LDOS at that energy difference. This fact was recently used to alter the branching ratio of multilevel emission lines from Eu^{3+} ions [236, 278]. A similar example are dye molecules at room temperature, which typically support multiple excited state and ground state levels due to coupling of the vibrational to the electronic states, leading to broad emission spectra. In such cases, it was shown that LDOS can cause strong changes in the emission spectrum [279–281]. Beside multilevel decay, another reason for broad emission spectra can be spectral diffusion, which has been observed for organic emitters [277] and quantum dots [276, 282, 283]. We will show that, if diffusion happens on time scales much faster than the lifetime, this leads to the same behaviour as with multi-level decay, *i.e.* the emission spectrum traces (collected) LDOS and the decay rate measures the spectral average of LDOS weighted by the intrinsic emission spectrum.

The quantum dots in our experiment belong to the second category. Individual dots show high quantum efficiency [243] and emission bandwidths of ∼50 nm (see Fig. 5.7), much broader than the LDOS linewidths in the hybrid system (< 2 nm). We do not know whether our QDs are spectrally broad due to decay into multiple electronic or vibrational modes, or due to rapid spectral diffusion. Both mechanisms have been suggested for CdSe and CdSe/ZnSe QDs [284–286]. Slow diffusion, however, can be excluded as it was shown for similar (CdSe) QDs that emission spectra were broad (∼30 nm) even on ∼100-fs time scales [287]. This indicates that if spectral diffusion takes place, it is much faster than the lifetime. Hence, even if the exact mechanism of linewidth broadening is disputed, the resulting dependencies of emission spectra and decay rates on LDOS are the same. For simplicity, we will discuss here the case of a multilevel emitter, such as Eu^{3+}. The derivation of a spectrally diffusing emitter is given in Section 7.A.

Emission spectra of broadband emitters in a narrowband photonic environment

Consider an emitter with a intrinsic emission spectrum $p(\omega)$ in a photonic environment with frequency-dependent local density of states $\mathrm{LDOS}(\omega)$. The observed emission spectrum can be described as [279]

$$I(\omega) = N_{\mathrm{ex}} \frac{p(\omega)\gamma(\omega)}{\int p(\omega)\gamma(\omega)d\omega}\eta(\omega), \tag{7.2}$$

where N_{ex} is the number of emitter excitations, the fraction represents the probability of decay to a state with frequency difference ω, $\gamma(\omega) = \gamma_0 \mathrm{LDOS}(\omega)$ is the frequency-dependent decay rate, and $\eta(\omega)$ is the frequency-resolved quantum efficiency, given as [66]

$$\eta(\omega) = \eta_{\mathrm{C}}(\omega)\,\frac{\gamma_{\mathrm{r}}(\omega)}{\gamma(\omega)} = \eta_{\mathrm{C}}(\omega)\,\frac{\gamma_{0,\mathrm{r}}\,\mathrm{LDOS}(\omega)}{\gamma_{0,\mathrm{nr}} + \gamma_{0,\mathrm{r}}\,\mathrm{LDOS}(\omega)}. \tag{7.3}$$

Here, $\eta_{\mathrm{C}}(\omega)$ is the collection efficiency and $\gamma_{0,\mathrm{r}}$ and $\gamma_{0,\mathrm{nr}}$ are the intrinsic radiative and non-radiative decay rates of the emitter, which obey $\gamma_{0,\mathrm{r}}+\gamma_{0,\mathrm{nr}} = \gamma_0$. Material absorption and finite numerical aperture are captured in $\eta_{\mathrm{C}}(\omega)$, whereas intrinsic emitter losses are captured in $\gamma_{0,\mathrm{nr}}$. Eq. (7.2) holds for any two-level or multilevel emitter, and even for a rapidly diffusing emitter, as shown in Section 7.A. In the case that $\mathrm{LDOS}(\omega)$ varies much more rapidly with frequency than $p(\omega)$ in the vicinity of a frequency ω_1 (*e.g.* a broadband emitter coupled to a narrow LDOS resonance), we may simplify Eq. (7.2) to

$$I(\omega) \approx \frac{N_{\mathrm{ex}} p(\omega_1)\gamma_{0,\mathrm{r}}}{\int p(\omega)\gamma(\omega)d\omega}\mathrm{LDOS}(\omega)\eta_{\mathrm{C}}(\omega). \tag{7.4}$$

From this we see that the spectral shape is entirely determined by LDOS and the collection efficiency $\eta_{\mathrm{C}}(\omega)$, a fact that has been used to quantify LDOS

using emission spectra of cavity-coupled emitters in the 'bad emitter' limit [288]. We can define the 'collected LDOS' as

$$\mathrm{LDOSC}(\omega) \equiv \mathrm{LDOS}(\omega)\eta_{\mathrm{C}}(\omega), \tag{7.5}$$

which represents the portion of LDOS leading to light emitted into the far-field and collected by the detector. The detected emission spectrum traces $\mathrm{LDOSC}(\omega)$. The emitter decay rate γ observed in a fluorescence decay trace, in contrast, is given by spectrally averaging $\gamma(\omega)$ as

$$\gamma = \langle\gamma(\omega)\rangle = \int p(\omega)\gamma(\omega)d\omega. \tag{7.6}$$

Moreover, from Eq. (7.2) we see that total, spectrally integrated intensity depends only on N_{ex} and the collection efficiency η_{C} for an emitter with unit quantum efficiency, in agreement with literature [76, 289].

Emission spectra in a hybrid system

Eq. (7.4) maps onto our hybrids, since the intrinsic QD emission spectra have linewidths of 50 nm, while hybrid linewidths are below 1 nm. Let us therefore find explicit expressions for LDOS and collection efficiency in a hybrid system, using the coupled-oscillator model from Chapter 2. Cavity parameters ($Q = 3 \cdot 10^4$, $V_{\mathrm{eff}} = 21\lambda^3$, $\omega_{\mathrm{c}}/2\pi = 377.57\,\mathrm{THz}$) are obtained from a finite element simulation (COMSOL v5.1) of a 200-nm thick Si_3N_4 microdisk with a diameter of 4 µm.[†] Bare antenna dipole moment α_{hom} and antenna-emitter coupling strength as captured in G_{bg} are obtained from the simulations of aluminium rod antennas on a Si_3N_4 substrate used in Section 6.5 (spectra shown in Fig. 5.4). Considering the quantum dot diameter of ∼10 nm, we assume the emitter to be 5 nm from the antenna apex and 5 nm above the substrate. Hybrid LDOS relative to vacuum can then be found from a slightly modified version of Eq. (2.46)

$$\mathrm{LDOS}(\omega) = \mathrm{LDOS}_{\mathrm{bg}} + \frac{6\pi\epsilon_0 c^3}{\omega^3}\,\mathrm{Im}\left\{\alpha_{\mathrm{H}}G_{\mathrm{bg}}^2 + 2G_{\mathrm{bg}}\alpha_{\mathrm{H}}\chi_{\mathrm{hom}} + \chi_{\mathrm{H}}\right\}. \tag{7.7}$$

Here, $\mathrm{LDOS}_{\mathrm{bg}} = 1.62$ is the relative LDOS of the background environment, which we find from the bare antenna simulations and which corresponds well to the LDOS of 1.6 felt by an in-plane dipole 15 nm from a Si_3N_4-air interface. Collection efficiency is assumed to be given by the fraction of power emitted as dipole radiation by the source and antenna (see Section 2.4.4). This assumption uses the fact that practically all radiation from the microdisk WGM

[†]Note that at such small diameters, bending losses dominate over the surface scattering and absorption that limit Q for the 8, 12 and 15 µm disks. This is evident from the fact that Q as obtained from a linear extrapolation of the Q of these larger disk is higher ($Q \approx 6 \cdot 10^4$) than the Q obtained from the simulations, which only contains bending losses.

is emitted in the in-plane direction, which is not collected by the objective. Our simulations show that $\sim 3\%$ of the radiation by a 4 µm disk is collected by a NA=0.95 objective. Given that the spectrometer fiber also selects a $\sim$1 µm detection area on the sample, this fraction will be even lower in practice.

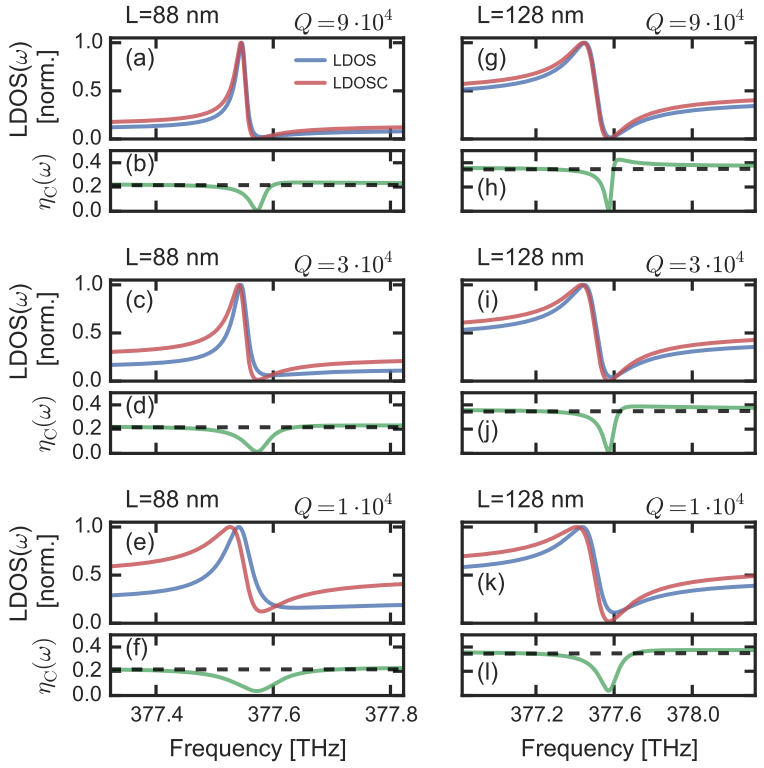

Figure 7.6: LDOS and LDOSC in a hybrid system. LDOS (blue) and collected LDOS (LDOSC, red), as well as collection efficiency $\eta_C(\omega)$ (green) in hybrid systems, for different antenna lengths L and bare cavity Q (both indicated above plots). The theoretical quality factor of the WGM cavities in this study is $3 \cdot 10^4$, corresponding to panels (c,d,i,j). The black dashed line indicates the bare antenna albedo A, which determines the collection efficiency away from the hybrid mode. For sufficiently high Q, or if the antenna is close enough to resonance to be the dominant source of loss, LDOS and LDOSC take on mostly the same lineshape. LDOS and LDOSC are normalized to their maxima, to facilitate comparison. Note that (a-f) and (g-l) have different x-axes.

Let us first compare the LDOS and LDOSC spectra for several examples of cavities and antennas, to learn what influences their spectral shape. Fig. 7.6 shows calculated spectra of LDOS, LDOSC and η_C for two different antenna lengths L and three different cavity quality factors. For both LDOS and LDOSC, we observe the familiar Fano-type lineshapes discussed in Chapter 3.

For a short antenna, far from resonance, LDOS resonances are narrow and lineshapes are close to Lorentzian peaks, while for an antenna closer to resonance (L=128 nm), resonances are broadened by antenna losses and the lineshapes are more asymmetric. This is the same behaviour as observed for the Fano resonances in the experimental hybrid spectra.

Interestingly, the lineshapes of LDOS and of LDOSC can be very similar under certain conditions. For the antenna near resonance, LDOS and LDOSC are very similar for all values of Q shown. For the short antenna, this is only true for the highest Q. This behaviour is best explained by considering the collection efficiency η_{C}. Collection efficiency is determined by bare antenna albedo A away from resonance. However, at the minimum of the Fano feature in LDOS, it drops significantly. This is due to destructive interference between field coupled directly from emitter to antenna, and field that travels via the cavity. This interference depolarizes the antenna, causing a drop in dipole radiation P_{r}. LDOS, however, remains finite at this frequency due to the contribution of the cavity mode, *i.e.* the χ_{H} term in Eq. (7.7). In other words, at the Fano dip, nearly all emission is transferred into the cavity decay channel, which is not collected by the objective, causing a dip in collection efficiency. This phenomenon was also observed recently in theoretical work on a different hybrid system [109]. In general, the dip in η_{C} causes a difference in lineshape between LDOS and LDOSC. However, if antenna losses dominate the hybrid linewidth, lineshapes are far broader than the dip in η_{C}, such that LDOSC lineshape remains mostly unaffected, except for a decrease of the minimum at the Fano dip. This explains why LDOSC and LDOS are similar for the long antenna, whereas for the short antenna, where antenna losses are lower, this is only the case if Q is high.

We have shown that in general, emission spectra of broadband emitters coupled to a narrowband LDOS resonance follow the spectral shape of the collected LDOS. However, our results suggest that these lineshapes can, under the right circumstances, be nearly equivalent to the lineshapes in LDOS. Let us therefore compare the lineshapes expected from our theoretical model to those measured in the hybrid systems. Fig. 7.5 shows this comparison for the linewidth, Fano phase and hybrid boost factor. Data is compared to theory values obtained from LDOS and from LDOSC, where we assumed $Q = 3 \cdot 10^4$ following the simulation result. For linewidth, LDOS and LDOSC give the same prediction, which corresponds very well to the trend in the data. This linewidth is just the hybrid linewidth also studied in Chapter 6, *i.e.* the cavity linewidth broadened according to the Bethe-Schwinger perturbation formulas Eqs. (2.28) and (2.29). Predictions of Fano phase θ and hybrid boost from LDOS and LDOSC differ for the smallest antennas, since there antenna losses are not very dominant. For θ, the difference is small and data agrees reasonably well with both curves. For the hybrid boost, however, we find overall good agreement of the data to the predictions from LDOSC, which is markedly different from that by LDOS at small antennas. A few datapoints,

however, show much higher boosts, lying closer to the prediction from LDOS. Since we would not expect our cavities to have quality factors higher than the theoretical limit set by bending losses, this likely indicates that for these hybrids, part of the cavity radiation is collected by the objective. Our calculation of LDOSC assumes no cavity radiation is collected, yet in reality we do collect a finite fraction, as we have seen in the taper-coupled measurements in Chapter 6 (see for example Fig. 6.3f). For the smallest antennas the majority of fluorescence is emitted as cavity radiation, so collecting just a small fraction of it can make a large difference to collection efficiency, causing LDOSC to be closer to LDOS in lineshape. This could explain why these hybrid modes show such high boosts, close to the boosts in LDOS. Finally, Fig. 7.5 also shows curves obtained directly from finite element simulations of the complete hybrid system, similar to those discussed in Section 3.5, where we take aluminium antennas rather than gold ellipsoids and place the constant current source again 5 nm from the antenna apex and the substrate. We see that resulting LDOS lineshapes show excellent agreement with those from our coupled-oscillator model, confirming again the validity of our analysis.

These results show that LDOSC can be significantly boosted in a hybrid system, with respect to a bare antenna. Owing to the geometry of our sample, in which cavity radiation is very poorly collected, the measured boosts in LDOSC are always lower than boosts in LDOS. Therefore, we may interpret these boosts as a lower bound on the LDOS boosts experienced by the emitters in a hybrid system. This indicates the great potential of hybrid systems for emission control: at hybrid resonances far detuned from an antenna resonance, LDOS is boosted by more than an order of magnitude with respect to the antenna. Tuning closer to antenna resonance allows increasing the bandwidth of operation. Hybrid boost decreases, but since antenna LDOS increases simultaneously, overal LDOS should remain similar.

7.4 LDOS enhancements measured from quantum dot decay rates

Fluorescence decay curves were measured for each hybrid system. Additionally, for comparison we measured decay curves of 5 different individual QDs, dilutely dispersed on a glass substrate, as well as a decay curve of a QD ensemble attached to a large Al pad of 30 nm thickness. During the hybrid measurements, both pump and detection polarizers are aligned to the antenna long axis. Fig. 7.7g-h,j-k show two examples of fluorescent decay traces measured in hybrid systems. We can see that fluorescence decays significantly faster than for a bare QD on glass, which is shown in Fig. 7.7a,b. Within the first 3 ns, signal has decayed by approximately two orders of magnitude. Beside this rapid decay, a slow component similar to that of the QD on glass appears present as well.

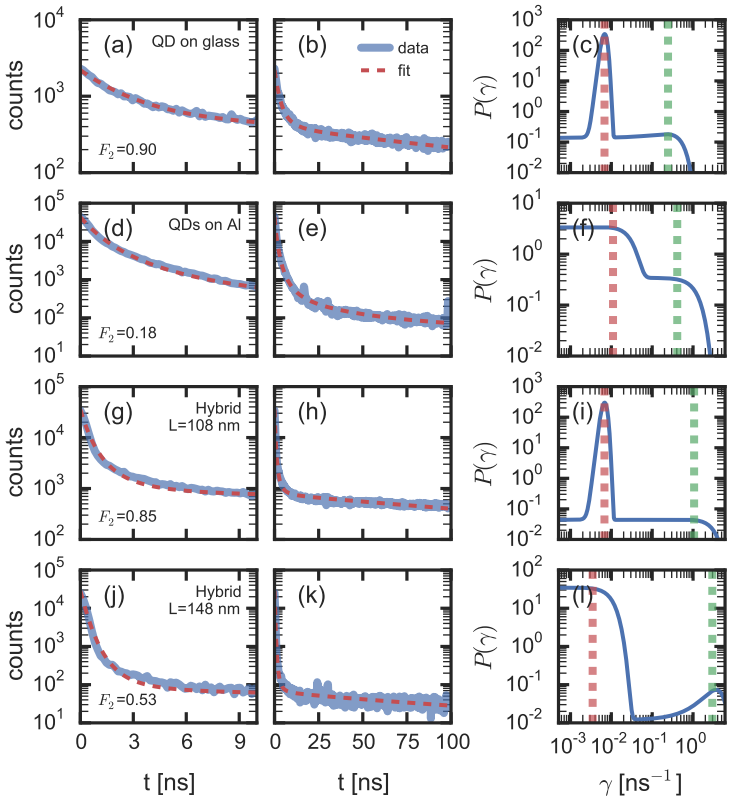

Figure 7.7: Fluorescence decay in hybrid systems. Fluorescence decay curves, showing just the first 10 ns or the full 100 ns, as well as fitted decay rate distributions $P(\gamma)$. We show data for a single QD on glass **(a-c)**, an ensemble of QDs on a large Al pad **(d-f)**, and for two hybrid systems with antenna lengths L of 108 nm **(g-i)** and 148 nm **(j-l)**. Data (blue line) is fitted (red dashed line) with a bimodal distribution of decay rates. Fractions of light in the slow decay rates F_2 are indicated. In the rightmost panels, the dashed green (red) lines indicate the expectation values $\langle\gamma_1\rangle$ ($\langle\gamma_2\rangle$) of decay rate in the fast (slow) modes of the distributions. Note that, although these distributions may have finite amplitude outside the range of rates shown here, those rates are not taken into account when calculating decay curves, due to the finite integration bounds γ_{min} and γ_{max}.

To extract decay rates and relative weights of the slow and fast components, we fit the data with a bimodal distribution of decay rates. Since the signal comes from more than a single QD, a bi-exponential decay is not suited for the hybrid data. A practical solution that is frequently employed for analysing decay curves of emitter ensembles, is to use a distribution of decay rates

[290, 291]. The decay curve $f(t)$ is then described by

$$f(t) = \int_0^\infty P(\gamma)\gamma e^{-\gamma t} d\gamma, \tag{7.8}$$

with $P(\gamma)$ the decay rate distribution. With respect to the conventional description [290], we added the extra factor γ in the integrand. Provided that $P(\gamma)$ is normalized such that $\int_0^\infty P(\gamma)d\gamma = 1$, this ensures that $f(t)$ obeys $\int_0^\infty f(t)dt = 1$. Therefore, the weight of a particular rate in $P(\gamma)$ can be interpreted as the contribution of that rate to the integral of the decay trace, *i.e.* the total signal. In practice, we do not let the integral in Eq. (7.8) run from 0 to ∞ but use realistic integration bounds γ_{min} and γ_{max}, given respectively by the inverse of 20 times our measurement time window (100 ns) and by $1/\Delta t$, where Δt is the time resolution of our timing card (0.16 ns).

Part of our signal will likely come from emitters positioned very close to the antenna apex, yet there is also a contribution from emitters positioned further from the apex. The emitters near the apex should experience large LDOS, being in the antenna hotspot, while the emitters that are not attached to the apex will experience significantly lower LDOS. Remember that, although LDOS at the hybrid mode peaks may be high, what counts for the observed decay rate γ is the spectrally averaged LDOS as given in Eq. (7.6). We thus expect γ to be determined mostly by the bare antenna, which offers broadband LDOS enhancement, and not by the hybrid modes. The contribution of both fast and slow emitters to the decay curve, as well as the bi-exponential decay observed for individual QDs, rationalizes a fit using a bimodal decay rated distribution

$$P(\gamma) = \frac{(1-A_2)}{\sigma_1\sqrt{2\pi}}\exp\left[\frac{(\gamma-\mu_1)^2}{2\sigma_1^2}\right] + \frac{A_2}{\sigma_2\sqrt{2\pi}}\exp\left[\frac{(\gamma-\mu_2)^2}{2\sigma_2^2}\right], \tag{7.9}$$

where μ_1 and μ_2 are the peak lifetimes in respectively the first and second mode, σ_1 and σ_2 are their respective variances and A_2 is the weight of the second mode to the total distribution. From the fitted distributions, we calculate expectation values $\langle\gamma_1\rangle$ and $\langle\gamma_2\rangle$ for decay rates in the first and second mode, respectively, as $\langle\gamma_1\rangle = \int_{\gamma_{\text{min}}}^{\gamma_{\text{max}}} \gamma\, P_{(A_2=0)}(\gamma)\, d\gamma$ and similarly for $\langle\gamma_2\rangle$. Moreover, we calculate fractions F_1 and F_2 of the detected light coming from mode 1 and mode 2 as the integrated area under the respective modes, relative to the total area under $P(\gamma)$. Note that if the modes are sufficiently narrow and centered far from γ_{min} and γ_{max}, we simply obtain $\langle\gamma_1\rangle = \mu_1$, $\langle\gamma_2\rangle = \mu_2$, $F_1 = 1 - A_2$ and $F_2 = A_2$. From here on, we choose $\mu_1 > \mu_2$ and refer to the first and second mode as the fast and slow decay rate modes. Note that we do not claim that the underlying distributions are perfectly described by a bimodal distribution. However, this serves as a parametrization of the results and allows a comparison between measurements.

Fig. 7.7g-l show exemplary fits to the decay curves of the hybrid systems using the bimodal decay rate distribution, as well as the fitted decay rate

distributions $P(\gamma)$. The same fit is performed on measurements of a single QD on glass and of a QD ensemble on a large Al patch, with results shown in Fig. 7.7a-c and d-f, respectively. ‡ The model fits the data well. The accelerated decay observed in the hybrid data is visible in the decay rate distribution as an increase of the $\langle\gamma_1\rangle$. We also observe a decrease of F_2 compared to the bare QD, indicating that more light is coming from the rapid decays. One could argue that the accelerated decay rates in the hybrid systems arise simply from nonradiative quenching, as the QDs are placed very close to a metal. However, a comparison with QDs on a large Al patch shows that these QDs do not have fast decay rates as high as those on the hybrids. In fact, $\langle\gamma_1\rangle$ is comparable to that in QDs on glass.

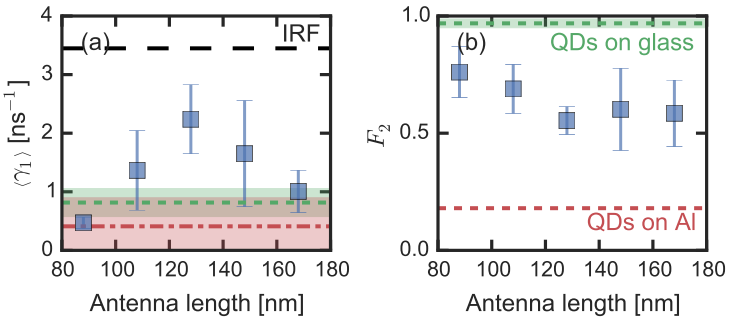

Figure 7.8: Fitted decay rates γ and slow decay fractions F_2. (a) Fast-mode decay rate expectation values $\langle\gamma_1\rangle$ obtained from fits on hybrid systems, as function of antenna length. We compare values for the hybrids (blue markers) to the value for a individual QDs on glass (green dashed line), and for QDs on an Al substrate (red dashed line). The $1/e$ time of the instrument response function (IRF) is indicated by the black dashed line. **(b)** Fractions of light in the slow decay rates F_2. Again, hybrid data is compared to QDs on glass (green) and QDs on Al (red). In both (a) and (b), error bars and shaded areas indicate standard deviations or, for QDs on Al in panel (a), the width of the lifetime distribution.

Fig. 7.8 shows $\langle\gamma_1\rangle$ and F_2 for all the hybrid systems, as function of antenna length. We observe a clear trend of decay rate peaking around an antenna length of 128 nm at 2.2(6) ns^{-1}, approximately 2.8 times faster than for QDs on glass (0.8(0.5) ns^{-1}). Moreover, the lower values of F_2 in the hybrid systems as compared to the QDs on glass indicate that more light is coming from the fast decays in these systems. Whereas a QD on glass emits 97(4)% of its light with a slow decay rate (associated to the bright state, see Section 5.5), in the hybrids this fraction starts at 76(11)% for the lowest antennas and drops to 55(6)% for antennas of 128 nm length. These trends show that there is a

‡In (e) and (k), small peaks are visible around 30 ns, which are attributed to APD afterpulsing. To ensure that they do not influence the fit, we disregard the 10-ns time window around 30 ns containing most of the peaks during the fit procedure.

decay rate enhancement in these hybrids. This enhancement is likely to be an effect of the bare antenna rather than fluorescence quenching, for two reasons. Firstly, decay rates peak when the antenna length is tuned approximately to resonance with the QDs, and are significantly higher than for QDs on an Al patch. If quenching would be dominant, we would expect these rates to be roughly equal. Secondly, if the fast decay component in the hybrid systems would come from strongly quenched quantum dots, we should expect only a small contribution of these decays in $P(\gamma)$. Instead, this contribution is much larger in the hybrids than in the bare QDs. Whether to assign the enhanced values of $\langle\gamma_1\rangle$ to an acceleration of the bright or dark state lifetime is unclear. The fact that F_2 is lower than for the QDs on glass, suggests that at least part of the fast decay mode can be attributed to quantum dots in the bright state. However, we cannot be sure, as we do not know if, for example, the presence of the Al has affected the QD blinking statistics. For this, experiments on hybrids containing only a single QD per antenna would be required. In that case, one can use only the counts from the bright state in a decay trace, which has been shown to yield a single exponential [242, 246]. This would allow an unambiguous retrieval of bright state lifetime. Combining this information with the hybrid boosts measured on the QD spectra, one could then determine a lower boundary for the LDOS at the hybrid peak. Finally, we note that no significant difference was found between $\langle\gamma_2\rangle$ on the hybrids and the QDs on glass. In all cases, $\langle\gamma_2\rangle \approx 0.008$ ns^{-1}. On the hybrids, this can be understood as the contribution of QDs that are too far from the antenna to experience significant LDOS.

7.5 Conclusions and outlook

We have fabricated antenna-cavity hybrids dressed with fluorescent quantum dots positioned at the antenna hotspots. Quantum dot fluorescence spectra and fluorescence decay curves were measured. Spectra showed Fano-type resonances, which we associated to the hybridized whispering-gallery modes of the cavity. We showed that in systems of broadband emitters coupled to narrowband LDOS resonances, fluorescence spectra take on the spectral shape of the collected LDOS (LDOSC). This was supported by the fact that measured Fano linewidth and lineshape were found to vary with antenna length, in good agreement with theoretical values for LDOSC resonances. Furthermore, we observed strong fluorescence boosts at the peaks of hybrid modes, which indicates a strong enhancement of LDOSC in the hybrid system with respect to the bare antenna alone. These hybrid boosts grow with decreasing antenna length, up to a maximum of $\sim$14 for the shortest antennas, in good agreement with the prediction from LDOSC. These boosts provide a lower bound on LDOS boosts experienced by the emitters in a hybrid system. Our results demonstrate the symbiotic behaviour in antenna-cavity hybrids. For cavities

red-detuned from the antenna resonance, LDOS can be significantly enhanced with respect to that of the antenna alone.

Fluorescence decay measurements showed a strong decay rate enhancement in hybrid systems, as compared to quantum dots on glass. We ascribe this enhancement to an effect mainly of the antenna alone, since the hybrid modes offer only LDOS enhancements over a small fraction of the emitter linewidth. Decay rates peaked when antennas were near resonance with the quantum dots, a strong indication of antenna effects.

These results constitute the first experimental observation of tunable Fano-type lineshapes and strongly enhanced LDOS for single-photon emitters in hybrid antenna-cavity systems. Earlier works have observed fluorescence in hybrid systems [97, 110], though not from single-photon emitters. Moreover, emitters were never placed at the antenna hotspot, thus not making optimal use of the confinement provided by antenna, while still suffering from the losses it induces. In this work, instead, emitters benefit optimally from the antenna confinement, being right at the antenna hotspot.

In future experiments, we propose to use hybrids containing a single quantum dot per antenna, which is feasible using the fabrication techniques employed in this work. This would allow the unambiguous retrieval of LDOS from the bright state lifetime. Combined with the hybrid boosts measured from the quantum dot spectra, one could then determine a lower boundary for the LDOS at the hybrid peak. Moreover, employing emitters with emission bandwidths below the hybrid linewidths, possibly at cryogenic temperatures, would allow a direct measurement of LDOS through the emitter lifetime. This would also open up the possibility of bringing hybrid systems towards the strong coupling regime, which was suggested to be theoretically feasible in a different antenna-cavity geometry [109].

Appendices

7.A Spectrum and decay rate of a spectrally diffusing emitter

Here we derive the emission spectrum and decay rate of a spectrally diffusing emitter in a structured photonic environment. We emphasize that our derivation is fully classical. Quantum-mechanical models of emitters with dephasing coupled to a single optical cavity mode can be found for example in [292–294].

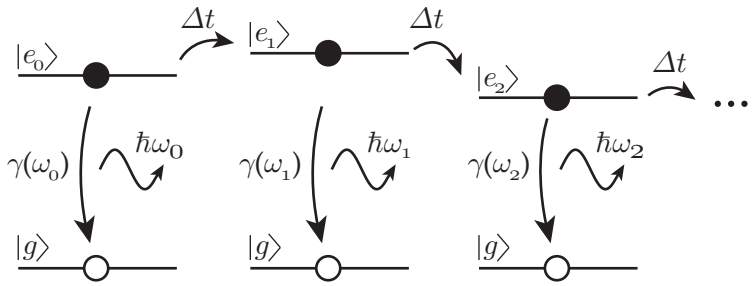

Figure 7.9: Sketch of an emitter showing spectral diffusion. After every time Δt it hops to a new excited state $|e\rangle$. In each state, it has a probability of decaying to the groundstate $|g\rangle$, emitting a photon at energy $\hbar\omega$.

Consider a system as depicted in Fig. 7.9. An emitter is prepared at $t = 0$ in the excited state $|\mathrm{e}_0\rangle$. It can make the transition to a ground state $|\mathrm{g}\rangle$, at energy difference $\hbar\omega_0$, emitting a photon of frequency ω_0. Suppose the emitter wanders around with a characteristic time scale Δt, hopping to a new state $|\mathrm{e}\rangle$. Assuming temporally uncorrelated hopping probability, it has a spectrum of new states to choose from at each hopping event, governed by the spectral probability density $p(\omega)$ of hopping to a state with energy $\hbar\omega$ relative to $|\mathrm{g}\rangle$, which is normalized such that $\int_\omega p(\omega)d\omega = 1$ [§]. We could interpret $p(\omega)$ as the intrinsic emission spectrum of the emitter (*i.e.* its spectrum if it were in an environment with frequency-independent photonic density of states), when measured on timescales much longer than the hopping time Δt.

[§]Note that we might as well have chosen to describe the system as hopping between available groundstates $|g_j\rangle$. Although this seems like a less physical scenario, for the analysis this choice is irrelevant.

7.A.1 Emission spectrum

One may now ask: what is the chance that an emitter decays with transmission frequency ω_e precisely after N jumps. Suppose that we first examine a *specific* trajectory that does this - and that previously visited the specific list of frequencies $\omega_1, \omega_2, \ldots \omega_{N-1}$. Suppose also that the probability to survive a time span Δt at a frequency ω_i is written as s_{ω_i}. Our specifically chosen trajectory first needs that you survive the first $N-1$ jumps, and then precisely in the Nth bin, you require decay. The likelihood of this particular trajectory is

$$\mathcal{P}^{N,\omega_e}_{\omega_1,\omega_2,\ldots} = \left(\prod_{i=1}^{N-1} p(\omega_i) s_{\omega_i} \right) p(\omega_e)(1 - s_{\omega_e}). \tag{7.10}$$

Now note that the likelihood to *somehow* end up decaying at ω_e precisely after N jumps is obtained by summing over all possible trajectories. Assuming that the draws from time bin to time bin are uncorrelated, this means that

$$\mathcal{P}^{N,\omega_e} = \left[\iint \ldots \int \left(\prod_{i=1}^{N-1} p(\omega_i) s_{\omega_i} \right) d\omega_1 d\omega_2 \ldots d\omega_{N-1} \right] p(\omega_e)(1 - s_{\omega_e}). \tag{7.11}$$

simplifies to

$$\mathcal{P}^{N,\omega_e} = \langle s \rangle^{N-1} p(\omega_e)(1 - s_{\omega_e}). \tag{7.12}$$

Here we introduced the spectrally averaged survival probability

$$\langle s \rangle = \int p(\omega_i) s_{\omega_i} d\omega. \tag{7.13}$$

For instance, suppose Δt is much smaller than any γ in the system, then we can take [11]

$$s_\omega = 1 - \gamma(\omega)\Delta t \quad \text{and} \quad \langle s \rangle = 1 - \langle \gamma(\omega) \rangle \Delta t \tag{7.14}$$

with $\langle \cdot \rangle$ the spectral averaging. Alternatively, if Δt is not taken short, we have to assume single exponential decay, with a rate dependent on the frequency bin, and find instead

$$s_\omega = e^{-\gamma(\omega)\Delta t} \quad \text{and} \quad \langle s \rangle = \langle e^{-\gamma(\omega)\Delta t} \rangle. \tag{7.15}$$

From Fermi's golden rule we know that $\gamma(\omega)$ is proportional to the optical local density of states (LDOS) [11].

Now, the probability to finally end up with a decay favouring a particular color ω_e after any number of steps, is obtained from

$$\mathcal{P}(\omega_e) = \sum_{N=1}^{\infty} \mathcal{P}^{N,\omega_e} = \left[\sum_{N=1}^{\infty} \langle s \rangle^{N-1} \right] p(\omega_e)(1 - s_{\omega_e}) = \frac{p(\omega_e)(1 - s_{\omega_e})}{1 - \langle s \rangle} \tag{7.16}$$

It is easily verified that this expression is properly normalized, that is, $\int_{\omega_e} \mathcal{P}(\omega_e) d\omega_e = 1$. Note that here the quantity s strictly relates to *total* decay rates, and $\mathcal{P}(\omega_e)$ relates to the chance to decay, not necessarily that this results in a photon. To this end we introduce the frequency resolved instantaneous quantum efficiency $\eta(\omega)$ as [66]

$$\eta(\omega) = \eta_{\mathrm{C}}(\omega) \frac{\gamma_{\mathrm{r}}(\omega)}{\gamma(\omega)} = \eta_{\mathrm{C}}(\omega) \frac{\gamma_{0,\mathrm{r}} \,\mathrm{LDOS}(\omega)}{\gamma_{0,\mathrm{nr}} + \gamma_{0,\mathrm{r}} \,\mathrm{LDOS}(\omega)}, \tag{7.17}$$

with $\eta_{\mathrm{C}}(\omega)$ the frequency-dependent collection efficiency and $\gamma_{0,\mathrm{r}}$ and $\gamma_{0,\mathrm{nr}}$ the intrinsic radiative and non-radiative decay rates of the emitter. Material absorption and finite numerical aperture are captured in $\eta_{\mathrm{C}}(\omega)$, whereas intrinsic emitter losses are captured in $\gamma_{0,\mathrm{nr}}$. The expected photon count rate per emitter excitation is then

$$\mathcal{C}(\omega_e) = \frac{p(\omega_e)(1 - s_{\omega_e})}{1 - \langle s \rangle} \eta(\omega_e). \tag{7.18}$$

You can now expand this as

$$\mathcal{C}(\omega_e) = \frac{1 - e^{-\gamma(\omega_e)\Delta t}}{1 - \langle e^{-\gamma(\omega)\Delta t} \rangle} p(\omega_e) \eta(\omega_e). \tag{7.19}$$

The photon count rate traces the product of the intrinsic emitter spectrum and the spectrally resolved quantum efficiency times a factor dependent on Δt. If Δt is large (slow diffusion), one finds a ratio unity, *i.e.* the spectrum does not trace LDOS variation (unless through $\eta(\omega_e)$, which is proportional to LDOS only if $\gamma_{0,\mathrm{nr}} \gg \gamma_{0,\mathrm{r}}$). In contrast, for Δt very small, one can use $1 - e^{-x} \approx x$, and interchange Taylor expansion and averaging to obtain

$$\mathcal{C}(\omega_e) \approx \frac{\gamma(\omega_e)}{\langle \gamma(\omega) \rangle} p(\omega_e) \eta(\omega). \tag{7.20}$$

Now the spectrum traces the ratio of *total* LDOS to the spectrally averaged total LDOS.

7.A.2 Decay rate

The emitter decay curve $f(t)$ is described by the probability that the emitter survives $N-1$ hopping events and then decays precisely after N jumps, where $N = t/\Delta t$. Analogous to Eq. (7.10), the likelihood of a particular trajectory is

$$\mathcal{P}^N_{\omega_1, \omega_2, \ldots} = \left(\prod_{i=1}^{N-1} p(\omega_i) s_{\omega_i} \right) p(\omega_N)(1 - s_{\omega_N}), \tag{7.21}$$

and consequently the likelihood of somehow decaying precisely after N jumps, *i.e.* $f(t)$, is

$$f(t) = \mathcal{P}^N = \langle s \rangle^{N-1} \langle 1 - s \rangle. \tag{7.22}$$

If we assume again that Δt is much shorter than any γ in the system, we obtain

$$f(t) = [\,1 - \langle\gamma(\omega)\rangle\Delta t\,]^{N-1}\,\langle\gamma(\omega)\rangle\Delta t. \tag{7.23}$$

It is readily verified that this is properly normalized, such that $\sum_{N=0}^{\infty} f(t) = 1$. If Δt is short,

$$f(t) \approx e^{-\langle\gamma(\omega)\rangle t}\langle\gamma(\omega)\rangle\Delta t, \tag{7.24}$$

where we used $N\Delta t = t$ and the power series expression for an exponential. This shows that the emitter exponentially decays with a decay rate given by the spectral average of $\gamma(\omega)$.

Chapter 8

Controlling nanoantenna polarizability through back-action via a single cavity mode

The polarizability α determines the absorption, extinction and scattering by small particles. Beyond being purely set by scatterer size and material, polarizability can also be affected by back-action: the influence of the photonic environment on the scatterer. As such, controlling the strength of back-action provides a tool to tailor the (radiative) properties of nanoparticles. Here, we control the back-action between broadband scatterers and a single mode of a high-quality cavity. We demonstrate that back-action from a microtoroid ring resonator significantly alters the polarizability of an array of nano-rods: the polarizability is renormalized as fields scattered from — and returning to — the nano-rods via the ring resonator depolarize the rods. Moreover, we show that it is possible to control the strength of the back-action by exploiting the diffractive properties of the array. This perturbation of a strong scatterer by a nearby cavity has important implications for hybrid plasmonic-photonic resonators and the understanding of coupled optical resonators in general.

8.1 Introduction

The scattering, absorption and extinction cross-section of small scatterers is often attributed to the dielectric properties of the particle, *i.e.,* the scatterer's volume, shape and its refractive index with respect to the host medium [119]. Central to this argument, for scatterers with a physical size much smaller than the wavelength, is the so-called *polarizability*, which contains the frequency-dependent susceptibility that quantifies the strength of the dipole moment induced in the scatterer by an incident field. A rather subtle notion is that the polarizability also depends on the mode structure offered by the photonic environment (Fig. 8.1). To illustrate this, consider that extinction, *i.e.*, the total power that a scatterer extracts from an incident beam [119] is directly proportional to the imaginary part of polarizability. According to the optical theorem [120], this power is distributed over Ohmic heating and scattering, with the contribution of scattering being proportional to the squared magnitude of polarizability and the local density of states (LDOS) [12]. The fact that LDOS, *i.e.*, the number of available photonic modes for the scatterer to radiate into, enters the polarizability is known as back-action: a correction on the total field that drives a polarizable scatterer. This correction is neglected in standard (Rayleigh) scattering theory [119]. However, even for a single scatterer placed in free-space, back-action leads to additional damping (depolarization) and thus needs to be integrated in a self-consistent description of any system [120, 158]. For a scatterer coupled to a cavity mode, this back-action can lead to a strong modification of the polarizability near the cavity resonance, as discussed in Section 2.4.2. Although back-action effects on quantum emitters [19] have been routinely studied, very few studies exist that probe back-action on plasmonic scatterers. First, Buchler *et al.* [136] revealed that the spectral width of a nanoantenna's plasmon resonance can be modulated when the antenna approaches a reflector, whereas more recently Heylman *et al.* [137] demonstrated that the absorption cross-section of a single nanoantenna can be modified via coupling to a microtoroid cavity. It was

Figure 8.1: Cavity-induced modification of antenna polarizability (a) A single polarizable scatterer, probed in a transmission experiment. **(b)** A simple Fabry-Pérot cavity modifies the local density of states and alters the scattering properties of a plasmonic scatterer. **(c)** A spectrally narrow cavity mode can suppress the imaginary part of the polarizability α of a plasmonic scatterer.

also shown by Zhang et al. [295] that, under specific driving conditions, coupling of a single *molecule* to an antenna can lead to similar modification of the antenna response, which demonstrates the generality of this phenomenon. While back-action on a single antenna is perhaps the most intuitive example to study, one is not limited to a *single* antenna or resonator to observe back-action. For any resonating system that is coupled to a bath of modes, the properties of this bath will influence the susceptibility (polarizability) of the resonating system. Crucially, this change in susceptibility carries information on the properties of the bath, and a measurement of the modified susceptibility thus provides a non-invasive method to obtain information on the bath. It has been proposed [118] that if the bath is represented by the single mode of a cavity, the modified susceptibility would, in principle, allow access to the Purcell factor [14] of the cavity mode.

Here we experimentally investigate back-action on polarizability in a hybrid antenna-cavity system, demonstrating a strongly modified extinction response of an array of gold nano-rods due to back-action imparted by a single whispering-gallery mode (WGM) of a microtoroid ring resonator. At conditions where the cavity offers a high mode density for the scatterers to radiate into, the nano-rods' susceptibility to an incoming field is suppressed: the cavity mode density thus effectively depolarizes the nano-rods (Fig. 8.1c), yielding an experimental signature that relates to electromagnetically induced transparency [296]. A unique feature of the array, as our experiments reveal, is that it is possible to control the strength of the measured back-action by careful tuning of a diffraction order of the array, phase-matching its wavevector with the WGM of the cavity. Using a coupled-oscillator model we retrieve an antenna-cavity cooperativity and provide a lower bound on the cavity Purcell factor [14] at the lattice origin. Our results have strong relevance in the context of recent proposals on hybrid plasmonic-photonic resonators [100, 105, 109, 110, 112, 113, 118, 297, 298] as a unique venue for huge Purcell factors [14] and quantum strong coupling with single emitters. While the most intuitive consideration for such a proposal is to assess how scatterers perturb cavity resonances [130], in fact, this work shows that one rather has to ask what opportunities the cavity offers to control antenna polarizability.

8.2 Experimental methods

An ideal experiment to probe cavity-induced back-action would directly measure the complex-valued polarizability α in presence and absence of the cavity. This is not a trivial task: polarizability is not a directly measurable quantity in optics. Instead one has to rely on far-field measurements of extinction and scattering cross sections to deduce $\mathrm{Im}[\alpha]$ and $|\alpha|^2$ respectively. Such quantitative polarizability measurements are challenging even for scatterers in an uniform environment [299, 300]. The proximity of the cavity further compli-

cates the task of strictly probing the scatterers only. Practically, this means that direct excitation of the cavity mode by the incident beam, as well as radiation from the cavity directly into the detection channel, should be prevented, as both would contaminate the interrogation of the scatterer's response. We approach these constraints by a combination of experimental techniques. First, we use a WGM resonator that only allows in- and outcoupling of light under select wavevector matching conditions. Second, we use an array of antennas, as opposed to a single antenna, to obtain a strong extinction-like signal that can be probed in specular reflection with a nearly collimated plane wave, again using wavevector conservation to separate the extinction channel from all other scattering channels. Crucially, we demonstrate that the use of an array allows tailoring of the coupling strength between cavity and array via wavevector matching, controlled by the angle of incidence. Note that our choice for an array results in a measurement probing back-action on the *lattice* polarizability [134].

8.2.1 Sample fabrication

We study reflection from an array of gold nano-antennas, coupled to a whispering-gallery mode in a silica microtoroid. A high Q silica microtoroid (diameter $\approx 36\,\mu\mathrm{m}$) is fabricated on the edge of a silicon sample (see Fig. 8.2a). For the fabrication protocol we largely followed methods that have been previously reported in for example [301, 302]. In this work, spin-coating (ma-N 2410) and subsequent cleaving of the sample enabled targeted e-beam lithography of the cavity on the edge of the sample. The toroid supports whispering-gallery modes (WGMs) of high quality factor Q, and for the remainder of this chapter we will focus on a fundamental TE-polarized mode (linewidth $\kappa/2\pi \approx 30$ MHz) at resonance frequency $\omega_c/2\pi \approx 194.4$ THz.

Gold nano-antennas are fabricated in an array (150 $\mu\mathrm{m}$ by 150 $\mu\mathrm{m}$) on a glass coverslide of 170 $\mu\mathrm{m}$ thickness. A positive resist (ZEP-520) layer of 130 nm thickness is spin-coated on the coverslide, and nanoantennas are defined using electron beam lithography. The antenna width and thickness

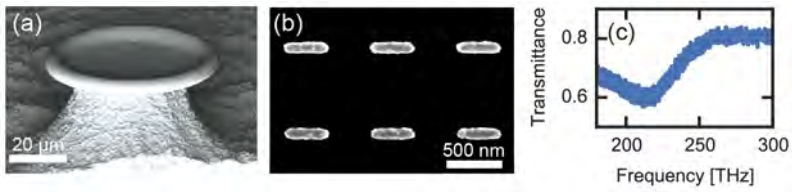

Figure 8.2: Silica microtoroid and gold nano-antennas. **(a)** SEM image of a silica microtoroid on a Si substrate. Note that the toroid in this work is smaller (30 $\mu\mathrm{m}$ diameter). **(b)** SEM image of the nano-antenna array. **(c)** Transmission measurement of the antenna array, showing a resonance at 208 THz.

were designed to be 120 and 40 nm and the length is approximately 400 nm (see Fig. 8.2b). The pitch along the short axes of the antennas is 1500 nm, with a pitch along the long axes of 800 nm. Gold is evaporated thermally at 0.05 nm/s. We characterize the spectral properties of the array in a transmission measurement (under normal incidence) using Fourier-Transform Infrared spectroscopy, obtaining a broadband resonant response at resonance frequency $\omega_{\mathrm{a}}/2\pi \approx 208$ THz and linewidth $\gamma/2\pi \approx 55$ THz (see Fig. 8.2c).

8.2.2 Measurement setup

Our experimental system is sketched in Fig. 8.3a. A more detailed diagram is shown in Fig. 8.3b. We perform narrowband spectroscopy by scanning the frequency of a tunable laser (New-Focus TLB-6728, 1520-1570 nm, <100 kHz linewidth). The antennas are illuminated through a high-NA objective (Nikon, CFI Apo TIRF 100x, NA ≈ 1.33, used with index-matching oil) with an incident field polarized (s-polarization) along the principal dipole axis of the rods, which themselves are oriented to match a high-Q TE-polarized mode of the microtoroid. Focusing the incoming laser beam onto the back-focal-plane (BFP) of the objective gives precise control over the angle of incidence of the drive field. The position of this focus, *i.e.* the angle of incidence, is controlled using a translation stage. For scatterers arranged in a periodic array, scattering takes the form of diffraction into well-defined angles (wavevectors, Fig. 8.3c). We discard the (-2) and (-1) diffraction orders propagating back into the substrate using Fourier-filtering such that our detector is only sensitive to the specular reflection signal. In addition we employ a real-space filter, selecting a circular area of $\sim 4.5\,\mu\mathrm{m}$ in diameter, to reduce background signals not originating from antennas coupled to the cavity. A tapered fiber is used to directly excite the cavity mode (in a separate experiment) and obtain information on the cavity mode profile and polarization of the cavity mode. We also use the fiber to check that, with the cavity positioned in front of the glass substrate away from the antenna array, we do not directly excite the cavity mode with the incident drive field (and associated wavevectors) used in our experiment. Cavity and tapered fiber position are controlled using 3-axis piezoelectric actuators.

To illustrate our experimental arrangement, Fig. 8.3d displays an overlay of Fourier-space data obtained by BFP imaging (without Fourier-filter) on an infra-red camera (Allied Vision Goldeye P008). We identify 1) the radiation profile of the two propagating cavity modes, obtained by direct excitation of the cavity using an evanescently coupled tapered fiber (color scale), and 2) the position of the three diffraction orders of the array (indicated by arrows). In the experiment, the incoming wavevector is chosen such ($k_y = 0$ and $k_{\parallel}/k_0 \approx 0.8$) that the (-2) diffraction order of the array (which is evanescent in air) overlaps with one of the propagating whispering-gallery

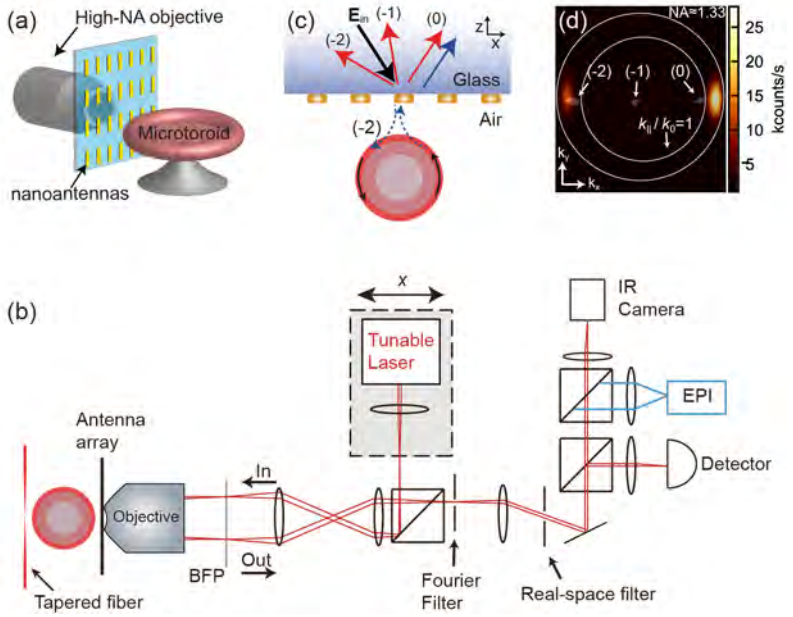

Figure 8.3: Experimental setup and measurement scheme. (a) Cartoon of the hybrid antenna-cavity system. **(b)** Experimental setup. The input laser is focused in the back focal plane (BFP) and can be moved to change the incoming angle at the sample. The reflection passes through a Fourier filter to select the specular reflection, and through a real-space filter to select only antennas close to the cavity. An infra-red incoherent source (EPI) is used in EPI-illumination for navigation and to determine the objective NA. **(c)** For some incoming field $\mathbf{E}_{\mathrm{in}}$, the (-2) diffraction order associated with the array evanescently couples to the toroid. back-action from the cavity on the array is measured in the specular reflection signal. **(d)** An overlay of Fourier-images obtained via back-focal-plane imaging. The transparent white blobs indicated by arrows are diffraction orders, with 0 indicating the specular reflection. The (-2) order overlaps with one of the cavity modes (indicated with the color scale). As such, we excite the cavity mode *via* the antenna-array. The inner and outer white circles indicate the edge of the light cone ($k_{||}/k_0 = 1$) and the objective NA, respectively. These were obtained from a reflection measurement where illuminate the BFP homogeneously using an incoherent source, and are slightly displaced due to a sample tilt. Cavity mode intensities are not equal because only one of the modes is excited directly by the taper.

modes in the microtoroid, allowing the incoming field to efficiently scatter to the cavity mode *via* the antennas. Our system thus allows for a proper back-action measurement: the antennas can couple to the cavity, yet the detected signal is exclusively a probe of antenna polarizability. Any change in detected signal upon approaching the cavity can thus be directly attributed to cavity-mediated back-action fields that renormalize the antennas response.

8.2.3 Measuring extinction

In the experiment we probe the antennas through zero-order reflectance at a small (around 30°) incident angle, where zero-order reflectance is a direct measure of extinction, *i.e.*, Im$[\alpha]$ [303]. Since extinction is usually associated to zero-order transmittance and not reflectance, this claim requires substantiation. To predict the lineshape in reflectance, we quote an expression from De Abajo [134] for the specular reflection signal r' that one expects from a particle array (with real-space lattice area A) in free space. The observed reflection depends on the self-consistent single particle polarizability α_{E}, corrected by the lattice-summed Green's function $G_{xx}(0)$, and reads *

$$r' = \frac{2\pi ik/A}{\alpha_{\mathrm{E}}^{-1} - G_{xx}(0)}, \tag{8.1}$$

where k is the wavenumber. In our case, the antennas lie on a glass-air interface which in itself is reflective. Introducing the lattice dressed polarizability $\alpha^{-1} \equiv \alpha_{\mathrm{E}}^{-1} - G_{xx}(0)$ and the background reflection r_{glass} of our interface (see [304] for an elaborate discussion on properties of plasmonic nanoantenna arrays on interfaces) we arrive at

$$r' = r_{\text{glass}} + \frac{2\pi ik\alpha}{A}. \tag{8.2}$$

Generally, the Fresnel coefficient r_{glass} is real valued. Using this notion one can continue to write the specular reflectance $|r'|^2$ as

$$|r'|^2 = r_{\text{glass}}^2 - r_{\text{glass}}\frac{4\pi k}{A}\mathrm{Im}[\alpha] + \frac{4\pi^2k^2}{A^2}|\alpha|^2, \tag{8.3}$$

which evidences that the imaginary part of the polarizability Im$[\alpha]$ leads to a reduction in specular reflectance, whereas the scattering term scaling with $|\alpha|^2$ results in an increased reflectance. Alternatively one can express Eq. (8.3) as a function of the extinction cross section $\sigma_{\text{ext}} = 4\pi k\mathrm{Im}[\alpha]$ and scattering cross section $\sigma_{\text{scat}} = \frac{8}{3}\pi k^4|\alpha|^2$, which gives

$$|r'|^2 = r_{\text{glass}}^2 - \frac{r_{\text{glass}}}{A}\sigma_{\text{ext}} + \frac{3}{2}\frac{\pi}{A^2k^2}\sigma_{\text{scat}}. \tag{8.4}$$

From this expression we learn that a reduction in reflectance, with respect to the background signal coming from the interface, can be associated with extinction. This conclusion is supported by calculations using a full electrodynamic model, discussed in Section 8.4.2. For a plasmon particle or array such a reduction occurs over a wide frequency range that is commensurate with its bandwidth (an example is shown in Fig. 8.4a). In addition, Eq. (8.4) shows

*Note that in [134] and in Eqs. (8.1) to (8.4), α is given in CGS units. To convert to SI units, α should be multiplied by $4\pi\epsilon$, with ϵ the permittivity in the host medium.

that dilute lattices, such as ours, result in a more pure extinction measurement than dense lattices, for which the scattering term contributes more strongly to the observed signal as a result of the larger proportionality factor $(A^2k^2)^{-1}$. In essence, destructive interference causes a reduction in reflectance, similar to the textbook scenario of extinction measurements that measure destructive interference between forward scattered light and the direct beam. In analogy to standard transmittance measurements probing extinction, we here define the extinction E as $E \equiv 1 - |r|^2$, with the normalized reflectance $|r|^2$ given by $|r|^2 \equiv |r'|^2/|r_{\mathrm{glass}}|^2$. The use of $|r|^2$ has the advantage that results obtained at different excitation angles (leading to different values of r_{glass}) are more easily compared. Moreover, the introduction of the variable E simplifies the interpretation of our experiment: a decrease in antenna-extinction (increasing $|r|^2$) is mapped to decreasing values for E. Inspired by the case of a single scatterer at resonance with a cavity discussed *e.g.* in Section 2.4.2, our prediction is that the polarizability will show a reduction over a narrow spectral region [118, 137] once the antennas are subject to back-action through the cavity mode, *i.e.*, once they are offered the additional possibility of radiation damping due to the Purcell factor associated with the cavity mode. This will then also appear as a minimum in E (see Fig. 8.4b).

8.3 Experimental results

8.3.1 Observation of cavity-mediated back-action

Figure 8.4c displays the response of the antenna array in absence (orange points) and presence (blue points) of the cavity for an incident beam with $k_{\parallel}/k_0 = 0.84$. The narrow frequency window displayed in Fig. 8.4c is close to the plasmon resonance, evident from the fact that E is close to unity, meaning that $|r|^2$ is close to zero. Comparing the trace without cavity and with the cavity approached to several microns distance away (antennas weakly couple to the cavity) shows a small back-action effect of the cavity on the array, visible as a $\sim 1\%$ dip in E. This dip is tantamount to a *reduction* in the extinction that the antennas cause when they are offered the cavity as an additional channel to radiate into. Expressed in polarizability, our measurement implies a decrease in $\mathrm{Im}[\alpha]$ due to back-action, occurring over a narrow bandwidth that is commensurate with the linewidth (∼30MHz) of the high-Q cavity mode. In Fig. 8.4c the cavity-array distance was several microns, limiting the back-action experienced by the antennas. Moving the cavity closer to the array results in much larger effects. For instance, Fig. 8.4d shows a $> 25\%$ change in polarizability when approaching the cavity to within approximately 1 micron (about 6.5 times the evanescent decay length of the squared mode field) from the antennas. This is direct evidence that the *magnitude* of polarizability can be substantially controlled by the photonic environment.

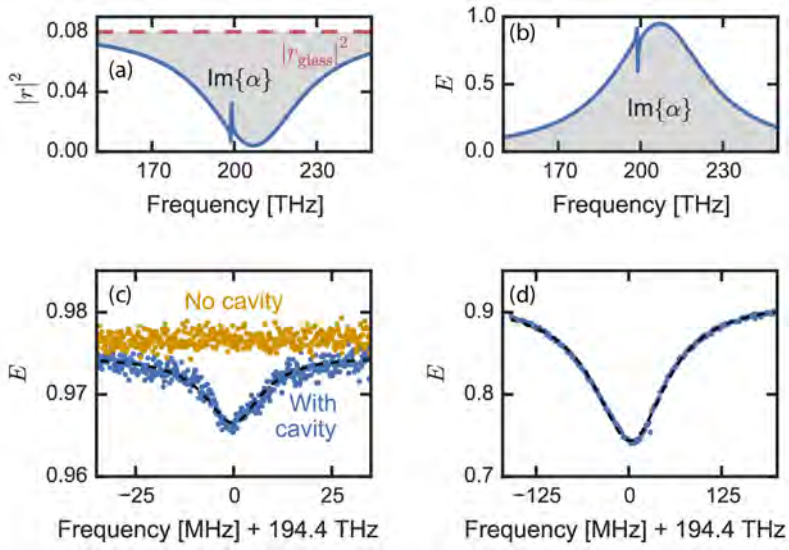

Figure 8.4: Cavity-induced back-action. **(a)** Sketch of a typical reflectance signal $|r'|^2$ as measured in the experiment. The plasmon feature introduces a broadband dip, with respect to the non-resonant $|r_{\text{glass}}|^2$ value. **(b)** Sketch of the extinction E, obtained from (a). We expect the cavity mode to reduce $\text{Im}\{\alpha\}$ (and thus E) in a narrow frequency band. **(c-d)** Experiment. **(c)** With the cavity present (blue points), the extinction E decreases by 1% at the cavity frequency, a feature that is absent without cavity (orange points). **(d)** At smaller cavity-array distance the dip increases to 25%, indicating a strong suppression of antenna extinction. The cavity linewidth increases compared to (c) as a result of increased cavity losses.

8.3.2 Tuning back-action strength through phase matching

While our experiment probes several antennas, it was previously realized that for single antennas the polarizability modification must be directly linked to the cavity Purcell factor at the location of the antenna [118]. In other words, one viewpoint on our experiment is that it evidences that the polarizability of a nano-antenna is modified, which is mathematically expressed as $\alpha^{-1} = \alpha_0^{-1} - G$, with $\text{Im}[G]$ the LDOS and $\text{Re}[G]$ the Lamb shift [305] provided by the cavity mode. As such, an antenna is analogous to a quantum emitter in the sense that it probes the LDOS of the cavity. The effect of an LDOS peak, however, is distinctly different: the antenna emission is quenched on resonance rather than, as would be the case for an emitter, enhanced. The fact that in our experiment the mode density provided by the cavity results from a single Lorentzian mode offers an alternative viewpoint. In essence, the reduction of polarizability over the cavity bandwidth can be viewed as a 'transparency' feature in direct analogy to electromagnetically/plasmon/optomechanically induced transparency [296, 306–309]. In these systems, a broad resonator

(here: plasmonic scatterer) is rendered 'transparent' in its susceptibility to driving over a narrow frequency band due to coupling to a narrow resonator (here: WGM resonator), even though that narrow resonator is not directly driven. Beyond purely Lorentzian transparency dips, one can obtain Fano-type [310] lineshapes depending on the phase of the coupling constants that connect the broad and narrow resonance. Inspired by this analogy we explore the shape of the back-action feature by varying the angle of incidence of the incoming drive field. As shown in Fig. 8.5a, this effectively sweeps the (-2) diffraction order over the finite k-space width of the cavity mode, thus varying the degree to which the array and the cavity mode are coupled through phase-matching. From the resulting spectra (Fig. 8.5b) we qualitatively observe a dependence of the back-action strength and lineshape on the incoming angle, which is expressed as a varying depth and asymmetry of the cavity-induced dip. In line with the phase-matching argument, visual inspection of Fig. 8.5a and Fig. 8.5b shows that cavity-mediated back-action is most prominent when the cavity mode profile and the (-2) diffraction order of the array experience better overlap. In Section 8.4.2, this behavior is verified using analytical coupled dipole calculations.

The antenna-cavity cooperativity

Full quantification of the back-action is not straightforward, as it requires analysis of the Fano lineshapes. A detailed multiple scattering analysis particular for our system, which will be discussed in Section 8.4.2, shows that the plasmon antennas in our experiment are simultaneously subject to the resonant back-action of the cavity and a nonresonant back-action term from the interface on which the antennas are placed (glass-air) [12, 311]. The nonresonant back-action is governed by the complex Fresnel coefficient associated with the interface, which exhibits a phase change for the (evanescent) (-2) diffraction order upon sweeping $k_{\parallel}/k_0$. In our experiment we measure the scatterers' response in the presence of all back-action, which is a coherent sum of the broadband interface-induced back-action plus the resonant cavity-mediated back-action. Sweeping $k_{\parallel}$ thus directly affects the Fano lineshape that we observe. We develop a simple model based on coupled-mode theory [127] that can disentangle the resonant back-action from the nonresonant background. Treating the array and cavity as resonators, coupled at rate g, both described by a Lorentzian response with complex field amplitudes a and c, respectively, we solve the driven system

$$\begin{pmatrix} \Delta_{\mathrm{a}} + i\gamma/2 & g \\ g & \Delta_{\mathrm{c}} + i\kappa/2 \end{pmatrix} \begin{pmatrix} a \\ c \end{pmatrix} = \begin{pmatrix} i\sqrt{\gamma_{\mathrm{ex}}} s_{\mathrm{in}} \\ 0 \end{pmatrix} \tag{8.5}$$

for a. Here we defined $\Delta_{\mathrm{a}} \equiv \omega - \omega_{\mathrm{a}}$ and $\Delta_{\mathrm{c}} \equiv \omega - \omega_{\mathrm{c}}$, where ω is the frequency of the incident field s_{in} driving the array and γ_{ex} the rate at which the array and input/output channel are coupled. Antenna and cavity resonance

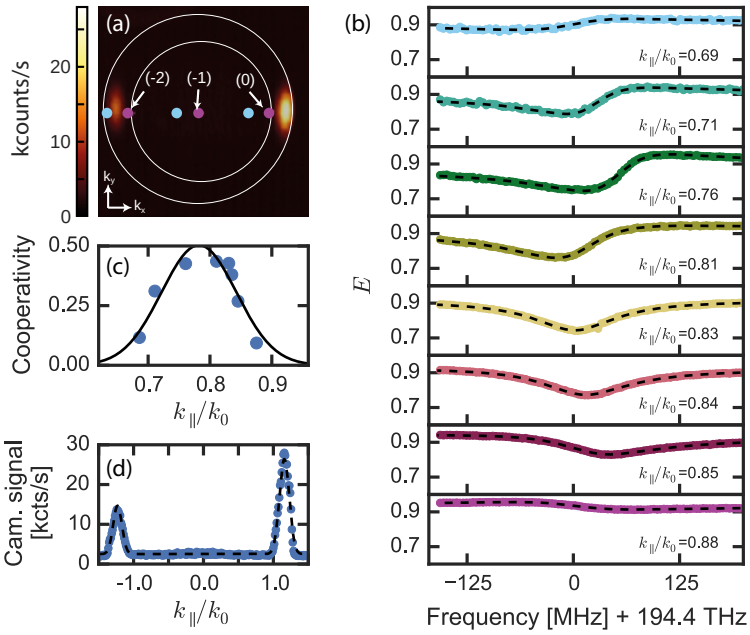

Figure 8.5: Tuning back-action through angle of incidence. (a) Fourier-image overlay that shows the position of the diffraction orders at the start (blue dot, $k_\parallel = 0.69\,k_0$) and stop (pink dot, $k_\parallel = 0.88\,k_0$) values of the $k_\parallel$ sweep displayed in panel (b). **(b)** The strength and lineshape of the back-action strongly depend on the incoming angle. The black dashed lines are fits using our coupled-mode model (Eq. (8.7)). **(c)** Values for the cooperativity obtained from fitting our coupled-mode model to the spectra in panel (b). Black line: fit with a Gaussian lineshape. **(d)** Horizontal cross-cut through the cavity radiation pattern shown in (a). A 2-Gaussian fit (dashed black line) yields cavity modes with peak position and width in good agreement with results from the cooperativity profile in (c).

frequencies are ω_a and ω_c, and their damping rates are γ and κ, respectively. Next, we use the input-output relation $s_\mathrm{out} = s_\mathrm{in} - \sqrt{\gamma_\mathrm{ex}}a$ [127] (such that $r = s_\mathrm{out}/s_\mathrm{in}$) and parametrize the coupling via the cooperativity $C = 4g^2/(\gamma\kappa)$, the determining quantity for the strength of the sharp spectral feature observed in electromagnetically/optomechanically induced transparency [23, 258]. We obtain

$$r = \frac{s_\mathrm{out}}{s_\mathrm{in}} = 1 - \frac{2i\gamma_\mathrm{ex}}{2\Delta_\mathrm{a} + i\gamma(1 + C\frac{\kappa/2}{-i\Delta_\mathrm{c}+\kappa/2})}. \tag{8.6}$$

Introducing an arbitrary phase pickup ϕ in the direct reflection channel (first term in Eq. (8.6)) and assuming $\omega \approx \omega_\mathrm{a}$, we find

$$|r|^2 = \left|\exp(i\phi) - \frac{2\eta}{1 + C\frac{\kappa/2}{-i(\Delta_\mathrm{c}-\Delta)+\kappa/2})}\right|^2, \tag{8.7}$$

where $\eta \equiv \gamma_{\mathrm{ex}}/\gamma$ and Δ is an additional small detuning that captures small fluctuations in ω_{c} due to *e.g.* thermal drift. We use Eq. (8.7) to fit our experimental data in Fig. 8.5b, yielding values for C as a function of $k_{\parallel}$ (Fig. 8.5c, blue points). A Gaussian lineshape (black line) is fit (center(width): $k_{\parallel}/k_0 \approx 0.78(0.14)$) to the blue data points, giving a maximum cooperativity of $C \approx 0.5$. Notably, the width and center of the Gaussian agree with expected values based on a fit to the cross-cut of the cavity mode profile (shown in Fig. 8.5d), which reveals modes with linewidths of $\sim 0.15k_0$. The cavity mode to which we couple via second order diffraction is centered at $k_{\parallel}/k_0 = -1.23$. Considering the incident free-space wavelength of 1540 nm and a pitch of 1500 nm, one would expect maximum coupling between the array and cavity (via the 2nd order diffraction) for an incident wavevector of $[-1.23 + 2 \times (1540/1500)] = 0.82k_0$, which matches with the experimentally observed incident wavevector $0.78k_0$ for which we observe our maximum in cooperativity.

The relation between cooperativity and Purcell factor

The cooperativity quantifies the degree of coupling between the array and the cavity. More than that, in the limit of a *single* scatterer and single cavity mode, it is directly equivalent to the product of the scatterer albedo (A) and the cavity Purcell factor (F, see Eq. (3.1)) at the location of the scatterer. This can be seen by rewriting our expression for the hybridized polarizability α_{H} in such a system (Eq. (2.36)), obtained from the coupled-oscillator model discussed in Chapter 2. If we make the assumption that we are close to both cavity and antenna resonance, such that $\omega_{\mathrm{a}}^2 - \omega^2 \approx 2\omega_{\mathrm{a}}\Delta_{\mathrm{a}}$ and $\omega_{\mathrm{c}}^2 - \omega^2 \approx 2\omega_{\mathrm{c}}\Delta_{\mathrm{c}}$, we find

$$\begin{aligned}\alpha_{\mathrm{H}} &\approx \frac{\beta/\omega_{\mathrm{a}}}{-2\Delta_{\mathrm{a}} - i\gamma_{\mathrm{i}} - i\gamma_{\mathrm{r}} - i\frac{\beta Q}{\epsilon_0 \epsilon V_{\mathrm{eff}}\omega_{\mathrm{a}}}\frac{\kappa/2}{-i\Delta_{\mathrm{c}}+\kappa/2}} \\ &= \frac{\beta/\omega_{\mathrm{a}}}{-2\Delta_{\mathrm{a}} - i\gamma\left(1 + AF\frac{\kappa/2}{-i\Delta_{\mathrm{c}}+\kappa/2}\right)},\end{aligned} \tag{8.8}$$

where β is antenna oscillator strength, V_{eff} cavity effective mode volume and $Q = \omega_{\mathrm{c}}/\kappa$. Furthermore, γ_{i} and γ_{r} are antenna Ohmic and radiative damping rates, respectively, with $\gamma = \gamma_{\mathrm{i}} + \gamma_{\mathrm{r}}$ and $A = \gamma_{\mathrm{r}}/\gamma$, and we used the expression $\gamma_{\mathrm{r}} = \beta\omega^2\sqrt{\epsilon}/(6\pi c^3\epsilon_0)$ for γ_{r} in a homogeneous medium (see Eq. (2.22)). Comparison of Eq. (8.8) with the resonant term in Eq. (8.6) shows that the cooperativity C is equal to the AF product in the case of a single scatterer.

In our experiment the cooperativity can not be directly cast into a Purcell factor, as we probe an array of antennas at specific wavevector, meaning that we probe a lattice-sum dressed polarizability [134] that experiences back-action from a wavevector-resolved mode density. We can, however, make an estimation of the Purcell factor by comparing our measurements to rigorous coupled dipole calculations which will be discussed in Section 8.4.1. This reveals that measured cooperativity of $C = 0.5$ actually corresponds to a value

of $C = 1.7$ as it is felt by a single antenna, without a lattice, located at the lattice origin. Considering that $A < 1$, the back-action feature in our experiment is tantamount to a modest Purcell factor of $F \geq 1.7$. Obviously this effect could be much stronger in experiments where the scatterers are placed right in the mode maximum, as opposed to the arrangement in our setup where scatterers are placed at in the evanescent tail (estimated $|E|^2$ decay length of 145 nm, based on finite-element simulations) of the cavity mode at approximately $1\,\mu\mathrm{m}$ distance. We verified that the obtained value of $F \geq 1.7$ is in reasonable agreement with results from finite element simulations on a microtoroid. These simulations predict $F \approx 0.54$ at 1 µm distance, which however rises quickly with decreasing distance (*e.g.* to 2.1 at 800 nm distance). It is important to note that the quoted cavity-array distance of 1 µm was only approximately determined by comparing the experimental cavity linewidth-broadening due to the glass substrate to a finite element simulation.

8.4 Modeling of an antenna array coupled to a microcavity

In Section 8.3.2 we use a general coupled-oscillator model to fit our experimental data. This allowed us to disentangle the resonant and non-resonant features in the data and retrieve the apparent cooperativity between the antenna lattice and the cavity. However, these results leave us with two open questions. (1) What is the origin of the non-resonant background in our measurements? (2) How can we relate the measured cooperativity to the Purcell factor of the cavity, given that we do not measure a single antenna but an array? In this section we therefore go beyond the simple coupled-oscillator model and instead employ a full electrodynamic theory to answer these questions. Doing so, we provide a deeper understanding of the rich behaviour that occurs in these complex system.

As our system consists of two very distinct elements, *i.e.* a quasi-infinite lattice of scatterers and a finite-sized cavity, no obvious choice of theoretical model exists. We therefore consider two extremes, neither of which models the system perfectly, yet each with its own merits. In both cases, the models treat each antenna in the array as a separate dipole and calculate the total response of the array using an analytical point-dipole model (see for example [134, 311]). It is essential to understand that in such a coupled dipole model a dipole is driven not only by the driving field and its own backscattered field, but also by the field scattered by the other dipoles. For a lattice of N identical scatterers, the dipole moment of particle n reads

$$\mathbf{p}_n = \overleftrightarrow{\alpha}_0 \left[\mathbf{E}_{\mathrm{ext}}(\boldsymbol{r}_n) + \sum_m^N \overleftrightarrow{G}(\boldsymbol{r}_n, \boldsymbol{r}_m, \omega)\mathbf{p}_m \right], \tag{8.9}$$

with $\mathbf{E}_{\mathrm{ext}}(\boldsymbol{r}_n)$ the driving field and $\overleftrightarrow{\alpha}_0$ the electrostatic particle polarizability. The Green's function $\overleftrightarrow{G} = \overleftrightarrow{G}_{\mathrm{bg}} + \overleftrightarrow{G}_{\mathrm{c}}$ is the total Green's function, consisting, in our case, of the background and the cavity contributions. Each of the two models solves Eq. (8.9) in a different way.

The first model, discussed in Section 8.4.1, considers a finite array, coupled to the finite-sized cavity. The array is assumed to be in vacuum. This 'finite' approach has the benefit that it allows us to assign a position dependent Purcell factor that each individual antenna in the array is subject to. In other words, the strength of this approach is that it can take into account important aspects of the cavity that include the cavity mode profile, Q and effective mode volume V_{eff}, as well as the fact that the toroid curvature means that only a finite set of particles are in its mode. This allows us to answer the second question above by connecting the observed cooperativity to the cavity Purcell factor. While its strength is the description of the finite-sized cavity, its weakness is that it can only deal with a finite number of particles and can not account for the air-glass interface on which the particles are placed in the experiment.

The second method we discuss (Section 8.4.2) is complementary as it assumes an infinite array of scatterers including all retarded electrodynamic interactions. However, because an infinite array requires Ewald summation in k-space, this method approximates the cavity as a translation invariant resonantly reflecting slab. For an infinite periodic array, the polarizability is entirely summarized by the polarizability of a particle at the origin [134]. Importantly, it has recently been shown that the theory that typically describes such infinite arrays in vacuum [134] can be extended to take into account a reflective surface on which the particles are placed [311]. As the resulting theory only requires Fresnel reflection and transmission coefficients, in fact one can even use stacked (resonant) planar layers as an interface [304]. This is also the approach we take in this second, 'infinite' model: we essentially lump the response of the glass-air interface and cavity into a single Fresnel coefficient, and calculate the response of the array using the resulting 'engineered' metasurface. As our calculation in this second scenario allows us to include interfaces such as the glass-air interface that characterizes our sample surface, we are able to reproduce the angle-dependent Fano lineshapes that are observed in our experiment (Fig. 8.5b).

8.4.1 Finite array and cavity

In our experiment we did not probe the response of a single scatterer, but instead measured on an array of dipoles. Here we use a brute-force coupled dipole model to show that the response of an array qualitatively matches the response of a single scatterer when coupled to a single cavity mode. The spectral lineshapes that we calculate in both scenarios are similar, although lattice effects can lead to a significantly stronger response for some particles

in the array, compared to that of the single scatterer case. We first introduce the coupled dipole model, before deriving the Greens function of a single whispering-gallery mode (WGM) and finally showing the results that we obtain using our model.

Effective polarizability retrieval in a finite lattice

For N dipoles, Eq. (8.9) leads to a set of $3N$ coupled equations of motion. To simplify the math, we take the particles to be only polarizable along the y-axis, reducing Eq. (8.9) from $3N$ to N equations. Reshuffling the terms, we can now write an equation of the form

$$\overleftrightarrow{M}^{-1}\tilde{\mathbf{P}} = \tilde{\mathbf{E}}_{\mathrm{ext}} \tag{8.10}$$

with

$$\overleftrightarrow{M}^{-1} = \begin{pmatrix} \alpha_{yy}^{-1} - G_{yy}(r_0, r_0) & -G_{yy}(r_0, r_1) & \dots & -G_{yy}(r_0, r_N) \\ -G_{yy}(r_1, r_0) & \alpha_{yy}^{-1} - G_{yy}(r_1, r_1) & \dots & \vdots \\ \vdots & & \ddots & \\ -G_{yy}(r_N, r_0) & \dots & & \alpha_{yy}^{-1} - G_{yy}(r_N, r_N) \end{pmatrix} \tag{8.11}$$

and where $\tilde{\mathbf{P}}$ and $\tilde{\mathbf{E}}_{\mathrm{ext}}$ are column vectors of length N containing the dipole moments of all particles and the driving fields at their positions, respectively. We can solve this system of equations by setting up $\overleftrightarrow{M}^{-1}$ and numerically inverting it. One then multiplies it with the driving fields $\tilde{\mathbf{E}}_{\mathrm{ext}}$ to obtain $\tilde{\mathbf{P}}$. Dividing $\tilde{\mathbf{P}}$ element-wise by $\tilde{\mathbf{E}}_{\mathrm{ext}}$, one obtains the effective polarizability α_{eff} of each particle, defined as usual through $p_n = \alpha_{\mathrm{eff}} E_{\mathrm{ext}}(\boldsymbol{r}_n)$. The effective polarizability, averaged over the number of particles in the detection area, determines the response of the lattice to an incident field.

The cavity Green's function

To couple multiple dipoles via the cavity, we require an explicit expression that describes the full cavity Green function $\overleftrightarrow{G}_{\mathrm{c}}(\boldsymbol{r}, \boldsymbol{r}', \omega)$. The field of a single cavity mode can be described as (see Section 2.2.2)

$$\mathbf{E}(\boldsymbol{r}, \omega) = a(\omega)\mathbf{e}_{\mathrm{c}}(\boldsymbol{r}), \tag{8.12}$$

where $a(\omega)$ is the frequency-dependent amplitude and $\mathbf{e}_{\mathrm{c}}(\boldsymbol{r})$ is the normalized field profile. If a dipole $\mathbf{p}'$ at position $\boldsymbol{r}'$ is coupled to the cavity, we find $a(\omega)$ by solving the cavity equation of motion (Eq. (2.20), with $s_{\mathrm{in}} = 0$, taking the small linewidth approximation $\kappa \ll \omega_{\mathrm{c}}$ and evaluating near cavity resonance) as

$$a(\omega) = \frac{i}{4}[\mathbf{e}_{\mathrm{c}}^*(\boldsymbol{r}') \cdot \mathbf{p}'] \frac{\omega_{\mathrm{c}}}{-i\Delta_{\mathrm{c}} + \kappa/2}. \tag{8.13}$$

The cavity Green's function is defined through the cavity fields generated at position $\boldsymbol{r}$ by a dipole at position $\boldsymbol{r}'$ as

$$\mathbf{E}(\boldsymbol{r}) = \overleftrightarrow{G}_{\mathrm{c}}(\boldsymbol{r}, \boldsymbol{r}', \omega)\mathbf{p}'. \tag{8.14}$$

Plugging in Eqs. (8.12) and (8.13) for $\mathbf{E}(\boldsymbol{r})$ and reshuffling terms, we get

$$G_{\mathrm{c}}(\boldsymbol{r}', \boldsymbol{r}, \omega) = L(\omega)\, \mathbf{e}_{\mathrm{c}}(\boldsymbol{r})\mathbf{e}_{\mathrm{c}}^{*}(\boldsymbol{r}')\,, \tag{8.15}$$

with $L(\omega) = \frac{i}{4}\frac{\omega_{\mathrm{c}}}{-i\Delta+\kappa/2}$ the Lorentzian lineshape function.

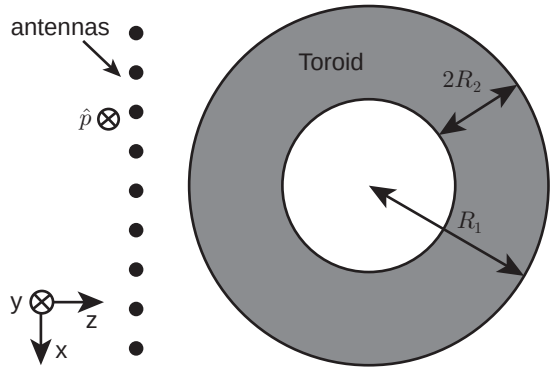

Figure 8.6: Sketch of an array of antennas near a cavity. The antennas form a 2D lattice in the x-y plane. The antennas have their dipole moments oriented along the y-axis. The cavity is a microtoroid with major and minor radii R_1 and R_2, respectively.

From Eq. (8.15) it is clear that we require an expression for the spatial mode profile of the cavity. It was shown that the mode profile of a fundamental TE WGM in a microtoroid with major radius R_1 and minor radius R_2, outside the glass of the cavity, takes on the shape [302]

$$\mathbf{e}_{\mathrm{c}}(\boldsymbol{r}) = \mathbf{e}_{\mathrm{c}}(y = 0, r = R_1)e^{-y^2/2r_y^2}e^{-\kappa_r(r-R_1)}e^{\pm il\phi}, \tag{8.16}$$

where $\mathbf{e}_{\mathrm{c}}(y = 0, r = R_1)$ is the field somewhere on the edge of the cavity, in the equatorial plane, r_y is a Gaussian width along the y-direction (which depends on R_1, R_2 and l), $\kappa_r \approx \frac{2\pi\sqrt{\epsilon_c - \epsilon}}{\lambda}$ (with ϵ_c and ϵ the permittivities of the cavity and the surrounding, respectively) is the radial decay length and l is the azimuthal mode number. r and ϕ are cylindrical coordinates, where we have taken the origin to lie in the toroid center. See Fig. 8.6 for a sketch of the geometry. A plus or a minus sign in the azimuthal dependence determines whether it is the anticlockwise (ACW) or clockwise (CW) mode in the toroid. Note that the total cavity Green's function is the sum of the CW and ACW mode contributions. Since we only want to know the field in the plane of the antennas, close to where the toroid approaches the lattice, we can make a

Taylor expansion around $x = 0$ in the Gaussian term. Doing the same in the last term describing the azimuthal dependence, we obtain for the field in the plane of the antennas

$$\mathbf{e}_{\mathrm{c}}(\boldsymbol{r}) = \mathbf{e}_{\mathrm{c}}(\{x, y\} = 0, z = R_1) e^{-x^2/2r_x^2} e^{-y^2/2r_y^2} e^{-\kappa_r(|z|-R_1)} e^{\pm i k_c x}, \tag{8.17}$$

where $r_x = \sqrt{z/4\kappa_r}$ and $k_c = -l/z$ is the effective wavevector of the cavity mode in the antenna plane. From Eq. (8.15), the cavity Green's function in the plane of the antennas ($z = z_0$) can now be described as

$$G_{\mathrm{c}}(\boldsymbol{r}', \boldsymbol{r}, \omega) = L(\omega) \overleftrightarrow{O} e^{-(x^2+x'^2)/2r_x^2} e^{-(y^2+y'^2)/2r_y^2} e^{\pm i k_c (x-x')}. \tag{8.18}$$

where $\boldsymbol{r}'$ and $\boldsymbol{r}$ are the source and detection positions, respectively, and

$$\begin{aligned} \overleftrightarrow{O} &= \mathbf{e}_{\mathrm{c}}(\{y, x\} = 0, z = R_1) \mathbf{e}_{\mathrm{c}}^*(\{y, x\} = 0, z = R_1) e^{-2\kappa_r(|z_0|-R_1)} \\ &= \mathbf{e}_{\mathrm{c}}(\boldsymbol{r}_0) \mathbf{e}_{\mathrm{c}}^*(\boldsymbol{r}_0) \end{aligned} \tag{8.19}$$

is a matrix with the fields at the origin $\boldsymbol{r}_0$ of the lattice. It is easy to verify that, for a dipole $\mathbf{p}$ at position $\boldsymbol{r}$

$$\mathrm{Im}\left\{\hat{p} \cdot \overleftrightarrow{G}_{\mathrm{c}}(\boldsymbol{r}, \boldsymbol{r}, \omega_{\mathrm{c}}) \cdot \hat{p}\right\} = \frac{Q}{V_{\mathrm{eff}}(\boldsymbol{r}) \epsilon_0 \epsilon(\boldsymbol{r})} = \frac{F k^3}{6\pi \epsilon_0 \epsilon}, \tag{8.20}$$

with V_{eff} defined in Eq. (2.23). This confirms that the dipole experiences additional radiation damping in proportion to the cavity Purcell factor F [118], as also discussed in Section 8.3.2.

Results

For simplicity, we restrict ourselves to a lattice of scatterers in vacuum. The Greens function of the background $\overleftrightarrow{G}_{\mathrm{bg}}(\boldsymbol{r}_n, \boldsymbol{r}_m, \omega)$ is then a well-known expression [12]. [†] We ignore its real part for $\boldsymbol{r}_m = \boldsymbol{r}_n$, taking the divergent electrostatic contribution to be included in the static polarizability $\overleftrightarrow{\alpha}_0$. The cavity Greens function is the sum of the CW and ACW contributions described in Eq. (8.18). As we assume that the scatterers are only polarizable along the y-axis, we only require the yy-component of $\overleftrightarrow{O}$, which is related to the effective mode volume $V_{\mathrm{eff}}(\boldsymbol{r}_0)$ felt by a y-oriented dipole at the lattice origin through $O_{yy} = 2/(V_{\mathrm{eff}}(\boldsymbol{r}_0)\epsilon_0\epsilon(\boldsymbol{r}_0))$.

We assume particles with a Lorentzian polarizability α_0 with resonance frequency $\omega_{\mathrm{a}} = 2\pi c/\lambda_{\mathrm{a}}$, λ_{a} =1.5 µm, oscillator strength corresponding to a

[†]Note that one could, in principle, also include the glass-air interface, since the Green's function near an interface is also known [12]. However, it involves an integral over reciprocal space which, although solvable [311], is computationally very intensive to perform. In practice, this limits the lattice size to no more than a few particles.

sphere of volume of $1.5{\cdot}10^{-3}\mu m^3$ and an ohmic damping rate γ_i of $\omega_a/10$, matching literature values of gold [139]. The dipoles are positioned in a square lattice as in the experiment with pitches d_x =1.5 µm and d_y =0.8 µm, containing 465 particles, *i.e.* 31 (15) particles in the x-(y-)direction. Our cavity is made of glass ($n = 1.5$) and surrounded by air, has a major radius of 18 µm, l=100, $\omega_c = \omega_a$, $Q = 3 \cdot 10^6$ and is located at 2 µm distance from the lattice. This leads to a cavity in-plane wavevector of $k_c = 1.19\,k_0$ (in good correspondence with the experimentally observed $1.23\,k_0$) and a Gaussian width $r_x \approx 1.46\,\mu m$. We take $r_y = r_x/2.6$, corresponding to the measured cavity mode profile. We choose $V_{\text{eff}}(\boldsymbol{r}_0) = 5 \cdot 10^4 \lambda_c^3$ for the CW and ACW modes, which implies that the cavity Purcell factor (including both the CW and ACW mode) at the lattice origin is 9.1. We excite the lattice with a plane wave at an angle with the normal, along the x-axis, *i.e.* $\mathbf{k}_{\parallel} = k_{\parallel}\hat{\mathbf{x}}$.

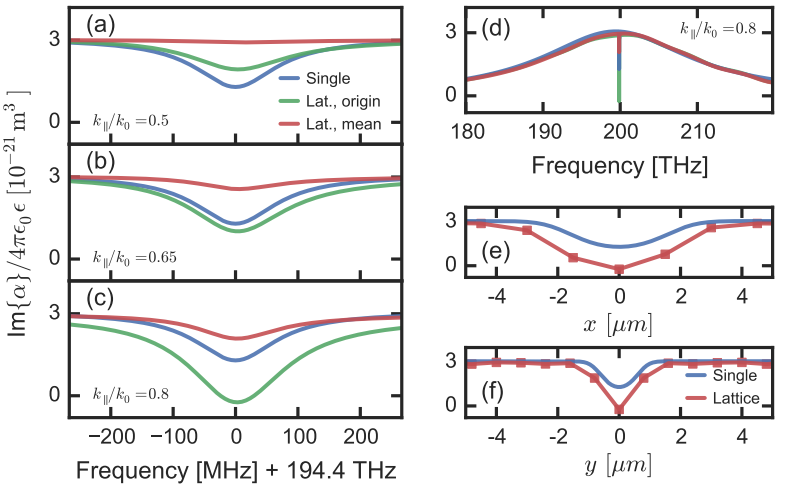

Figure 8.7: Effective polarizability α in a finite lattice of dipolar scatterers coupled to a WGM cavity. (a-c) Narrowband spectra of $\mathrm{Im}\{\alpha\}$, for three different incident parallel wavevectors $k_{\parallel}$ (indicated). We show $\mathrm{Im}\{\alpha\}$ for a single dipole (located at the lattice origin $\boldsymbol{r}_0$) without a lattice (blue) and for dipoles in a lattice, where we show the dipole at the lattice origin (green) and the mean value of the dipoles within a spatial region of 4.5 µm diameter around the origin (red). **(d)** Broadband spectrum of $\mathrm{Im}\{\alpha\}$ for $k_{\parallel}/k_0 = 0.8$, where we have optimal phase matching to the cavity mode via the (-2,0) diffraction order. Color coding is the same as in (a-c). **(e-f)** Spatial profiles of $\mathrm{Im}\{\alpha\}$ in the x- and the y-direction, centered at the lattice origin. We show $\mathrm{Im}\{\alpha\}$ for a single scatterer that is moved in the plane of the lattice (blue) and for the particles in the lattice (red). We chose $\omega = \omega_c$ and $k_{\parallel}/k_0 = 0.8$.

Figure 8.7 shows the effective polarizability of particles in this lattice. From Fig. 8.7 (a-c) we can see firstly that, while the polarizability of a single particle coupled to a cavity does not depend on angle of incidence, that of particles in a lattice does. We see exactly the type of phase-matching condition that

was also observed in our experiment (Fig. 8.5), where the effect of the cavity on polarizability is strongest when we are phase-matched to the cavity mode via the (-2,0) diffraction order. Here this occurs at $k_{\parallel}/k_0 = 0.8$. Moreover, we see that if phase-matching is achieved, the back-action effect introduced by the cavity can be stronger in a lattice than for a single particle: in a lattice, the particle at the origin has a more strongly modified polarizability than the single particle. This is because of the constructive interference of all particles radiating into the cavity, leading to an enhanced back-action field for particles near the origin. Figure 8.7 (d) displays the broadband polarizability of the dipoles, showing that both the single particle and the lattice follow the same Lorentzian lineshape outside the cavity spectral window. In Fig. 8.7 (e-f) we see that the particles close to the origin are more strongly affected by the cavity, *i.e.*, that the effect diminishes for antennas at larger distance from the origin, roughly following the 2D Gaussian profile of the cavity mode. To compare the analytical results with our experiment, we also show in Fig. 8.7 (a-d) the mean polarizability of particles within a spatial region of 4.5 μm diameter around the origin, corresponding to the size of the real-space filter used in our experiments. To first order, the field scattered by the dipoles within the filter area is proportional to their mean polarizability. We see that this shows the same lineshape, but the averaging decreases the effect of the cavity.

These results show that the polarizability in a finite lattice of dipoles is qualitatively similar to the polarizability of a single dipole. We can thus use the ratio between the averaged lattice response and that of the single particle to predict the response we would have obtained in our measurement if we would have measured on a single particle, instead of on an array of dipoles. For this purpose, we fit the curves for a single particle and for the averaged lattice response at optimal phase matching ($k_{\parallel}/k_0 = 0.8$, Fig. 8.7c) with our simple coupled-oscillator model (Eq. (8.7)). We find a cooperativity of 1.4 and 0.41 for the single particle and the averaged lattice response, respectively. The former is in good agreement with the AF product in these calculations, i.e $A = 0.15$, $F = 9.1$, $AF = 1.37$. We therefore expect that the experimentally measured maximum cooperativity of 0.5 implies a cooperativity of 1.7 for a single particle (in absence of other scatterers) located at the lattice origin. Thus the Purcell factor at the lattice origin must be higher than 1.7. This value of $F \geq 1.7$ is in reasonable agreement with results from finite element simulations on a microtoroid, as discussed in Section 8.3.2.

8.4.2 Infinite array and cavity

In this section we will discuss an infinite array of scatterers in front of an interface. With this model we aim to justify a specific claim made in the main text, namely that the Fano lineshapes that we observe in our experiment result from non-trivial background signals originating from the interface. Before we move to the details of our model, we first briefly recall the foundations

of lattice sum theory, which describes infinite arrays of scatterers (see for example [134, 311]). We then discuss how we implemented the cavity in our model, followed by a discussion of the calculation results.

Lattice sum theory

The dipole moment $\mathbf{p}_n$ of a dipole in a lattice is described by Eq. (8.9). In the case of an infinite lattice of identical particles, one can simplify this equation using the fact that the solutions $\mathbf{p}_n$ will have a Bloch wave form, i.e. $\mathbf{p}_n = e^{i\mathbf{k}_\parallel^{\mathrm{ext}}\boldsymbol{r}_n}\mathbf{p}_0$, with $\mathbf{k}_\parallel^{\mathrm{ext}}$ the in-plane wavevector of the incident light and $\mathbf{p}_0$ the dipole moment of the particle at the lattice origin. Equation (8.9) can then be written as [134]

$$\mathbf{p}_n = \left[\overleftrightarrow{\alpha}_0^{-1} - \overleftrightarrow{\mathcal{G}}(\mathbf{k}_\parallel^{\mathrm{ext}}, \boldsymbol{r}_n, \omega)\right]^{-1} \mathbf{E}_{\mathrm{ext}}(\boldsymbol{r}_n) \tag{8.21}$$

with

$$\overleftrightarrow{\mathcal{G}}(\mathbf{k}_\parallel^{\mathrm{ext}}, \boldsymbol{r}_n, \omega) = \sum_{n'} \overleftrightarrow{G}(\boldsymbol{r}_{n'}, \boldsymbol{r}_n, \omega) e^{i\mathbf{k}_\parallel^{\mathrm{ext}}(\boldsymbol{r}_{n'} - \boldsymbol{r}_n)} \tag{8.22}$$

the lattice-summed Green's function, i.e. the field at $\boldsymbol{r}_n$ generated by all particles in the lattice (including the n-th particle itself). To find the response of the lattice, one should solve Eq. (8.22). We will not discuss in detail on how to do this, but instead point to the relevant literature (see *e.g.* [311, 312] for details). The formalism as it is described by Eqs. (8.21) and (8.22) is well established for 2D lattices in homogeneous space, using Ewald summation for exponential convergence of the lattice sums in the case that $\overleftrightarrow{G}$ is $\overleftrightarrow{G}_{\mathrm{hom}}$ (with $\overleftrightarrow{G}_{\mathrm{hom}}$ the Green function for homogeneous space) [134]. Recently, Kwadrin *et al.* [311] showed how to generalize this approach for the case of lattices placed in front of a single reflective interface. In this case, one separates $\overleftrightarrow{G}$ as the sum of $\overleftrightarrow{G}_{\mathrm{hom}}$ and a reflected Green function $\overleftrightarrow{G}_{\mathrm{refl}}$, where $\overleftrightarrow{G}_{\mathrm{refl}}$ is written in the angular spectrum representation [12], taking the wavevector dependent Fresnel coefficient as an input. After solving for $\overleftrightarrow{\mathcal{G}}$, the subsequently obtained lattice- and interface-corrected polarizability $\overleftrightarrow{\alpha}_{\mathrm{lat}}$, defined as [134]

$$\overleftrightarrow{\alpha}_{\mathrm{lat}} = \left[\overleftrightarrow{\alpha}_0^{-1} - \overleftrightarrow{\mathcal{G}}(\mathbf{k}_\parallel^{\mathrm{ext}}, 0, \omega)\right]^{-1}, \tag{8.23}$$

can be used to calculate far-field observables such as, for example, reflection and transmission properties [12].

Simple model for cavity interaction

It is important to realize that Eq. (8.21) only holds if the entire system obeys translation invariance (or has a common periodicity). Only in that case is the

$\mathbf{p}_n$ guaranteed to have a Bloch waveform. Due to the finite extent of the microtoroid cavity, however, translation invariance is not maintained in our system. To nonetheless approximate the experiment, we propose to mimic the cavity response by a resonant planar structure. This is a feasible approach, because the extension of lattice sum theory to lattices near mirrors, as reported by [311], is not restricted to a single reflective interface. Instead, one can also consider an array of scatterers positioned in a half space in front of an arbitrary multi-layer stack [304]. This approach simply relies on replacing the Fresnel coefficient of the single interface with the multi-layer reflection coefficient r_{eff}.

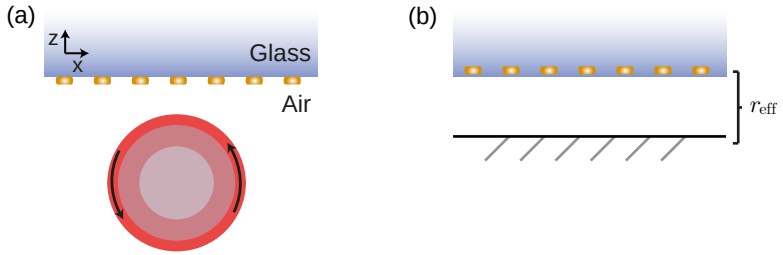

Figure 8.8: Geometry used in the infinite lattice calculations. (a) Actual experimental geometry. **(b)** Geometry assumed in the infinite lattice theory. The finite-sized cavity is replaced by a resonant multistack, and the antennas are placed just inside the glass.

Our model now considers a geometry as shown in Fig. 8.8 — an infinite antenna array placed 50 nm from a glass-air interface, inside the glass. Behind the glass-air interface, there is a multilayer stack which models the cavity. The total lumped reflection coefficient, including interface and cavity, is given by the well-known expression for an etalon [313]

$$r_{\mathrm{eff}} = \frac{r_{\mathrm{int},12} + r_{\mathrm{c}} e^{2ik_{z,\mathrm{air}}d}}{1 - r_{\mathrm{int},21} r_{\mathrm{c}} e^{2ik_{z,\mathrm{air}}d}}, \tag{8.24}$$

where $r_{\mathrm{int},12}$ ($r_{\mathrm{int},21}$) is the reflection coefficient of the glass-air interface, incident from the glass (air) side, r_{c} is the cavity reflection coefficient, $k_{z,\mathrm{air}}$ is the component of the k-vector in air perpendicular to the lattice plane, and d is the distance between cavity and interface (which, for simplicity, we set to zero). Due to the resonant nature of the single cavity mode (in frequency and wavevector), r_{eff} is equivalent to $r_{\mathrm{int},12}$, except for very specific frequencies and wavevectors at which it is possible to excite the cavity. For our calculations, we approximate r_{cav} as

$$r_{\mathrm{cav}} \equiv \frac{i\kappa_{\mathrm{ex}}}{(-i\Delta_{\mathrm{c}} + \kappa/2}, \tag{8.25}$$

with

$$\kappa_{\mathrm{ex}} \equiv \frac{\kappa}{2} \times e^{(-|k_{\parallel} - k_{\parallel,\mathrm{c}}|^2)/(2\sigma^2)}. \tag{8.26}$$

the effective coupling rate to the cavity. We recognize that r_{c} takes on a similar shape as the cavity Green's function G_{c} (Eq. (8.18)). Its frequency-dependency is given by a Lorentzian, and the momentum dependency shows Gaussian peaks centered at $\pm k_{\parallel,\mathrm{c}}$ (the wavevector of the cavity mode) with a width given by σ. It can be easily shown that a spatial Fourier transform of G_{c} in the detector coordinate $\boldsymbol{r}$ would lead to a similar double Gaussian dependency (matching the measured Fourier pattern shown in Fig. 8.3d). The part of G_{c} that is not contained in r_{c}, is the dependence on source position $\boldsymbol{r}'$, because this would break translational invariance. As such, the resonant planar structure has an equal interaction with all antennas in the array, in contrast to the microtoroid in the experiment which interacts only with a select number of antennas. We note that the pre-factor $\kappa/2$ in Eq. (8.26) is chosen such that Eq. (8.25) yields unity reflection for perfect phase-matching and $\omega = \omega_{\mathrm{c}}$, maximizing the effect of our resonant structure. A drawback of our model is that we can not easily determine the 'real' pre-factor that we should use. In reality, the pre-factor should relate to the cavity-array distance, and determine the strength of the back-action.

Finally, a difference with the experimental situation is the positioning of the antenna array inside the glass environment, which is necessary to lump the interface and cavity as a simple reflective multilayer. This positioning will slightly influence the total field at the position of the array. However, taking into account that s-polarized fields are continuous across the boundary, and that we positioned our antennas at a distance of $\lambda/20$ from the substrate, we estimate the resulting difference originating from this change in position to be relatively small.

Calculation results

Using our model, we plot the specular reflectance spectra for two different illumination conditions in Fig. 8.9a (normal incidence) and Fig. 8.9b ($k_{\parallel}/k_0 = 0.78$). [‡] In both scenarios we observe a broadband dip together with a glass-related background reflection signal. This means that the reduction in reflection can be attributed to the plasmon resonance. Our calculations thus validate our claim in Section 8.2.3 that a dip in reflectance is a measure for extinction, and that an increase in reflectance signals a *reduction* in extinction. The exact shape of the broadband dip varies slightly with incident angle, because the particle-particle interactions, captured in the Green's function $\overleftrightarrow{\mathcal{G}}$, depend on this angle. The narrowband, angle-dependent resonances in reflection that are typical for lattices in a homogeneous medium and associated to Rayleigh anomalies [134], however, are not observed. This is due to the

[‡] We use a cavity with $\omega_{\mathrm{c}}/2\pi = 194.4$ THz, $Q = 3 \cdot 10^6$, $k_{\parallel,\mathrm{c}}/k_0 = 1.23$ and $\sigma/k_0 = 0.07$. The antennas have $\omega_{\mathrm{a}} \approx \omega_{\mathrm{c}}$, $\gamma_i = \omega_{\mathrm{a}}/10$ and oscillator strength corresponding to a sphere of volume of $3.4{\cdot}10^{-3}\mu\mathrm{m}^3$, and organized in a lattice with pitches as in the experiment. They are only polarizable along the y-axis.

presence of the interface, which suppresses these narrow features, as was also observed earlier [314].

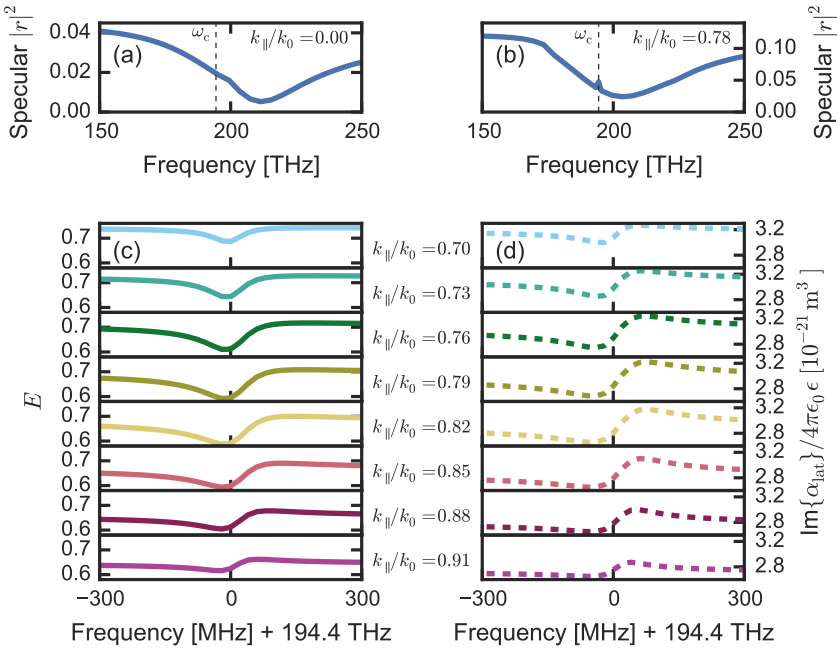

Figure 8.9: Calculation results for an infinite system. **(a)** The calculated specular reflectance of the array (for normal incidence) shows a clear broadband dip associated with the plasmon resonance. The dashed line indicates the resonance frequency associated with the cavity mode. **(b)** For $k_\parallel/k_0 = 0.78$, we observe roughly the same signature. Note that due to the larger angle of incidence, the background signal coming from the glass-air interface is higher than in (a). Importantly, the sharp feature that is visible at ω_c is directly related to the presence (back-action) of the cavity. **(c-d)** Narrowband spectra of extinction E **(c)** and lattice polarizability $\mathrm{Im}[\alpha_{\mathrm{lat}}]$ **(d)** for different $k_\parallel$ (indicated). Similar to our experiment, the calculation predicts a narrow bandwidth dip in extinction resulting from back-action, that is maximized for a wavevector for which the second diffraction order matches the wavevector of the cavity.

In addition to the broadband dip, we observe a small peak in the reflectance spectrum in Fig. 8.9b that is associated with the presence of the cavity. To investigate this in more detail, Fig. 8.9c displays narrowband extinction spectra for various $k_\parallel$, where extinction is defined as in the experiment ($E \equiv 1 - |r'|^2/|r_{\mathrm{glass}}|^2$). From this figure we directly observe a dip in E similar to that in the experimental spectra in Fig. 8.5. Importantly, the depth of this dip significantly depends on the angle of incidence, showing that the we can reproduce the main feature of our experiment using our model. In addition, these calculations provide access to the (corrected) polarizability α_{lat} of the array. Figure 8.9d shows the imaginary part of α_{lat} as we obtain

it from our model. We observe a rapid change of polarizability around the cavity resonance frequency, indicative of cavity-induced back-action. Similar to the extinction, this plot shows that the back-action and its effect on α_{lat} can be controlled via the incident angle of the incoming drive field. Interestingly, whereas the extinction (Fig. 8.9c) displays a clear dip, the polarizability has a more asymmetric Fano-like resonant signature. We attribute this somewhat surprising discrepancy in shape between E and $\mathrm{Im}[\alpha_{\mathrm{lat}}]$ to the fact that we do not perform a pure extinction measurement, but instead also partly probe $|\alpha_{\mathrm{lat}}|^2$, which can be related to scattering by the antennas. The interplay between these two contributions, scattering and extinction, most likely gives rise to a more complex behaviour.

Finally, we observe a change in resonance lineshape both in extinction and in polarizability as $k_{\|}$ is varied, similar to what was observed in the experiment. From our model, we can trace the origin of this change as a phase change in r_{int}, the reflection coefficient of the glass-air interface. Back-action from the multilayer, i.e. the contribution of $\overleftrightarrow{G}_{\mathrm{refl}}$ to $\overleftrightarrow{\mathcal{G}}$, is mostly determined by its reflection r_{eff} evaluated at the angles of the diffraction orders (which is also why we see cavity back-action only when a diffraction order overlaps with the cavity mode). At the angle of the (-2) diffraction order, the glass-air interface shows total internal reflection, for which r_{int} becomes complex and its phase depends strongly on angle. In contrast, the phase of the cavity reflection coefficient r_{c} does not depend on angle. This explains the shape change of the Fano lineshape. We do, however, observe a difference in Fano lineshapes between calculations (Fig. 8.9c) and experiment (Fig. 8.5b). For example, for large angle of incidence (bottom panel in both figures) the Fano lineshapes have opposite asymmetry, *i.e.* opposite phase. We attribute this difference to the positioning of the antennas. In the experiment we place the array on the air side of the interface, while in the calculation we put them inside the glass environment. For evanescent waves (*i.e.* at the angle of the (-2) diffraction order) the phase of r_{int} when incident from the air side is opposite to that experienced when entering from the glass side. This opposite phase alters the observed shape of the extinction signal.

In conclusion, we have developed a full electrodynamic model for an infinite lattice of point scatterers coupled to a resonant multilayer stack which mimics a WGM cavity. Using this model, we were able to reproduce the main features in our experiment. As in the experiment, a suppression of extinction by the antenna array was observed, with strength tunable through angle of incidence. We showed that the effective antenna polarizability is similarly modified, which links the observed extinction dip to cavity-mediated back-action on the antenna. Furthermore, the lineshape change observed in both theory and experiment was explained as originating from the complex reflection coefficient of the glass-air interface.

8.5 Conclusion and outlook

We have shown that cavity back-action can alter the polarizability of an array of scatterers, and that the strength of the back-action can be controlled via the incoming drive field. Whereas in this work the Purcell enhancement provided by the cavity effectively depolarizes the nano-rods, which is related to the fact that the cavity and array are nearly resonant, it has been predicted in Section 2.4.2 that both an increase and decrease in polarizability can be obtained by controlling the detuning between cavity and scatterers. As the antenna polarizability dictates properties such as scattering and extinction, but also near-field enhancement and local density of states, this result demonstrates the feasibility of antenna-cavity hybrids as a tunable platform for scattering and emission control. We expect that this type of control over antenna polarizability will facilitate the exploration of antenna-cavity hybrids for applications such as single-photon sources, strong coupling to single quantum emitters, as well as classical applications like single-molecule sensing [26, 105, 109, 118].

Chapter 9

Experimental observation of a polarization vortex at an optical bound state in the continuum

Optical bound states in the continuum (BICs) are states supported by a photonic structure that are compatible with free-space radiation, yet become perfectly bound for one specific in-plane momentum and wavelength. Recently, it was predicted that light radiated by such modes around the BIC momentum-frequency condition should display a vortex in its far-field polarization profile, making the BIC topologically protected. We study a one-dimensional grating supporting a transverse-magnetic mode with a BIC near 700 nm wavelength, verifying the existence of the BIC using reflection measurements, which show a vanishing reflection feature. Using k-space polarimetry, we measure the full polarization state of reflection around the BIC, highlighting the presence of a topological vortex. We use an electromagnetic dipole model to explain the observed BIC through destructive interference between two hybridized resonances inside the grating unit cell, characteristic of a Friedrich-Wintgen type BIC. Our findings shed light on the origin of BICs and verify their topological nature.

9.1 Introduction

A single accelerated point charge must radiate electromagnetic fields. This well-known law of classical physics is at the foundation of much of the technological advances in the field of photonics. However, it has been found that certain extended charge distributions exist which may oscillate without producing radiation [316, 317]. A well-known example is the waveguide mode supported by a slab of a high-index dielectric, supporting oscillating displacement currents which are decoupled from radiation by a momentum mismatch [125]. Recent works have shown that simple photonic structures can support another type of bound states named embedded eigenstates [318] — states of light that are bound despite the fact that they are not protected from coupling to the radiation continuum through either symmetry, or momentum mismatch [319, 320]. Also known as bound states in the continuum (BIC), these states have infinite lifetime, not because they are forbidden from leaking, but because different radiation channels interfere destructively with each other in the far field [321] (see Fig. 9.1). Such bound states of light have been demonstrated for dielectric systems with 1D and 2D periodicity [320, 322, 323], and have been proposed to occur also in lossless 3D finite plasmonic systems [324, 325], even if for realistic optical materials they may be unattainable. Owing to their unbounded quality factor, they are deemed to hold great promise for enhancing light-matter interactions [319], including applications in solid-

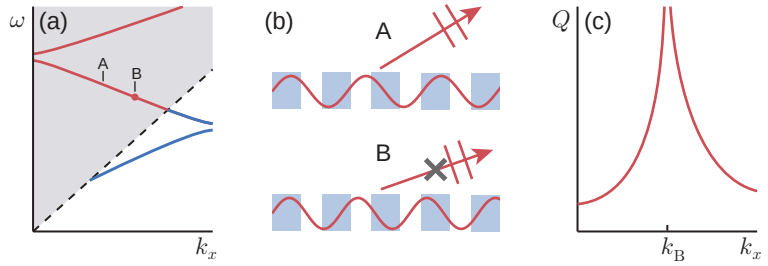

Figure 9.1: Sketch of a bound state in the continuum (BIC). Although BICs can occur in nearly any type of structure [315], this sketch shows an example based on a waveguide with 1D periodicity. **(a)** Dispersion diagram of a waveguide mode in a periodic structure. The periodicity causes the waveguide dispersion to fold at the edge of the Brillouin zone, placing part of the dispersion below (blue line) and part above (red line) the light line of the surrounding medium (dashed line). Above the light line this becomes a leaky mode, as it is momentum-matched to outgoing waves (for example, at point A). However, for certain geometries a point may appear on the leaky mode dispersion at which radiation stops and the mode is perfectly bound again (point B). **(b)** Waveguide mode profile at points A and B, showing only the Bloch wave vector that is above the light line. At point A the mode couples to outgoing waves, whereas at point B this radiation is cancelled, despite the fact that both wave vectors are matched to outgoing waves. **(c)** Near point B, the quality factor Q of the leaky mode diverges, indicating perfect trapping.

state lasers [326, 327], sensing [328] and narrowband filters [329]. Zhen *et al.* [330] have predicted that 2D BICs are expected to be inherently robust, due to the fact that they are intimately related to a topological invariant in their polarization properties. This property elegantly connects photonic BICs to a wide range of topological phenomena.

In this work, we provide experimental evidence for the prediction by Zhen *et al.*, by tracing the polarization of far-field radiation associated with the leaky-wave dispersion of a grating that exhibits a BIC. Our measurements show two BICs associated with a polarization vortex, each of topological charge $+1$. Whereas earlier studies have demonstrated very high quality factors of BICs in similar dielectric 1D [331] and 2D [322, 326] periodic systems, no experiments thus far have studied their topological nature. We argue that the polarization vortex is a much more robust evidence for the radiation cancellation mechanism from which BICs arise than simply monitoring the amplitude and Q-factor of the leaky-wave signature in reflectivity. Indeed, while theory predicts infinite Q and a vanishing amplitude reflection signature for ideal BICs, in real systems the embedded eigenstate and its far field signature are limited to finite Q by roughness, loss, imperfections and the unavoidable finite size of the sample. The vortex is robust to such sample imperfections. Interestingly, not only do we observe the vortex despite a background reflection present in our measurements, but this background also leads to an additional fingerprint of the vortex, observable in the helicity of the far-field reflection. Furthermore, we provide a simple theoretical model that sheds light on the polarization vortex at a BIC in terms of the radiation properties of magnetic and electric dipoles induced on the dielectric elements of the grating. The BIC can be considered as a hybridized mode arising from this magnetic and electric resonance, which are coupled through far-field interference. This represents a 'bare bones' physical model that fully predicts the topological polarization properties of BICs, which fits well with the observed phenomena, and offers new insights into the origin of these anomalous states.

9.2 Signature of a BIC in reflection

9.2.1 Sample and experimental setup

Figure 9.2a-b shows the one-dimensional silicon nitride (Si_3N_4) grating studied in this work. We deliberately choose the simplest possible structure that can support a BIC, inspired by the design proposed by Zhen *et al.* [330]. The grating (n=2.05, 200 nm thick) is fabricated on top of an 8 µm silicon oxide (SiO_2) membrane and embedded in an index-matching environment (n=1.517), with a periodicity d of 350 nm, fill fraction of 63% and overall dimensions of about 0.22 x 0.24 mm^2. Silicon wafers covered by 8 µm thermal

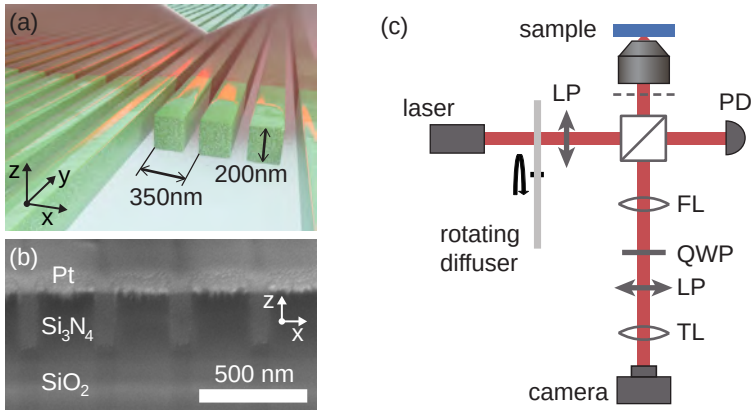

Figure 9.2: Experimental sample and setup. (a) Sketch of the 1D Si_3N_4 grating, using a cut-out to indicate pitch and hight. The red shading indicates a laser beam reflecting of the grating. **(b)** Sample cross-section (Pt only used for electron microscopy). **(c)** Experimental setup. The input light passes a rotating diffuser and linear polarizer (LP). We image the objective back focal plane using the Fourier lens (FL) and tube lens (TL). Laser power is monitored using a photodiode (PD). Another LP and a quarter waveplate (QWP) allow polarimetry.

oxide and 200 nm Si3N4 (stoichiometric, grown by low pressure chemical vapour deposition) are first etched with KOH (30 wt%) from the back to open up a freestanding membrane of 0.22 x 0.24 mm width, supported by a silicon frame. At this size, the membranes are as large as our microscope field of view, yet small enough to avoid bending or rupture. Next, we spin-coat a 250 nm layer of ZEP520a resist and perform e-beam lithography (20 keV, Raith eLine, writing in Fixed-Beam-Moving-Stage configuration) to create a 1x1 mm grating on top of, and next to, the membrane. After development (MIBK:isopropanole 9:1, 20 seconds) we etch the grating into the nitride using an Oxford Instruments Plasmalab 100 Cobra ICP (80 sccm CHF_3, 16 sccm SF_6 at 2500 W ICP power and 50W RF power) for 22 seconds. This procedure optimizes side-wall angle definition.

A BIC is observable as the disappearance and subsequent reappearance of a resonant feature in the sample reflectance spectrum [322]. We therefore require a setup to measure reflection as function of wavelength and incidence angle. We have chosen to employ a k-space imaging scheme [332–336] as shown in Fig. 9.2c. In contrast to traditional ellipsometry — where angle of incidence is varied by mechanical scanning— this offers the crucial advantage of measuring all angles of incidence that fit the NA of a microscope objective in parallel on a CCD, without needing any scanned rotation stage. The sample is illuminated through a NA=1.39 (Olympus UPLanSApo, 100x) objective and reflected light is collected through the same objective. We apply n=1.517 immersion oil (Fluka 10976) on both sides of the sample membrane. The collec-

tion optics is exactly as reported in Osorio *et al.* [336], with the sole distinction that we inserted a beamsplitter (45:55 R:T pellicle) to combine/split the input and output light. Rather than imaging the sample, we image the back focal plane (BFP) of the objective using a Fourier lens. This maps in-plane momentum $(k_x, k_y) = nk_0(\cos\phi\sin\theta, \sin\phi\sin\theta)$ (with n the surrounding index and k_0 the vacuum wavenumber), encoding for angles of incidence θ and ϕ with an effective angular resolution of about 0.5°. If we remove the Fourier lens, we have a real-space field of view on the camera of 90x67 μm (corresponding to 257 grating periods). For wavelength resolution, we use a supercontinuum laser (NKT, SuperK extreme, 8 W power) as tuneable light source between 500 and 900 nm, filtered to 1 nm bandwidth by an acousto-optical tuneable filter (Crystal Technologies). The laser wavelength is scanned in steps of 5 or 10 nm for the measurements with x- and y-polarized input polarizations, respectively. At each wavelength, 15 camera images are averaged for better signal-to-noise ratio. We correct for laser intensity fluctuations between consecutive scans using the signal of a photodiode. A spinning diffuser (sandblasted glass) in the illumination ensures that we simultaneously offer a very homogeneous illumination of the entire objective BFP (all wave vectors are probed) as well as a large area of illumination on the sample (overfilling the camera field of view). These are requirements to observe the narrow features in k-space associated to the BIC. We calibrated the wave vector axis by the grating orders of a large-pitch grating, while we calibrated the intensity axis by verifying the Fresnel coefficients of a bare silicon and a bare ZnSe substrate. Note that measuring reflectivity requires a reference. This is provided by taking a gold substrate as high-reflectivity standard, and using an absorptive color filter as "dark" reference for background subtraction. We have verified that the method is robust to our tolerances in setting focus and sample/objective tilt.

9.2.2 Results

We have chosen the parameters of our system such that it can support a BIC. Analytical calculations of the grating reflectivity, performed using rigorous coupled wave analysis (RCWA) [337], reveal that this grating supports both a TM- and a TE-like leaky mode (see Fig. 9.3a). These are waveguide modes that couple to free space through grating diffraction, as evident from their folded-back dispersion [338]. On the k_x-axis, the TM (TE) mode is polarized in the x-direction (y-direction). Hence, input polarization determines which of the two modes is visible. It was theoretically shown that systems which have up-down mirror symmetry and where permittivity ϵ obeys $\epsilon(x, y, z) = \epsilon^*(-x, -y, z)$ can support BICs that are robust against small variations of sample geometry [330]. Our system fulfils these criteria, and we can see a BIC occurring near 720 nm wavelength in Fig. 9.3a, evident from the disappearance of the TM mode reflection at this wavelength. Fig. 9.4a shows how resonance linewidth

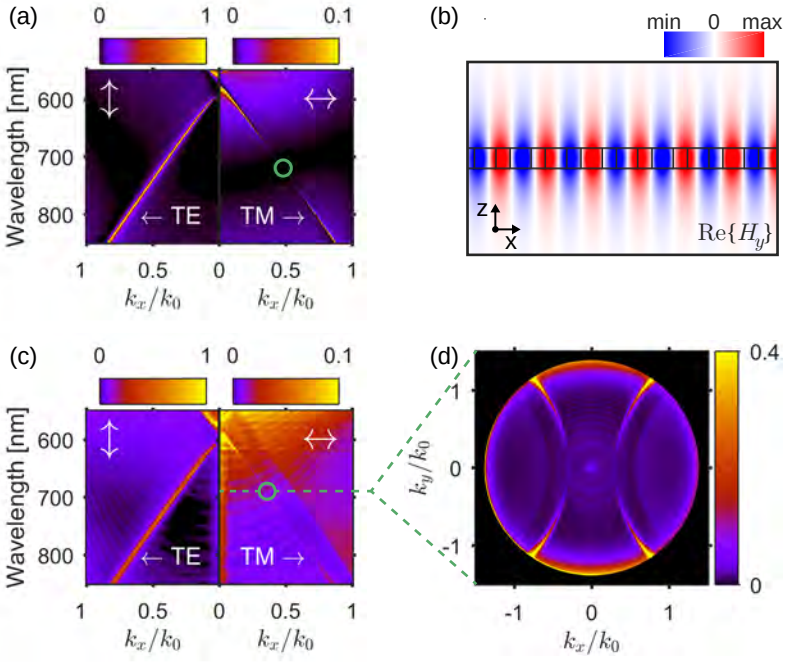

Figure 9.3: Calculated and measured signature of a BIC. (a) Grating reflectivity from RCWA for x- (y-) polarized input beams (horizontal (vertical) arrows). Green circle: the BIC. **(b)** Field profile of the TM mode, driven by a plane wave with $k_x/k_0 = 0.45$ at 720 nm wavelength. We plot $\mathrm{Re}\{H_y\}$ where H_y is the y-component of the scattered magnetic field by the grating. The TM mode is strongly bound to the grating slab. Black lines indicate material boundaries in the grating. **(c)** Measured reflectivity. **(d)** Measured Fourier image of reflection at 690 nm wavelength. TM and TE modes appear as closely spaced, bright rings.

decreases drastically when approaching this wavelength. We verified that as one approaches the exact BIC condition, the quality factor diverges.

Driving the system with an x-polarized plane wave very close to the BIC condition (720 nm wavelength, $k_x/k_0 = 0.446$) and solving for the scattered field in a full-wave numerical simulation (COMSOL v5.3), we find a mode profile shown in Fig. 9.3b. For modes with very large quality factor, the scattered field profile at the resonance condition is practically entirely determined by the contribution of only that mode (that is, the TM mode). We recognize that a guided mode is launched in the grating, which decays away from the plane of the grating and shows very low leakage to propagating waves (high quality factor).

Figure 9.3c shows a cut at $k_y = 0$ through the measured grating reflection diagram that can be directly compared to the calculated dispersion in Fig. 9.3a. The TM leaky wave dispersion is clearly visible and disappears around 690

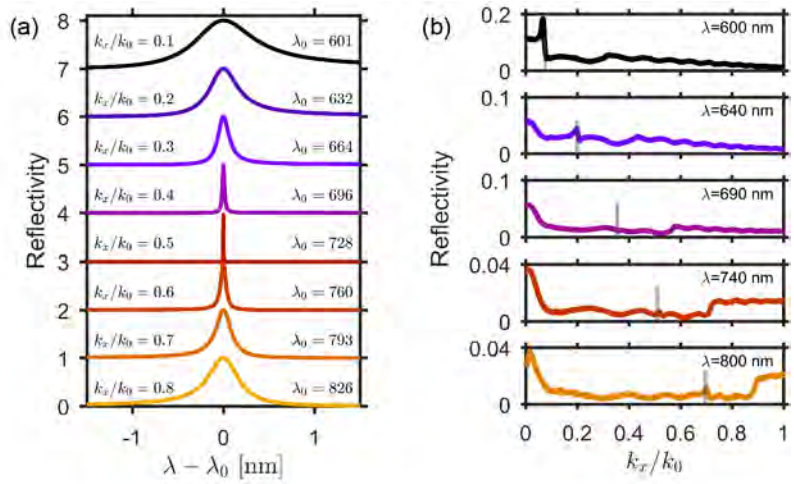

Figure 9.4: Calculated and measured linewidth narrowing. (a) Calculated TM mode reflection spectra at fixed values of k_x/k_0 (indicated in the figure). We zoom in on a narrowband region around the resonance wavelength λ_0 (also indicated). A strong decrease of linewidth is visible when approaching the BIC condition at ∼728 nm wavelength. **(b)** Measured reflection crosscuts at fixed wavelength, for horizontal input polarization. They correspond to horizontal slices from (the right side of) Fig. 9.3c. Grey vertical lines indicate the position of the TM mode. We see a strong peak at low wavelength, which disappears around 690 nm, and reappears for higher wavelength.

nm wavelength—the signature of a BIC. For clarity, Fig. 9.4b shows this disappearance and reappearance of the TM mode reflection feature through crosscuts along the k_x axis. These results are in good agreement with calculations, while the wavelength shift of the BIC is likely caused by a difference in grating fill factor and refractive index of the surrounding medium. Weak interference fringes are visible due to a slight index mismatch between the thermal oxide membrane and the surrounding index-matching oil. The bright feature in Fig. 9.3c at large wave vector (offset to larger $|k_x|$ by $|k_x/k_0| = 0.15$ from the TM leaky wave) arises not from specular reflection, but contains an additional contribution from the first grating diffraction order. As this does not overlap with the leaky-wave features this diffraction order does not affect our analysis. Figure 9.3d shows a different cut through our data, i.e., a single-frequency slice measured in a single camera shot. This evidences the high angular-resolution mapping of the leaky-wave TE and TM features, which appear as concentric bright circles centred at the reciprocal lattice vectors $k_x = \pm 2\pi/d$ and with radius in units of $|\mathbf{k}|/k_0$ equal to the mode index.

9.3 Observation of a polarization vortex at the BIC

The BIC was predicted [330] to coincide with a vortex in the polarization direction of far-field radiation of the leaky TM mode. This polarization structure is sketched in Fig. 9.5a, which represents a schematized version of calculation results discussed in Section 9.4. The diagram indicates the polarization state of far-field radiation associated with the leaky mode as a function of the 2D parallel momentum (k_x, k_y). Right at the BIC, the polarization state shows a vortex, defined as a point around which the polarization vector makes one or more full 2π rotations. A topological charge q can be assigned to such a point, defined as [330]

$$q = \frac{1}{2\pi} \oint_C \nabla_{\mathbf{k}} \psi(\mathbf{k})\, d\mathbf{k}, \tag{9.1}$$

where C is a closed path around the point, traversed in the counter clockwise direction, and ψ is the angle that the polarization vector makes with the x-axis. The charge can be either positive or negative, and the magnitude indicates the number of times ψ winds around the vortex. The vortices sketched in Fig. 9.5a are of charge $+1$.

9.3.1 Measuring polarization

To experimentally observe the polarization vortices implies a significant challenge: to precisely track the polarization response not just at a single wavelength, but across the entire leaky wave dispersion surface, i.e., as a function of parallel momenta k_x and k_y while matching, for each parallel momentum, the frequency to the leaky wave dispersion relation. This would be extremely tedious with a traditional ellipsometer that scans angle by angle, but is straightforward in our k-space imaging technique by using a linear polarizer and a quarter wave-plate that are introduced in the detection arm as Stokes polarimeter [333, 336]. By imaging the (k_x, k_y) plane and scanning wavelength, we can easily collect a three-dimensional data cube of reflection as function of k_x, k_y and λ. Performing this measurement for six different polarizer settings allows the retrieval of the full polarization state of light (that is, the Stokes parameters [333]) at each point in this cube. We summarize the polarization ellipse of reflected light by the orientation ψ of its major axis relative to the x-axis and the ellipticity angle χ (definitions in Fig. 9.5b). The magnitude of χ determines how elliptical the polarization is, while its sign indicates handedness. Figure 9.5c shows intensity, ψ and χ of the sample reflection, for several fixed-frequency data slices at wavelengths above, at, and below the BIC. Each slice crosses both the TE and the TM leaky dispersion. Only at the TM branch does the ellipse orientation ψ change sign around the wavelength of the BIC. Going from low to high wavelength (from left to right in Fig. 9.5c), the value of ψ near the TM-mode feature switches from negative to positive for positive k_y (red $\rightarrow$ blue), and the opposite for negative k_y (blue

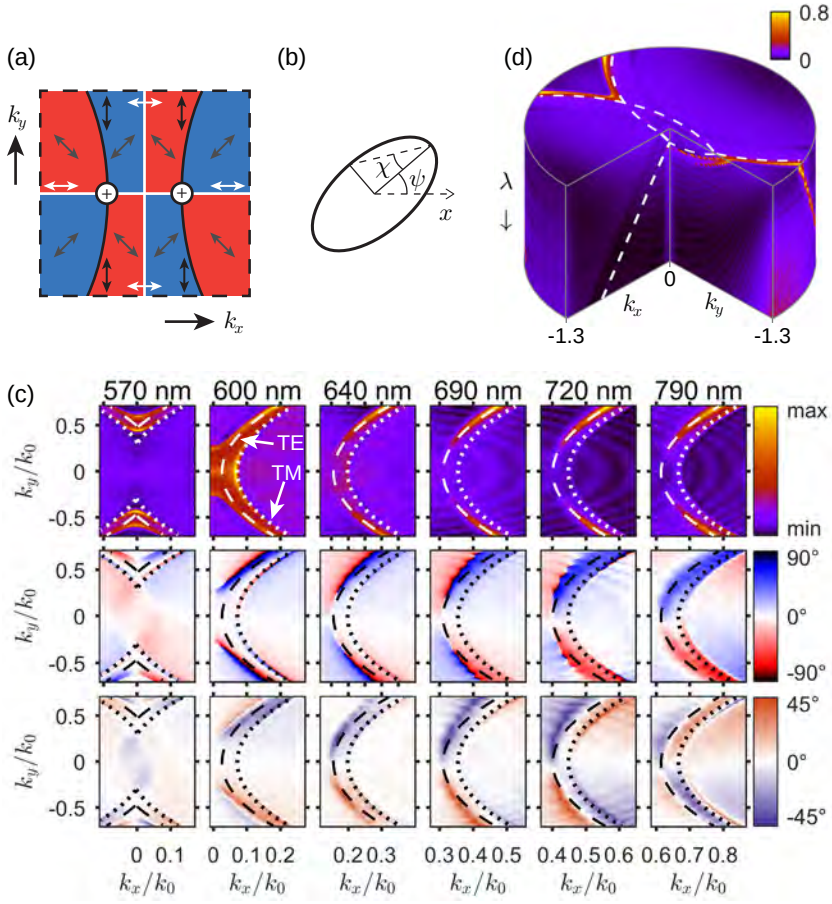

Figure 9.5: Polarization properties of the leaky modes. **(a)** Sketch of the expected polarization of the TM mode radiation. Around each BIC (circles), the polarization angle makes a 2π rotation, corresponding to vortices of topological charge +1. Note that this is not an iso-frequency contour, but a projection of the TM-dispersion surface on the (k_x, k_y) plane. **(b)** Sketch of the polarization ellipse and polarization angles ψ and χ. **(c)** Single-wavelength shots showing intensity (top) and polarization angles ψ (middle) and χ (bottom) of the sample reflection. We zoom in on the TM mode crossing with the positive x-axis. Input light was x-polarized. Dotted (dashed) circles follow TM (TE) mode dispersion. Both modes display clearly distinct features in the maps of ψ and χ. The TM mode disappears on the x-axis around 690nm. Around this point, also ψ changes sign for the TM mode above and below the x-axis, in agreement with the presence of a vortex. Intensity minima (in camera counts) are (left to right) [5, 3, 18, 16, 15, 5] and the respective maxima are [224, 231, 375, 558, 680, 155]. **(d)** Visualization of one of our data cubes, plotting measured reflectivity in 2D momentum vs. wavelength space. The wavelength range is 550 nm to 850 nm. White dashed lines indicate the TM mode dispersion surface. Note that TE and TM modes lie very close to each other.

→ red). This is consistent with the type of behaviour sketched in Fig. 9.5a, and represents the signature of a vortex in the polarization state of the TM-mode radiation. Moreover, these results show excellent agreement with intensity and polarization maps calculated analytically using RCWA, which are shown in Fig. 9.6.

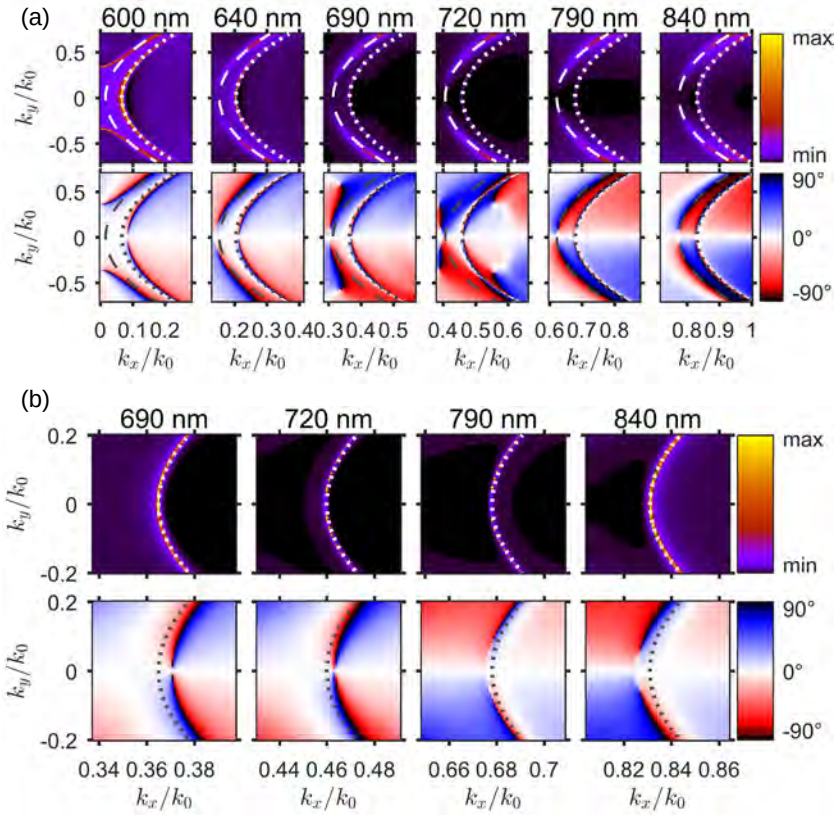

Figure 9.6: Reflected intensity and polarization, calculated from RCWA. (a) Single-wavelength shots showing intensity (top) and polarization angle ψ (bottom) of the sample reflection. These maps are calculated using RCWA, and can be directly compared to those in Fig. 9.5c. We used the same grating as for Fig. 9.3a, except that we added a small index difference between the top (n=1.517) and bottom (n=1.46) medium to account for the finite background reflection in our measurements. Dotted (dashed) circles follow TM (TE) mode dispersion. We see a switching of polarization angle around the BIC wavelength (∼728 nm). Note that we show the same wavelengths as in Fig. 9.5c, except for omitting the map at 570 nm and including one at 840 nm. This was done to show more clearly the polarization switching, because the theoretical BIC lies at somewhat higher wavelength than the experimental. **(b)** Zoomed-in images at the highest four wavelengths in (a), which support very narrow TM modes. This shows more clearly the switching of polarization around the BIC wavelength. We observe a vortex-like feature in every iso-frequency slice, which shifts through the TM branch at the BIC wavelength.

9.3.2 Projecting the dispersion surface

To better visualize the vortices, we track the polarization response over the TM leaky mode dispersion surface, instead of examining fixed-frequency slices. At each iso-frequency image, the TM and TE modes can be parametrized by circles centered at $k_x/k_0 = \lambda/d$, with a radius equal to the effective index. Due to the sample asymmetry between the x- and y-direction, we allow for a slight elliptical correction, i.e. different effective indices n_x and n_y along the x- and the y-directions, respectively. This correction lead to a maximum relative index difference of 2%. By fitting to the intensity profiles, we find that the TM mode is well described by effective indices of

$$n_x = 1.796 - 2.6 \cdot 10^{-4}\lambda - \Theta\left[\lambda - 610\,\mathrm{nm}\right] \cdot 2.5 \cdot 10^{-4}\lambda$$
$$n_y = 1.80 - 3.0 \cdot 10^{-4}\lambda,$$

with λ the free-space wavelength in nm. Here, the last term in n_x, containing the Heaviside function $\Theta[x]$, helps to track the mode at low wavelengths, where the circles approach the Γ-point and experience band bending, leading to a deviation from the elliptical shape. The resulting dispersion surface $(k_x, k_y, \omega(k_x, k_y))$ is indicated by the dashed lines in Fig. 9.5d, which shows an example of one of our data cubes. Similarly, the TE mode can be parametrized by circles with effective indices

$$n_x = 1.785 - 1.8 \cdot 10^{-4}\lambda - \Theta\left[\lambda - 650\,\mathrm{nm}\right] \cdot 2.2 \cdot 10^{-4}\lambda$$
$$n_y = 1.82 - 2.8 \cdot 10^{-4}\lambda.$$

Once the mode dispersion is found, we build up a "collapsed resonance" image by sampling our data on the dispersion surface and projecting this onto the (k_x, k_y) plane. Figure 9.7 shows such 'collapsed resonance' maps of ψ and χ, for TM and TE modes. Two vortices are visible in the ψ map of the TM mode, both on the x axis at opposing $k_x/k_0 = \pm 0.4$. Around these points, we see ψ flip quadrants four times, indicating a full 2π rotation. Comparison to Fig. 9.5a shows that this matches the expected polarization profile for vortices of charge $+1$. This observation directly proves that the BIC is associated to a polarization vortex of in its far field.

Somewhat surprisingly, we see in Fig. 9.7 that not only ψ shows the presence of a vortex, also the ellipticity parameter χ changes dramatically around the BIC. This is also visible in the χ maps in Fig. 9.5c. Theory predicts the BIC and TM leaky wave to have a linear polarization response [330], so one might expect χ to be identically zero throughout k-space. In contrast, Fig. 9.5c shows that both TE and TM modes are visible as distinct, non-zero features in χ. In our experiment the signal mixes with a weak background reflection due to the imperfect matching between the immersion oil and the thermal oxide membrane. This background is not exactly in phase or co-polarized with the TM reflection, leading to an elliptically polarized reflection. The vortex in ψ

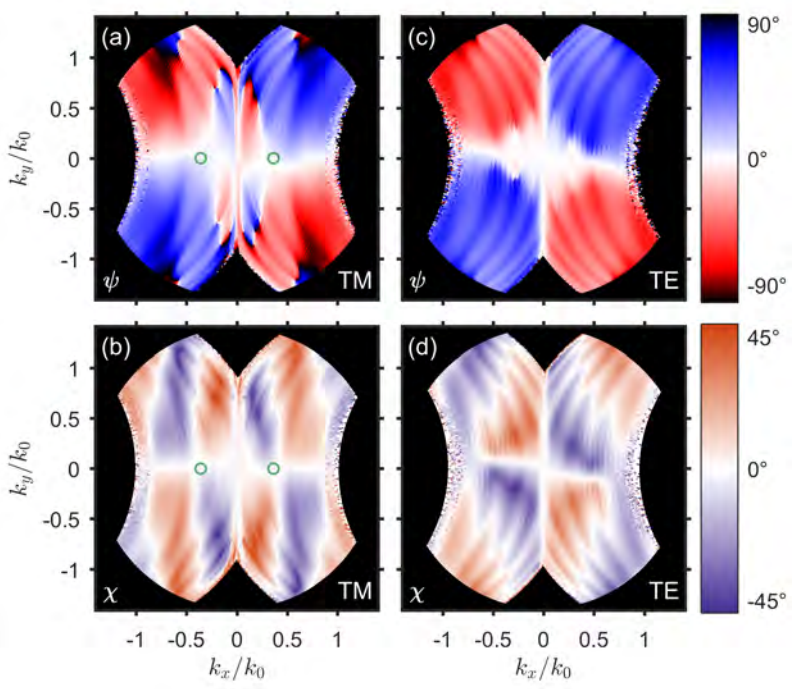

Figure 9.7: Collapsed resonance plots tracing polarization properties over the leaky-wave dispersion surface. We show polarization angles ψ **(a,c)** and χ **(b,d)** for the TM mode **(a,b)** and the TE mode **(c,d)**. At the BIC locations (indicated by the green circles), a polarization vortex is visible in the map of ψ for the TM mode, which is not present in the TE mode. Also the map of TM mode polarization ellipticity χ shows a clear transition around the BIC. All images were taken with input polarization along the x-axis.

for the TM contribution is then imprinted onto the ellipticity profile as a four-fold change of handedness around the BIC, which thus acts as another strong indication of the presence of the polarization vortex at the BIC. Importantly, the nodal lines in ψ and χ, namely, lines where ψ and/or χ equal 0 or 90 degrees, are seen to cross at non-high-symmetry points only in the maps of the TM mode (that is, the branch with the BIC) while nodal-line crossings are clearly absent in the maps of the TE mode (branch with no BIC) except at the origin. In Section 9.4, we will further show how a background contribution can cause a vortex in χ using a simple dipole model.

Finally, we note that, while Fig. 9.5c and Fig. 9.7 show results for x-polarized input beams, we also performed measurements with y-polarized input. These results are discussed in Section 9.A and show good agreement with the results presented here, further confirming the existence of the vortices in the polarization response.

9.4 A simple dipole model for characterization of the BIC

While the presence of a vortex with quantized topological charge explains the robustness of the BIC, it does not tell us what microscopic mechanism underlies it. It was shown by Friedrich and Wintgen that a particular subclass of BICs arises from destructive far-field interference between two resonators [319, 339, 340]. Far-field interference introduces an effective (complex) coupling between the two resonators, leading to the formation of hybrid modes. Under certain conditions, interference can become completely destructive, which renders one of the modes lossless. To identify these resonators in our grating, in Section 9.4.1 we calculate the contributions of electric and magnetic dipole elements to the polarization currents induced in the grating unit cell using full-wave numerical simulations. The results from this analysis are then used in Section 9.4.2 to construct a 'bare bones' dipole model which models the grating as a non-diffractive sheet of non-interacting electromagnetic dipoles. We find that this highly simplified model nevertheless is able to predict both the occurrence of the observed BICs, as well as that of the polarization vortex, which shows clearly that this BIC is of the Friedrich-Wintgen type. Moreover, it is shown that the model can be used to reproduce the anomalous χ-profile of the TM mode that was observed in Fig. 9.7, if a weak background contribution is included, arising from the TE mode and direct reflection by the interface below the grating. Finally, in Section 9.4.3 we demonstrate the versatility of the dipole model by showing that a different combination of dipoles can produce topological charge bouncing, as predicted to occur for BICs in one-dimensional dielectric gratings [330].

9.4.1 Induced polarization currents in the grating

Using full-wave numerical simulations (COMSOL v5.3), we excite the grating at an angle and wavelength (710 nm) very close to the BIC. We then decompose the induced polarization currents in the unit cell into their multipolar contributions.* Fig. 9.8 shows the contributions from the 3 dominant induced electric and magnetic dipoles. At the TM resonance, the z-oriented electric dipole p_z and y-oriented magnetic dipole m_y exhibit a resonant peak, dominating over all other multipolar contributions. We find that these dipoles oscillate in phase with an amplitude ratio $|m_y|/|p_z|$ of 0.48 at resonance. This fact suggests that the BIC might be understood by considering the radiation properties of these two dipolar contributions alone.

*In this chapter, we use units for electric and magnetic fields, dipole moments and polarizabilities as defined in earlier electromagnetic point scattering work [341]. This facilitates comparison between electric and magnetic components, since in this unit system electric and magnetic dipoles have the same units and an electric and a magnetic dipole of equal strength radiate an equal total amount of power.

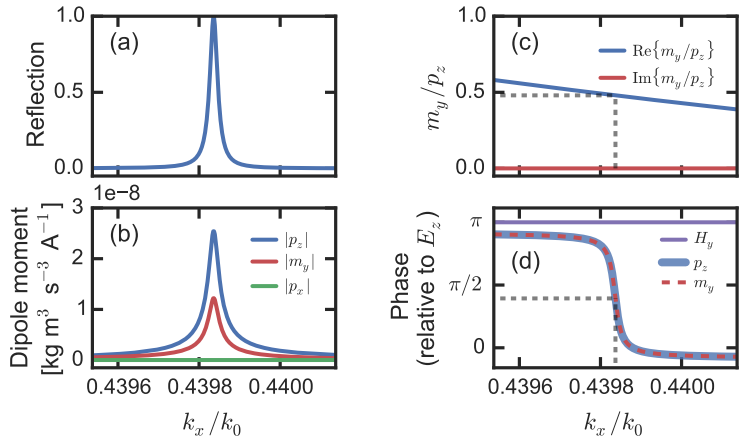

Figure 9.8: Full-wave numerical calculations of the induced dipoles in the grating unit cell. Calculated grating reflectivity **(a)**, induced dipole moments p_x, p_z and m_y **(b)**, the ratio between dominant components m_y and p_z **(c)** and the phases of these dipole moments and the driving field **(d)**, as function of in-plane momentum k_x of an incident plane wave. Reflectivity and two dipole moments p_z and m_y peak as the incident wave is scanned over the resonance condition, and we find a ratio $m_y/p_z = 0.48$ here. Note that the imaginary part of m_y/p_z is six orders of magnitude smaller than its real part, indicating that dipole moments oscillate in phase, as also seen in (d). Dipole moments are per unit length.

9.4.2 Mimicking the grating with a sheet of electromagnetic dipoles

As it appears that the grating response is dominated by a combination of just two dipolar components p_z and m_y, we now proceed to set up a 'bare bones' dipole model to mimic the grating. Let us first consider what the radiation profile of this combination of dipoles looks like. To facilitate comparison with the experiment, we study radiation by a dipole exactly at an interface ($z = 0$) between two media of refractive index 1.5 (top) and 1.45 (bottom), where we look at radiation into the top medium. Far-fields $\mathbf{E}$ and $\mathbf{H}$ radiated by the dipole are calculated according to $\mathbf{E}_{\mathrm{FF}}(\theta,\phi) = \overleftrightarrow{G}(\theta,\phi)\mathbf{p}$, with $E_{\mathrm{FF}} = (E_x, E_y, Ez, H_x, H_y, H_z)$, $\overleftrightarrow{G}(\theta,\phi)$ the Green's function for a dipole near an interface in the angular spectrum representation [12] and $\mathbf{p} = (p_x, p_y, p_z, m_x, m_y, m_z)$ the electromagnetic dipole moment. The calculated far-fields are transformed to the back-focal-plane (BFP) of an ideal objective [12] to create images that can be compared to our measurements. We took the free-space wavelength to be 700 nm.

Fig. 9.9 shows the far-field radiation patterns and polarization profiles of p_z and m_y separately and in the combination approximately as it is found in our grating, *i.e.* with $m_y = 0.5p_z$. Surprisingly, we find that this leads to a node

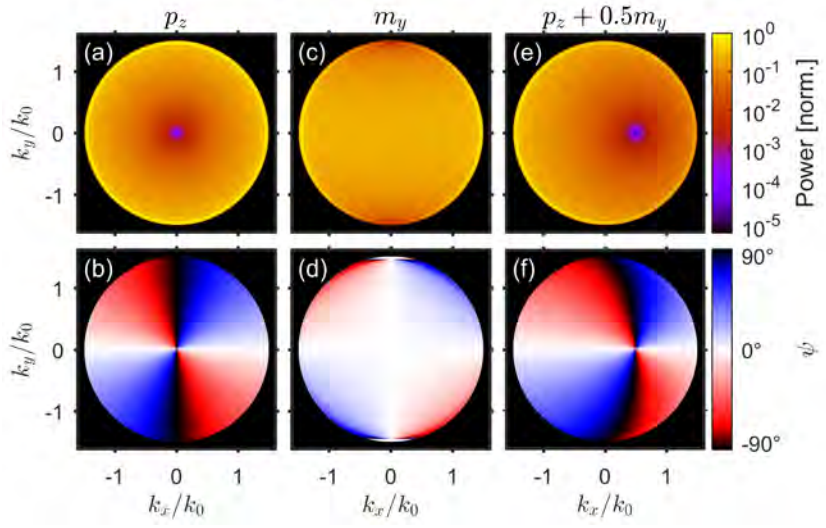

Figure 9.9: Intensity and polarization of electromagnetic dipole emission patterns. We show k-space images of the radiated power (top row) and polarization angle ψ (bottom row) by a z-oriented electric dipole p_z **(a-b)**, a y-oriented magnetic dipole m_y **(c-d)**, and the sum of the two, with $p_z = 1$ and $m_y = 0.5$ **(e-f)**. The individual dipoles display a simple dipolar radiation pattern, while the combination shows a node at a non-high-symmetry point that coincides with a polarization vortex. Radiated power maps in the top row are normalized to their maxima.

in the radiation pattern, as well as a corresponding vortex in polarization. The location of the node at $k_x/k_0 \approx 0.5$ matches the location of the BIC in the simulations ($k_x/k_0 \approx 0.45$). It appears that precisely in the direction of the BIC, this combination of dipoles does not radiate. We note that combinations of electrical and magnetic dipoles have been known to show directional emission patterns, such as that shown in Fig. 9.9e [342, 343]. Here, the location of the intensity node can be tuned using the ratio of p_z and m_y — a stronger magnetic component shifts the node outward, until it reaches the edge of k-space (i.e. grazing angles) exactly at $m_y/p_z = n$, where n is the index of the surrounding medium. This is similar to the famous Kerker condition [344], in this case with the dipole situated at an interface. A negative m_y/p_z ratio flips the node location to the left half-space. Note that this behaviour is reminiscent of the results of Zhen *et al.* [330], where it was shown that BICs in dielectric gratings shift their location if the system parameters, *e.g.* grating fill fraction, are changed. Such changes would also change the relative contributions of electric and magnetic dipole components to polarization currents.

To better mimic the conditions in our experiment, we now drive the dipoles by a plane wave, rather than letting them oscillate at a fixed magnitude. We consider a non-diffractive sheet of non-interacting polarizable

particles, in which the response of the sheet is simply given by the response of the single particle times the particle density [134]. We then monitor the reflected light in the specular direction. The induced dipole moment in the single dipolar particle can be described as $\mathbf{p} = \overleftrightarrow{\alpha} \cdot E_{\mathrm{ext}}(\boldsymbol{r}_0)$, where $\overleftrightarrow{\alpha}$ is a 6-by-6 electromagnetic polarizability tensor [341], and $E_{\mathrm{ext}}(\boldsymbol{r}_0)$ is the 6-element vector containing the electric and magnetic fields at the location $\boldsymbol{r}_0$ of the dipole. We take $\overleftrightarrow{\alpha}$ to be a diagonal matrix, with the diagonal elements $\left(\alpha^p_{xx}, \alpha^p_{yy}, \alpha^p_{zz}, \alpha^m_{xx}, \alpha^m_{yy}, \alpha^m_{zz}\right)$ determining the electric and magnetic polarizability along each axis. The total reflected fields in the specular direction $(\theta_{\mathrm{s}}, \phi_{\mathrm{s}})$ are then given as [341]

$$\mathbf{E}_{\mathrm{r}} = \mathbf{E}_{\mathrm{r,bg}}\left(\theta_{\mathrm{s}}, \phi_{\mathrm{s}}\right) + \frac{2\pi i k_0 n}{\mathcal{A}\cos\theta} \overleftrightarrow{M}\left(\theta_{\mathrm{s}}, \phi_{\mathrm{s}}\right) \cdot \mathbf{p}_0 \tag{9.2}$$

where $\mathbf{E}_{\mathrm{r,bg}}\left(\theta_{\mathrm{s}}, \phi_{\mathrm{s}}\right)$ describes the background contribution due to reflection at the interface, $\mathcal{A}$ is the lattice unit cell area, n the refractive index of the upper medium $\mathbf{p}_0$ the dipole moment of the particle at the origin. The dimensionless tensor $\overleftrightarrow{M}$ is of order unity and depends only on direction, effectively describing the radiation patterns of each dipole [341]. The second term in Eq. (9.2) thus describes the light emitted by the particles in the specular direction. Driving plane waves are taken to be x-polarized in the BFP of the ideal objective, and we subsequently transform them to waves in the sample plane [12]. The total reflected fields are again transformed back onto the BFP, as was also done for Fig. 9.9.

Figure 9.10 shows k-space images of reflected power and polarization angles ψ and χ for an electromagnetic dipole with and without background terms. We take $\mathcal{A} = 0.01\ \mu\mathrm{m}^2$ and take all elements of the polarizability $\overleftrightarrow{\alpha}$ to be zero, except $\alpha^p_{zz} = 2.7 \cdot 10^4\ \mathrm{nm}^3$ (roughly corresponding to the polarizability of a 30 nm sphere) and $\alpha^m_{yy} = 0.17\alpha^p_{zz}$, leading to induced p_z and m_y dipoles only. The numbers were chosen such, that a plane wave incident under an angle close to that of the BIC induces p_z and m_y dipoles with a relative amplitude and phase relation as found in the grating unit cell. In Fig. 9.10a,b we notice a similar behaviour as in Fig. 9.9e,f, with a node in reflection on the positive x-axis coinciding with a vortex in polarization angle ψ. However, a copy of this node can now be found on the negative x-axis. This is because, if the driving plane wave propagation direction is mirrored in the y-axis, the relative phase between its E_z and H_y components is changed from π to 0. This leads to a reversed sign in the relative phase of the induced dipoles p_z and m_y which, as mentioned earlier in this section, moves the node to the other half-space. Figure 9.10b reminds strongly of the type of polarization profile predicted by Zhen et al. [330] for similar structures, and is qualitatively similar to our measured polarization profile. Also note in Fig. 9.10c that the polarization is linear, in accordance with theoretical predictions [330].

Figure 9.10d-f show the case where additional polarizability elements $\alpha^p_{yy} = i\,\alpha^p_{zz}$ and $\alpha^m_{zz} = 0.2i\,\alpha^p_{zz}$ are added to the polarizability tensor, to

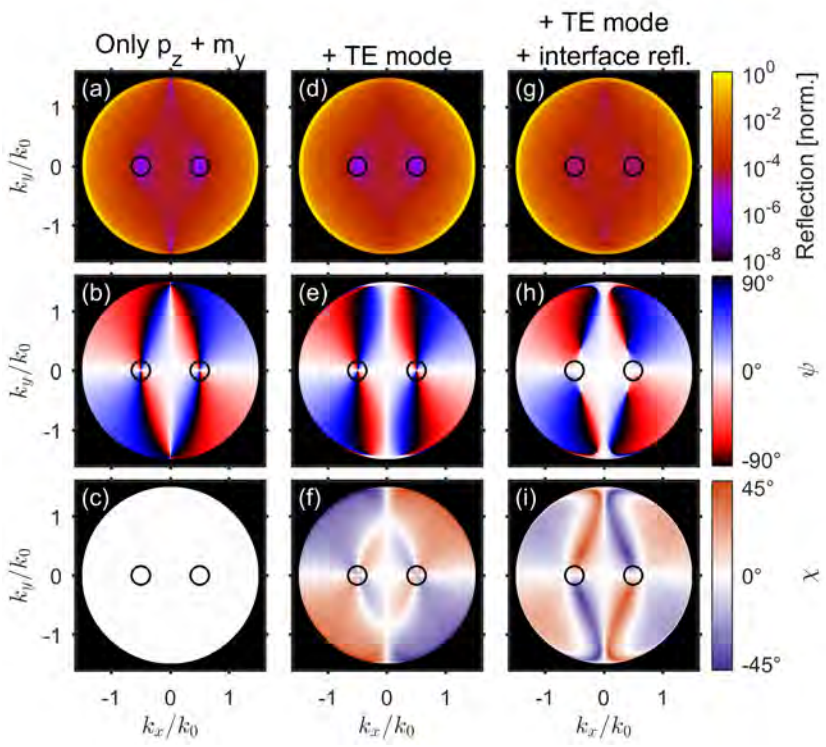

Figure 9.10: Reflection from a dipole sheet and the effect of a background contribution. We show k-space images of the reflected power (top row), polarization angle ψ (middle row) and ellipticity angle χ (bottom row) from a sheet of electromagnetic dipoles. **(a-c)** Dipoles with non-zero polarizability elements α^p_{zz} and α^m_{yy}, with two BICs left and right of the origin. **(d-f)** Dipoles with the same α^p_{zz} and α^m_{yy} as in (a-c), but with additional non-zero elements α^p_{yy} and α^m_{zz}, which are used to model the TE mode. **(g-i)** Same dipoles as in (d-f), now also including a non-resonant reflection contribution from the interface. Reflection maps are normalized to their maxima.

qualitatively mimic the TE mode in the experiment. A similar analysis as discussed in Section 9.4.1 for the TM mode found that illumination of the grating with an s-polarized plane wave at the TE resonance condition leads to a dominant y-polarized electric dipole p_y and a weaker in-phase z-polarized magnetic dipole m_y. It can be seen in Fig. 9.10d-f that the presence of the TE mode does not destroy the nodes, as it is not excitable by x-polarized plane waves on the k_x axis, and that the map of ψ is not strongly affected near the BICs. However, the interference between the vortex contribution of p_z and m_y on the one hand, and the out-of-phase p_y and m_x contributions on the other, lead to a non-zero ellipticity with a crossing of two nodal lines at the vortex, as shown in Fig. 9.10f. Such a crossing was also observed

in the experiment (Fig. 9.7). Note that p_y and m_x do not necessarily need to be $\pi/2$ out of phase with α^p_{zz} to achieve this effect, as chosen here. It simply needs to have a phase difference $0 < \Delta\phi < \pi$. In the experiment, a weak non-resonant reflection from the oil-glass interface is also expected to influence the polarization. Figure 9.10g-i show the case where, on top of the TE mode contributions, the non-resonant Fresnel reflection $\mathbf{E}_{\mathrm{r,bg}}(\theta_\mathrm{s}, \phi_\mathrm{s})$ from the interface was included. We see that this makes the nodes disappear, and the vortices in ψ changes to a profile that strongly resembles our experimental result from Fig. 9.7a. Also, the crossings of the nodal lines in the map of χ remain, shifting slightly outward from the locations of the vortices, as was also experimentally observed (Fig. 9.7b and Fig. 9.13b).

In conclusion, we have developed a simple electromagnetic dipole model that nevertheless fully captures the essential properties of the BIC — the disappearance of reflection and the associated polarization vortex. This provides a novel, simple and intuitive explanation for the presence of a BIC in these type of gratings, based on Friedrich-Wintgen-type interference between two radiation modes in the unit cell of the grating. Moreover, through this model we were able to explain the surprising nodal line crossings in the maps of ellipticity angle χ observed in the experiment. These can arise due to the interference of light from the TM mode, containing the vortex, with light from the TE mode and a non-resonant background reflection.

9.4.3 Topological charge bouncing

An interesting prediction by Zhen et al. [330] is that, since topological charge is a conserved quantity, vortices with charges of the same sign can bounce as the geometrical parameters of the system are varied. This effect can be observed using our simple dipole model. A change in e.g. grating thickness or grating fill factor would lead to a change in the relative strengths of the dipole contributions to the polarization currents in the grating. We can thus mimic such geometric deformations by changing the relative dipole strength in our model. The vortices studied in Section 9.4.2 do not bounce but instead slowly converge towards the origin for increasing electric dipole strength. However, also other combinations of dipoles can show vortices. In Fig. 9.11 we show reflected intensity and polarization plots for dipole sheet with three different combination of x-oriented electric polarizability α^p_{xx} and y-oriented magnetic polarizability α^m_{yy}. The dipoles are located in a medium of index 1.5. The polarization of the incident plane waves is the same as in Fig. 9.10. Note that this combination of dipoles is aligned with the fields of a TM mode on the x-axis, and could thus describe vortices in TM-like modes. For $\alpha^m_{yy}/\alpha^p_{xx} = -1.2$, we see two polarization vortices of charge $+1$ on the x-axis coinciding with nodes in reflection. As we change the relative strength, the vortices move to the Γ-point and subsequently 'bounce' to opposite sides on the y-axis. This is exactly the type of behaviour observed by Zhen et al. for BIC's of a TM-like

mode in a 1D grating [330]. Also note that the coincidence of the two vortices at the Γ-point corresponds to the Kerker condition mentioned in Section 9.4.2 [344].

These results show that the applicability of our dipole model goes beyond the structure experimentally studied in this work. We speculate that any Friedrich-Wintgen BIC in 1D and 2D structures can be explained through some combination of dipoles or multipoles. Combinations of dipoles may be able to match the behaviour of BICs on the lowest-frequency TM- and TE-like branches in 1D or 2D gratings, whose induced polarization currents contain negligible multipolar terms. An extension of the model including multipoles could be applicable to BICs in higher-order branches, as recent results on BIC-like modes in single nano-rods suggest [345].

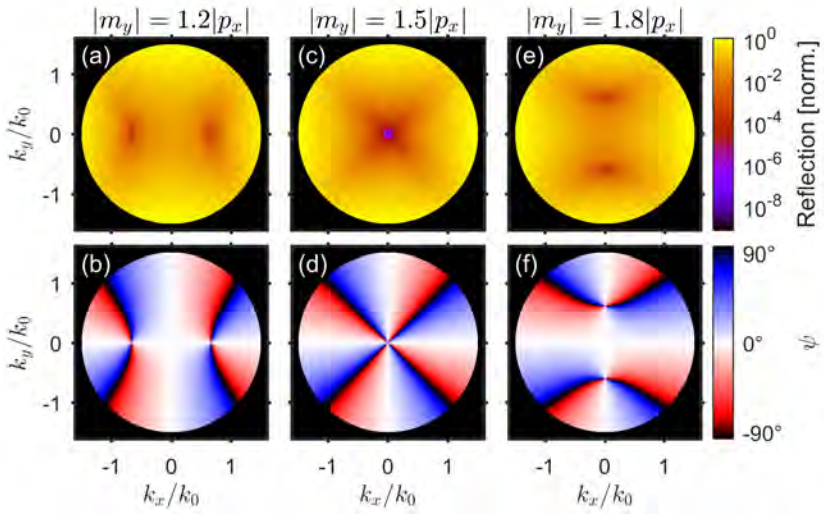

Figure 9.11: Charge bouncing in the dipole model. We show k-space images of the reflected power (top row) and polarization angle ψ (bottom row) from a sheet of electromagnetic dipoles. The dipoles had a nonzero electric x-polarizability α^p_{xx} and a magnetic y-polarizability α^m_{yy}. We consider three different ratios of these polarizability elements: $\alpha^m_{yy}/\alpha^p_{xx} = -1.2$ **(a-b)**, -1.5 **(c-d)** and -1.8 **(e-f)**. Going from low to high ratio, we can see the vortices move from the x-axis to the Γ-point and then bouncing to opposite sides on the y-axis.

9.5 Conclusion and outlook

In conclusion, we experimentally demonstrated the existence of a polarization vortex at an optical bound state in the continuum. Using angle- and wavelength-resolved polarimetric reflectivity measurements on a silicon ni-

tride grating, we traced the TM-like leaky-mode dispersion surface and directly observed a polarization singularity associated with each BIC. We classify the BIC as a Friedrich-Wintgen bound state using a simple dipole model that explains its origin as the result of complete destructive interference between hybridized electric and magnetic dipolar radiation contributions. This result confirms that BICs are tied to a topological property, namely, a vortex of the polarization state in wavevector space. This vortex hence is robust in its existence under continuous perturbations and imperfections that do not destroy the underlying symmetries of the structure. In addition, we assert that measuring the existence of this topological property is more robust evidence for a BIC then standard reflection spectroscopy. Standard reflection measurements provide evidence for a BIC by the disappearance of a reflection signal, which furthermore should present an arbitrarily high Q-factor while approaching the BIC frequency. Observation is challenging because it places nominally infinitely stringent demands on wave vector and frequency resolution. Moreover, finite sample size, absorption and sample disorder will smear out the BIC signature and lead to finite-Q resonances. Instead, the vortex is a robust signature of the radiation cancellation mechanism that defines the BIC, which can be robustly and easily measured from polarization properties around instead of at the BIC condition. Our experimental method is applicable to BICs in any 2D structure with parallel momentum conservation, can be extended to 1D and 0D structures, and allows to study vortices of higher topological charge, in which case one would observe more alternating regions of positive and negative angle ψ, when traversing a loop around the vortex. We believe that, by offering the first experimental evidence of the connection of bound states in the continuum and topological photonic effects, our findings may open new exciting directions in the study and application of robust BICs in different practical scenarios.

Appendices

9.A Polarization measurements for a y-polarized input beam

In Figs. 9.5 and 9.13 we showed results from polarization measurements where the input beam was chosen to be x-polarized (when entering the objective). This is chosen such that we couple preferentially to the TM mode in the vicinity of the k_x-axis, where the BICs are located. However, measurements with the orthogonal input polarization were also performed, and shown in Figs. 9.12 and 9.13.

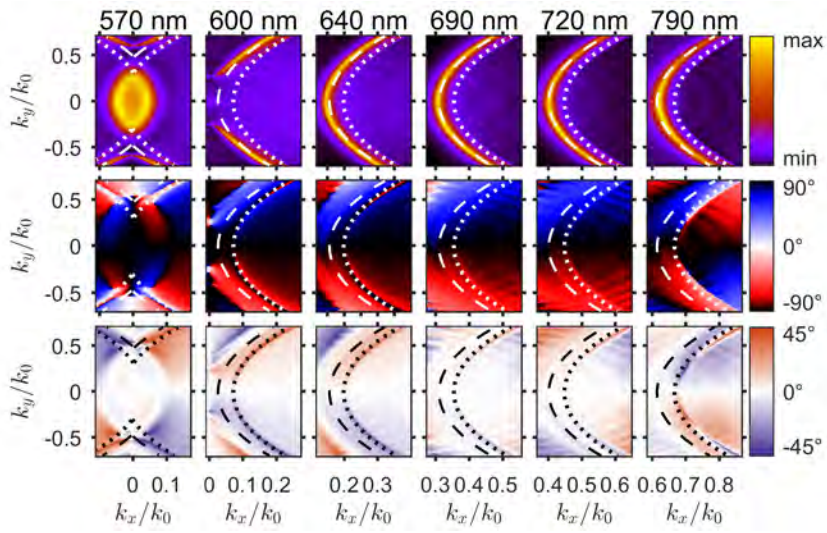

Figure 9.12: Reflected intensity and polarization, for y-polarized input. Single-wavelength shots showing intensity (top) and polarization angles ψ (middle) and χ (bottom) of the sample reflection, similar to Fig. 9.5c yet with the input beam y-polarized. Dotted (dashed) circles follow TM (TE) mode dispersion. Importantly, the same dispersion relation was used to produce the circles as with with x-polarized input (Fig. 9.5c). Here, the y-polarized input causes the TE mode to dominate, and the TM mode to be invisible on the x-axis due to its orthogonal polarization. Nevertheless, one can see the same behaviour for ψ and χ of the TM mode as for x-polarized input: both change sign around the wavelength of the BIC, indicative of the vortex. Intensity minima (in camera counts) in the top row images are (from left to right) [1, 1, 8, 3, 1, 3, 1] and the respective maxima are [908, 896, 1348, 1399, 1770, 1808, 850].

In Fig. 9.12, one can observe that for y-polarized input, the same trends are visible as noted in Fig. 9.5c (x-polarized input)—the modes are clearly visible and we can see ψ switch quadrants around 690 nm, the wavelength of the BIC.

A notable difference is that the TM mode signature disappears close to the x-axis, due to polarization mismatch. The TE mode is dominant throughout most of k-space for y-polarized input, as this mode is better matched to the input polarization and is naturally brighter due to the absence of a BIC.

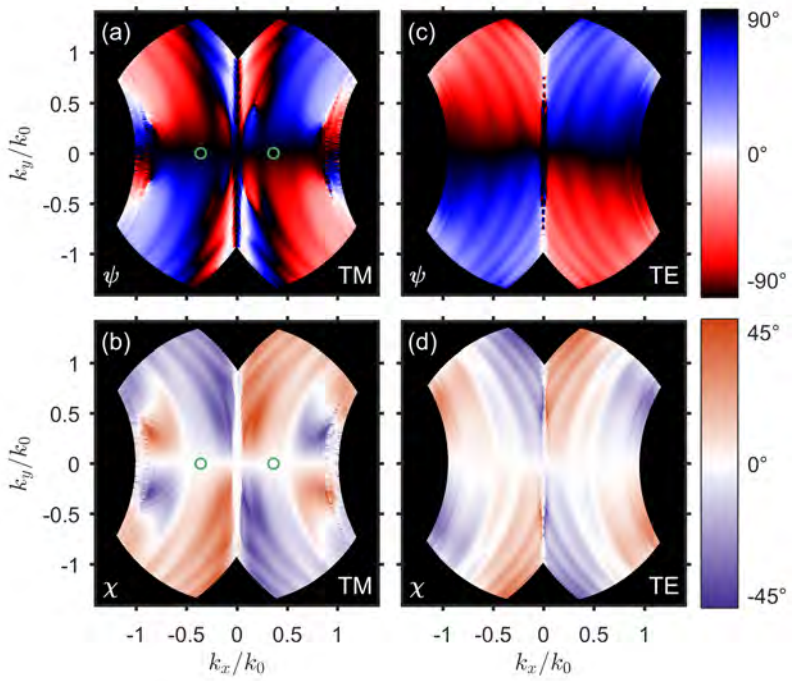

Figure 9.13: Collapsed resonance plots of the leaky-wave dispersion surface, for y-polarized input light. Analogous to Fig. 9.7, we show polarization angles ψ **(a,c)** and χ **(b,d)** for the TM mode **(a,b)** and the TE mode **(c,d)**. Here, input polarization was y-polarized. We may again recognize the presence of vortices at the BIC locations (green circles) in the map of ψ for the TM mode, which is clearly absent in the TE mode.

Figure 9.13 shows the collapsed-resonance images of ψ and χ of the TM and TE modes, now for y-polarized input light. The same dispersion relation was used to produce these plots and those in Fig. 9.7. We can see the vortex clearly in the TM mode ψ map — in the upper right quadrant, for example, ψ changes from red to blue with increasing k_x. Note that this transition does not occur close to the x-axis, since there the TM mode disappears and the reflected signal is dominated by the background and the TE mode. In the TM mode χ map we can see a similar crossing of nodal lines as in Fig. 9.7, with the difference that the sign of χ (that is, polarization handedness) has flipped. This is to be expected, since the ellipticity in reflection arises from the addition of TM reflection and a background contribution. If the TM contribution remains

constant in polarization and the background changes from nearly x-polarized to y-polarized, the sign of handedness flips. For the TE mode, we see a clear absence of a vortex in the map of ψ. We can observe a slight handedness in the χ map, much weaker than for the TM mode because the TE mode reflection is far stronger than the background. A similar crossing of nodal lines as in the TM map is faintly visible, which we attribute to the TM mode forming a very weak background to the TE mode, leading to a trace of its ellipticity being visible in the TE map.

References

[1] J. N. Tinsley, M. I. Molodtsov, R. Prevedel, D. Wartmann, J. Espigulé-Pons, M. Lauwers, and A. Vaziri, *Direct detection of a single photon by humans*, Nat. Commun. **7**, 12172 (2016).

[2] J. Hecht, *City of light: The story of fiber optics* (Oxford University Press, New York, 1999), 2nd ed.

[3] F. Vollmer, and S. Arnold, *Whispering-gallery-mode biosensing: Label-free detection down to single molecules*, Nat. Methods **5**, 591 (2008).

[4] P. Zijlstra, P. M. R. Paulo, and M. Orrit, *Optical detection of single non-absorbing molecules using the surface plasmon resonance of a gold nanorod*, Nat. Nanotechnol. **7**, 379 (2012).

[5] E. Abbe, *Beiträge zur Theorie des Mikroskops und der mikroskopischen Wahrnehmung*, Arch. für Mikroskopische Anat. **9**, 413 (1873).

[6] D. E. Chang, V. Vuletić, and M. D. Lukin, *Quantum nonlinear optics - photon by photon*, Nat. Photonics **8**, 685 (2014).

[7] K. J. Vahala, *Optical microcavities*, Nature **424**, 839 (2003).

[8] H. Raether, *Surface plasmons on smooth and rough surfaces and on gratings* (Springer, Giessen, 1988).

[9] W. L. Barnes, A. Dereux, and T. W. Ebbesen, *Surface plasmon subwavelength optics*, Nature **424**, 824 (2003).

[10] J. A. Schuller, E. S. Barnard, W. Cai, Y. C. Jun, J. S. White, and M. L. Brongersma, *Plasmonics for extreme light concentration and manipulation*, Nat. Mater. **9**, 193 (2010).

[11] G. Grynberg, A. Aspect, and C. Fabre, *Introduction to quantum optics: from the semi-classical approach to quantized light* (Cambridge University Press, New York, 2010).

[12] L. Novotny, and B. Hecht, *Principles of nano-optics* (Cambridge University Press, New York, 2012), 2nd ed.

[13] F. Marquier, C. Sauvan, and J.-J. Greffet, *Revisiting quantum optics with surface plasmons and plasmonic resonators*, ACS Photonics **4**, 2091 (2017).

[14] E. M. Purcell, *Spontaneous emission probabilities at radio frequencies*, Phys. Rev. **69**, 681 (1946).

[15] S. M. S. M. Dutra, *Cavity quantum electrodynamics : the strange theory of light in a box* (John Wiley & Sons, Hoboken, New Jersey, 2005).

[16] A. Auffèves, D. Gerace, J.-M. Gérard, M. F. Santos, L. C. Andreani, and J.-P. Poizat, *Controlling the dynamics of a coupled atom-cavity system by pure dephasing*, Phys. Rev. B **81**, 245419 (2010).

[17] R. Sprik, B. A. van Tiggelen, and A. Lagendijk, *Optical emission in periodic dielectrics*, Europhys. Lett. **35**, 265 (1996).

[18] P. Anger, P. Bharadwaj, and L. Novotny, *Enhancement and quenching of single-molecule fluorescence*, Phys. Rev. Lett. **96**, 113002 (2006).

[19] K. H. Drexhage, *Influence of a dielectric interface on fluorescence decay time*, J. Lumin. **1,2**, 693 (1970).

[20] D. J. Heinzen, and M. S. Feld, *Vacuum radiative level shift and spontaneous-emission linewidth of an atom in an optical resonator*, Phys. Rev. Lett. **59**, 2623 (1987).

[21] D. Miller, *Device requirements for optical interconnects to silicon chips*, Proc. IEEE **97**, 1166 (2009).

[22] K. L. Tsakmakidis, R. W. Boyd, E. Yablonovitch, and X. Zhang, *Large spontaneous-emission enhancements in metallic nanostructures: Towards LEDs faster than lasers*, Opt. Express **24**, 17916 (2016).

[23] P. Lodahl, S. Mahmoodian, and S. Stobbe, *Interfacing single photons and single quantum dots with photonic nanostructures*, Rev. Mod. Phys. **87**, 347 (2015).

[24] S. A. Mann, R. R. Grote, R. M. Osgood, A. Alù, and E. C. Garnett, *Opportunities and limitations for nanophotonic structures to exceed the Shockley-Queisser limit*, ACS Nano **10**, 8620 (2016).

[25] M. T. Hill, and M. C. Gather, *Advances in small lasers*, Nat. Photonics **8**, 908 (2014).

[26] F. Vollmer, and L. Yang, *Label-free detection with high-Q microcavities: a review of biosensing mechanisms for integrated devices*, Nanophotonics **1**, 267 (2012).

[27] H. Bethe, and J. Schwinger, *Perturbation theory for cavities* (Massachusetts Institute of Technology, Radiation Laboratory, Cambridge, MA, 1943).

[28] P. Zoller, T. Beth, D. Binosi, R. Blatt, H. Briegel, D. Bruss, T. Calarco, J. I. Cirac, D. Deutsch, J. Eisert, A. Ekert, C. Fabre, N. Gisin, P. Grangiere, M. Grassl, et al., *Quantum information processing and communication*, Eur. Phys. J. D **36**, 203 (2005).

[29] H. J. Kimble, *The quantum internet*, Nature **453**, 1023 (2008).

[30] J. L. O'Brien, A. Furusawa, and J. Vučković, *Photonic quantum technologies*, Nat. Photonics **3**, 687 (2009).

[31] B. Lounis, and M. Orrit, *Single-photon sources*, Rep. Prog. Phys. **68**, 1129 (2005).

[32] P. Senellart, G. Solomon, and A. White, *High-performance semiconductor quantum-dot single-photon sources*, Nat. Nanotechnol. **12**, 1026 (2017).

[33] C. Santori, D. Fattal, and Y. Yamamoto, *Single-photon devices and applications* (John Wiley & Sons, Weinheim, 2010).

[34] J. M. Raimond, M. Brune, and S. Haroche, *Manipulating quantum entanglement with atoms and photons in a cavity*, Rev. Mod. Phys. **73**, 565 (2001).

[35] G. Rempe, H. Walther, and N. Klein, *Observation of quantum collapse and revival in a one-atom maser*, Phys. Rev. Lett. **58**, 353 (1987).

[36] R. J. Thompson, G. Rempe, and H. J. Kimble, *Observation of normal-mode splitting for an atom in an optical cavity*, Phys. Rev. Lett. **68**, 1132 (1992).

[37] A. Reinhard, T. Volz, M. Winger, A. Badolato, K. J. Hennessy, E. L. Hu, and A. Imamoğlu, *Strongly correlated photons on a chip*, Nat. Photonics **6**, 93 (2012).

[38] D. W. Vernooy, V. S. Ilchenko, H. Mabuchi, E. W. Streed, and H. J. Kimble, *High-Q measurements of fused-silica microspheres in the near infrared*, Opt. Lett. **23**, 247 (1998).

[39] S. John, *Localization of light*, Phys. Today **44**, 32 (1991).

[40] G. Khitrova, H. M. Gibbs, M. Kira, S. W. Koch, and A. Scherer, *Vacuum Rabi splitting in semiconductors*, Nat. Phys. **2**, 81 (2006).

[41] F. D. Martini, G. Innocenti, G. R. Jacobovitz, and P. Mataloni, *Anomalous spontaneous emission time in a microscopic optical cavity*, Phys. Rev. Lett. **59**, 2955 (1987).

[42] A. Boca, R. Miller, K. M. Birnbaum, A. D. Boozer, J. McKeever, and H. J. Kimble, *Observation of the vacuum Rabi spectrum for one trapped atom*, Phys. Rev. Lett. **93**, 233603 (2004).

[43] O. Gazzano, S. Michaelis de Vasconcellos, C. Arnold, A. Nowak, E. Galopin, I. Sagnes, L. Lanco, A. Lemaître, and P. Senellart, *Bright solid-state sources of indistinguishable single photons*, Nat. Commun. **4**, 1425 (2013).

[44] X. Ding, Y. He, Z.-C. Duan, N. Gregersen, M.-C. Chen, S. Unsleber, S. Maier, C. Schneider, M. Kamp, S. Höfling, C.-Y. Lu, and J.-W. Pan, *On-demand single photons with high extraction efficiency and near-unity indistinguishability from a resonantly driven quantum dot in a micropillar*, Phys. Rev. Lett. **116**, 020401 (2016).

[45] S. Strauf, N. G. Stoltz, M. T. Rakher, L. A. Coldren, P. M. Petroff, and D. Bouwmeester, *High-frequency single-photon source with polarization control*, Nat. Photonics **1**, 704 (2007).

[46] J. P. Reithmaier, G. Sęk, A. Löffler, C. Hofmann, S. Kuhn, S. Reitzenstein, L. V. Keldysh, V. D. Kulakovskii, T. L. Reinecke, and A. Forchel, *Strong coupling in a single quantum dot-semiconductor microcavity system*, Nature **432**, 197 (2004).

[47] T. J. Kippenberg, S. M. Spillane, and K. J. Vahala, *Demonstration of ultra-high-Q small mode volume toroid microcavities on a chip*, Appl. Phys. Lett. **85**, 6113 (2004).

[48] K. Srinivasan, and O. Painter, *Linear and nonlinear optical spectroscopy of a strongly coupled microdisk-quantum dot system*, Nature **450**, 862 (2007).

[49] E. Peter, P. Senellart, D. Martrou, A. Lemaître, J. Hours, J.-M. Gérard, and J. Bloch, *Exciton-photon strong-coupling regime for a single quantum dot embedded in a microcavity*, Phys. Rev. Lett. **95**, 067401 (2005).

[50] T. J. Kippenberg, S. M. Spillane, D. K. Armani, and K. J. Vahala, *Ultralow-threshold microcavity Raman laser on a microelectronic chip*, Opt. Lett. **29**, 1224 (2004).

[51] T. Asano, Y. Ochi, Y. Takahashi, K. Kishimoto, and S. Noda, *Photonic crystal nanocavity with a Q-factor exceeding eleven million*, Opt. Express **25**, 1769 (2017).

[52] S. Noda, M. Fujita, and T. Asano, *Spontaneous-emission control by photonic crystals and nanocavities*, Nat. Photonics **1**, 449 (2007).

[53] T. Yoshie, A. Scherer, J. Hendrickson, G. Khitrova, H. M. Gibbs, G. Rupper, C. Ell, O. B. Shchekin, and D. G. Deppe, *Vacuum Rabi splitting with a single quantum dot in a photonic crystal nanocavity*, Nature **432**, 200 (2004).

[54] K. Hennessy, A. Badolato, M. Winger, D. Gerace, M. Atatüre, S. Gulde, S. Fält, E. L. Hu, and A. Imamoğlu, *Quantum nature of a strongly coupled single quantum dot-cavity system*, Nature **445**, 896 (2007).

[55] A. Faraon, I. Fushman, D. Englund, N. Stoltz, P. Petroff, and J. Vučković, *Coherent generation of non-classical light on a chip via photon-induced tunnelling and blockade*, Nat. Phys. **4**, 859 (2008).

[56] A. Sipahigil, R. E. Evans, D. D. Sukachev, M. J. Burek, J. Borregaard, M. K.

Bhaskar, C. T. Nguyen, J. L. Pacheco, H. A. Atikian, C. Meuwly, R. M. Camacho, F. Jelezko, E. Bielejec, H. Park, M. Lončar, et al., *An integrated diamond nanophotonics platform for quantum-optical networks*, Science **354**, 847 (2016).

[57] B. Ellis, M. A. Mayer, G. Shambat, T. Sarmiento, J. Harris, E. E. Haller, and J. Vučković, *Ultralow-threshold electrically pumped quantum-dot photonic-crystal nanocavity laser*, Nat. Photonics **5**, 297 (2011).

[58] S. Noda, *Photonic crystal lasers - ultimate nanolasers and broad-area coherent lasers [Invited]*, J. Opt. Soc. Am. B **27**, B1 (2010).

[59] S. Strauf, K. Hennessy, M. T. Rakher, Y.-S. Choi, A. Badolato, L. C. Andreani, E. L. Hu, P. M. Petroff, and D. Bouwmeester, *Self-tuned quantum dot gain in photonic crystal lasers*, Phys. Rev. Lett. **96**, 127404 (2006).

[60] H. Altug, D. Englund, and J. Vučković, *Ultrafast photonic crystal nanocavity laser*, Nat. Phys. **2**, 484 (2006).

[61] A. F. Koenderink, *On the use of Purcell factors for plasmon antennas.*, Opt. Lett. **35**, 4208 (2010).

[62] P. T. Kristensen, C. Van Vlack, and S. Hughes, *Generalized effective mode volume for leaky optical cavities.*, Opt. Lett. **37**, 1649 (2012).

[63] C. Sauvan, J. P. Hugonin, I. S. Maksymov, and P. Lalanne, *Theory of the spontaneous optical emission of nanosize photonic and plasmon resonators*, Phys. Rev. Lett. **110**, 237401 (2013).

[64] J. Yang, M. Perrin, and P. Lalanne, *Analytical formalism for the interaction of two-level quantum systems with metal nanoresonators*, Phys. Rev. X **5**, 021008 (2015).

[65] U. Resch-Genger, M. Grabolle, S. Cavaliere-Jaricot, R. Nitschke, and T. Nann, *Quantum dots versus organic dyes as fluorescent labels*, Nat. Methods **5**, 763 (2008).

[66] A. F. Koenderink, *Single-photon nanoantennas*, ACS Photonics **4**, 710 (2017).

[67] L. Novotny, *Effective wavelength scaling for optical antennas*, Phys. Rev. Lett. **98**, 266802 (2007).

[68] G. M. Akselrod, C. Argyropoulos, T. B. Hoang, C. Ciracì, C. Fang, J. Huang, D. R. Smith, and M. H. Mikkelsen, *Probing the mechanisms of large Purcell enhancement in plasmonic nanoantennas*, Nat. Photonics **8**, 835 (2014).

[69] C. Belacel, B. Habert, F. Bigourdan, F. Marquier, J.-P. Hugonin, S. Michaelis de Vasconcellos, X. Lafosse, L. Coolen, C. Schwob, C. Javaux, B. Dubertret, J.-J. Greffet, P. Senellart, and A. Maitre, *Controlling spontaneous emission with plasmonic optical patch antennas*, Nano Lett. **13**, 1516 (2013).

[70] R. Chikkaraddy, B. de Nijs, F. Benz, S. J. Barrow, O. A. Scherman, E. Rosta, A. Demetriadou, P. Fox, O. Hess, and J. J. Baumberg, *Single-molecule strong coupling at room temperature in plasmonic nanocavities*, Nature **535**, 127 (2016).

[71] A. G. Curto, G. Volpe, T. H. Taminiau, M. P. Kreuzer, R. Quidant, and N. F. van Hulst, *Unidirectional emission of a quantum dot coupled to a nanoantenna*, Science **329**, 930 (2010).

[72] H. Aouani, O. Mahboub, E. Devaux, H. Rigneault, T. W. Ebbesen, and J. Wenger, *Plasmonic antennas for directional sorting of fluorescence emission*, Nano Lett. **11**, 2400 (2011).

[73] R. Faggiani, J. Yang, and P. Lalanne, *Quenching, plasmonic, and radiative decays in nanogap emitting devices*, ACS Photonics **2**, 1739 (2015).

[74] K. J. Russell, T.-L. Liu, S. Cui, and E. L. Hu, *Large spontaneous emission enhancement in plasmonic nanocavities*, Nat. Photonics **6**, 459 (2012).

[75] S. Bidault, A. Devilez, V. Maillard, L. Lermusiaux, J.-M. Guigner, N. Bonod, and J. Wenger, *Picosecond lifetimes with high quantum yields from single-photon-emitting colloidal nanostructures at room temperature*, ACS Nano **10**, 4806 (2016).

[76] A. Kinkhabwala, Z. Yu, S. Fan, Y. Avlasevich, K. Müllen, and W. E. Moerner, *Large single-molecule fluorescence enhancements produced by a bowtie nanoantenna*, Nat. Photonics **3**, 654 (2009).

[77] H. Groß, J. M. Hamm, T. Tufarelli, O. Hess, and B. Hecht, *Near-field strong coupling of single quantum dots*, Sci. Adv. **4**, eaar4906 (2018).

[78] K. Matsuzaki, S. Vassant, H.-W. Liu, A. Dutschke, B. Hoffmann, X. Chen, S. Christiansen, M. R. Buck, J. A. Hollingsworth, S. Götzinger, and V. Sandoghdar, *Strong plasmonic enhancement of biexciton emission: controlled coupling of a single quantum dot to a gold nanocone antenna*, Sci. Rep. **7**, 42307 (2017).

[79] X.-W. Chen, M. Agio, and V. Sandoghdar, *Metallodielectric hybrid antennas for ultrastrong enhancement of spontaneous emission*, Phys. Rev. Lett. **108**, 233001 (2012).

[80] A. Mohammadi, F. Kaminski, V. Sandoghdar, and M. Agio, *Fluorescence enhancement with the optical (bi-) conical antenna*, J. Phys. Chem. C **114**, 7372 (2010).

[81] T. Coenen, E. J. R. Vesseur, A. Polman, and A. F. Koenderink, *Directional emission from plasmonic Yagi-Uda antennas probed by angle-resolved cathodoluminescence spectroscopy*, Nano Lett. **11**, 3779 (2011).

[82] L.-M. Duan, and H. J. Kimble, *Scalable photonic quantum computation through cavity-assisted interactions*, Phys. Rev. Lett. **92**, 127902 (2004).

[83] W. Kim, V. P. Safonov, V. M. Shalaev, and R. L. Armstrong, *Fractals in microcavities: Giant coupled, multiplicative enhancement of optical responses*, Phys. Rev. Lett. **82**, 4811 (1999).

[84] S. I. Shopova, C. W. Blackledge, and A. T. Rosenberger, *Enhanced evanescent coupling to whispering-gallery modes due to gold nanorods grown on the microresonator surface*, Appl. Phys. B **93**, 183 (2008).

[85] F. De Angelis, M. Patrini, G. Das, I. Maksymov, M. Galli, L. Businaro, L. C. Andreani, and E. Di Fabrizio, *A hybrid plasmonic-photonic nanodevice for label-free detection of a few molecules*, Nano Lett. **8**, 2321 (2008).

[86] V. R. Dantham, S. Holler, C. Barbre, D. Keng, V. Kolchenko, and S. Arnold, *Label-free detection of single protein using a nanoplasmonic-photonic hybrid microcavity*, Nano Lett. **13**, 3347 (2013).

[87] M. A. Santiago-Cordoba, M. Cetinkaya, S. V. Boriskina, F. Vollmer, and M. C. Demirel, *Ultrasensitive detection of a protein by optical trapping in a photonic-plasmonic microcavity*, J. Biophotonics **5**, 629 (2012).

[88] F. Liang, Y. Guo, S. Hou, and Q. Quan, *Photonic-plasmonic hybrid single-molecule nanosensor measures the effect of fluorescent labels on DNA-protein dynamics*, Sci. Adv. **3**, e1602991 (2017).

[89] A. Bozzola, S. Perotto, and F. De Angelis, *Hybrid plasmonic-photonic whispering*

gallery mode resonators for sensing: a critical review, Analyst **142**, 883 (2017).

[90] M. D. Baaske, and F. Vollmer, *Optical observation of single atomic ions interacting with plasmonic nanorods in aqueous solution*, Nat. Photonics **10**, 733 (2016).

[91] Y.-W. Hu, B.-B. Li, Y.-X. Liu, Y.-F. Xiao, and Q. Gong, *Hybrid photonic-plasmonic mode for refractometer and nanoparticle trapping*, Opt. Commun. **291**, 380 (2013).

[92] P.-T. Lin, H.-Y. Chu, T.-W. Lu, and P.-T. Lee, *Trapping particles using waveguide-coupled gold bowtie plasmonic tweezers*, Lab Chip **14**, 4647 (2014).

[93] D. Conteduca, F. Dell'Olio, F. Innone, C. Ciminelli, and M. N. Armenise, *Rigorous design of an ultra-high Q/V photonic/plasmonic cavity to be used in biosensing applications*, Opt. Laser Technol. **77**, 151 (2016).

[94] D. Conteduca, C. Reardon, M. G. Scullion, F. Dell'Olio, M. N. Armenise, T. F. Krauss, and C. Ciminelli, *Ultra-high Q/V hybrid cavity for strong light-matter interaction*, APL Photonics **2**, 086101 (2017).

[95] J.-N. Liu, Q. Huang, K.-K. Liu, S. Singamaneni, and B. T. Cunningham, *Nanoantenna-microcavity hybrids with highly cooperative plasmonic-photonic coupling*, Nano Lett. **17**, 7569 (2017).

[96] M. R. Gartia, S. Seo, J. Kim, T.-W. Chang, G. Bahl, M. Lu, G. L. Liu, and J. G. Eden, *Injection-seeded optoplasmonic amplifier in the visible*, Sci. Rep. **4**, 6168 (2015).

[97] T. Zhang, S. Callard, C. Jamois, C. Chevalier, D. Feng, and A. Belarouci, *Plasmonic-photonic crystal coupled nanolaser*, Nanotechnology **25**, 315201 (2014).

[98] M. Mivelle, P. Viktorovitch, F. I. Baida, A. El Eter, Z. Xie, T.-P. Vo, E. Atie, G. W. Burr, D. Nedeljkovic, J.-Y. Rauch, S. Callard, and T. Grosjean, *Light funneling from a photonic crystal laser cavity to a nano-antenna: overcoming the diffraction limit in optical energy transfer down to the nanoscale.*, Opt. Express **22**, 15075 (2014).

[99] M. Chamanzar, and A. Adibi, *Hybrid nanoplasmonic-photonic resonators for efficient coupling of light to single plasmonic nanoresonators*, Opt. Express **19**, 22292 (2011).

[100] W. Ahn, S. V. Boriskina, Y. Hong, and B. M. Reinhard, *Photonic-plasmonic mode coupling in on-chip integrated optoplasmonic molecules.*, ACS Nano **6**, 951 (2012).

[101] F. Ren, H. Takashima, Y. Tanaka, H. Fujiwara, and K. Sasaki, *Two-photon excited fluorescence from a pseudoisocyanine-attached gold tip via a plasmonic-photonic hybrid system*, Opt. Express **23**, 21730 (2015).

[102] W. Ahn, X. Zhao, Y. Hong, and B. M. Reinhard, *Low-power light guiding and localization in optoplasmonic chains obtained by directed self-assembly.*, Sci. Rep. **6**, 22621 (2016).

[103] B. Chen, R. Bruck, D. Traviss, A. Z. Khokhar, S. Reynolds, D. J. Thomson, G. Z. Mashanovich, G. T. Reed, and O. L. Muskens, *Hybrid photon-plasmon coupling and ultrafast control of nanoantennas on a silicon photonic chip*, Nano Lett. **18**, 610 (2018).

[104] S. V. Boriskina, and B. M. Reinhard, *Spectrally and spatially configurable superlenses for optoplasmonic nanocircuits*, PNAS **108**, 3147 (2011).

[105] Y.-F. Xiao, Y.-C. Liu, B.-B. Li, Y.-L. Chen, Y. Li, and Q. Gong, *Strongly enhanced light-matter interaction in a hybrid photonic-plasmonic resonator*, Phys. Rev. A **85**, 031805 (2012).

[106] M. K. Dezfouli, R. Gordon, and S. Hughes, *Modal theory of modified spontaneous*

emission of a quantum emitter in a hybrid plasmonic photonic-crystal cavity system, Phys. Rev. A **95**, 013846 (2017).

[107] S. Liu, J. Li, R. Yu, and Y. Wu, *Generation of long-time maximum entanglement between two dipole emitters via a hybrid photonic-plasmonic resonator*, Phys. Rev. A **87**, 2 (2013).

[108] P. Peng, Y.-C. Liu, D. Xu, Q.-T. Cao, G. Lu, Q. Gong, and Y.-F. Xiao, *Enhancing coherent light-matter interactions through microcavity-engineered plasmonic resonances*, Phys. Rev. Lett. **119**, 233901 (2017).

[109] B. Gurlek, V. Sandoghdar, and D. Martín-Cano, *Manipulation of quenching in nanoantenna-emitter systems enabled by external detuned cavities: A path to enhance strong-coupling*, ACS Photonics **5**, 456 (2018).

[110] M. Barth, S. Schietinger, S. Fischer, J. Becker, N. Nüsse, T. Aichele, B. Löchel, C. Sönnichsen, and O. Benson, *Nanoassembled plasmonic-photonic hybrid cavity for tailored light-matter coupling*, Nano Lett. **10**, 891 (2010).

[111] S. Cui, X. Zhang, T.-l. Liu, J. Lee, D. Bracher, K. Ohno, D. Awschalom, and E. L. Hu, *Hybrid plasmonic photonic crystal cavity for enhancing emission from near-surface nitrogen vacancy centers in diamond*, ACS Photonics **2**, 465 (2015).

[112] R. Ameling, and H. Giessen, *Cavity plasmonics: large normal mode splitting of electric and magnetic particle plasmons induced by a photonic microcavity.*, Nano Lett. **10**, 4394 (2010).

[113] R. Ameling, and H. Giessen, *Microcavity plasmonics: strong coupling of photonic cavities and plasmons*, Laser Photon. Rev. **7**, 141 (2013).

[114] A. Vázquez-Guardado, A. Safaei, S. Modak, D. Franklin, and D. Chanda, *Hybrid coupling mechanism in a system supporting high order diffraction, plasmonic, and cavity resonances*, Phys. Rev. Lett. **113**, 263902 (2014).

[115] M. Bahramipanah, S. Dutta-Gupta, B. Abasahl, and O. J. F. Martin, *Cavity-coupled plasmonic device with enhanced sensitivity and figure-of-merit*, ACS Nano **9**, 7621 (2015).

[116] F. Wang, and H. Harutyunyan, *Tailoring the quality factors and nonlinear response in hybrid plasmonic-dielectric metasurfaces*, Opt. Express **26**, 120 (2018).

[117] M. S. Tame, K. R. McEnery, Ş. K. Özdemir, J. Lee, S. A. Maier, and M. S. Kim, *Quantum plasmonics*, Nat. Phys. **9**, 329 (2013).

[118] M. Frimmer, and A. F. Koenderink, *Superemitters in hybrid photonic systems: A simple lumping rule for the local density of optical states and its breakdown at the unitary limit*, Phys. Rev. B **86**, 235428 (2012).

[119] C. F. Bohren, and D. R. Huffman, *Absorption and scattering of light by small particles* (John Wiley & Sons, New York, 1983).

[120] P. de Vries, D. V. van Coevorden, and A. Lagendijk, *Point scatterers for classical waves*, Rev. Mod. Phys. **70**, 447 (1998).

[121] S. Haroche, *Cavity quantum electrodynamics*, in *Fundam. Syst. Quantum Opt. Proc. Les Houches Summer Sch. Sess. LIII*, edited by J. Dalibard, J.-M. Raimond, and J. Zinn-Justin (Elsevier, Amsterdam, 1992).

[122] A. Lagendijk, and B. A. van Tiggelen, *Resonant multiple scattering of light*, Phys. Rep. **270**, 143 (1996).

[123] F. Bernal Arango, and A. F. Koenderink, *Polarizability tensor retrieval for magnetic and plasmonic antenna design*, New J. Phys. **15**, 073023 (2013).

[124] F. Bernal Arango, T. Coenen, and A. F. Koenderink, *Underpinning hybridization intuition for complex nanoantennas by magnetoelectric quadrupolar polarizability retrieval*, ACS Photonics **1**, 444 (2014).

[125] J. D. Jackson, *Classical electrodynamics* (John Wiley & Sons, Hoboken, NJ, 1999), 3rd ed.

[126] W. Yan, R. Faggiani, and P. Lalanne, *Rigorous modal analysis of plasmonic nanoresonators*, Phys. Rev. B **97**, 205422 (2018).

[127] H. A. Haus, *Waves and fields in optoelectronics* (Prentice-Hall, Englewood Cliffs, NJ, 1984), 1st ed.

[128] J. C. Knight, G. Cheung, F. Jacques, and T. A. Birks, *Phase-matched excitation of whispering-gallery-mode resonances by a fiber taper*, Opt. Lett. **22**, 1129 (1997).

[129] S. M. Spillane, T. J. Kippenberg, O. J. Painter, and K. J. Vahala, *Ideality in a fiber-taper-coupled microresonator system for application to cavity quantum electrodynamics*, Phys. Rev. Lett. **91**, 043902 (2003).

[130] F. Ruesink, H. M. Doeleman, R. Hendrikx, A. F. Koenderink, and E. Verhagen, *Perturbing open cavities: Anomalous resonance frequency shifts in a hybrid cavity-nanoantenna system*, Phys. Rev. Lett. **115**, 203904 (2015).

[131] M. L. Gorodetsky, A. D. Pryamikov, and V. S. Ilchenko, *Rayleigh scattering in high-Q microspheres*, J. Opt. Soc. Am. B **17**, 1051 (2000).

[132] T. J. Kippenberg, S. M. Spillane, and K. J. Vahala, *Modal coupling in traveling-wave resonators*, Opt. Lett. **27**, 1669 (2002).

[133] R. Waldron, *Perturbation theory of resonant cavities*, Proc. IEE Part C Monogr. **107**, 272 (1960).

[134] F. J. García de Abajo, *Colloquium : Light scattering by particle and hole arrays*, Rev. Mod. Phys. **79**, 1267 (2007).

[135] M. F. Limonov, M. V. Rybin, A. N. Poddubny, and Y. S. Kivshar, *Fano resonances in photonics*, Nat. Photonics **11**, 543 (2017).

[136] B. C. Buchler, T. Kalkbrenner, C. Hettich, and V. Sandoghdar, *Measuring the quantum efficiency of the optical emission of single radiating dipoles using a scanning mirror.*, Phys. Rev. Lett. **95**, 063003 (2005).

[137] K. D. Heylman, N. Thakkar, E. H. Horak, S. C. Quillin, C. Cherqui, K. A. Knapper, D. J. Masiello, and R. H. Goldsmith, *Optical microresonators as single-particle absorption spectrometers*, Nat. Photonics **10**, 788 (2016).

[138] N. Thakkar, M. T. Rea, K. C. Smith, K. D. Heylman, S. C. Quillin, K. A. Knapper, E. H. Horak, D. J. Masiello, and R. H. Goldsmith, *Sculpting fano resonances to control photonic-plasmonic hybridization*, Nano Lett. **17**, 6927 (2017).

[139] J. J. Penninkhof, L. A. Sweatlock, A. Moroz, H. A. Atwater, A. van Blaaderen, and A. Polman, *Optical cavity modes in gold shell colloids*, J. Appl. Phys. **103**, 123105 (2008).

[140] H. Mertens, A. F. Koenderink, and A. Polman, *Plasmon-enhanced luminescence near noble-metal nanospheres: Comparison of exact theory and an improved Gersten*

and Nitzan model, Phys. Rev. B **76**, 115123 (2007).

[141] P. Lodahl, A. Floris van Driel, I. S. Nikolaev, A. Irman, K. Overgaag, D. Vanmaekelbergh, and W. L. Vos, *Controlling the dynamics of spontaneous emission from quantum dots by photonic crystals*, Nature **430**, 654 (2004).

[142] B. Peng, Ş. K. Özdemir, M. Liertzer, W. Chen, J. Kramer, H. Yilmaz, J. Wiersig, S. Rotter, and L. Yang, *Chiral modes and directional lasing at exceptional points*, PNAS **113**, 6845 (2016).

[143] T. J. A. Kippenberg, *Nonlinear optics in ultra-high Q whispering-gallery optical microcavities*, Ph.D. thesis, California Institute of Technology (2004).

[144] M. Borselli, *High-Q microresonators as lasing elements for silicon photonics*, Ph.D. thesis, California Institute of Technology (2006).

[145] M. D. Eisaman, J. Fan, A. Migdall, and S. V. Polyakov, *Invited review article: Single-photon sources and detectors*, Rev. Sci. Instrum. **82**, 071101 (2011).

[146] J. N. Anker, W. P. Hall, O. Lyandres, N. C. Shah, J. Zhao, and R. P. Van Duyne, *Biosensing with plasmonic nanosensors.*, Nat. Mater. **7**, 442 (2008).

[147] A. J. Qavi, A. L. Washburn, J.-Y. Byeon, and R. C. Bailey, *Label-free technologies for quantitative multiparameter biological analysis.*, Anal. Bioanal. Chem. **394**, 121 (2009).

[148] M. Arcari, I. Söllner, A. Javadi, S. Lindskov Hansen, S. Mahmoodian, J. Liu, H. Thyrrestrup, E. H. Lee, J. D. Song, S. Stobbe, and P. Lodahl, *Near-unity coupling efficiency of a quantum emitter to a photonic crystal waveguide*, Phys. Rev. Lett. **113**, 093603 (2014).

[149] L. Novotny, and N. F. van Hulst, *Antennas for light*, Nat. Photonics **5**, 83 (2011).

[150] D. K. Gramotnev, and S. I. Bozhevolnyi, *Plasmonics beyond the diffraction limit*, Nat. Photonics **4**, 83 (2010).

[151] H. J. Kimble, *Strong interactions of single atoms and photons in cavity QED*, Phys. Scr. **T76**, 127 (1998).

[152] H. Mertens, and A. Polman, *Strong luminescence quantum-efficiency enhancement near prolate metal nanoparticles: Dipolar versus higher-order modes*, J. Appl. Phys. **105**, 044302 (2009).

[153] J. N. Farahani, D. W. Pohl, H.-J. Eisler, and B. Hecht, *Single quantum dot coupled to a scanning optical antenna: A tunable superemitter*, Phys. Rev. Lett. **95**, 017402 (2005).

[154] C. Foot, *Atomic physics* (Oxford University Press, Oxford, UK, 2005).

[155] Z. Ruan, and S. Fan, *Design of subwavelength superscattering nanospheres*, Appl. Phys. Lett. **98**, 043101 (2011).

[156] D. Englund, D. Fattal, E. Waks, G. Solomon, B. Zhang, T. Nakaoka, Y. Arakawa, Y. Yamamoto, and J. Vucković, *Controlling the spontaneous emission rate of single quantum dots in a two-dimensional photonic crystal.*, Phys. Rev. Lett. **95**, 013904 (2005).

[157] R. Guo, E. Rusak, I. Staude, J. Dominguez, M. Decker, C. Rockstuhl, I. Brener, D. N. Neshev, and Y. S. Kivshar, *Multipolar coupling in hybrid metal-dielectric metasurfaces*, ACS Photonics **3**, 349 (2016).

[158] M. Agio, and A. Alù, *Optical antennas* (Cambridge University Press, New York, 2013), 1st ed.

[159] Z. Jacob, I. I. Smolyaninov, and E. E. Narimanov, *Broadband Purcell effect: Radiative decay engineering with metamaterials*, Appl. Phys. Lett. **100**, 181105 (2012).

[160] N. Engheta, *Circuits with light at nanoscales: Optical nanocircuits inspired by metamaterials*, Science **317**, 1698 (2007).

[161] F. Monticone, and A. Alu, *Leaky-wave theory, techniques, and applications: From microwaves to visible frequencies*, Proc. IEEE **103**, 793 (2015).

[162] M. S. Eggleston, K. Messer, L. Zhang, E. Yablonovitch, and M. C. Wu, *Optical antenna enhanced spontaneous emission*, PNAS **112**, 1704 (2015).

[163] M. Staffaroni, J. Conway, S. Vedantam, J. Tang, and E. Yablonovitch, *Circuit analysis in metal-optics*, Photonics Nanostructures - Fundam. Appl. **10**, 166 (2012).

[164] A. Alù, and N. Engheta, *Achieving transparency with plasmonic and metamaterial coatings*, Phys. Rev. E **72**, 016623 (2005).

[165] S. Tretyakov, P. Alitalo, O. Luukkonen, and C. Simovski, *Broadband electromagnetic cloaking of long cylindrical objects*, Phys. Rev. Lett. **103**, 103905 (2009).

[166] A. Alù, M. G. Silveirinha, A. Salandrino, and N. Engheta, *Epsilon-near-zero metamaterials and electromagnetic sources: Tailoring the radiation phase pattern*, Phys. Rev. B **75**, 155410 (2007).

[167] R. Fleury, and A. Alù, *Enhanced superradiance in epsilon-near-zero plasmonic channels*, Phys. Rev. B **87**, 201101 (2013).

[168] E. T. F. Rogers, and N. I. Zheludev, *Optical super-oscillations: sub-wavelength light focusing and super-resolution imaging*, J. Opt. **15**, 094008 (2013).

[169] G. T. Di Francia, *Super-gain antennas and optical resolving power*, Nuovo Cim. **9**, 426 (1952).

[170] V. M. Shalaev, *Optical negative-index metamaterials*, Nat. Photonics **1**, 41 (2007).

[171] A. Alu, and N. Engheta, *Optical metamaterials based on optical nanocircuits*, Proc. IEEE **99**, 1669 (2011).

[172] F. Monticone, N. M. Estakhri, and A. Alù, *Full control of nanoscale optical transmission with a composite metascreen*, Phys. Rev. Lett. **110**, 203903 (2013).

[173] D. Strickland, and G. Mourou, *Compression of amplified chirped optical pulses*, Opt. Commun. **55**, 447 (1985).

[174] N. Engheta, A. Salandrino, and A. Alù, *Circuit elements at optical frequencies: Nanoinductors, nanocapacitors, and nanoresistors*, Phys. Rev. Lett. **95**, 095504 (2005).

[175] A. Alù, and N. Engheta, *Tuning the scattering response of optical nanoantennas with nanocircuit loads*, Nat. Photonics **2**, 307 (2008).

[176] A. Alù, and N. Engheta, *Input impedance, nanocircuit loading, and radiation tuning of optical nanoantennas*, Phys. Rev. Lett. **101**, 043901 (2008).

[177] J.-J. Greffet, M. Laroche, and F. Marquier, *Impedance of a nanoantenna and a single quantum emitter*, Phys. Rev. Lett. **105**, 117701 (2010).

[178] J. Shi, F. Monticone, S. Elias, Y. Wu, D. Ratchford, X. Li, and A. Alù, *Modular assembly of optical nanocircuits*, Nat. Commun. **5**, 3896 (2014).

[179] A. E. Krasnok, A. P. Slobozhanyuk, C. R. Simovski, S. A. Tretyakov, A. N. Poddubny, A. E. Miroshnichenko, Y. S. Kivshar, and P. A. Belov, *An antenna model for the Purcell effect*, Sci. Rep. **5**, 12956 (2015).

[180] P. B. Johnson, and R. W. Christy, *Optical constants of the noble metals*, Phys. Rev. B **6**, 4370 (1972).

[181] J. E. Sipe, and J. V. Kranendonk, *Macroscopic electromagnetic theory of resonant dielectrics*, Phys. Rev. A **9**, 1806 (1974).

[182] H. Jackson, *Introduction to electronic circuits* (Prentice-Hall, Englewood Cliffs, NJ, 1959).

[183] D. M. Pozar, *Microwave engineering* (Wiley, 2011), 4th ed.

[184] A. D. Rakić, A. B. Djurišić, J. M. Elazar, and M. L. Majewski, *Optical properties of metallic films for vertical-cavity optoelectronic devices*, Appl. Opt. **37**, 5271 (1998).

[185] M. Frimmer, and A. F. Koenderink, *Spontaneous emission control in a tunable hybrid photonic system*, Phys. Rev. Lett. **110**, 217405 (2013).

[186] S. I. Shopova, R. Rajmangal, S. Holler, and S. Arnold, *Plasmonic enhancement of a whispering-gallery-mode biosensor for single nanoparticle detection*, Appl. Phys. Lett. **98**, 243104 (2011).

[187] P. Wang, Y. Wang, Z. Yang, X. Guo, X. Lin, X.-C. Yu, Y.-F. Xiao, W. Fang, L. Zhang, G. Lu, Q. Gong, and L. Tong, *Single-band 2-nm-line-width plasmon resonance in a strongly coupled Au nanorod*, Nano Lett. **15**, 7581 (2015).

[188] Y. Hong, W. Ahn, S. V. Boriskina, X. Zhao, and B. M. Reinhard, *Directed assembly of optoplasmonic hybrid materials with tunable photonic-plasmonic properties*, J. Phys. Chem. Lett. **6**, 2056 (2015).

[189] J. Do, K. N. Sediq, K. Deasy, D. M. Coles, J. Rodríguez-Fernández, J. Feldmann, and D. G. Lidzey, *Photonic crystal nanocavities containing plasmonic nanoparticles assembled using a laser-printing technique*, Adv. Opt. Mater. **1**, 946 (2013).

[190] L. Lalouat, B. Cluzel, P. Velha, E. Picard, D. Peyrade, J. P. Hugonin, P. Lalanne, E. Hadji, and F. de Fornel, *Near-field interactions between a subwavelength tip and a small-volume photonic-crystal nanocavity*, Phys. Rev. B **76**, 041102 (2007).

[191] M. Burresi, T. Kampfrath, D. van Oosten, J. C. Prangsma, B. S. Song, S. Noda, and L. Kuipers, *Magnetic light-matter interactions in a photonic crystal nanocavity*, Phys. Rev. Lett. **105**, 123901 (2010).

[192] F. I. Baida, and T. Grosjean, *Double-way spectral tunability for the control of optical nanocavity resonance*, Sci. Rep. **5**, 17907 (2016).

[193] H. Kelkar, D. Wang, D. Martín-Cano, B. Hoffmann, S. Christiansen, S. Götzinger, and V. Sandoghdar, *Sensing nanoparticles with a cantilever-based scannable optical cavity of low finesse and sub-λ^3 volume*, Phys. Rev. Appl. **4**, 054010 (2015).

[194] C.-H. Su, A. D. Greentree, and L. C. L. Hollenberg, *Towards a picosecond transform-limited nitrogen-vacancy based single photon source*, Opt. Express **16**, 6240 (2008).

[195] I. Aharonovich, A. D. Greentree, and S. Prawer, *Diamond photonics*, Nat. Photonics **5**, 397 (2011).

[196] D. Wang, H. Kelkar, D. Martin-Cano, T. Utikal, S. Götzinger, and V. Sandoghdar, *Coherent coupling of a single molecule to a scanning Fabry-Perot microcavity*, Phys.

Rev. X **7**, 021014 (2017).

[197] J. Meijer, B. Burchard, M. Domhan, C. Wittmann, T. Gaebel, I. Popa, F. Jelezko, and J. Wrachtrup, *Generation of single color centers by focused nitrogen implantation*, Appl. Phys. Lett. **87**, 261909 (2005).

[198] G. P. Acuna, F. M. Moller, P. Holzmeister, S. Beater, B. Lalkens, and P. Tinnefeld, *Fluorescence enhancement at docking sites of DNA-directed self-assembled nanoantennas*, Science **338**, 506 (2012).

[199] E. B. Ureña, M. P. Kreuzer, S. Itzhakov, H. Rigneault, R. Quidant, D. Oron, and J. Wenger, *Excitation enhancement of a quantum dot coupled to a plasmonic antenna*, Adv. Mater. **24**, OP314 (2012).

[200] E. Bermúdez-Ureña, C. Gonzalez-Ballestero, M. Geiselmann, R. Marty, I. P. Radko, T. Holmgaard, Y. Alaverdyan, E. Moreno, F. J. García-Vidal, S. I. Bozhevolnyi, and R. Quidant, *Coupling of individual quantum emitters to channel plasmons*, Nat. Commun. **6**, 7883 (2015).

[201] F. T. Rabouw, M. Frimmer, A. Mohtashami, and A. F. Koenderink, *Nanoscale lithographic positioning of fluorescing quantum dot nanocrystals on planar samples*, Opt. Mater. (Amst). **35**, 1342 (2013).

[202] B. J. M. Hausmann, T. M. Babinec, J. T. Choy, J. S. Hodges, S. Hong, I. Bulu, A. Yacoby, M. D. Lukin, and M. Lončar, *Single-color centers implanted in diamond nanostructures*, New J. Phys. **13**, 045004 (2011).

[203] S. J. P. Kress, P. Richner, S. V. Jayanti, P. Galliker, D. K. Kim, D. Poulikakos, and D. J. Norris, *Near-field light design with colloidal quantum dots for photonics and plasmonics*, Nano Lett. **14**, 5827 (2014).

[204] P. Richner, P. Galliker, T. Lendenmann, S. J. P. Kress, D. K. Kim, D. J. Norris, and D. Poulikakos, *Full-spectrum flexible color printing at the diffraction limit*, ACS Photonics **3**, 754 (2016).

[205] C. M. Galloway, M. P. Kreuzer, S. S. Aćimović, G. Volpe, M. Correia, S. B. Petersen, M. T. Neves-Petersen, and R. Quidant, *Plasmon-assisted delivery of single nano-objects in an optical hot spot*, Nano Lett. **13**, 4299 (2013).

[206] A. de Hoogh, B. Hommersom, and A. F. Koenderink, *Wavelength-selective addressing of visible and near-infrared plasmon resonances for SU8 nanolithography*, Opt. Express **19**, 11405 (2011).

[207] G. Volpe, M. Noack, S. S. Aćimović, C. Reinhardt, and R. Quidant, *Near-field mapping of plasmonic antennas by multiphoton absorption in poly(methyl methacrylate)*, Nano Lett. **12**, 4864 (2012).

[208] X. Zhou, J. Wenger, F. N. Viscomi, L. Le Cunff, J. Béal, S. Kochtcheev, X. Yang, G. P. Wiederrecht, G. Colas des Francs, A. S. Bisht, S. Jradi, R. Caputo, H. V. Demir, R. D. Schaller, J. Plain, et al., *Two-color single hybrid plasmonic nanoemitters with real time switchable dominant emission wavelength*, Nano Lett. **15**, 7458 (2015).

[209] R. G. Hobbs, W. P. Putnam, A. Fallahi, Y. Yang, F. X. Kärtner, and K. K. Berggren, *Mapping photoemission and hot-electron emission from plasmonic nanoantennas*, Nano Lett. **17**, 6069 (2017).

[210] E. Cortés, W. Xie, J. Cambiasso, A. S. Jermyn, R. Sundararaman, P. Narang, S. Schlücker, and S. A. Maier, *Plasmonic hot electron transport drives nano-localized*

chemistry, Nat. Commun. **8**, 14880 (2017).

[211] M. Borselli, T. J. Johnson, and O. Painter, *Beyond the Rayleigh scattering limit in high-Q silicon microdisks: theory and experiment*, Opt. Express **13**, 1515 (2005).

[212] N. Daldosso, M. Melchiorri, F. Riboli, F. Sbrana, L. Pavesi, G. Pucker, C. Kompocholis, M. Crivellari, P. Bellutti, and A. Lui, *Fabrication and optical characterization of thin two-dimensional Si3N4 waveguides*, Mater. Sci. Semicond. Process. **7**, 453 (2004).

[213] A. Gorin, A. Jaouad, E. Grondin, V. Aimez, and P. Charette, *Fabrication of silicon nitride waveguides for visible-light using PECVD: A study of the effect of plasma frequency on optical properties*, Opt. Express **16**, 13509 (2008).

[214] A. Gondarenko, J. S. Levy, and M. Lipson, *High confinement micron-scale silicon nitride high-Q ring resonator*, Opt. Express **17**, 11366 (2009).

[215] M. W. Knight, L. Liu, Y. Wang, L. Brown, S. Mukherjee, N. S. King, H. O. Everitt, P. Nordlander, and N. J. Halas, *Aluminum plasmonic nanoantennas*, Nano Lett. **12**, 6000 (2012).

[216] C. Langhammer, M. Schwind, B. Kasemo, and I. Zorić, *Localized surface plasmon resonances in aluminum nanodisks*, Nano Lett. **8**, 1461 (2008).

[217] M. W. Knight, N. S. King, L. Liu, H. O. Everitt, P. Nordlander, and N. J. Halas, *Aluminum for plasmonics*, ACS Nano **8**, 834 (2014).

[218] Y. Chen, *Nanofabrication by electron beam lithography and its applications: A review*, Microelectron. Eng. **135**, 57 (2015).

[219] C. P. Michael, M. Borselli, T. J. Johnson, C. Chrystal, and O. Painter, *An optical fiber-taper probe for wafer-scale microphotonic device characterization*, Opt. Express **15**, 4745 (2007).

[220] D. Bera, L. Qian, T.-K. Tseng, and P. H. Holloway, *Quantum dots and their multimodal applications: A review*, Materials (Basel). **3**, 2260 (2010).

[221] I. Aharonovich, D. Englund, and M. Toth, *Solid-state single-photon emitters*, Nat. Photonics **10**, 631 (2016).

[222] M. Saffman, T. G. Walker, and K. Mølmer, *Quantum information with Rydberg atoms*, Rev. Mod. Phys. **82**, 2313 (2010).

[223] S. Weiss, *Fluorescence spectroscopy of single biomolecules*, Science **283**, 1676 (1999).

[224] A. Maser, B. Gmeiner, T. Utikal, S. Götzinger, and V. Sandoghdar, *Few-photon coherent nonlinear optics with a single molecule*, Nat. Photonics **10**, 450 (2016).

[225] J. Hwang, M. Pototschnig, R. Lettow, G. Zumofen, A. Renn, S. Götzinger, and V. Sandoghdar, *A single-molecule optical transistor*, Nature **460**, 76 (2009).

[226] E. Snoeks, A. Lagendijk, and A. Polman, *Measuring and modifying the spontaneous emission rate of erbium near an interface*, Phys. Rev. Lett. **74**, 2459 (1995).

[227] J. Kalkman, L. Kuipers, A. Polman, and H. Gersen, *Coupling of Er ions to surface plasmons on Ag*, Appl. Phys. Lett. **86**, 041113 (2005).

[228] S. A. Empedocles, R. Neuhauser, K. Shimizu, and M. G. Bawendi, *Photoluminescence from single semiconductor nanostructures*, Adv. Mater. **11**, 1243 (1999).

[229] S. Buckley, K. Rivoire, and J. Vučković, *Engineered quantum dot single-photon sources*, Rep. Prog. Phys. **75**, 126503 (2012).

[230] F. Jelezko, and J. Wrachtrup, *Single defect centres in diamond: A review*, Phys. Status Solidi A **203**, 3207 (2006).

[231] T. Iwasaki, F. Ishibashi, Y. Miyamoto, Y. Doi, S. Kobayashi, T. Miyazaki, K. Tahara, K. D. Jahnke, L. J. Rogers, B. Naydenov, F. Jelezko, S. Yamasaki, S. Nagamachi, T. Inubushi, N. Mizuochi, et al., *Germanium-vacancy single color centers in diamond*, Sci. Rep. **5**, 12882 (2015).

[232] C. Toninelli, K. Early, J. Bremi, A. Renn, S. Götzinger, and V. Sandoghdar, *Near-infrared single-photons from aligned molecules in ultrathin crystalline films at room temperature*, Opt. Express **18**, 6577 (2010).

[233] A. Mohtashami, and A. F. Koenderink, *Suitability of nanodiamond nitrogenâĂŞva-cancy centers for spontaneous emission control experiments*, New J. Phys. **15**, 043017 (2013).

[234] E. A. Ekimov, S. G. Lyapin, K. N. Boldyrev, M. V. Kondrin, R. Khmelnitskiy, V. A. Gavva, T. V. Kotereva, and M. N. Popova, *Germanium-vacancy color center in isotopically enriched diamonds synthesized at high pressures*, JETP Lett. **102**, 701 (2015).

[235] L. Aigouy, A. Cazé, P. Gredin, M. Mortier, and R. Carminati, *Mapping and quantifying electric and magnetic dipole luminescence at the nanoscale*, Phys. Rev. Lett. **113**, 076101 (2014).

[236] F. T. Rabouw, P. T. Prins, and D. J. Norris, *Europium-doped NaYF4 nanocrystals as probes for the electric and magnetic local density of optical states throughout the visible spectral range*, Nano Lett. **16**, 7254 (2016).

[237] M. Pelton, C. Santori, J. Vučković, B. Zhang, G. S. Solomon, J. Plant, and Y. Yamamoto, *Efficient source of single photons: A single quantum dot in a micropost microcavity*, Phys. Rev. Lett. **89**, 233602 (2002).

[238] I. Söllner, S. Mahmoodian, S. L. Hansen, L. Midolo, A. Javadi, G. Kiršanskė, T. Pregnolato, H. El-Ella, E. H. Lee, J. D. Song, S. Stobbe, and P. Lodahl, *Deterministic photon-emitter coupling in chiral photonic circuits*, Nat. Nanotechnol. **10**, 775 (2015).

[239] T. B. Hoang, G. M. Akselrod, C. Argyropoulos, J. Huang, D. R. Smith, and M. H. Mikkelsen, *Ultrafast spontaneous emission source using plasmonic nanoantennas*, Nat. Commun. **6**, 7788 (2015).

[240] N. Livneh, M. G. Harats, D. Istrati, H. S. Eisenberg, and R. Rapaport, *Highly directional room-temperature single photon device*, Nano Lett. **16**, 2527 (2016).

[241] M. Kuno, D. P. Fromm, H. F. Hamann, A. Gallagher, and D. J. Nesbitt, *Nonexponential "blinking" kinetics of single CdSe quantum dots: A universal power law behavior*, J. Chem. Phys. **112**, 3117 (2000).

[242] F. T. Rabouw, M. Kamp, R. J. A. van Dijk-Moes, D. R. Gamelin, A. F. Koenderink, A. Meijerink, and D. Vanmaekelbergh, *Delayed exciton emission and its relation to blinking in CdSe quantum dots*, Nano Lett. **15**, 7718 (2015).

[243] A. Kwadrin, and A. F. Koenderink, *Gray-tone lithography implementation of Drexhage's method for calibrating radiative and nonradiative decay constants of fluorophores*, J. Phys. Chem. C **116**, 16666 (2012).

[244] N. McElroy, R. Page, D. Espinbarro-Valazquez, E. Lewis, S. Haigh, P. O'Brien,

and D. Binks, *Comparison of solar cells sensitised by CdTe/CdSe and CdSe/CdTe core/shell colloidal quantum dots with and without a CdS outer layer*, Thin Solid Films **560**, 65 (2014).

[245] B. Rogez, H. Yang, E. Le Moal, S. Lévêque-Fort, E. Boer-Duchemin, F. Yao, Y.-H. Lee, Y. Zhang, K. D. Wegner, N. Hildebrandt, A. Mayne, and G. Dujardin, *Fluorescence lifetime and blinking of individual semiconductor nanocrystals on graphene*, J. Phys. Chem. C **118**, 18445 (2014).

[246] B. R. Fisher, H.-J. Eisler, N. E. Stott, and M. G. Bawendi, *Emission intensity dependence and single-exponential behavior in single colloidal quantum dot fluorescence lifetimes*, J. Phys. Chem. B **108 (1)**, 143 (2004).

[247] L. Forget, F. Wilwers, J. Delhalle, and Z. Mekhalif, *Surface modification of aluminum by n-pentanephosphonic acid: XPS and electrochemical evaluation*, Appl. Surf. Sci. **205**, 44 (2003).

[248] P. H. Mutin, G. Guerrero, and A. Vioux, *Hybrid materials from organophosphorus coupling molecules*, J. Mater. Chem. **15**, 3761 (2005).

[249] M.-A. Neouze, and U. Schubert, *Surface modification and functionalization of metal and metal oxide nanoparticles by organic ligands*, Monatshefte für Chemie - Chem. Mon. **139**, 183 (2008).

[250] P. H. Mutin, V. Lafond, A. F. Popa, M. Granier, L. Markey, and A. Dereux, *Selective surface modification of SiO2-TiO2 supports with phosphonic acids*, Chem. Mater. **16**, 5670 (2004).

[251] S. Attavar, M. Diwekar, M. R. Linford, M. A. Davis, and S. Blair, *Passivation of aluminum with alkyl phosphonic acids for biochip applications*, Appl. Surf. Sci. **256**, 7146 (2010).

[252] R. M. Stoltenberg, C. Liu, and Z. Bao, *Selective surface chemistry using alumina nanoparticles generated from block copolymers*, Langmuir **27**, 445 (2011).

[253] C. C. Reinhart, and E. Johansson, *Colloidal 3-mercaptopropionic acid capped lead sulfide quantum dots in a low boiling point solvent*, J. Am. Chem. Soc. **139**, 5827 (2017).

[254] T. Gan, N. Zhao, G. Yin, M. Tu, J. Liu, and W. Liu, *Mercaptopropionic acid-capped Mn-doped ZnS quantum dots as a probe for selective room-temperature phosphorescence detection of Pb 2+ in water*, New J. Chem. **41**, 13425 (2017).

[255] T. Zhang, *Plasmonic-photonic hybrid nanodevice*, Ph.D. thesis, Ecole Centrale de Lyon (2012).

[256] G. Kiršanskė, H. Thyrrestrup, R. S. Daveau, C. L. Dreeßen, T. Pregnolato, L. Midolo, P. Tighineanu, A. Javadi, S. Stobbe, R. Schott, A. Ludwig, A. D. Wieck, S. I. Park, J. D. Song, A. V. Kuhlmann, et al., *Indistinguishable and efficient single photons from a quantum dot in a planar nanobeam waveguide*, Phys. Rev. B **96**, 165306 (2017).

[257] J. Zhu, Ş. K. Özdemir, Y.-F. Xiao, L. Li, L. He, D.-R. Chen, and L. Yang, *On-chip single nanoparticle detection and sizing by mode splitting in an ultrahigh-Q microresonator*, Nat. Photonics **4**, 46 (2010).

[258] M. Aspelmeyer, T. J. Kippenberg, and F. Marquardt, *Cavity optomechanics*, Rev. Mod. Phys. **86**, 1391 (2014).

[259] J. D. Thompson, T. G. Tiecke, N. P. de Leon, J. Feist, A. V. Akimov, M. Gullans, A. S. Zibrov, V. Vuletic, and M. D. Lukin, *Coupling a single trapped atom to a nanoscale optical cavity*, Science **340**, 1202 (2013).

[260] A. Goban, C.-L. Hung, S.-P. Yu, J. Hood, J. Muniz, J. Lee, M. Martin, A. McClung, K. Choi, D. Chang, O. Painter, and H. Kimble, *Atom-light interactions in photonic crystals*, Nat. Commun. **5**, 3808 (2014).

[261] S. Mujumdar, A. F. Koenderink, T. Sünner, B. C. Buchler, M. Kamp, A. Forchel, and V. Sandoghdar, *Near-field imaging and frequency tuning of a high-Q photonic crystal membrane microcavity*, Opt. Express **15**, 17214 (2007).

[262] F. Intonti, S. Vignolini, F. Riboli, A. Vinattieri, D. S. Wiersma, M. Colocci, L. Balet, C. Monat, C. Zinoni, L. H. Li, R. Houdré, M. Francardi, A. Gerardino, A. Fiore, and M. Gurioli, *Spectral tuning and near-field imaging of photonic crystal microcavities*, Phys. Rev. B **78**, 041401 (2008).

[263] T. Grosjean, A. El Eter, M. Mivelle, T.-P. Vo, A. Belkhir, C. Ecoffey, G. Le Gac, D. Nedeljkovic, A. Rahmani, C. Seassal, S. Callard, and F. Baida, *Extraordinary blueshift of a photonic crystal nanocavity by reducing its mode volume with an opaque microtip*, Appl. Phys. Lett. **101**, 051102 (2012).

[264] E. Verhagen, S. Deléglise, S. Weis, A. Schliesser, and T. J. Kippenberg, *Quantum-coherent coupling of a mechanical oscillator to an optical cavity mode*, Nature **482**, 63 (2012).

[265] B. D. Hauer, P. H. Kim, C. Doolin, A. J. MacDonald, H. Ramp, and J. P. Davis, *On-chip cavity optomechanical coupling*, EPJ Tech. Instrum. **1**, 4 (2014).

[266] P. Miao, Z. Zhang, J. Sun, W. Walasik, S. Longhi, N. M. Litchinitser, and L. Feng, *Orbital angular momentum microlaser*, Science **353**, 464 (2016).

[267] B. Peng, Ş. K. Özdemir, S. Rotter, H. Yilmaz, M. Liertzer, F. Monifi, C. M. Bender, F. Nori, and L. Yang, *Loss-induced suppression and revival of lasing*, Science **346**, 328 (2014).

[268] J. Wiersig, *Enhancing the sensitivity of frequency and energy splitting detection by using exceptional points: Application to microcavity sensors for single-particle detection*, Phys. Rev. Lett. **112**, 203901 (2014).

[269] W. Chen, Ş. K. Özdemir, G. Zhao, J. Wiersig, and L. Yang, *Exceptional points enhance sensing in an optical microcavity*, Nature **548**, 192 (2017).

[270] M. Frimmer, Y. Chen, and A. F. Koenderink, *Scanning emitter lifetime imaging microscopy for spontaneous emission control*, Phys. Rev. Lett. **107**, 123602 (2011).

[271] R. Loudon, *The quantum theory of light* (Oxford Science Publications, Oxford, 1983).

[272] W. Becker, *Advanced time-correlated single photon counting techniques* (Springer Berlin / Heidelberg, 2005).

[273] M. Barth, N. Nüsse, J. Stingl, B. Löchel, and O. Benson, *Emission properties of high-Q silicon nitride photonic crystal heterostructure cavities*, Appl. Phys. Lett. **93**, 021112 (2008).

[274] A. N. Oraevsky, *Whispering-gallery waves*, Quantum Electron. **32**, 377 (2002).

[275] S. Kühn, U. Håkanson, L. Rogobete, and V. Sandoghdar, *Enhancement of single-molecule fluorescence using a gold nanoparticle as an optical nanoantenna*, Phys. Rev.

Lett. **97**, 017402 (2006).

[276] S. A. Empedocles, and M. G. Bawendi, *Influence of spectral diffusion on the line shapes of single CdSe nanocrystallite quantum dots*, J. Phys. Chem. B **103**, 1826 (1999).

[277] N. R. Verhart, M. Müller, and M. Orrit, *Spectroscopy of single dibenzoterrylene molecules in para-dichlorobenzene*, ChemPhysChem **17**, 1524 (2016).

[278] S. Karaveli, and R. Zia, *Strong enhancement of magnetic dipole emission in a multilevel electronic system*, Opt. Lett. **35**, 3318 (2010).

[279] A. Chizhik, F. Schleifenbaum, R. Gutbrod, A. Chizhik, D. Khoptyar, A. J. Meixner, and J. Enderlein, *Tuning the fluorescence emission spectra of a single molecule with a variable optical subwavelength metal microcavity*, Phys. Rev. Lett. **102**, 073002 (2009).

[280] C. Toninelli, Y. Delley, T. Stöferle, A. Renn, S. Götzinger, and V. Sandoghdar, *A scanning microcavity for in situ control of single-molecule emission*, Appl. Phys. Lett. **97**, 021107 (2010).

[281] S. Bär, A. Chizhik, R. Gutbrod, F. Schleifenbaum, A. Chizhik, and A. J. Meixner, *Microcavities: tailoring the optical properties of single quantum emitters*, Anal. Bioanal. Chem. **396**, 3 (2010).

[282] R. G. Neuhauser, K. T. Shimizu, W. K. Woo, S. A. Empedocles, and M. G. Bawendi, *Correlation between fluorescence intermittency and spectral diffusion in single semiconductor quantum dots*, Phys. Rev. Lett. **85**, 3301 (2000).

[283] A. Srivastava, M. Sidler, A. V. Allain, D. S. Lembke, A. Kis, and A. Imamoğlu, *Optically active quantum dots in monolayer WSe2*, Nat. Nanotechnol. **10**, 491 (2015).

[284] A. I. Ekimov, I. A. Kudryavtsev, A. L. Efros, T. V. Yazeva, F. Hache, M. C. Schanne-Klein, A. V. Rodina, D. Ricard, and C. Flytzanis, *Absorption and intensity-dependent photoluminescence measurements on CdSe quantum dots: assignment of the first electronic transitions*, J. Opt. Soc. Am. B **10**, 100 (1993).

[285] S. V. Goupalov, R. A. Suris, P. Lavallard, and D. S. Citrin, *Homogeneous broadening of the zero-optical-phonon spectral line in semiconductor quantum dots*, Nanotechnology **12**, 518 (2001).

[286] M. Wolf, and J. Berezovsky, *Homogeneous and inhomogeneous sources of optical transition broadening in room temperature CdSe/ZnS nanocrystal quantum dots*, Appl. Phys. Lett. **105**, 143105 (2014).

[287] H. Seiler, S. Palato, C. Sonnichsen, H. Baker, and P. Kambhampati, *Seeing multiexcitons through sample inhomogeneity: Band-edge biexciton structure in CdSe nanocrystals revealed by two-dimensional electronic spectroscopy*, Nano Lett. **18**, 2999 (2018).

[288] H. Kaupp, C. Deutsch, H.-C. Chang, J. Reichel, T. W. Hänsch, and D. Hunger, *Scaling laws of the cavity enhancement for nitrogen-vacancy centers in diamond*, Phys. Rev. A **88**, 053812 (2013).

[289] G. Sun, J. B. Khurgin, and R. A. Soref, *Practical enhancement of photoluminescence by metal nanoparticles*, Appl. Phys. Lett. **94**, 101103 (2009).

[290] A. F. van Driel, I. S. Nikolaev, P. Vergeer, P. Lodahl, D. Vanmaekelbergh, and W. L. Vos, *Statistical analysis of time-resolved emission from ensembles of semiconductor quantum dots: Interpretation of exponential decay models*, Phys. Rev. B **75**, 035329

(2007).

[291] M. D. Leistikow, J. Johansen, A. J. Kettelarij, P. Lodahl, and W. L. Vos, *Size-dependent oscillator strength and quantum efficiency of CdSe quantum dots controlled via the local density of states*, Phys. Rev. B **79**, 045301 (2009).

[292] G. Cui, and M. G. Raymer, *Emission spectra and quantum efficiency of single-photon sources in the cavity-QED strong-coupling regime*, Phys. Rev. A **73**, 053807 (2006).

[293] S. Hughes, and P. Yao, *Theory of quantum light emission from a strongly-coupled single quantum dot photonic-crystal cavity system*, Opt. Express **17**, 3322 (2009).

[294] H. Sumikura, E. Kuramochi, H. Taniyama, and M. Notomi, *Purcell enhancement of fast-dephasing spontaneous emission from electron-hole droplets in high-Q silicon photonic crystal nanocavities*, Phys. Rev. B **94**, 195314 (2016).

[295] Y. Zhang, Q.-S. Meng, L. Zhang, Y. Luo, Y.-J. Yu, B. Yang, Y. Zhang, R. Esteban, J. Aizpurua, Y. Luo, J.-L. Yang, Z.-C. Dong, and J. G. Hou, *Sub-nanometre control of the coherent interaction between a single molecule and a plasmonic nanocavity*, Nat. Commun. **8**, 15225 (2017).

[296] K. J. Boller, A. Imamoğlu, and S. E. Harris, *Observation of electromagnetically induced transparency*, Phys. Rev. Lett. **66**, 2593 (1991).

[297] M. A. Schmidt, D. Y. Lei, L. Wondraczek, V. Nazabal, and S. A. Maier, *Hybrid nanoparticle-microcavity-based plasmonic nanosensors with improved detection resolution and extended remote-sensing ability*, Nat. Commun. **3**, 1108 (2012).

[298] M. R. Foreman, and F. Vollmer, *Level repulsion in hybrid photonic-plasmonic microresonators for enhanced biodetection*, Phys. Rev. A **88**, 23831 (2013).

[299] M. Husnik, S. Linden, R. Diehl, J. Niegemann, K. Busch, and M. Wegener, *Quantitative experimental determination of scattering and absorption cross-section spectra of individual optical metallic nanoantennas*, Phys. Rev. Lett. **109**, 233902 (2012).

[300] M. Husnik, J. Niegemann, K. Busch, and M. Wegener, *Quantitative spectroscopy on individual wire, slot, bow-tie, rectangular, and square-shaped optical antennas*, Opt. Lett. **38**, 4597 (2013).

[301] D. K. Armani, T. J. Kippenberg, S. M. Spillane, and K. J. Vahala, *Ultra-high-Q toroid microcavity on a chip*, Nature **421**, 925 (2003).

[302] G. Anetsberger, *Novel cavity optomechanical systems at the micro- and nanoscale and quantum measurements of nanomechanical oscillators*, Ph.D. thesis, LMU Munchen (2010).

[303] H. C. van de Hulst, *Light Scattering by Small Particles* (John Wiley & Sons, New York, 1957).

[304] Y. Chen, Y. Zhang, and A. F. Koenderink, *General point dipole theory for periodic metasurfaces: magnetoelectric scattering lattices coupled to planar photonic structures*, Opt. Express **25**, 21358 (2017).

[305] W. E. Lamb Jr., and R. C. Retherford, *Fine structure of the hydrogen atom by a microwave method*, Phys. Rev. **72**, 241 (1947).

[306] S. Zhang, D. A. Genov, Y. Wang, M. Liu, and X. Zhang, *Plasmon-induced transparency in metamaterials*, Phys. Rev. Lett. **101**, 047401 (2008).

[307] N. Liu, L. Langguth, T. Weiss, J. Kästel, M. Fleischhauer, T. Pfau, and H. Giessen, *Plasmonic analogue of electromagnetically induced transparency at the Drude damping limit.*, Nat. Mater. **8**, 758 (2009).

[308] S. Weis, R. Rivière, S. Deléglise, E. Gavartin, O. Arcizet, A. Schliesser, and T. J. Kippenberg, *Optomechanically induced transparency*, Science **330**, 1520 (2010).

[309] A. H. Safavi-Naeini, T. P. M. Alegre, J. Chan, M. Eichenfield, M. Winger, Q. Lin, J. T. Hill, D. E. Chang, and O. Painter, *Electromagnetically induced transparency and slow light with optomechanics*, Nature **472**, 69 (2011).

[310] U. Fano, *Effects of configuration interaction on intensities and phase shifts*, Phys. Rev. **124**, 1866 (1961).

[311] A. Kwadrin, C. I. Osorio, and A. F. Koenderink, *Backaction in metasurface etalons*, Phys. Rev. B **93**, 104301 (2016).

[312] C. M. Linton, *Lattice sums for the Helmholtz equation*, SIAM Rev. **52**, 630 (2010).

[313] H. P. Urbach, and G. L. J. A. Rikken, *Spontaneous emission from a dielectric slab*, Phys. Rev. A **57**, 3913 (1998).

[314] B. Auguié, X. M. Bendaña, W. L. Barnes, and F. J. García de Abajo, *Diffractive arrays of gold nanoparticles near an interface: Critical role of the substrate*, Phys. Rev. B **82**, 155447 (2010).

[315] F. Monticone, H. M. Doeleman, W. Den Hollander, A. F. Koenderink, and A. Alù, *Trapping light in plain sight: Embedded photonic eigenstates in zero-index metamaterials*, Laser Photon. Rev. **12**, 1700220 (2018).

[316] G. Gbur, in *Prog. Opt. Vol. 45*, edited by E. Wolf (Elsevier, 2003), chap. 5, pp. 273–316.

[317] P. Ehrenfest, *Ungleichförmige Elektrizitätsbewegungen ohne Magnet-und Strahlungsfeld*, Phys. Zeitschrift **11**, 708 (1910).

[318] J. von Neuman, and E. Wigner, *Uber merkwürdige diskrete Eigenwerte. Uber das Verhalten von Eigenwerten bei adiabatischen Prozessen*, Phys. Zeitschrift **30**, 467 (1929).

[319] C. W. Hsu, B. Zhen, A. D. Stone, J. D. Joannopoulos, and M. Soljačić, *Bound states in the continuum*, Nat. Rev. Mater. **1**, 16048 (2016).

[320] D. C. Marinica, A. G. Borisov, and S. V. Shabanov, *Bound states in the continuum in photonics*, Phys. Rev. Lett. **100**, 183902 (2008).

[321] Y. Yang, C. Peng, Y. Liang, Z. Li, and S. Noda, *Analytical perspective for bound states in the continuum in photonic crystal slabs*, Phys. Rev. Lett. **113**, 037401 (2014).

[322] C. W. Hsu, B. Zhen, J. Lee, S.-L. Chua, S. G. Johnson, J. D. Joannopoulos, and M. Soljačić, *Observation of trapped light within the radiation continuum*, Nature **499**, 188 (2013).

[323] E. N. Bulgakov, and A. F. Sadreev, *Bloch bound states in the radiation continuum in a periodic array of dielectric rods*, Phys. Rev. A **90**, 053801 (2014).

[324] M. G. Silveirinha, *Trapping light in open plasmonic nanostructures*, Phys. Rev. A **89**, 023813 (2014).

[325] F. Monticone, and A. Alù, *Embedded photonic eigenvalues in 3D nanostructures*, Phys. Rev. Lett. **112**, 213903 (2014).

[326] A. Kodigala, T. Lepetit, Q. Gu, B. Bahari, Y. Fainman, and B. Kanté, *Lasing action from photonic bound states in continuum*, Nature **541**, 196 (2017).

[327] S. T. Ha, Y. H. Fu, N. K. Emani, Z. Pan, R. M. Bakker, R. Paniagua-Domínguez, and A. I. Kuznetsov, *Directional lasing in resonant semiconductor nanoantenna arrays*, Nat. Nanotechnol. p. 1 (2018).

[328] A. A. Yanik, A. E. Cetin, M. Huang, A. Artar, S. H. Mousavi, A. Khanikaev, J. H. Connor, G. Shvets, and H. Altug, *Seeing protein monolayers with naked eye through plasmonic Fano resonances*, PNAS **108**, 11784 (2011).

[329] J. M. Foley, S. M. Young, and J. D. Phillips, *Symmetry-protected mode coupling near normal incidence for narrow-band transmission filtering in a dielectric grating*, Phys. Rev. B **89**, 165111 (2014).

[330] B. Zhen, C. W. Hsu, L. Lu, A. D. Stone, and M. Soljačić, *Topological nature of optical bound states in the continuum*, Phys. Rev. Lett. **113**, 257401 (2014).

[331] Y. Plotnik, O. Peleg, F. Dreisow, M. Heinrich, S. Nolte, A. Szameit, and M. Segev, *Experimental observation of optical bound states in the continuum*, Phys. Rev. Lett. **107**, 183901 (2011).

[332] M. A. Lieb, J. M. Zavislan, and L. Novotny, *Single-molecule orientations determined by direct emission pattern imaging*, J. Opt. Soc. Am. B **21**, 1210 (2004).

[333] C. Fallet, *Angle resolved Mueller polarimetry, applications to periodic structures*, Ph.D. thesis, Ecole Polytechnique X (2011).

[334] I. Sersic, C. Tuambilangana, and A. F. Koenderink, *Fourier microscopy of single plasmonic scatterers*, New J. Phys. **13**, 083019 (2011).

[335] J. A. Kurvits, M. Jiang, and R. Zia, *Comparative analysis of imaging configurations and objectives for Fourier microscopy*, J. Opt. Soc. Am. A **32**, 2082 (2015).

[336] C. I. Osorio, A. Mohtashami, and A. F. Koenderink, *K-space polarimetry of bullseye plasmon antennas*, Sci. Rep. **5**, 9966 (2015).

[337] M. G. Moharam, T. K. Gaylord, E. B. Grann, and D. A. Pommet, *Formulation for stable and efficient implementation of the rigorous coupled-wave analysis of binary gratings*, J. Opt. Soc. Am. A **12**, 1068 (1995).

[338] K. Sakoda, *Optical properties of photonic crystals*, vol. 80 of *Springer Series in Optical Sciences* (Springer-Verlag, Berlin/Heidelberg, 2005).

[339] H. Friedrich, and D. Wintgen, *Interfering resonances and bound states in the continuum*, Phys. Rev. A **32**, 3231 (1985).

[340] T. Lepetit, and B. Kanté, *Controlling multipolar radiation with symmetries for electromagnetic bound states in the continuum*, Phys. Rev. B **90**, 241103 (2014).

[341] I. Sersic, C. Tuambilangana, T. Kampfrath, and A. F. Koenderink, *Magnetoelectric point scattering theory for metamaterial scatterers*, Phys. Rev. B **83**, 245102 (2011).

[342] A. Alù, and N. Engheta, *How does zero forward-scattering in magnetodielectric nanoparticles comply with the optical theorem?*, J. Nanophotonics **4**, 041590 (2010).

[343] I. Staude, A. E. Miroshnichenko, M. Decker, N. T. Fofang, S. Liu, E. Gonzales, J. Dominguez, T. S. Luk, D. N. Neshev, I. Brener, and Y. Kivshar, *Tailoring directional scattering through magnetic and electric resonances in subwavelength silicon nanodisks*, ACS Nano **7**, 7824 (2013).

[344] M. Kerker, D.-S. Wang, and C. L. Giles, *Electromagnetic scattering by magnetic spheres*, J. Opt. Soc. Am. **73**, 765 (1983).

[345] M. V. Rybin, K. L. Koshelev, Z. F. Sadrieva, K. B. Samusev, A. A. Bogdanov, M. F. Limonov, and Y. S. Kivshar, *High-Q supercavity modes in subwavelength dielectric resonators*, Phys. Rev. Lett. **119**, 243901 (2017).

Summary

Light is at the heart of many technologies in our modern society. It can visualize tiny cells or entire galaxies, measure sub-nanometer displacements or individual viruses in blood, imprint complex patterns on a microchip or transport enormous amounts of information. For these and other applications, control over the flow of light and its interaction strength with matter is pivotal. Optical resonators, which compress and store light for a finite time, have been instrumental in providing such control. The current state of the art for these resonators consists of optical cavities, which store light for many thousands or millions of oscillations, and plasmonic antennas, which instead squeeze light to sizes much below the wavelength. While these have shown impressive results, both approaches suffer from intrinsic drawbacks that limit large-scale implementations, particularly the realization of a network for optical quantum information processing. This thesis explores how hybrid resonances can overcome these limitations and provide new methods to guide and store light. Such resonances combine two or more resonances in a non-trivial manner, such that the hybrid resonance is more than simply the sum of the individual resonances. In particular, we study two types of hybrid resonances — those arising in a coupled cavity-antenna system (Chapters 2 to 8), and so-called 'bound states in the continuum' (Chapter 9).

Chapter 1 introduces the concept of light-matter interaction and summarizes the current best efforts at controlling this interaction through optical cavities, plasmonic antennas or combinations thereof. We then continue with a theoretical study of hybrid cavity-antenna systems. In Chapter 2, we develop a simple and intuitive model, based on coupled harmonic oscillators, to describe the interaction between a plasmonic antenna and a cavity resonance. Despite its simplicity, the model captures the essential physics of this interaction, and holds for any cavity or antenna geometry. It connects in one framework various properties of such systems, including mode hybridization, cavity perturbation, modifications of the local density of states (LDOS) and photon collection efficiency. This chapter lays the foundations for analyses performed in several subsequent chapters.

Chapter 3 employs the coupled-oscillator model to study theoretically the LDOS in cavity-antenna hybrids. We demonstrate that hybrids can support larger LDOS than their bare constituents. The conditions for such symbiotic behaviour, however, are far from trivial. We find that, contrary to intuition, operating near antenna resonance is detrimental to LDOS due to destructive interference between cavity and antenna. In contrast, at frequencies red-detuned from the antenna resonance, constructive interference can lead to very large LDOS, even breaking a fundamental limit governing the LDOS for a single antenna. Moreover, we show how hybrid systems can be designed to support quality factors Q and mode volumes V anywhere in between those

of the cavity and of the antenna. Also, photon collection efficiency can be high, despite plasmonic losses. These properties make them very attractive candidates for single-photon sources, which require efficient operation, large LDOS and bandwidths matching those of realistic emitters.

Chapter 4 applies concepts from electrical engineering to hybrid cavity-antenna systems by developing a circuit analogy for these hybrids. Since this is based on an analogous circuit for a nano-antenna, we first discuss two different versions of such a circuit from literature and show that the two are equivalent. We then find the circuit for a hybrid system and show how a cavity can help an antenna reach an upper limit on radiation, set by the maximum power transfer theorem. This limit compliments the well-known unitary limit on antenna radiation, and we elucidate the interplay between these limits for lossy antennas. Our results show that cavities act as conjugate-matching networks at optical frequencies, matching the antenna to its radiation load. Such networks allow maximum power transfer from a lossy generator to a load and are common in radio-frequency network engineering, yet they have remained elusive at optical frequencies.

Having established theoretically that hybrid systems are a promising platform for strong light-matter interactions, and having found design rules to benefit optimally from these interactions, Chapter 5 then takes us to the experimental work. This chapter describes the fabrication of cavity-antenna systems, loaded with fluorescent quantum dots. Hybrid systems composed of whispering-gallery-mode microdisk cavities and aluminium antennas are fabricated with high precision and repeatability using a two-step lithography process. A study of LDOS effects requires fluorescent emitters, positioned accurately in the hybrid system. We present a novel method to deterministically position fluorescent colloidal quantum dots in such systems, which uses a PMMA resist mask and a linker molecule to covalently bind the dots to the hybrid structures. This allows highly selective placement of quantum dots with lithographic resolution.

The hybrid systems fabricated as described in Chapter 5 are studied experimentally in Chapter 6. A crucial property of cavity-antenna hybrids is the ability to tune the bandwidth over a large range, which enables coupling to realistic emitters. Here, we experimentally observe more than two orders of magnitude linewidth tuning in hybrid systems, simply by changing antenna length. For this, we measure antenna-induced linewidth broadening and shifts for antennas and disks of various sizes, using a combination of tapered-fiber spectroscopy and free-space microscopy. We show that our results can be explained using cavity perturbation theory, and observe a deviation from this theory at antenna sizes for which the dipole approximation breaks down.

In Chapter 7 we put the theoretical predictions from Chapter 3 — which state that LDOS can be strongly boosted in a hybrid system — to the test. Fluorescence spectra, measured on the hybrid systems loaded with quantum

dots, reveal Fano-type asymmetric resonances. These arise due to quantum dot emission into the hybrid modes. Our results demonstrate that LDOS is strongly boosted at these modes, up to 14 times higher than the LDOS provided by the antenna alone. While LDOS is commonly measured through a change of the fluorescent decay rate of the emitter, we argue that, for a broadband emitter coupled to a narrowband LDOS resonance, *relative* LDOS can be obtained from the emission spectrum. Our analysis is supported by an excellent agreement between theory and experiment in the linewidth, -shape and fluorescence boosts. Additionally, fluorescence decay rate measurements show a strong increase of decay rate, which we attribute mainly to the antenna. Combined, these results demonstrate that large LDOS enhancements are possible in hybrid systems.

Rich new physics arises when a cavity is coupled not just to a single antenna, but instead to a lattice of antennas. In Chapter 8 we experimentally study such an antenna lattice, coupled to an ultra-high-Q microtoroid cavity. Through an intricate extinction measurement performed in reflection, we find that back-action by the cavity on the antennas causes a strong suppression of the antenna polarizability. This matches the theoretical prediction in Chapter 3 for a single antenna, which stated that an antenna is spoiled by a cavity if both are on resonance. There are, however, important differences between a single scatterer and a lattice. We show that in a lattice, antenna-cavity coupling can be modified by changing the angle of incidence, because this coupling requires momentum-matching between the Bloch waves in the lattice and the cavity mode.

The final Chapter 9 of this thesis studies hybrid resonances of a different type. Bound states in the continuum (BICs) are modes found, for example, inside a photonic crystal slab, which are normally leaky yet become perfectly bound at one particular wavelength. Such states were observed experimentally only recently in optics and are puzzling from a fundamental point of view, as well as interesting for applications due to their (theoretically) infinite photon lifetime. We experimentally demonstrate that such a state coincides with a polarization vortex in momentum-space. To do so, we develop a new ellipsometry method to quickly measure polarization-resolved reflection at many angles and wavelengths. The existence of the vortex implies that the BIC is topologically protected, such that it is robust against small variations in geometry. Moreover, we demonstrate that a hybridized resonance underlies the perfect confinement of this mode. An electric and a magnetic dipole resonance inside the crystal unit cell couple through interference in the far-field, leading to a perfectly bound state when complete destructive interference between the two is achieved.

Samenvatting

Licht is de energiebron van biologisch leven en stelt ons in staat om de wereld om ons heen waar te nemen. Tegenwoordig staat licht ook aan de basis van een groot aantal moderne technologiëen. Het wordt gebruikt om beelden te maken van onze cellen en van verre sterrenstelsels, om bewegingen kleiner dan een atoom of individuele virusdeeltjes in bloed te detecteren. Men kan er minuscule patronen mee schrijven op een computerchip, of enorme hoeveelheden data mee versturen. Voor deze en andere toepassingen is het cruciaal dat we controle hebben over hoe licht zich voortplant en over de wisselwerking tussen licht en materie. Hiervoor worden optische resonatoren gebruikt — een soort 'klankkasten' voor licht, die het licht opslaan en concentreren. Onder deze resonatoren vindt men twee uitblinkers: optische (micro)trilholtes, die licht soms wel miljoenen trillingen kunnen vasthouden, en plasmon-antennes, die licht kunnen samenpersen tot een schaal ver onder diens golflengte. Hoewel beide succesvol worden toegepast, is elk van hen onderworpen aan fundamentele limieten die implementatie op grote schaal, bijvoorbeeld als elementen in een optisch kwantumnetwerk, op dit moment in de weg staan. In dit proefschrift onderzoeken wij hoe hybride resonanties deze limieten kunnen omzeilen en nieuwe manieren bieden om licht op te slaan en te geleiden. Zulke resonanties combineren twee of meerdere eigentoestanden tot een verrassend nieuw soort resonantie, die meer is dan de som van de twee onderliggende componenten. Wij kijken in het bijzonder naar twee soorten hybride resonanties — diegene die ontstaat in een gekoppeld trilholte-antenne systeem (Hoofdstuk 2 tot 8) en een soort die we een 'gevangenis zonder muren' zullen noemen (Hoofdstuk 9).

Hoofdstuk 1 introduceert het concept van licht-materie interactie en geeft een overzicht van de huidige stand van de wetenschap wat betreft het versterken van deze interactie door gebruik van optische trilholtes, antennes of combinaties hiervan. Hierna beginnen we met een theoretische studie van hybride trilholte-antenne systemen. In Hoofdstuk 2 ontwikkelen we een intuïtief model, gebaseerd op gekoppelde harmonische oscillatoren, dat de interactie tussen een plasmon-antenne en een trilholte beschrijft. Ondanks zijn eenvoud beschrijft dit model de essentie van deze interactie en is het toepasbaar op ieder type antenne of trilholte. Dit hoofdstuk schept een theoretisch kader om de verscheidene fenomenen in hybride systemen te begrijpen en vormt tevens de basis voor veel van de analyses in latere hoofdstukken.

In Hoofdstuk 3 wordt ons gekoppelde-oscillator model gebruikt om de lokale toestandsdichtheid (LDOS) in hybrides van trilholtes en antennes te bestuderen. Deze LDOS bepaalt de levensduur van fluorescente bronnen in het systeem en meet de sterkte van interactie tussen licht en materie. De resultaten tonen aan dat hybrides hogere LDOS kunnen hebben dan de trilholte of antenne alleen. Dit gebeurt echter onder zeer tegenintuïtieve voorwaarden.

Zo is het voor de LDOS funest om bij frequenties rond de antenneresonantie te werken, waar destructieve interferentie de LDOS juist onderdrukt. Bij lagere frequenties daarentegen kan de LDOS in hybrides zelfs een fundamentele limiet voor een enkele antenne doorbreken. Ook laten we zien dat hybrides nog meer voordelige eigenschappen hebben ten opzichte van de antenne en trilholtes alleen. Hun bandbreedte en het volume waarin het licht samengeperst wordt kunnen namelijk vrijwel elke gewenste waarde tussen die van de antenne en de trilholte aannemen. Tegelijkertijd kan de collectie-efficiëntie hoog zijn. Deze eigenschappen maken hybrides interessant als bronnen van enkele fotonen, waarvoor hoge efficiëntie, hoge LDOS en praktische bandbreedtes nodig zijn.

Hoofdstuk 4 beschrijft dezelfde hybride trilholte-antenne systemen met behulp van een equivalent stroomcircuit. Dit maakt het mogelijk om kennis uit de radartechnologie, waar dit soort circuits al decennia worden gebruikt, op onze hybrides toe te passen. Twee verschillende, eerder in de literatuur voorgestelde circuits voor een enkele nano-antenne worden besproken, waarbij we laten zien dat deze equivalent zijn. Vervolgens laten we met het circuit voor een hybride zien hoe een trilholte een antenne kan helpen om een fundamentele limiet voor diens lichtverstrooiing te bereiken, die volgt uit een bekend theorema uit de circuitleer. Dit toont aan dat trilholtes werken als geconjugeerde koppelingsnetwerken bij optische frequenties — netwerken die een stroom- of spanningsbron met een complexe weerstand verbinden op zo'n manier dat het overgedragen vermogen maximaal is.

Waar Hoofdstuk 2 tot 4 theoretisch aantonen dat hybrides van trilholtes en antennes veelbelovend zijn en ontwerpregels geven om hun prestaties te optimaliseren, begint met Hoofdstuk 5 het experimentele werk. Dit hoofdstuk beschrijft hoe deze hybrides gemaakt kunnen worden en voorzien kunnen worden van fluorescente nanokristallen. Met een tweestaps lithografie proces plaatsen we aluminium nano-antennes met hoge precisie en reproduceerbaarheid bovenop trilholtes in de vorm van een microschijf. Om LDOS te kunnen meten, moeten ook fluorescente lichtbronnen geplaatst worden. We presenteren daarom een nieuwe methode om fluorescente nanokristallen op hybrides te plaatsen, gebruik makend van een PMMA masker en een moleculaire link om de nanokristallen aan de hybride te binden. Hiermee bereiken we zeer hoge selectiviteit en lithografische precisie.

Hoofdstuk 6 is gewijd aan experimenteel onderzoek naar de eigentoestanden van onze hybride systemen. Een belangrijke eigenschap van hybrides is de mogelijkheid om hun bandbreedte te kiezen over een groot bereik. In dit experiment observeren we een verandering van de bandbreedte in een hybride systeem van meer dan twee ordes van grootte, enkel door de lengte van de antenne te veranderen. Hiervoor gebruiken we een combinatie van nauwbandige spectroscopie en microscopie en meten we de eigenschappen van hybrides met verschillende afmetingen antennes en microschijven. Voor kleine antennes kunnen onze resultaten goed verklaard worden met storings-

theorie, terwijl we een afwijking van deze theorie zien voor antennes die zo groot worden dat de dipoolbenadering niet langer opgaat.

Een van de meest opzienbarende voorspellingen uit Hoofdstuk 3 is dat de LDOS sterk verhoogd kan worden in een hybride systeem. In Hoofdstuk 7 testen we deze voorspelling in een experiment. We meten hiervoor fluorescentiespectra van de nanokristallen op de hybride systemen. Deze laten asymmetrische Fano-resonanties zien, die ontstaan omdat de kristallen bij voorkeur licht uitzenden in de hybride eigentoestanden. Onze resultaten laten zien dat LDOS inderdaad sterk is toegenomen, tot wel 14 keer hoger dan de LDOS van de losse antenne. Hoewel LDOS gewoonlijk gemeten wordt via een verandering in de levensduur van een fluorescente lichtbron, betogen wij dat, in het geval van een breedbandige lichtbron gekoppeld aan een nauwbandige LDOS-resonantie, de *relatieve* LDOS via het spectrum gemeten kan worden. Een goede overeenkomst tussen onze data en theorie bevestigt deze stelling. Daarnaast meten we ook de levensduur van de nanokristallen in de hybride systemen. Deze blijkt sterk verkort, wat we hoofdzakelijk toewijzen aan de antenne. De combinatie van deze resultaten laat zien dat zeer hoge LDOS inderdaad behaald kan worden in hybride systemen.

Wanneer men een trilholte niet met een enkele antenne maar met een rooster van antennes koppelt, ontstaan interessante nieuwe fenomenen. In Hoofdstuk 8 doen we een experiment met een dergelijk systeem. Door de extinctie van het rooster in reflectie te meten, ontdekken we dat terugkoppeling door de trilholte op de antennes zorgt voor een sterke vermindering in polariseerbaarheid van de antenne. Hoewel dit strookt met een voorspelling uit Hoofdstuk 3 voor een trilholte en een enkele antenne, zijn er ook belangrijke verschillen tussen een enkele antenne en een rooster. Zo laten wij zien dat de koppelingssterkte tussen antennes en trilholte afhangt van de hoek van inval waarbij gemeten wordt, omdat voor deze koppeling behoud van impuls tussen de Bloch-golven in het rooster en het licht in de trilholte vereist is.

Ten slotte behandelt Hoofdstuk 9 een ander type hybride resonantie. Er bestaan structuren, zoals sommige fotonische kristallen, waarin licht in een perfect opgesloten toestand terecht kan komen, ondanks het feit dat deze toestand gekoppeld is aan uitgaande golven en het licht dus eigenlijk zou moeten weglekken. Deze 'gevangenis zonder muren' — de toestand waarin het licht gevangen zit — is ooit voorspeld in de kwantummechanica voor elektronen, maar is recent experimenteel geobserveerd voor licht. De toestand is interessant vanwege zijn raadselachtige oorsprong, maar ook voor toepassingen vanwege de potentieel oneindige opslagtijd. Wij laten experimenteel zien dat deze toestand samenvalt met een polarisatievortex in het stralingspatroon van het kristal. Hiervoor ontwikkelen we een nieuwe type ellipsometrie waarmee we snel de polarisatie-afhankelijke reflectie kunnen meten bij vele invalshoeken en golflengtes. Het bestaan van de vortex impliceert dat deze toestand topologisch beschermd is, dus bestand is tegen kleine geometrische veranderingen. Ook tonen wij aan dat de perfecte opsluiting van deze toe-

stand veroorzaakt wordt door een hybride resonantie. Een elektrische en magnetische dipoolresonantie in het kristal koppelen door interferentie in het verre veld, wat leidt tot perfecte opsluiting precies dan wanneer complete destructieve interferentie wordt bereikt.

List of publications

Related to this thesis

1. H. M. Doeleman, E. Verhagen and A. F. Koenderink, *Antenna-cavity hybrids: matching polar opposites for Purcell enhancements at any linewidth*, ACS Photonics **3**, 1943–1951 (2016). (**Chapter 2 and 3**)

2. H. M. Doeleman, A. Alù, F. Monticone and A. F. Koenderink, *Cavities as conjugate-matching networks for antennas at optical frequencies*, in preparation. (**Chapter 4**)

3. H. M. Doeleman and A. F. Koenderink, *Orders-of-magnitude linewidth tuning in hybrid cavity-antenna systems*, in preparation. (**Chapter 5 and 6**)

4. H. M. Doeleman, C. Dieleman, B. Ehrler and A. F. Koenderink, *Observation of strong and tunable fluorescence enhancement in hybrid systems*, in preparation. (**Chapter 5 and 7**)

5. F. Ruesink*, H. M. Doeleman*, E. Verhagen and A. F. Koenderink, *Controlling nanoantenna polarizability through backaction via a single cavity mode*, Phys. Rev. Lett. **120**, 206101 (2018). (**Chapter 8**)

6. H. M. Doeleman, F. Monticone, W. den Hollander, A. Alù and A. F. Koenderink, *Experimental observation of a polarization vortex at an optical bound state in the continuum*, Nat. Photonics **12**, 397 (2018). (**Chapter 9**)

Other

7. F. Ruesink, H. M. Doeleman, R. Hendrikx, A. F. Koenderink, and E. Verhagen, *Perturbing open cavities: anomalous resonance frequency shifts in a hybrid cavity-nanoantenna system.*, Phys. Rev. Lett. **115**, 203904 (2015)

8. F. Monticone, H.M. Doeleman, W. den Hollander, A.F. Koenderink and A. Alù, *Trapping light in plain sight: embedded photonic eigenstates in zero-index metamaterials*, Laser Photon. Rev. **12**, 1700220 (2018).

9. K.C. Cognée, H.M. Doeleman, P. Lalanne and A.F. Koenderink, *Perturbation of whispering-gallery-mode resonances by plasmonic phased arrays*, in preparation.

* These authors contributed equally.

Acknowledgements

No man is an island entire of itself; every man
is a piece of the continent, a part of the main;
...

John Donne

Why do people work? What makes them love it, despite the setbacks, despite the dull parts or the anxiety over if your work is good enough? For me, this comes down to three things. I love creating beautiful things, I love to learn, and I love the thrill of discovery. Doing a PhD at AMOLF has offered me all these joys. Yet, that would not have been the case if it had not been for the help of others.

I am immensely thankful to my advisor, Femius. I came here to learn, and most of that learning was from you. In the five and a half years we've worked together, your vast knowledge and quick mind have never ceased to amaze me. You've taught me the essentials of being an experimental physicist — from aligning mirrors to choosing the right detector — but also to appreciate the value of a well-performed experiment, regardless of the outcome. You've given me the theoretical tools to understand my experiments, from coupled-dipole theory to the right choice of simulation mesh. But it is not sufficient for a scientist to just do measurements, we should also be able to convey their outcome to an audience. So you've helped me to structure my writing and to identify the novelty of my work. Besides these valuable lessons, I have enjoyed our hikes through Utah and your enthusiasm about peculiar rock formations... I don't think a young scientist could wish for a better training.

A PhD can be lonely, if one carries the responsibility for a project alone. Yet I have never felt like this, owing mostly to the great people with which I have had the joy of collaborating. Freek, thank you for the code, for the laughs, for the toroids, for the shared outrage, for the discussions about life after our PhDs and for being such a pleasant and structured counterbalance to my occasional chaos. Kevin, thank you for always being ready to discuss results, for sharing the joys and frustrations of tapers and Victorinox, for being always open and honest, occasionally offensive, and for being a true Fountainhead — you seem to have a new idea every week (all of them interesting, some also feasible). Wouter, thank you for your great work on our BIC-project, for making me run faster, for your trust in me and for the positive attitude that made working with you a pleasure. Isabelle, you lit up our office and our group with your positivity and your comics. I am already enjoying the project we just started. Thank you for Shania Twain, for the melons, for the balloons and the puns. Stay just the way you are. Francesco, working with you has been inspirational. You ooze creative genius, and like all good scientists, your

interests go far beyond your own expertise. In fact, yours even extend to psychology, specifically the reception of Deepak Chopra. I think we form a great team and I am very proud of our results. Andrea, thank you for the fantastic ideas you have brought forward during our many discussions. Your contributions to our group and to our joint projects have strongly broadened my perspective on physics. Christiaan, thank you for taking over the hybrid experiments, and for the great ideas you have had to improve on my initial efforts. I am glad that you will continue this work, and I am confident great things will come out. Ewold, I am grateful for your crucial help in kick-starting the hybrid theory project, and for the many discussions we have had since then, not just about science. I was always welcome to drop by your office if I had a question, which I often did and which has always been helpful. Christian and Bruno, your vast knowledge of quantum dots and your help in the functionalization process we developed has been invaluable.

Physics is great. But unlike some physicists think, we cannot do everything. Luckily, at AMOLF we simple researchers are surrounded by people who can help us overcome the vast gaps in our capabilities. Dimitry, Andries, Bob and Hans, thank you for teaching me about nano-fabrication, for developing part of my fabrication process and for running a beautiful facility. One of the results I am most proud of — the fabrication of antenna-cavity hybrids — would have been impossible without your work. Marko, Brahim, Idsart, and Niels, thank you for helping me set up my experiments, building Victorinox and developing a beautiful software package that enabled my measurements. Henk-Jan, Iliya and Ricardo, in another life I might have become a mechanical designer. One of the things I loved most about my work, was brainstorming with you about mechanical designs. Perhaps that is why I started so many hobby projects like night lamps, plastic toroids and necklaces... Somehow, you always manage to turn my messy hand-drawn sketches into a beautiful and functional design. For creating my experimental setup, as well as helping with these hobby projects, I am very grateful to Hinco and the guys at the mechanical workshop as well, in particular Wouter, Mark, Niels, Jan and Tom. Often I have felt a little jealous of you — you create something beautiful every day. Floortje, thank you for making my life — and surely that of everybody at AMOLF — so much easier and so much more fun.

I am very grateful to the current and past members of the Resonant Nanophotonics group — Martin, Andrej, Felipe, Abbas, Lutz, Hinke, Clara, Cocoa, Floor, Mengqi, Alessandro, Remmert, Kevin, Annemarie, Wouter, Christiaan, Noor, Ruslan, Chris, Isabelle, Remi, Radoslaw, Ilse, Sylvianne and Tomas — with whom I have always freely shared ideas, testing their validity and getting ideas for new directions. Thank you for being inventive and critical and for taking the time. All of you have inspired me during my time at AMOLF, yet I want to mention some in particular. Thank you Martin for guiding me through my first steps into nanophotonics, and through an important life choice. Thank you Clara for being a social cornerstone to our

group. Thank you Annemarie for showing that its possible to be a great physicist *and* pop sick dance moves.

AMOLF is formed not out of isolated groups, but out of a cohesive body of researchers and support staff who share results, frustrations, equipment and most of all coffee. I am grateful for this collaborative atmosphere, and for all the great people at AMOLF that made it so. Benjamin B., thanks for all the coffee talk and for owning the dancefloor, every time. Sander, Ruben, Parisa, Jorik, Verena, Mark, Andrea, Jenny, Nick, Freek, Nikhil, Toon, Juha, Giada, Rick, Sophie, Said, David, Robin, Beniamino, Sebastian, Lorenzo, Dolphine, Filippo, Moritz, Christian, Benjamin D., Hans, Lukas and Giorgio, thank you for being an inspiration, for all the fun and for the help.

Much of what I learned was learned during the Nanophotonics colloquia or poster sessions, so I am deeply indebted to those group leaders at AMOLF that have organised and participated in these — Albert, Femius, Ad, Kobus, Esther, Said, Ewold, Erik, Bruno, and Jaime.

Robert Spreeuw, Klaasjan van Druten and Ben van Linden van den Heuvell, thank you for all the time you have taken and for all your valuable input on my work. I was extremely fortunate to have such devoted advisors.

Deze promotie heeft veel van mijn tijd gevraagd, dus ik ben dankbaar dat mijn vrienden en familie desalniettemin geduldig zijn geweest en mij altijd hebben gesteund. Ove, Folkert en Arthur, dank dat jullie nooit hebben nagelaten mijn academische ambities belachelijk te maken. Wat zijn die publicaties immers waard als je 5-0 achterstaat met Fifa? Lieve ouders, niks van dit was gelukt zonder jullie steun. Lieve Lotte en Susanne, ik vind het heerlijk dat wij elkaar door alle bedrijven heen zo veel blijven zien en dat het altijd zo voelt als thuis. Ik ben mijn ouders, zusjes en schoonouders Frits en Agnes ook ontzettend dankbaar voor alle hulp in het afgelopen jaar. Het schrijven van dit proefschrift, dat samenviel met de geboorte van Elias, is alleen maar mogelijk geweest dankzij jullie hulp. Ten slotte, lieve Simone, wat zou dit allemaal voor zin hebben gehad zonder jou? Dank voor je geduld, maar ook voor je ongeduld als ik weer eens te lang door ging. Dank voor al je ideeën en dank dat je me ten minste met één been op de grond houdt.

About the author

Hugo Michiel Doeleman was born in Amsterdam. In 2011 he obtained a BSc degree ('cum laude') in Physics and Astronomy at the University of Amsterdam (UvA), for which he spent one year on an exchange program at the Technical University of Vienna, Austria. In 2013 he graduated with a Master's degree ('cum laude') in Physics at the University of Amsterdam. During his Master's program he performed research at AMOLF, Amsterdam, to write a short thesis on solar cell efficiency limits, supervised by prof. dr. Albert Polman, and his main thesis on light scattering by cavity-antenna hybrid systems, supervised by prof. dr. Femius Koenderink and dr. Ewold Verhagen. After a brief period working in Indonesia as a business development manager at an online start-up owned by Rocket Internet, he started a PhD in the research group of prof. dr. Femius Koenderink at AMOLF in 2014. The results of his PhD research are presented in this thesis.

For the 'Faces of Science' program by the Royal Dutch academy of Sciences (KNAW), Hugo writes popular blogs on topics related to his PhD, which can be found online. In his spare time, he likes to sing and he enjoys sports like running, snowboarding and golf. He is father to a son, Elias (2018).